Synthesis and Implementation of Sensor-less Shunt Controllers for Piezoelectric and Electromagnetic Vibration Control

Andrew J. Fleming

B.E. (Elec.) Hons.

*A thesis submitted in fulfilment
of the requirements for the degree of*

Doctor of Philosophy

School of Electrical Engineering
and Computer Science

The University of Newcastle
Callaghan, N.S.W. 2308
Australia

February, 2004

The UNIVERSITY
of NEWCASTLE

AUSTRALIA

Declaration

I hereby certify that the work embodied in this thesis is the result of original research and has not been submitted for a higher degree to any other University or Institution.

_____

Andrew J. Fleming

February, 2004

ACKNOWLEDGEMENTS

Research in this area is an undertaking requiring much support in the areas of infrastructure, theoretical expertise, mechanical design, manufacturing, and electronics. To the fulfillment of these requirements, I have the following individuals to acknowledge.

I would like to thank my supervisor Dr. S. O. Reza Moheimani for his support and guidance throughout the course of this research.

I am also indebted to my colleague Dr. Sam Behrens for his assistance in mechanical design and fabrication, electrical fabrication, physical modeling, and theoretical analysis. I would also like to thank my other colleagues, Mr. Dominik Niederberger and Mr. Ben Vautier whose discussion and suggestions have contributed much to the content of my research. Dr. Will Heath and Dr. Adrian Wills have also been of great assistance in mathematical matters.

The department technical staff, Mr. Ian Powell, Mr. Roy Murcott, and Mr. Russell Hicks have been an invaluable source of experience in the design and manufacture of electronic instruments and mechanical devices.

On a personal note, I'd also like to thank my good friends Sam, Glenn, Pete, Ben, and Simon, whose company have made my time in Newcastle both enjoyable and productive.

LIST OF PUBLICATIONS

Outcomes throughout the course of this research have included: 3 patent applications, a research monograph, 15 international journal papers, and 20 conference papers. Details are listed below.

Patent Applications

1. *An Impedance Synthesizing Arrangement, an Improved Vibrational Damping Apparatus and a Method for Deriving a Digital Signal Processing Algorithm.*
   A. J. Fleming, S. Behrens, S. O. R. Moheimani
   PCT/AU01/00566   US Appln. No. 10/295822

2. *A Vibrational Damping System And a System for Harvesting Power from Structure Subject Vibrational Excitation.*
   A. J. Fleming, S. O. R. Moheimani
   Provisional

3. *An Electromagnetic Vibrational Damping Apparatus.*
   S. Behrens, A. J. Fleming, S. O. R. Moheimani
   Provisional

Books

1. *Spatial Control of Vibration.*
   S. O. R. Moheimani, D. Halim, A. J. Fleming
   World Scientific, ISBN 981-238-337-9

Journal Papers

1. *Control Orientated Synthesis of High Performance Piezoelectric Shunt Impedances for Structural Vibration Control.*
   A. J. Fleming, S. O. R. Moheimani
   IEEE Transactions on Control Systems Technology
   In Press

2. *Electromagnetic Shunt Damping for Passive Vibration Control.*
   A. J. Fleming, S. O. R. Moheimani
   IEEE/ASME Transaction on Mechatronics
   In Press

3. *Improved Current and Charge Amplifiers for Driving Piezoelectric Loads, and Issues in Signal Processing Design for Synthesis of Shunt Damping Circuits.*
   A. J. Fleming, S. O. R. Moheimani
   Journal of Intelligent Material Systems and Structures
   February 2004, Volume 15, Number 2, Pages 77-92

4. *Dynamics, Control, and Stability of Multivariable Piezoelectric Shunts.*
   A. J. Fleming, S. O. R. Moheimani, S. Behrens
   IEEE Transactions on Mechatronics
   In Press

5. *Precision Current and Charge Amplifiers for Driving Highly Capacitive Piezoelectric Loads.*
   A. J. Fleming, S. O. R. Moheimani
   IEE Electronics Letters
   Febuary 2003, Volume 39, Number 3, Pages 282-284

6. *On the Feedback Structure of Wideband Piezoelectric Shunt Damping Systems.*
   S. O. R. Moheimani, A. J. Fleming, S. Behrens
   IOP Smart Material and Structures
   January 2003, Volume 12, Pages 49-56

7. *Spatial System Identification of a Simply Supported Beam and a Trapezoidal Cantilever Plate.*
   A. J. Fleming, S. O. R. Moheimani
   IEEE Transactions on Control System Technology
   September 2003, Volume 11, Number 5, Pages 726-736

8. *Multiple Mode Current Flowing Passive Piezoelectric Shunt Controller.*
   S. Behrens, S. O. R. Moheimani, A. J. Fleming
   Journal of Sound and Vibration
   October 2003, Volume 5, Pages 929-942

9. *Reducing the Inductance Requirements of Piezoelectric Shunt Damping Systems.*
   A. J. Fleming, S. Behrens, S. O. R. Moheimani
   IOP Smart Materials and Structures
   January 2003, Volume 12, Pages 57-64

10. *A Highly Resonant Controller for Multi-mode Piezoelectric Shunt Damping.*
    S. O. R. Moheimani, A. J. Fleming, S. Behrens
    IEE Electronics Letters
    December 2001, Volume 37, Number 25, Pages 1505-1506

11. *A Broadband Controller for Piezoelectric Shunt Damping of Structural Vibration.*
    S. Behrens, A. J. Fleming, S. O. R. Moheimani
    IOP Smart Materials and Structures
    January 2003, Volume 12, Pages 18-28

12. *Adaptive Piezoelectric Shunt Damping.*
    A. J. Fleming, S. O. R. Moheimani
    IOP Smart Materials and Structures
    January 2003, Volume 12, Pages 36-48

13. *Optimization and Implementation of Multimode Piezoelectric Shunt Damping Systems.*

     A. J. Fleming, S. Behrens, S. O. R. Moheimani

     ASME/IEEE Transactions on Mechatronics

     March 2002, Volume 7, Number 1, Pages 87-94

14. *Subspace Based System Identification for an Acoustic Enclosure.*

     T. McKelvey, A. J. Fleming, S. O. R. Moheimani

     ASME Transactions on Vibration and Acoustics

     July 2002, Volume 124, Number 3, Pages 414-419

15. *Synthetic Impedance for Implementation of Piezoelectric Shunt Damping Circuits.*

     A. J. Fleming, S. Behrens, S. O. R. Moheimani

     IEE Electronics Letters

     August 2000, Volume 36, Number 18, Page 1525

Conference Proceedings

1. *Vibration Isolation Device Using a Shunted Electromagnetic Transducer.*
   S. Behrens, A. J. Fleming, S. O. R. Moheimani
   SPIE Smart Structures and Materials 2004, Damping and Isolation.
   March 2004, San Diego, CA

2. *Synthesis of Optimal Piezoelectric Shunt Impedances for Structural Vibration Control.*
   A. J. Fleming, S. O. R. Moheimani
   SPIE Smart Structures and Materials 2004, Damping and Isolation.
   March 2004, San Diego, CA

3. *Active H_2 and H_∞ Shunt Control of Electromagnetic Transducers.*
   A. J. Fleming, S. Behrens, S. O. R. Moheimani
   IEEE Conference on Decision and Control
   December 2003, Maui, HI

4. *Electromagnetic Shunt Damping.*
   S. Behrens, A. J. Fleming, S. O. R. Moheimani
   IEEE/ASME Int. Conference on Advanced Intelligent Mechatronics
   July 2003, Kobe, Japan

5. *Electrodynamic Vibration Suppression.*
   S. Behrens, A. J. Fleming, S. O. R. Moheimani
   SPIE Smart Structures and Materials 2003, Damping and Isolation
   March 2003, San Diego, CA

6. *Improved Current and Charge Amplifiers for Driving Piezoelectric Loads.*
   A. J. Fleming, S. O. R. Moheimani
   SPIE Smart Structures and Materials 2003, Damping and Isolation
   March 2003, San Diego, CA

7. *Robust Piezoelectric Passive Shunt Dampener.*
    A. J. Fleming, S. Behrens, S. O. R. Moheimani
    SPIE Smart Structures and Materials 2003, Damping and Isolation
    March 2003, San Diego, CA

8. *An Autonomous Piezoelectric Shunt Damping System.*
    A. J. Fleming, S. O. R. Moheimani
    SPIE Smart Structures and Materials 2003, Damping and Isolation
    March 2003, San Diego, CA

9. *Dynamics and Stability of Wideband Vibration Absorbers with Multiple Piezoelectric Transducers.*
    S. O. R. Moheimani, S. Behrens, A. J. Fleming
    IFAC Mechatronics 2002
    December 2002, Berkeley, CA

10. *Series-Parallel Impedance Structure for Piezoelectric Vibration Damping.*
    S. Behrens, A. J. Fleming, S. O. R. Moheimani
    SPIE Smart Materials, Nano-, and Micro Smart Systems
    December 2002, Melbourne, Australia

11. *The Effect of Artificially Reducing the Size of Inductor Values in Piezoelectric Shunt Damping Circuits.*
    A. J. Fleming, S. O. R. Moheimani
    IFAC Mechatronics 2002
    December 2002, Berkeley, CA

12. *Power Harvesting Piezoelectric Shunt Damping.*
    A. J. Fleming, S. O. R. Moheimani
    IFAC Mechatronics 2002
    December 2002, Berkeley, CA

13. *Spatial System Identification of a Simply Supported Beam and a Trapezoidal Cantilever Plate.*

    A. J. Fleming, S. O. R. Moheimani

    IEEE Conference on Decision and Control 2002

    December 2002, Las Vegas, NV

14. *Multiple Mode Passive Piezoelectric Shunt Dampener.*

    S. Behrens, S. O. R. Moheimani, A. J. Fleming

    IFAC Mechatronics 2002

    December 2002, Berkeley, CA

15. *On the Feedback Structure of Wideband Piezoelectric Shunt Damping Systems.*

    S. O. R. Moheimani, A. J. Fleming, S. Behrens

    IFAC World Congress

    2002, Barcelona, Spain

16. *New Method for Multiple-mode Shunt Damping of Structural Vibration using a Single Piezoelectric Transducer.*

    S. Behrens, A. J. Fleming, S. O. R. Moheimani

    SPIE Smart Structures and Materials, Damping and Isolation

    2001, Newport Beach, CA

17. *Adaptive Piezoelectric Shunt Damping.*

    A. J. Fleming, S. O. R. Moheimani

    SPIE Smart Structures and Materials

    March 2002, San Diego, CA

18. *Innovations in Piezoelectric Shunt Damping.*

    A. J. Fleming, S. Behrens, S. O. R. Moheimani

    SPIE Smart Structures and Devices

    December 2000, Melbourne, Australia

19. *Subspace Based System Identification of an Acoustic Enclosure.*

    T. McKelvey, A. J. Fleming, S. O. R. Moheimani

    IEEE International Conference on Control.

    September 2000, Anchorage, Alaska

20. *A New Approach to Piezoelectric Shunt Damping.*

    A. J. Fleming, S. Behrens, S. O. R. Moheimani

    IS3M International Symposium on Smart Structures and Microsystems

    October 2000, Hong Kong

To my parents, Graeme and Cathy Fleming

for your love and support.

CONTENTS

3   Implementation   37

ABSTRACT

Mechanical systems experience undesirable vibration in response to environmental and operational forces. Slight vibrations can limit the accuracy of sensitive instruments or cause error in micro- and nano-manufacturing processes. Larger vibrations, as experienced by load bearing structures, can cause fatigue and contribute to mechanical failure. The suppression of vibration is a necessity in many scientific and engineering applications.

Piezoelectric and electromagnetic transducers have been employed in countless applications as sensors, actuators, or both. In cases where traditional passive mechanical vibration control is inadequate, piezoelectric and electromagnetic actuators have been used within feedback control systems to suppress vibration. A counter-active force is applied in response to a measured vibration.

In this work, a new approach to the control of mechanical vibration is introduced. By presenting an appropriately designed electrical impedance to the terminals of a piezoelectric or electromagnetic transducer, vibration in the host structure can be suppressed. Standard LQG, $\mathcal{H}_2$, and $\mathcal{H}_\infty$ synthesis techniques are employed to facilitate the design of optimal shunt impedances. No feedback sensor or auxiliary transducer is required.

Vibration control problems are typically based on the minimization of displacement or velocity at a single point. For spatially distributed systems, such as aircraft wings, any single point may not suitably represent the overall structural vibration. Spatial system identification is introduced as a method for procuring global models of flexible structures. Spatial models can be used to properly specify the performance objective of an active vibration control system.

Experimental results are presented throughout to clarify and validate the concepts presented.

1

INTRODUCTION

Piezoelectric transducers have found countless application in such fields as vibration control [49], nano-positioning [28], acoustics [97], and sonar [110]. This work is concerned with the application of piezoelectric transducers in the field of structural noise and vibration control.

1.1 Piezoelectric Transducers

The phenomenon where a volume of material undergoes shape transformation when exposed to an electric field *and vice-versa*, is known as the piezoelectric effect. Pierre and Jacques Curie originally documented this effect in 1880 after observing the accumulation of electric charge on the surface of certain crystals under stress. After further investigation they were also able to demonstrate the complimentary effect where an applied field results in deformation.

A number of naturally occurring materials exhibit weak piezoelectric behaviour, examples include: quartz, tourmaline, topaz, and Rochelle salt [18]. Advances in materials science have permitted the manufacture of new piezoelectric materials with far superior properties. Such materials have given rise to practically applicable piezoelectric actuators.

A piezoelectric material is characterized by the existence of electric dipoles distributed throughout its volume. Each dipole represents a small domain whose constituent molecules are aligned and result in a net polarization. The presence of an electric field causes a crystalline deformation along the same axis in which each dipole is aligned. As it occurs

in commercially produced materials, the orientation of each dipole is random. In the presence of an applied electric field, the average deformation throughout the volume is zero. The same is true of the sensing effect; due to internal cancellation, an applied stress results in no net surface charge.

One of the key properties of a piezoelectric material is its Curie temperature. At this temperature the crystalline structure exhibits a simple cubic symmetry with no dipole moment. A piezoelectric transducer is manufactured by raising the temperature to just below the Curie temperature and applying a strong electric field. Through this polarizing (poling) treatment, domains most nearly aligned with the electric field expand at the expense of domains not aligned with the field. The element lengthens in the direction of the field. When the electric field is removed most of the dipoles are locked into a configuration of near alignment. The element retains a permanent polarization, the remnant polarization, and is permanently elongated.

When a poled piezoelectric material is compressed, the dipole moment is altered resulting in a net generated charge. This effect is referred to as the direct piezoelectric effect. Conversely, if an electric field is applied to the material, the element will lengthen and its perpendicular dimensions will contract.

The most commonly used piezoelectric material in actuating applications is lead zirconium titanate (PZT). PZT is a stiff ceramic material characterized by high d_{31} and d_{32} strain coefficients. Another material more commonly used in sensing applications is polyvinyllidene flouride (PVDF), a semi-crystalline polymer film. Although PVDF develops only around one fifth the strain of PZT for the same voltage, the material is extremely compliant and easily cut and bonded to irregular surfaces. PZT is around 40 times as stiff and has a permitivity 100 times greater than PVDF.

A more detailed description of piezoelectric materials, their properties, and applications can be found in references [42, 94, 60, 61, 62, 1, 3].
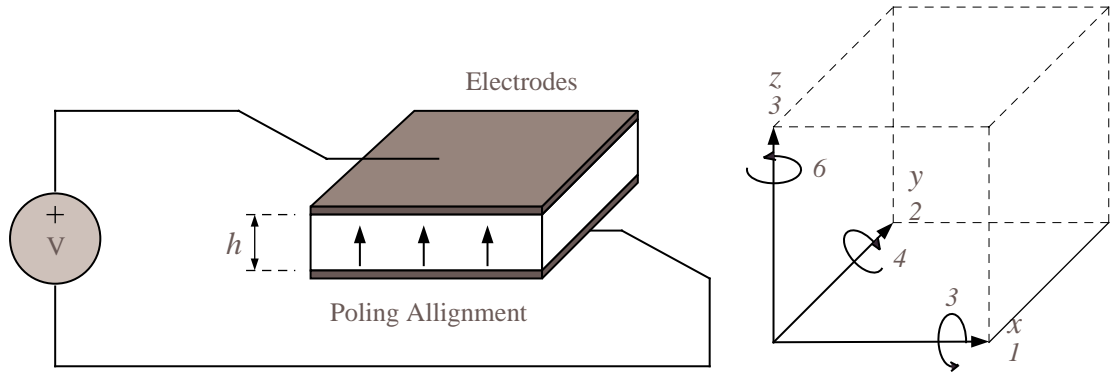
Figure 1.1: A piezoelectric transducer.

1.1.1 Modeling

Referring to Figure 1.1, the electro-mechanical behaviour of a piezoelectric transducer can be described by the following equations [42]:

$$\varepsilon^i = S_{ij}^E \sigma_j + d_{mi} E_m \tag{1.1}$$

$$D_m = d_{mi} \sigma_i + \zeta_{ik} E_k \tag{1.2}$$

where the indices $i, j = 1, 2, \ldots, 6$ and $m, k = 1, 2, 3$ refer to different directions within the material coordinate system. In equations (1.1) and (1.2) ε, σ, D, and E are respectively the strain, stress, electrical displacement (charge per unit area) and the electric field. In addition S^E, d, and ξ represent the elastic compliance, piezoelectric strain constant, and material permitivity.

The piezoelectric strain constant d_{ij} is defined as the free strain developed in the jth direction per unit of applied electric field in the ith direction. Piezoelectric actuators, as shown in Figure 1.1, are typically polarized in the z or 3 direction. For one dimensional motion, the z directional strain can be simplified to

$$\varepsilon^3 = d_{33} \frac{V}{h} \tag{1.3}$$

where V is the applied voltage and h is the material thickness. By definition, a voltage of
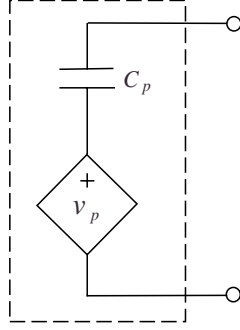
Figure 1.2: The electrically equivalent model of a piezoelectric transducer.

the same polarity as the poling orientation results in a positive strain or elongation. Due to the Poisson coupling, elongation in the z (3) direction implies a contraction in the x (1) and y (2) directions, thus d_{31} and d_{32} are opposite in sign to d_{33}. The developed x (1) and y (2) directional strain is

$$\varepsilon^1 = d_{31}\frac{V}{h} \tag{1.4}$$

$$\varepsilon^2 = d_{32}\frac{V}{h}. \tag{1.5}$$

In vibration control, piezoelectric transducers are laminated onto the surface of a host structure. As a sensor, the open circuit voltage is proportional to the strain over the region covered by the transducer. As an actuator, an applied voltage results in a moment or transverse force. To model such interaction, the electro-mechanical properties of the transducer must be coupled to the mechanical and dynamic response of the structure. A number of methods for deriving such models can be found in [4, 22, 42].

A common electrical model for coupled piezoelectric transducers is shown in Figure 1.2 [32, 48, 120]. The transducer behaves like a capacitor C_p is series with a strain-dependent voltage source v_p. Models including hysteresis, dielectric loss, and resistance can be found in [3].
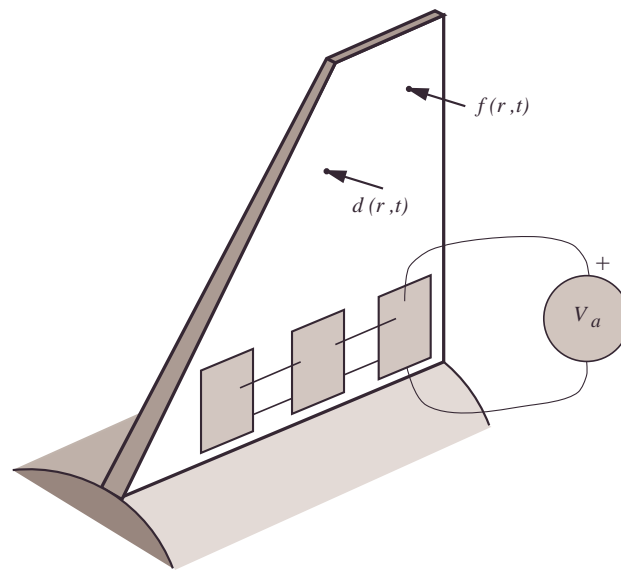
Figure 1.3: A flexible structure controlled by three electrically parallel piezo-electric transducers. The structure experiences a dynamic displacement $d(r, t)$ in response to a generally distributed force $f(r, t)$.
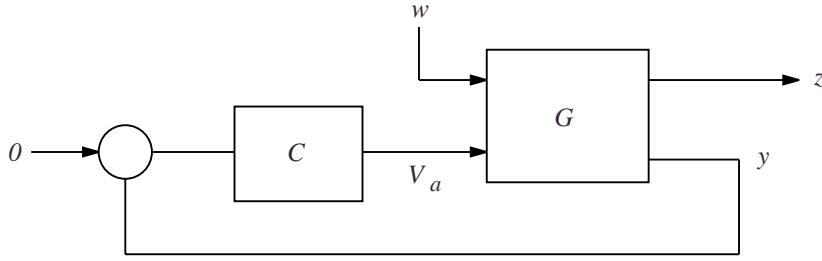
Figure 1.4: A typical active noise control problem.

1.2   Vibration Control

Piezoelectric transducers have been used extensively as actuators and sensors for vibration control in flexible structures. Consider the typical scenario shown in Figure 1.3. A flexible structure, bounded along the bottom edge, is excited by a force $f(r,t)$ distributed over the surface. The goal is to suppress resulting vibration measured at a point r. Depending on the application, it may be desirable to minimize displacement, strain, velocity, or acceleration.

1.2.1   Active feedback control

Active feedback control involves the use of sensors and actuators to minimize structural vibration. The vibration is sensed directly and used to derive an actuator voltage V_a counter-active to the applied disturbance. Typical vibration sensors include accelerometers, velocimeters, and strain sensors. The regulation problem is shown in Figure 1.4, where G is the plant model, C is the controller, w is the representative disturbance, z is the performance variable, and y is the measured output. The controller is designed to minimize the transfer function from an applied disturbance w to the performance variable z. As an example, in Figure 1.3, $d(r,t)$ is the performance signal, $f(r,t)$ is the disturbance, and V_a is the control signal. The measured output y would typically be obtained from an additional piezoelectric transducer or accelerometer.

The foremost difficulties associated with active feedback control are due mainly to the
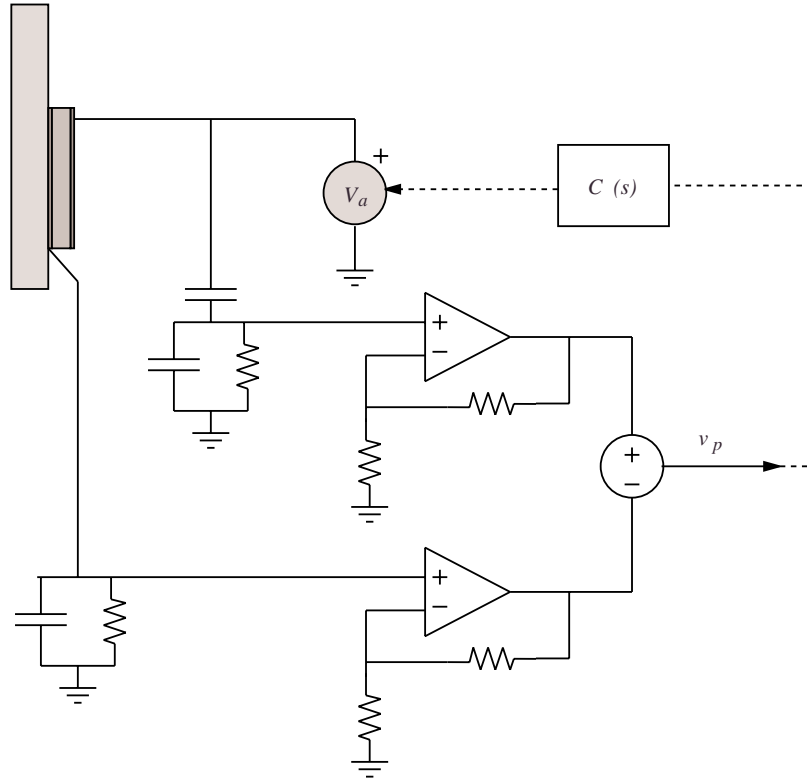
Figure 1.5: A sensori-actuator drive circuit that estimates the internal piezoelectric voltage [7].

intrinsic nature of the plant G. Mechanical systems are of high order and contain a large number of lightly damped modes. The modeling and control design for such systems is well known to pose significant challenges. In addition, environmental variation of the structural resonance frequencies can further complicate the problem by compromising stability margins and restricting performance. Examples of active feedback control incorporating piezoelectric actuators can be found in references [45, 46, 49, 73, 73].

1.2.2 Self-Sensing

In active vibration control, and many other applications, piezoelectric transducers are used exclusively as either sensors or actuators. Dosch, Inman, Garcia [32] and Anderson, Hagood, Goodliffe [7] were able to demonstrate a technique now referred to as piezoelectric

self-sensing, or sensori-actuation. By subtracting the capacitive voltage drop from the applied terminal voltage, a reconstruction of the internal piezoelectric strain voltage can be obtained. A circuit capable of performing this computation is shown in Figure 1.5. As illustrated, the reconstructed strain voltage effectively eliminates the need for an auxiliary feedback sensor or transducer. A similar technique estimating the rate-of-strain was also presented in [7].

Although piezoelectric self-sensing systems inherit the usual problems associated with active feedback control, an additional advantage is realized. The transfer function from an applied actuator voltage to the measured strain is perfectly collocated. This property gaurantees closed-loop stability for a certain class of controller, and in general, simplifies the design process [78].

The estimation in piezoelectric self-sensing techniques is highly sensitive to the transducer capacitance value. A sensing capacitance not perfectly matched to the transducer capacitance can result in significant errors in the strain estimation. If the estimate is used within a feedback control loop, such uncertainty may severely effect performance or cause instability. In addition to static error in the capacitance value, the transducer capacitance also varies with temperature, load, and age. An attempt to address the problem of capacitance sensitivity can be found in [118, 24, 2]. Despite the associated problems, a number of applications utilizing piezoelectric self-sensing actuators have appeared throughout the literature [5, 15, 50, 68, 115].

1.2.3 Shunt Control

Shunt control involves the connection of an electrical impedance to the terminals of a piezoelectric transducer, as shown in Figure 1.6. Impedance designs have included resistors, inductive networks, switched capacitors, switched networks, negative capacitors, and active impedances. A full appraisal of these techniques is presented in Chapter 2.

Compared to active feedback control, shunt damping has a number of associated benefits and disadvantages. The majority of shunt circuit configurations do not require a parametric model of the plant for design purposes, and are correspondingly easier to implement
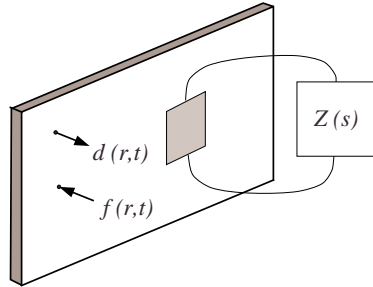
Figure 1.6: Piezoelectric shunt damping.

and tune. Shunt circuits do not require a feedback sensor, and in some circumstances, may not require any support electronics or power supply at all.

1.3   Applications

Piezoelectric vibration control has shown promise in a variety of applications ranging from consumer and sporting products to satellite and fighter aircraft vibration control systems.

In the consumer products category, a number of companies such as HEAD and K2 have invested in high-performance and novelty items such as composite piezoelectric tennis racquets, skis, and snowboards [15]. These products typically involve the use of a shunted piezoelectric transducer to decrease vibration. Benefits include increased user comfort, better handling, and performance.

The next generation of hard disk drives may also incorporate piezoelectric vibration control systems. By decreasing mechanical vibration in the disk head, the seek-time, and hence data rate and storage density can be increased [44].

A considerable research effort has been undertaken on the structural control of military aircraft. In certain modes of flight, buffet loads on wing and stabilizer airfoil can result in high levels of vibration. Such vibration can lead to mechanical fatigue and reduces the flight envelope and lift performance of an airfoil [108]. Examples include: FA-18 wing, body, and stabilizer control [57], and F-15 panel control [121]. A piezoelectric

Figure 1.7: A piezoelectric laminate FA-18 vertical stabilizer. The author is in the foreground (Courtesy of T. Ryall, DSTO, Fishermans Bend).

laminated FA-18 stabilizer is shown in Figure 1.7. Piezoelectric transducers have also been incorporated into helicopter rotor blades for the suppression of lightly damped lag modes in hingeless rotors [68].

Other noise control applications include: suppression of acoustic radiation from underwater submersibles [129], launch vehicle structural and acoustic noise mitigation [97, 31], acoustic transmission reduction panels [67, 107], and active antenna structures [45].

A primary consideration in the design of space structures is the vibration experienced during launch. In future, structures incorporating piezoelectric transducers may form the basis of light-weight, high performance mechanical components for use in space applications [5].

1.4   Outline

This thesis is presented in seven chapters: 1) Introduction, 2) Piezoelectric Shunt Damping, 3) Implementation, 4) Active Piezoelectric Shunt Control, 5) Electromagnetic Shunt Control, 6) Spatial System Identification, and 7) Conclusions.

Chapter 2 begins with a review of piezoelectric shunt damping techniques. The benefits and difficulties of each technique are discussed in relation to active feedback control and other shunt techniques. The difficulty in implementing resonant shunt damping circuits is addressed by introducing the synthetic impedance. Four modes of an experimental structure are shunt damped using this technique.

In Chapter 3, practical issues relating to the construction of a synthetic impedance are discussed. A new type of current and charge amplifier is presented that alleviates many of the previous problems associated with DC offsets and drift. A switch mode amplifier is also presented and tested experimentally by implementing a dual-mode piezoelectric shunt circuit.

A new technique for the design of piezoelectric shunt circuits is presented in Chapter 4. The problem of impedance design is cast as a standard regulator problem to allow the application of synthesis techniques such as LQG, $\mathcal{H}_2$, and $\mathcal{H}_\infty$. Superior performance to passive circuits is demonstrated experimentally on a cantilever beam.

Chapter 5 introduces the concept of electromagnetic shunt damping. Alike piezoelectric transducers, passive and active shunts can be connected to the terminals of an electromagnetic transducer in order to reduce structural vibration. A general modeling and design framework is presented for the shunt control of electromagnetic actuated systems. An experimental electromagnetic system is successfully controlled through the connection of an active shunt impedance.

In the design of active shunt and feedback controllers, a single point on the structure is often used to represent structural vibration. In Chapter 6, a technique is presented for obtaining spatially continuous dynamic models of flexible structures. Spatial models can be employed in the design of spatially weighted control systems.

The thesis is concluded in Chapter 7 with a brief summary of the results and suggestions for future research.

PIEZOELECTRIC SHUNT DAMPING

Piezoelectric shunt damping is a popular technique for vibration suppression in smart structures. Techniques encompassed in this broad description are characterized by the connection of an electrical impedance to a structurally bonded piezoelectric transducer. Such methods do not require an external sensor, may guarantee stability of the shunted system, and do not require parametric models for design purposes.

The first goal of this chapter is to provide a brief review of the various techniques falling into the category of piezoelectric shunt damping. A large sub-class of piezoelectric shunt damping circuits, the so-called resonant shunt damping circuits, are simple to design and known to introduce significant system damping. An introduction and appraisal of these techniques is presented in Section 2.1.1. In order to ascertain the structural influence of a piezoelectric shunt impedance, the interaction between mechanical structure, piezoelectric transducer, and electrical impedance is modeled in Section 2.3.

A number of practical issues have prevented the wide spread application of piezoelectric shunt damping systems. In Section 2.2, the *synthetic impedance* is introduced as a practical technique for implementation of resonant shunt circuits. The presented techniques are applied experimentally to a piezoelectric laminate structure.

2.1 Review: Piezoelectric Shunt Damping

A summary of common piezoelectric shunt damping techniques is shown in Figure 2.1. Each method is discussed in the following sub-sections.
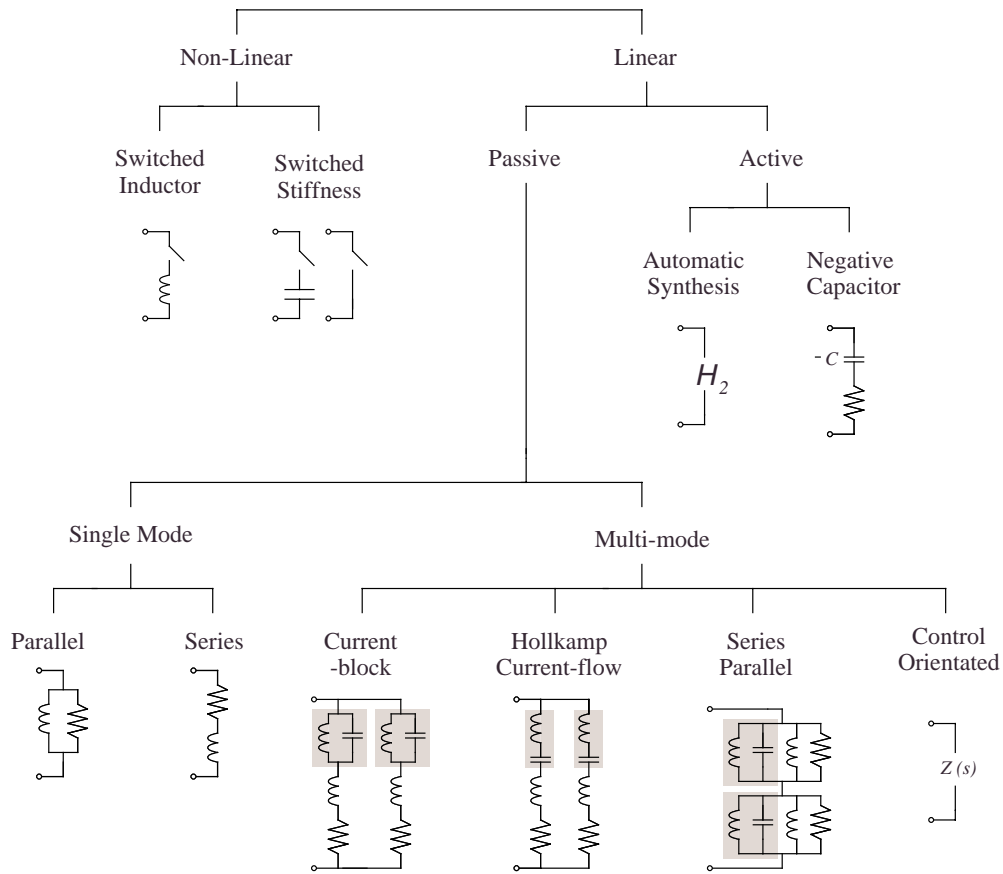
Figure 2.1: Summary of piezoelectric shunt damping techniques.
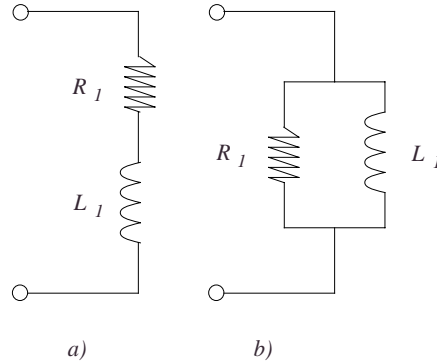
Figure 2.2: (a) Series and (b) Parallel single-mode shunt ciruits.

2.1.1 Linear Techniques

A linear shunt circuit is defined as any impedance with a linear current-to-voltage relationship over the bandwidth of interest. By this definition, adaptive techniques which contain extremely low-frequency non-linear behavior are classed as linear.

Single-mode

Although first appearing in [40], the concept of piezoelectric shunt damping is mainly attributed to Hagood and von Flotow [48]. A series inductor-resistor network, as shown in Figure 2.2 (a), was demonstrated to significantly reduce the magnitude of a single structural mode. Together with the inherent piezoelectric capacitance, the network is tuned to the resonance frequency of a single structural mode. Analogous to a tuned mechanical absorber, additional dynamics introduced by the shunt circuit act to increase the effective structural damping [48]. An analytic method for determining an effective resistance value was also presented by the same authors [48]. The parallel circuit variation shown in Figure 2.2 (b) was proposed by Wu [122]. Although the two circuits, series and parallel, achieve similar performance, the parallel structure is less sensitive to sub-optimal resistance values.

Resistive shunt damping was also proposed by Hagood and von Flotow in reference [48].
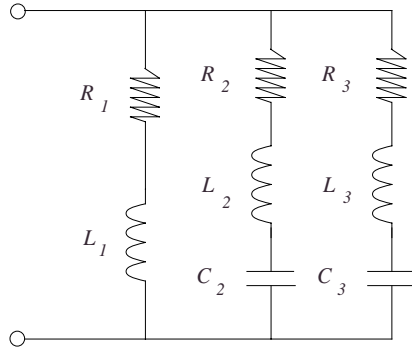
Figure 2.3: A three-mode Hollkamp shunt circuit [56].

With presently available transducers, a resistive impedance offers very little mechanical damping. The technique is equivalent to an extremely light visco-elastic damping treatment [48]. Future transducers utilizing high d_{33} electro-mechanical coupling factors may be of greater use.

Single-mode damping can be applied to reduce several structural modes with the use of as many piezoelectric patches and damping circuits. Problems may result if these piezoelectric patches are bonded to, or embedded in the host structure. First, the structure may not have sufficient room to accommodate all of the patches. Second, the structure may be altered or weakened when the piezoelectric patches are applied.

Multi-mode

After the initial introduction of single-mode damping, researchers began searching for a method of suppressing multiple structural modes with a single piezoelectric transducer.

Using the circuit shown in Figure 2.3, Hollkamp was able to suppress the second and third modes of a cantilever beam by 19 and 12 dB respectively. The circuit requires as many parallel branches as there are modes to control. A numerical optimization was proposed for determining suitable component values. This technique requires an objective function fully parameterized by all of the circuit elements. As a result, the optimization is highly
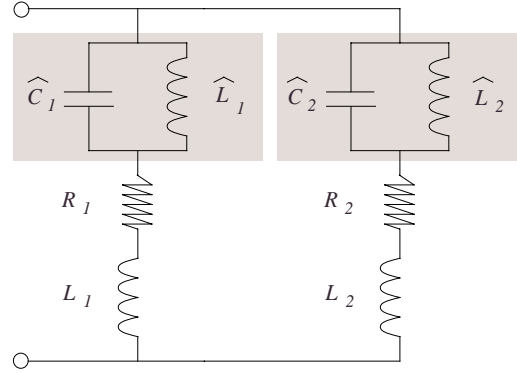
Figure 2.4: A dual-mode current-blocking shunt circuit [123].

non-linear and correspondingly difficult to solve.

Another technique, proposed by Wu and co-authors, is to insert *current-blocking* networks in each parallel branch [123, 124, 127]. Referring to Figure 2.4, each shaded current-blocking network is tuned to the frequency of an adjacent mode in order to decouple each branch. The number of anti-resonant circuits in each parallel branch depends on the number of structural modes to be shunt-damped simultaneously. In Figure 2.4, $R_1 - L_1$ and $R_2 - L_2$ are tuned to resonate at the frequency of a single structural mode. The current-blocking networks $\hat{L}_1 - \hat{C}_1$ and $\hat{L}_2 - \hat{C}_2$ are then tuned to the target resonance frequency of the neighboring branch. In this way, at the resonance frequency of each parallel branch, the remaining branch is effectively open circuit. A systematic approach for determining effective resistance values is presented in references [37, 11]. Even in its simplest form [127], the complexity and order of current-blocking topologies restrict their use to a maximum of three modes.

More recently, the *current-flowing* shunt circuit was introduced in [12, 14]. Shown in Figure 2.5, a current-flowing shunt circuit requires one parallel branch for each structural mode to be controlled. The shaded current flowing network $\hat{L}_i - C_i$ in each branch is tuned to approximate a short circuit at the target resonance frequency whilst approximating an open circuit at the frequencies of adjacent branches. The remaining inductor
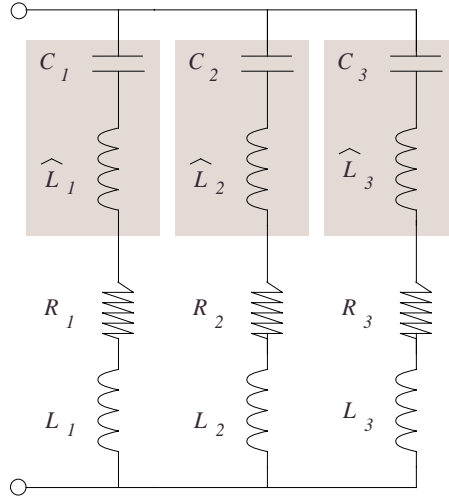
Figure 2.5: A three mode current-flowing shunt circuit [14].

and resistor in each branch $L_i - R_i$, are tuned to damp the ith target structural mode in a manner analogous to single-mode shunt damping. The current-flowing network decouples the multi-mode problem into a number of approximately independent single-mode designs. Unlike current-blocking techniques, the order of each current-flowing branch does not increase as the number of modes to be shunt damped simultaneously increases. Besides greatly simplifying the tuning procedure, current-flowing shunt circuits require less components and gracefully extend to damp a large number of modes simultaneously, e.g. five modes of a simply supported plate [14]. Further practical advantages are realized after simplifying the circuit, only a single non-floating inductor is required per branch [14].

The electrical dual of a current-flowing circuit, the so-called $series-parallel$ circuit shown in Figure 2.6 was proposed as a method for reducing inductive component values [39]. Each network in series $C_i - \hat{L}_i - L_i - R_i$ contains two sub-networks: a current-blocking network $C_i - \hat{L}_i$, and a parallel single-mode damping network $L_i - R_i$. Both the current-blocking and damping networks, $C_i - \hat{L}_i$ and $L_i - R_i$, are tuned to the same target resonance frequency ω_i. At this frequency, the current-blocking network has an extremely large impedance. All of the remaining current-blocking networks, tuned to other structural resonance frequencies, have a low impedance at ω_i. A voltage applied at the terminals results in a current that
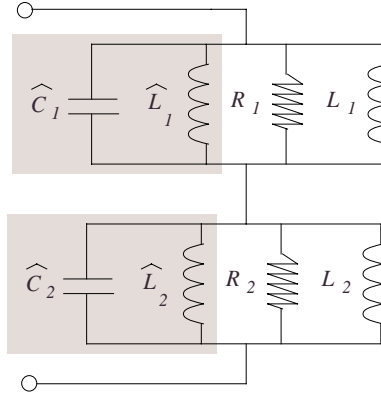
Figure 2.6: A dual mode series-parallel shunt circuit [39].

flows freely through the detuned current-blocking networks but is forced to flow through the active damping network. In this way, the circuit is decoupled so that each damping network $L_i - R_i$ can be tuned individually to a target resonance frequency. As described above, the series-parallel structure offers no great advantage over comparable techniques. Benefits arise from a suitable a choice in the arbitrary capacitances C_i. The recommended capacitance value is $10 - 20$ times that of the piezoelectric capacitance. In this case, the current blocking inductors become significantly smaller than the damping inductors. When the circuit is simplified by combining the damping and current-blocking inductors in each series network, the resulting single inductor is a fraction of that required in other single- or multi-mode circuits.

All of the multi-mode techniques discussed thus far are more or less direct extensions of the original single-mode circuits. A new approach to the design of passive piezoelectric shunt damping circuits was presented in [89]. By viewing the electrical impedance as parameterizing an equivalent collocated strain feedback controller, a shunt impedance can be found by working backwards from an effective feedback controller. Under certain conditions, the passivity, and hence stability of the shunted system can be guaranteed [89]. Present controller designs have benefits similar to that of current flowing circuits, they are low in order, easy to tune, and suitable for modally dense systems.

Active

Active shunt impedances cannot be realized using passive physical components. Although passivity, and hence stability is not guaranteed, active shunts are known to provide greater vibration suppression than passive circuits.

The negative capacitor shunt circuit [125, 10] is a simple technique for broad-band structural damping. By treating the internal piezoelectric voltage source as a supply, and the shunt impedance as a load, the traditional concept of maximum power transfer can be applied. The optimal impedance is equal in magnitude to the source impedance, but opposite in phase; hence the negative capacitor. Detrimentally, the optimal impedance is internally unstable and applies large control voltages from DC to out-of-bandwidth frequencies. An effective technique for stabilizing and *toning down* the control effort of a negative capacitor is presented in [10]. Although negative capacitor shunts are somewhat immune to variation in the structural resonance frequencies, any variation in the transducer impedance can heavily degrade performance and lead to instability. Under-water structural and acoustic vibration has been suppressed using a negative capacitance [129].

The final linear shunt technique to be discussed represents a large departure from previous approaches. Introduced in Chapter 4, the problem of shunt impedance design can be cast as a standard feedback control problem. Synthesis techniques such as LQG, $\mathcal{H}_2$, and $\mathcal{H}_\infty$ can be employed to design suitable impedances.

2.1.2   Non-linear techniques

In an attempt to eliminate the need for large inductors, a literature has also developed on the so-called *switched shunt* or *switched stiffness* techniques [27]. Three major subclasses exist where the piezoelectric element is switched into a shunt circuit comprising either: another capacitor [30], a resistor [23], or an inductor [102]. The required inductance is typically one tenth that required to implement a simple $L - R$ resonant shunt circuit designed to damp the same mode. Detrimentally, such techniques are only applicable to single degree of freedom structures or structures with sinusoidal excitation. Alike virtual

circuit implementation, an external power source is required for the gate drive and timing electronics.

2.1.3   Implementation Difficulties

Resonant single- and multi-mode piezoelectric shunt damping circuits consist of a network of passive inductors, resistors, and capacitors. On first inspection, it may appear that constructing the circuit is simply a task of assembling the correct component values. Problems arise when dealing with small piezoelectric capacitances or attempting to damp low frequency modes. In such cases, inductance values of greater than 1000 Henries may be required. The largest physical inductance available is approximately 1 Henry. These components are low-current, low-voltage, and display significant magnetic non-linearity.

Virtual inductors and Riodan gyrators [103] have been employed to implement large inductance values. Such virtual implementations are typically poor representations of ideal inductors. They are large in size, difficult to tune, and are sensitive to component age, temperature, and non-ideal characteristics.

Piezoelectric patches are capable of generating hundreds of volts for moderate structural excitations. This requires the entire circuit be constructed from high-voltage components. Further voltage limitations arise due to internal virtual circuit gains.

The minimum number of opamps required to implement a piezoelectric shunt damping circuit increases rapidly with the number of modes to be damped. At least 30 opamps are required to implement a three mode series configuration multi-mode shunt damping circuit with current-blocking networks in every branch. In general for this configuration, $2n + 4n(n-1)$ opamps are required to damp n modes. Current-flowing techniques require a considerably smaller number of opamps, $2n$ for n modes.

2.2   The Synthetic Impedance

The *synthetic impedance* is a two terminal device suitable for the implementation of piezoelectric shunt damping circuits. As shown in Figure 2.7, an arbitrary impedance $Z(s)$ can
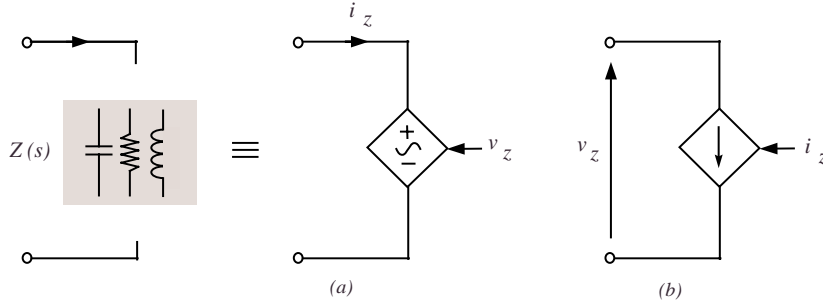
Figure 2.7: An arbitrary terminal impedance $Z(s)$ implemented by impedance synthesis (a) and admittance synthesis (b).

be established at the terminals by either a) measuring the current i_z and applying a voltage v_z, or b) *vice-versa*.

Referring to the first case shown in Figure 2.7 (a), the applied voltage $v_z(t)$ can be determined by the measured current $i_z(t)$, i.e. $v_z(t) = f(i_z(t))$. By fixing $v_z(t)$ as the output of a linear transfer function in $i_z(t)$, the controlled voltage source can be made to synthesize an arbitrary impedance $Z(s)$. In the Laplace domain,

$$V_z(s) = Z(s)I_z(s), \tag{2.1}$$

where $Z(s)$ is the desired terminal impedance.

Similarly, in the second case shown in Figure 2.7 (b), the applied current $i_z(t)$ can be determined by the measured voltage $v_z(t)$, i.e. $i_z(t) = f(v_z(t))$. By fixing $i_z(t)$ as the output of a linear transfer function in $v_z(t)$, the controlled current source can be made to synthesize an arbitrary admittance $Y(s)$. In the Laplace domain,

$$V_z(s) = Y(s)I_z(s), \tag{2.2}$$

where $Y(s) = \frac{1}{Z(s)}$ is the desired terminal admittance.

The choice of configuration, either synthetic impedance or synthetic admittance, will depend on the relative order of the desired impedance. As implementation of improper transfer functions is impractical [64], the choice should be made so that the required transfer function $Z(s)$ or $Y(s)$ is at least proper [64].
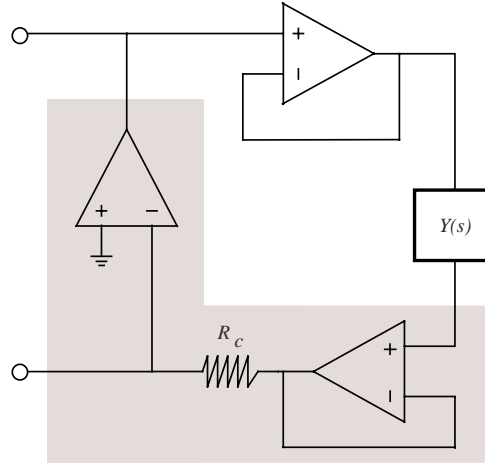
Figure 2.8: A simple synthetic admittance.

The schematic diagram of a simple synthetic admittance is shown in Figure 2.8. The shaded area represents a voltage-controlled-current-source (VCCS) with gain $\frac{1}{R_c}$ A/V. The filter $Y(s)$ can be realized either as an analog or digital transfer function.

Synthetic implementation is a unifying replacement for various virtual circuits including: virtual capacitors and inductors, negative impedance converters, transformers, and gyrators. Only a single high-voltage opamp is required to provide near ideal implementation of any arbitrary terminal impedance.

2.3   Modeling the Compound System

Consider the piezoelectric laminate structure shown in Figure 2.9. The goal is to suppress vibration resulting from two disturbances: V_a, the voltage applied to a disturbance patch, and $f(r,t)$, a generally distributed external force.

For generality, we enter the modeling process with knowledge *a priori* of the system dynamics. The transfer functions of interest are:

$$G_{va}(s) = \frac{V_p(s)}{V_a(s)} \quad G_{vv}(s) = \frac{V_p(s)}{V_z(s)} \quad G_{da}(r,s) = \frac{d(r,s)}{V_a(s)}, \tag{2.3}$$
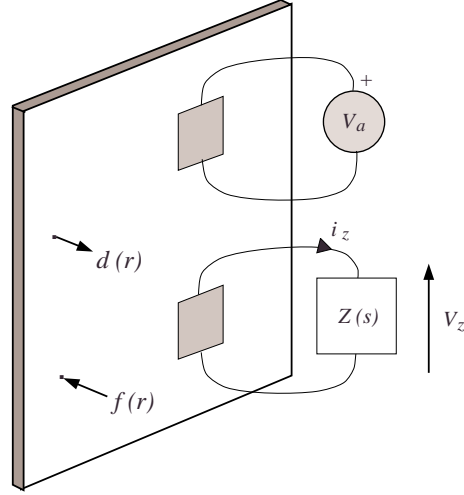
Figure 2.9: A general piezoelectric laminate structure excited by a distributed force $f(r, t)$, and the voltage V_a applied to a disturbance patch. The resulting vibration $d(r, t)$ is suppressed by the presence of an electrical impedance connected to the shunt transducer.

where $V_p(s)$ is the piezoelectric voltage induced in the shunt transducer. If the disturbance and shunt transducer are identical, collocated, and poled in opposite directions, $G_{va}(s) = -G_{vv}(s)$.

The above transfer functions can be derived analytically, for example by solving the Euler-Bernoulli beam equation [42]. Alternatively, system identification [77] can be employed to estimate these models directly from experimental data.

Following the modal analysis procedure [85], the resulting transfer functions have the familiar form

$$G_{da}(r, s) = \frac{d(r, s)}{V_a(s)} = \sum_{k=1}^{\infty} \frac{F_k \phi_k(r)}{s^2 + 2\zeta_k \omega_k s + \omega_k^2}, \tag{2.4}$$

$$G_{vv}(s) = \frac{V_p(s)}{V_z(s)} = \sum_{k=1}^{\infty} \frac{\alpha_k}{s^2 + 2\zeta_k \omega_k s + \omega_k^2}, \tag{2.5}$$

where F_k, and α_k represent the lumped modal and piezoelectric constants applicable to the kth mode of vibration.
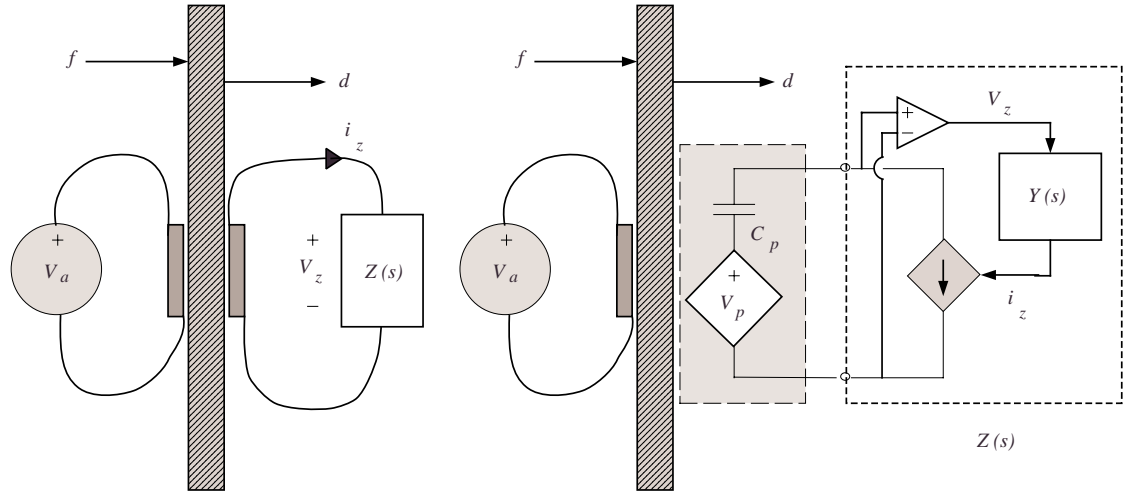
Figure 2.10: The physical and electrically equivalent view of a structure disturbed by an applied actuator voltage $V_a(s)$ and external force $f(r,s)$. The resulting vibration $d(r,s)$ is suppressed by the presence of a shunt impedance.

2.3.1   Modeling the Presence of a Shunt Circuit

Referring to Figure 2.10, the relationship between voltage and current in the Laplace domain is

$$V_z(s) = I_z(s)Z(s). \tag{2.6}$$

Applying Kirchoff's voltage law we obtain,

$$V_z(s) = V_p(s) - \frac{1}{C_p s} I_z(s), \tag{2.7}$$

where C_p represents shunt transducer capacitance. Combining (2.6) and (2.7) we obtain,

$$V_z(s) = \frac{Z(s)}{\frac{1}{C_p s} + Z(s)} V_p(s), \tag{2.8}$$

or

$$V_z(s) = \frac{C_p s Z(s)}{1 + C_p s Z(s)} V_p(s). \tag{2.9}$$

By applying the principle of superposition, the disturbance and shunt voltage strain contributions are,

$$V_p(s) = G_{va}(s)\, V_a(s) + G_{vv}(s) V_z(s). \tag{2.10}$$

The shunted composite system can be obtained from Equations (2.6), (2.7), and (2.10),

$$\frac{V_p(s)}{V_a(s)} = \frac{G_{va}(s)}{1 + G_{vv}(s)K(s)}. \tag{2.11}$$

where

$$K(s) = \frac{-Z(s)}{Z(s) + \frac{1}{C_p s}}. \tag{2.12}$$

The composite displacement transfer function can also be derived in a similar fashion,

$$\frac{d(r, s)}{V_a(s)} = \frac{G_{da}(r, s)}{1 + G_{vv}(s)K(s)}. \tag{2.13}$$

By again applying the principle of superposition, the effect of a generally distributed disturbance force $f(r, s)$ can be included,

$$V_p(s) = \frac{1}{1 + G_{vv}(s)K(s)} \left(G_{va}(s)V_a(s) + G_{vf}(r, s)f(r, s) \right), \tag{2.14}$$

$$d(r, s) = \frac{1}{1 + G_{vv}(s)K(s)} \left(G_{da}(r, s)V_a(s) + G_{df}(r, s)f(r, s) \right), \tag{2.15}$$

where $G_{df}(r, s)$ and $G_{vf}(r, s)$ are the respective transfer functions from an applied force $f(r, s)$ to the displacement $d(r, s)$ and shunt transducer piezoelectric voltage V_p, i.e.

$$G_{vf}(r, s) = \frac{V_p(s)}{f(r,s)} \qquad G_{df}(r, s) = \frac{d(r,s)}{f(r,s)} \ . \tag{2.16}$$

From Equation (2.11) it can be concluded that the presence of an electrical shunt impedance parameterizes an equivalent collocated strain feedback controller. A diagrammatic representation of equation (2.11) is shown in Figure 2.11. Further interpretation and analysis can be found in [89].

2.4   Experimental Application

In this section, the synthetic impedance is employed to damp four modes of a simply supported beam.
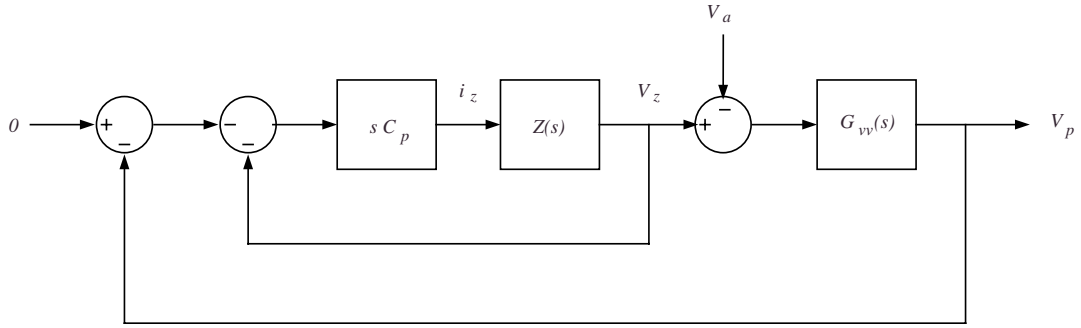
Figure 2.11: The strain-feedback interpretation of piezoelectric shunt damping.
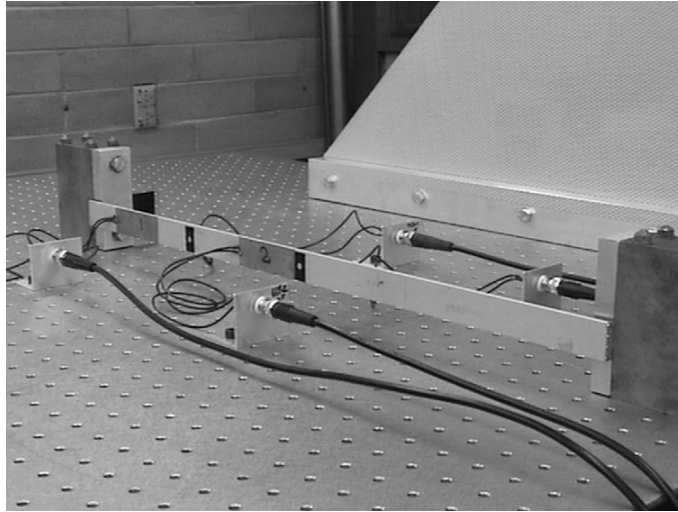
Figure 2.12: Beam apparatus.

2.4.1 Experimental Setup

The test structure is a uniform aluminum beam with rectangular cross section and experimentally pinned boundary conditions at both ends. A pair of collocated piezoelectric patches are attached symmetrically to either side of the structure as shown in Figures 2.12 and 2.13. The transducer placement provides reasonable control authority over the 2nd, 3rd, 4th, and 5th modes. Details of the beam and PIC151 piezoelectric patches are listed in Tables 2.1 and 2.2.
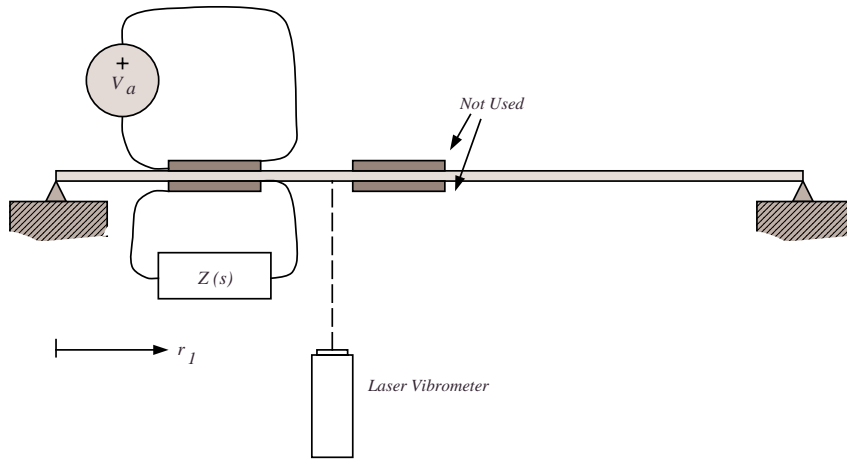
Figure 2.13: Experimental apparatus.

Length, L	$0.6\ m$
Width, w	$0.025\ m$
Thickness, h	$0.004\ m$
Young's modulus, E	$65 \times 10^9\ N/m^2$
Poisson's ratio, ν	0.3
Mass / unit area, ρ	$10.6\ kg/m^2$

Table 2.1: Parameters of the simply-supported beam.

Location r-direction, r_1	0.050 m
Length, L_p	0.0724 m
Thickness, h_p	0.00191 m
Width, w_p	0.025 m
Capacitance, C_p	105.77 nF
Young's modulus, E_p	62×10^9 N/m^2
Poisson's ratio, ν_p	0.3
Strain Constant, d_{31}	-320×10^{-12} m/V
Electromechanical coupling, k_{31}	0.44
Stress constant / voltage coefficient, g_{31}	-9.5×10^{-3} V m/N

Table 2.2: Physik Instrumente PIC151 piezoelectric parameters.

2.4.2   System Identification

In order to simulate the effect of an attached piezoelectric transducer, a model is required for the transfer function $G_{vv}(s)$. The transfer function from an applied actuator voltage $V_a(s)$, to the structural deflection at a point $d(r, s)$ will also be considered. A model with one input and two outputs is required,

$$\begin{bmatrix} V_p(s) \\ d(r, s) \end{bmatrix} = G_p(s) \, V_a(s), \tag{2.17}$$

where $G_p(j\omega) = \begin{bmatrix} G_{vv}(j\omega) \\ G_{da}(r, j\omega) \end{bmatrix}$ is the open-loop plant transfer function matrix.

Modeling of piezoelectric laminate structures is generally accomplished in the literature by means of either analytic modeling, finite element analysis, or system identification. Analytic modeling, typically involving the assumed modes approach [85], requires distinct models for both structural dynamics and piezoelectric transducers [42]. Detailed information regarding the structural and piezoelectric properties is required. Practical application typically involves the use of experimental data and a non-linear optimization to identify unknown parameters such as resonance frequencies, piezoelectric coupling coefficients, and modal amplitudes. Another popular technique is that of finite element (FE) analysis [26].

This is an approximate method that results in high order spatially discrete models. If sensor and actuator dynamics are known, an integrated model can be cast in state space form to facilitate control design [75]. Alike the modal analysis procedure, FE models are usually tuned using experimental data [35].

System identification can be employed to procure composite structural-piezoelectric models directly from experimental data. Although the field of system identification is extremely diverse [77], few techniques are capable of identifying MIMO systems directly without explicit parameterization of the model or a non-linear optimization. The residue consists mainly of the so-called subspace class of system identification algorithms. Such methods identify state space models by exploiting geometric properties of the input and output sequences. Frequency domain subspace methods have proven extremely effective in identifying high order resonant systems [83, 82]. In this work, a continuous time frequency domain subspace algorithm is employed[1] [116].

Using a Polytec laser scanning vibrometer (PSV-300) and Hewlett Packard spectrum analyzer (35670A), the frequency responses of $G_{vv}(s)$ and $G_{da}(r,s)$ were obtained. The measured and identified transfer functions are shown in Figure 2.14. In the bandwidth of interest, the identified model is a good representation of the underlying system.

2.4.3 Damping Performance

A four-mode current-flowing shunt circuit was designed according to the procedure presented in [12]. The simplified circuit schematic and component values are shown in Figure 2.15 and Table 2.3.

The simulated and experimental shunt-damped frequency responses are shown in Figures 2.16 and 2.17. As listed in Table 2.4, the peak amplitudes of the 2nd, 3rd, 4th and 5th modes were significantly reduced.

---

[1]A Matlab implementation of this algorithm and the algorithm of McKelvey [82] is freely available by contacting the author.
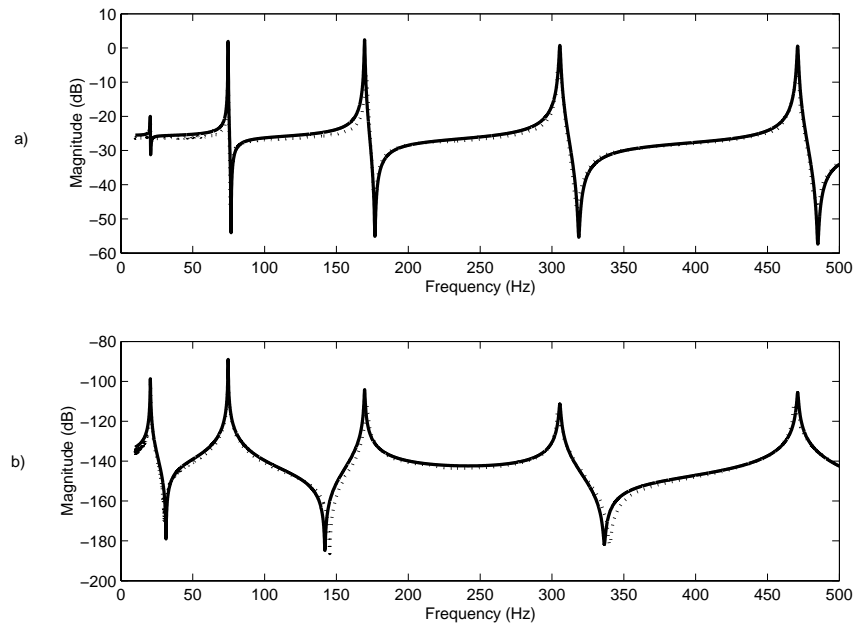
Figure 2.14: The measured (- -) and identified (—) magnitude frequency response of (a) $G_{vv}(s)$ and (b) $G_{da}(r = 0.17m, s)$.
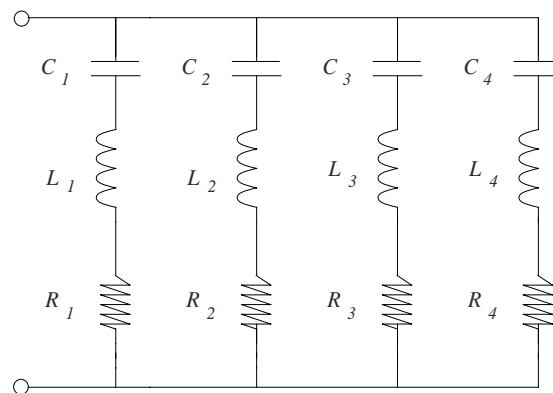
Figure 2.15: A simplified four-mode current-flowing circuit.

C_1	10 nF	L_1	480.0 H	R_1	1423 Ω
C_2	10 nF	L_2	92.6 H	R_2	1212 Ω
C_3	10 nF	L_3	29.6 H	R_3	913 Ω
C_4	10 nF	L_4	12.4 H	R_4	798 Ω

Table 2.3: Component Values.

Mode Number	Simulated Damping	Experimental Damping
2	14.5 dB	13.5 dB
3	8.2 dB	7.8 dB
4	14.1 dB	13.8 dB
5	16.4 dB	15.8 dB

Table 2.4: Damping performance.

2.5   Conclusions

Many techniques exist for vibration control in smart structures. Resonant piezoelectric shunt damping circuits provide guaranteed stability, reasonable performance, and are simple to design. When dealing with low frequency modes or transducers with small capacitance, inductance values of greater than 1000 Henries may be required. Virtual inductors and gyrators complicate the design, are expensive to construct, and severely limit the voltage range.

The synthetic impedance has been presented as a simple and practical method for implementation of piezoelectric shunt damping circuits. It can be used as a direct replacement for virtual circuits, negative impedance converters, transformers, and gyrators. The arbitrary nature of synthetic implementation also permits the implementation of new impedance designs without physical circuit realizations.

One important issue not raised during the discussion is that of performance robustness. Resonant shunt damping circuits are known to be highly sensitive to variations in structural resonance frequency and transducer capacitance [96]. Both of these quantities vary
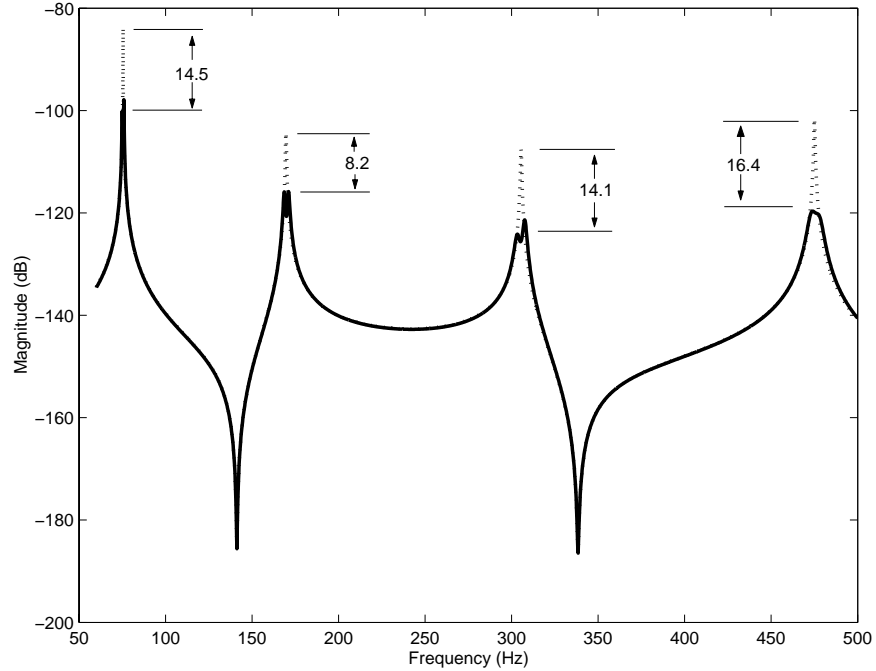
Figure 2.16: Simulated frequency response of the open-loop ($\cdots$) and shunt damped system (—). The transfer function is measured from an applied actuator voltage $V_a(s)$ to the resulting displacement $d(r = 0.17m, s)$.

substantially with temperature, age, and environmental conditions. By adapting component values in real-time, sensitivity to such variations can be reduced. Hollkamp first demonstrated a single-mode adaptive shunt where a motorized resistor was used to tune the inductance of a virtual circuit. An additional transducer was required to estimate the magnitude of vibration. A multi-mode single-transducer adaptive shunt circuit was later presented in [38]. Using the synthetic impedance, a background DSP task was employed to estimate and minimize a performance function related to the RMS strain. More recently, a technique based on relative phase-shift has been proposed that is faster to converge and displays less misadjustment [96]. This technique also requires a reference such as an additional transducer or accelerometer
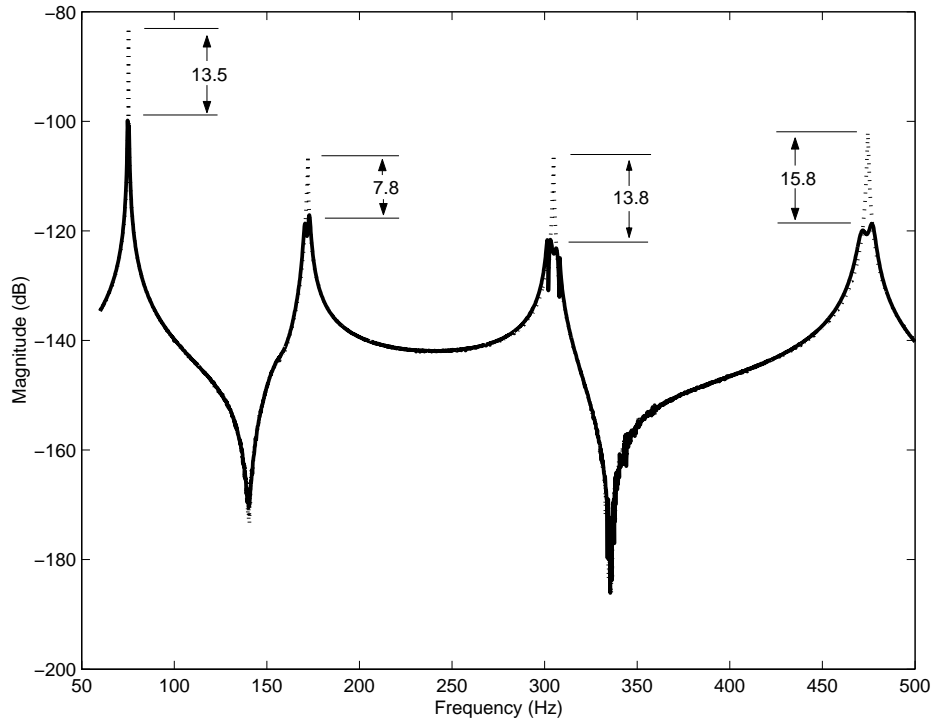
Figure 2.17: Experimental frequency response of the open-loop ($\cdots$) and shunt damped system (—). The transfer function is measured from an applied actuator voltage $V_a(s)$ to the resulting displacement $d(r = 0.17m, s)$.

3

IMPLEMENTATION

The difficulty in implementing large inductance values has severely limited the practical application of piezoelectric shunt damping circuits. In Chapter 2, the synthetic impedance was introduced as a new technique for realizing arbitrary analog networks. This chapter is dedicated to the construction and utilization of impedance synthesis devices.

One of the key components required to synthesize a piezoelectric shunt damping circuit is a controlled current source. The design and application of capacitive-load current drivers is reviewed in Section 3.1. To alleviate the problems of output voltage drift and poor low frequency performance, a new class of current and charge amplifiers are proposed.

The second key building block required for analog network synthesis is a signal filter representing the desired terminal impedance. In Section 3.2, a set of transformations are presented that link the topology of admittance block diagrams to shunt circuit schematics. This section is intended for both: practitioners, to simplify the design of analog and digital signal filters, and for researchers, as an alternative approach to analog network synthesis.

The efficiency of linear amplifiers when driving highly capacitive loads is extremely poor. In Section 3.3, a switch-mode current source is introduced as an alternative to linear driving circuits.

3.1   Compliance Feedback Current / Charge Drivers

One common theme across the diverse literature involving piezoelectric applications is the problem of hysteresis [3, 60]. When used in an actuating role, piezoelectric transducers display a significant amount of hysteresis in the transfer function from voltage to displacement [3, 60].

As discussed in [43] and references therein, a great number of techniques have been developed with the intention of reducing hysteresis. Included are: displacement feedback techniques, mathematical Preisach modeling [81] and inversion, phase control, polynomial approximation, and current or charge actuation [95].

Almost all contributions in this area make reference to the well known advantages of driving piezoelectric transducers with current or charge rather than voltage [95]. Simply by regulating the current or charge, a five-fold reduction in the hysteresis can be achieved [47]. A quote from a recent paper [29] is typical of the sentiment towards this technique:

> "While hysteresis in a piezoelectric actuator is reduced if the charge is regulated instead of the voltage [95], the implementation complexity of this technique prevents a wide acceptance [65]".

Although the circuit topology of a charge or current amplifier is much the same as a simple voltage feedback amplifier, the uncontrolled nature of the output voltage typically results in the load capacitor being charged up. Saturation and distortion occur when the output voltage, referred to as the compliance voltage, reaches the power supply rails. The stated *complexity* invariably refers to the need for additional circuitry to avoid charging of the load capacitor. A popular technique [80, 25], is to simply short circuit the load every 400 ms or so, periodically discharging the load capacitance and returning the DC compliance voltage to ground. This introduces undesirable high frequency disturbance and severely distorts low frequency charge signals.

3.1.1 Basic Circuit Configurations

This section introduces a new type of current and charge amplifier capable of providing high accuracy, ultra-low frequency regulation of current or charge. The *compliance feedback current or charge amplifier* contains an additional output voltage feedback loop that effectively estimates and rejects all sources of DC offset. This technique is intended as a viable alternative for previously presented current and charge amplifiers. In the following sub-sections, a full analysis is provided to clarify the problem and illustrate the simplicity of the solution.

Consider the simplified diagram of a generic current source [58] shown in Figure 3.1. The high gain feedback loop and voltage driver works to equate the applied reference voltage v_{ref}, to the sensing voltage v_s. In the Laplace domain, at frequencies well within the bandwidth of the control loop, the load current $I_L(s)$ is equal to $V_{ref}(s)/Z_s(s)$.

If $Z_s(s)$ is a resistor R_s,

$$I_L(s) = V_{ref}(s)/R_s, \tag{3.1}$$

i.e. we have a current amplifier with gain $1/R_s$ A/V.

If $Z_s(s)$ is a capacitor C_s,

$$\dot{q}_L = I_L(s) = V_{ref}(s)C_s s, \tag{3.2}$$

$$q_L = V_{ref}(s)C_s, \tag{3.3}$$

i.e. we have a charge amplifier with gain C_s $Columbs/V$.

As mentioned in the introduction, the foremost difficulty in employing such devices to drive highly capacitive loads is that of DC current or charge offsets. Inevitably, the voltage measured across the sensing impedance will contain a non-zero voltage offset, this and other sources of voltage or current offset within the circuit result in a net output current or charge offset. As a capacitor integrates DC current, the uncontrolled output voltage will ramp upward and saturate at the power supply rail. Any offset in v_o limits the compliance range of the current source and may eventually cause saturation. To limit the
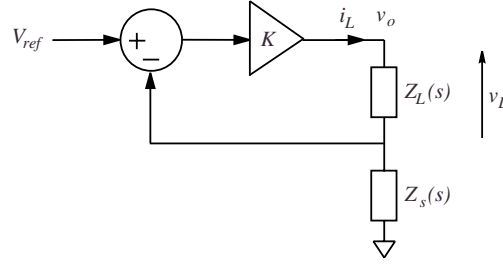
Figure 3.1: Generic current source.

DC impedance of the load, a parallel resistance is often used. With the parallel connection of $\frac{1}{C_L s}$ and R_L, the actual current $I_{Lc}(s)$ flowing through the capacitor is

$$I_{Lc}(s) = I_L(s)\frac{s}{s + \frac{1}{R_L C_L}}. \tag{3.4}$$

Additional dynamics have been added to the current source. The transfer function now contains a high-pass filter with cutoff $\omega_c = \frac{1}{R_L C_L}$. That is,

$$\frac{I_{Lc}(s)}{V_{ref}(s)} = \frac{1}{R_s}\frac{s}{s + \frac{1}{R_L C_L}}. \tag{3.5}$$

In contrast to the infinite DC impedance of a purely capacitive load, the load impedance now flattens out towards DC at $\omega_c = \frac{1}{R_L C_L}$, and has a DC impedance of R_L. Thus, a DC offset current of i_{dc} results in a compliance voltage offset of $v_{dc} = i_{dc}R_L$. In a typical piezoelectric driving scenario, with $C_L = 100 \ \eta F$, and $i_{dc} = 1\mu A$, a 1 $M\Omega$ parallel resistance is required to limit the DC compliance offset to 1 V. The frequency response from an applied reference voltage to the actual capacitive load current $I_{Lc}(s)$ is shown in Figure 3.2. Phase lead exceeds 5 degrees below 18 Hz. Such poor low frequency performance precludes the use of current amplifiers in applications requiring accurate low frequency tracking, e.g. Atomic Force Microscopy [28]. The advantages of piezoelectric current excitation are lost to the practical electronic difficulties in constructing a current source.

The following section introduces a new type of current source. The *compliance feedback current amplifier* compensates for any DC compliance offset without the addition of a parallel resistance. Low frequency bandwidths in the milli-Hertz range can be achieved with basic components.
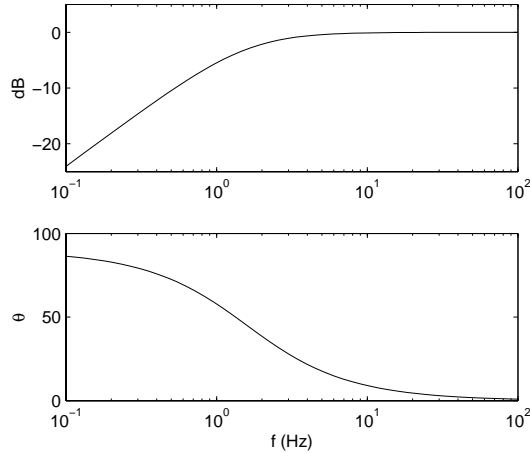
Figure 3.2: Typical frequency response from an applied reference voltage to the actual capacitive load current $I_{Lc}(s)$.

3.1.2   Analysis of Compliance Feedback Current and Charge amplifiers

The aim of this sub-section is to introduce a generalized compliance feedback current or charge amplifier. From the general description of its operation, we introduce a class of controllers that achieve excellent ultra-low frequency tracking and complete rejection of DC compliance voltages.

Figure 3.3 shows the schematic diagram of a compliance feedback current source. Neglecting the input associated with the compliance controller $C(s)$, the circuit is simply a realization of the diagram shown in Figure 3.1. The inverted[1] reference voltage v_{ref}, is maintained across the sensing impedance $Z_s(s)$ by the high gain feedback loop. Thus, $I_L(s) = -V_{ref}(s)/Z_s(s)$. The voltage drive circuit, represented by an opamp, is the only required high voltage component $v_o = K(v_+ - v_-)$, where K is the internal open-loop gain.

The additional input v_{bias} in the compliance feedback loop is included to allow for a non-zero compliance reference voltage. When a voltage is applied to v_{bias}, rather than regulating the DC compliance voltage to zero, the DC compliance voltage is regulated to v_{bias}. In cases where the operational voltage range of the piezoelectric transducer is non-symmetric,

---

[1]The inversion of v_{ref} is performed purely for convenience when implementing shunt damping circuits. The current is usually defined flowing *into* the current source.
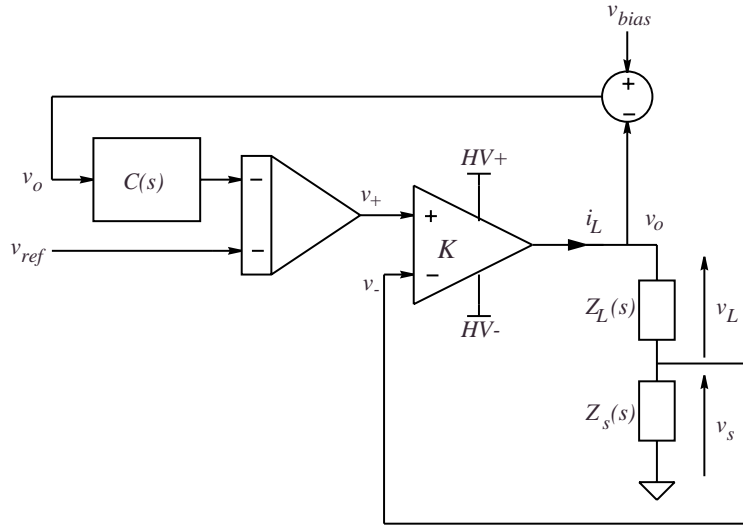
Figure 3.3: Simplified schematic of a compliance feedback current amplifier.

for example, a stack actuator, the application of a DC bias voltage electrically pre-stresses the actuator to allow bi-polar operation. Because we are now controlling both the current and voltage in different frequency regions, dynamic bi-polar charge and current signals can be tracked together with a desired DC electrical pre-stressing voltage. For purely capacitive loads, DC electrical pre-stressing requires no additional power.

For high power, or ultra-efficient current and charge amplifiers, the output driver stage can be replaced with a pulse width modulated DC-AC inverter [19, 87]. The time delay inherent in switching amplifiers, now enclosed in the current or charge feedback loop will limit the high frequency bandwidth of the amplifier. Aside from the addition of switching noise and current ripple, the following linear results also apply.

The voltages and currents of interest are related in the system block diagram shown in Figure 3.4. The auxiliary signal v_p models a load internal voltage source, e.g. the piezoelectric voltage. By definition, the polarity of the source hinders the current i_L.

To control the amplifier, there are two objectives. The first is to ensure good reference tracking of the current or charge signals. The second is to provide low frequency and DC regulation of the compliance voltage v_o. Obviously both goals cannot be achieved
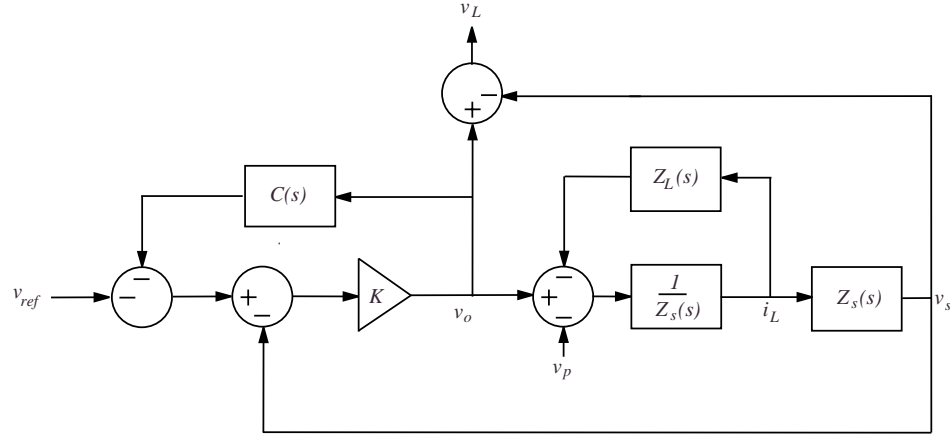
Figure 3.4: System block diagram of the circuit shown in Figure 3.3.

independently. To understand the trade-off between tracking performance and compliance regulation, two transfer functions are studied: 1) the transfer function from an applied reference voltage $V_{ref}(s)$ to the voltage measured across the sensing impedance $V_s(s)$, and 2) the transfer function from an applied reference voltage $V_{ref}(s)$ to the compliance voltage $V_o(s)$. Respectively, the first transfer function represents the tracking performance, while the second represents the charge or current offset rejection. As the most significant source of output voltage offset is usually DC error in the reference signal, input charge and current offset rejection is studied as opposed to an output disturbance.

In some circumstances, for example, scanning applications where absolute tracking accuracy is required for a short time, it may be beneficial to temporarily hold the output of the compliance controller static. During this time, the charge and current tracking will be perfect but the output voltage may drift from the reference point. To re-tune the circuit between scans, the compliance controller is simply re-activated and allowed to settle.

For a current source connected to a capacitive load, $Z_s(s) = R_s$ and $Z_L(s) = \frac{1}{C_L s}$, assuming $V_p(s) = 0$,

$$\frac{V_s(s)}{V_{ref}(s)} = \frac{-KR_s C_L s}{(1 + KC(s))(R_s C_L s + 1) + KR_s C_L s} \tag{3.6}$$

$$\frac{V_o(s)}{V_{ref}(s)} = \frac{-KR_s C_L s - K}{(1 + KC(s))(R_s C_L s + 1) + KR_s C_L s}. \tag{3.7}$$

The effect of three compliance controllers is discussed below. Figures 3.5, 3.6, and 3.7 compare the responses of each control strategy, proportional, integral, and PI. To be fair, numerical values are selected so that each strategy has a comparable low frequency tracking performance.

(a) Our first choice of controller is simply a proportional controller $C(s) = c$. The effect on the transfer functions $\frac{V_s(s)}{V_{ref}(s)}$ and $\frac{V_o(s)}{V_{ref}(s)}$ is shown in Figures 3.5 (a), and 3.6 (a). The transient response of the compliance voltage to a step in DC offset current is shown in Figure 3.7 (a). Analogous to the effect of adding a parallel resistor, the transfer function $\frac{V_o(s)}{V_{ref}(s)}$ *flattens out* towards DC, thus limiting the integration of offset currents. As shown in Figure 3.7 (a), any offset current results in a large compliance offset. Beneficially the voltage across the sensing resistance is still proportional to the load current, i.e. even though the dynamic response is no better than a simple resistor, we are now able to measure the load current even outside the bandwidth of the amplifier.

(b) To eliminate DC compliance offset, the next obvious choice is an integral control strategy $C(s) = \frac{\alpha}{s}$. Referring to figures 3.5, 3.6, and 3.7 (b), the DC compliance offset is completely rejected but a lightly damped low frequency resonance has been introduced. As demonstrated in Figure 3.7 (b), the result is an extremely poor settling time.

(c) Proportional-integral (PI) control $C(s) = \frac{\alpha s + \delta}{s}$ achieves complete rejection of offset currents while exhibiting a fast settling time in the transient response. Using the variables α, δ, and R_s, an arbitrary low frequency bandwidth can be obtained with full control over the system damping. Figures 3.5, 3.6, and 3.7 (c), show a superior performance in all of the qualifying responses. A PI controller is easily implemented using the simple opamp circuit shown in Figure 3.8. The corresponding transfer function is

$$\frac{V_{out}(s)}{V_{in}(s)} = \frac{\frac{1}{C_2 R_1} + \frac{R_2}{R_1}s}{s}. \tag{3.8}$$

For a charge amplifier connected to a capacitive load, $Z_s(s) = \frac{1}{C_s s}$ and $Z_L(s) = \frac{1}{C_L s}$, we may write,

$$\frac{V_s(s)}{V_{ref}(s)} = \frac{-KC_L}{(1 + KC(s))(C_L + C_s) + KC_L} \tag{3.9}$$
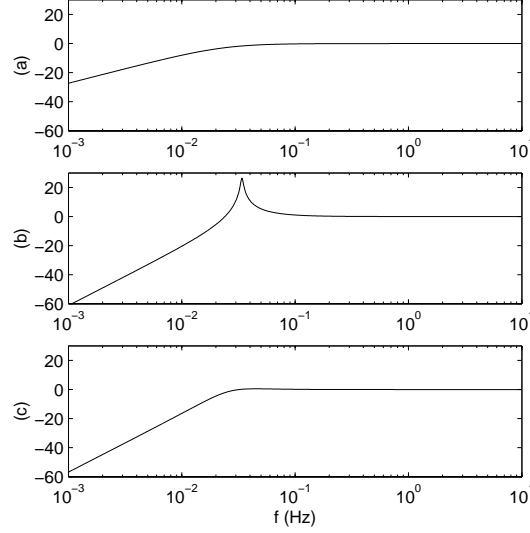
Figure 3.5: The current tracking performance $\frac{V_s(s)}{V_{ref}(s)}$ of a current source with capacitive load and compliance controller (a) Proportional (b) Integral (c) PI.

$$\frac{V_o(s)}{V_{ref}(s)} = \frac{-KC_L - KC_s}{(1 + KC(s))(C_L + C_s) + KC_L}. \tag{3.10}$$

The compliance controller design for charge amplifiers is considerably easier. Simple integral control $(C(s) = \frac{\alpha}{s})$ results in a first order response with complete regulation of DC offsets,

$$\frac{V_o(s)}{V_{ref}(s)} = \frac{-KC_L s - KC_s s}{(KC_L + C_L + C_s)s + K\alpha(C_L + C_s)}. \tag{3.11}$$

The location of the closed loop pole is easily manipulated by the variable α.

Note that charge amplifiers are actually susceptible to DC offsets in two of the circuit node-voltages: 1) the output compliance voltage v_o, and 2) the sensing voltage v_s. Offset in the sensing voltage results from input bias currents generated by the driving opamp. By choosing an opamp with low input bias current, for example an opamp with JFET input transistors [2], the problem can be solved by placing a large shunt resistor in parallel. Although this introduces additional dynamics, the low frequency cutoff in the sensing voltage measurement would typically be two orders of magnitude lower than that of the compliance regulation loop. The additional dynamics can be safely neglected.

---

[2]Junction Field Effect Transistors (JFETs) are commonly used in the input stages of high voltage opamps.
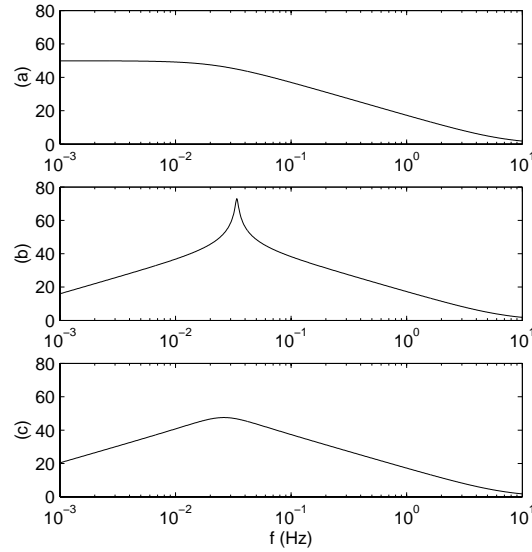
Figure 3.6: The compliance regulation performance $\frac{V_o(s)}{V_{ref}(s)}$ of a current source with capacitive load and compliance controller (a) Proportional (b) Integral (c) PI.

3.1.3 Experimental Results

Experimental results are presented for the prototype amplifier shown in Figure 3.9. This device supports much of the research presented in upcoming chapters. Features include:

- Maximum supply voltage of +/- 250 Volts.

- Peak output current of 32 Amps.

- On-board low voltage instrumentation supply.

- Reconfigurable to drive current, charge, voltage, or current rate-of-change.

- Variable bandwidth up to 150 kHz (when driving a 100 nF PZT load).

- Highly linear and low-cost discrete BJT components.

- Fully protected, high bandwidth, ultra-high impedance instrumentation of the terminal voltage, compliance voltage, current, charge, and current rate-of-change.

- Capable of accepting impedance cards (as discussed in Section 3.2.2).
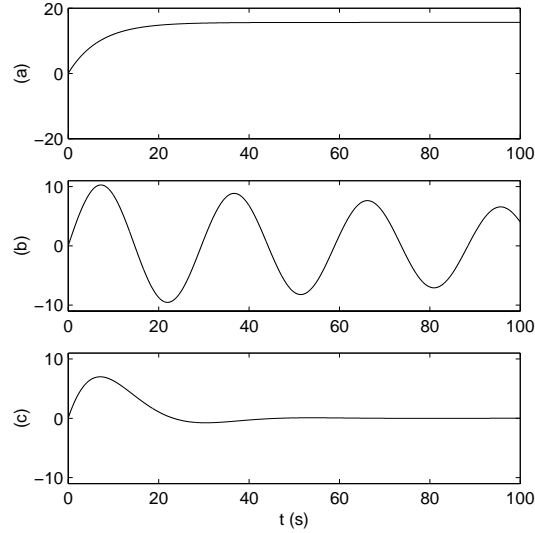
Figure 3.7: The transient response of the compliance voltage $V_s(s)$ to a step in DC offset current. (a) Proportional (b) Integral (c) PI.
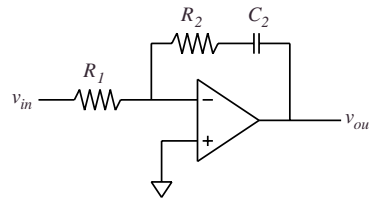
Figure 3.8: Opamp implementation of an inverting PI controller.

To illustrate the operation of the current amplifier, a 1 μF capacitor is driven at low frequencies with a current sensing resistor of 220 $k\Omega$. With $C(s) = \frac{0.004s + 0.00016}{s}$, the simulated compliance and tracking frequency responses are shown in Figures 3.10 and 3.11. The transient response to a step change in input current reference offset is shown in Figure 3.13. A 100 mHz signal is applied to examine the low frequency tracking performance, reference and measured currents are shown in Figure 3.12.

Similar experiments were carried out for a charge amplifier. Using a sensor capacitance of 10 μF, the compliance controller $C(s) = \frac{0.001}{s}$ provides the desired response. Analogous frequency and time domain results are presented in Figures 3.14, 3.15, 3.16, and 3.17.
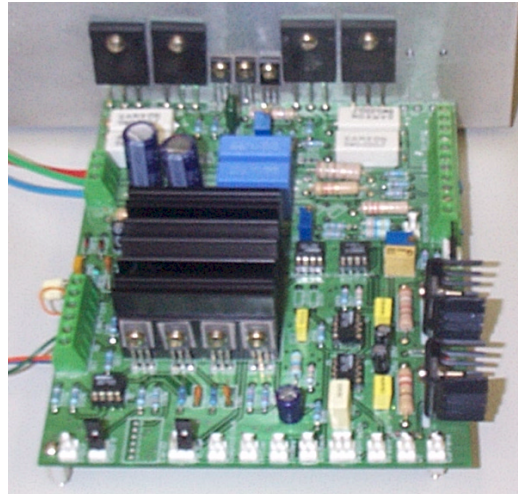
Figure 3.9: Photograph of a prototype current / charge amplifier.
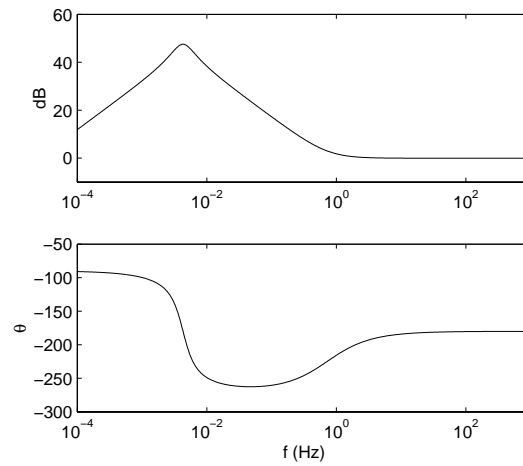
Figure 3.10: Simulated compliance frequency response $\frac{V_o(s)}{V_{ref}(s)}$ of the prototype current source.
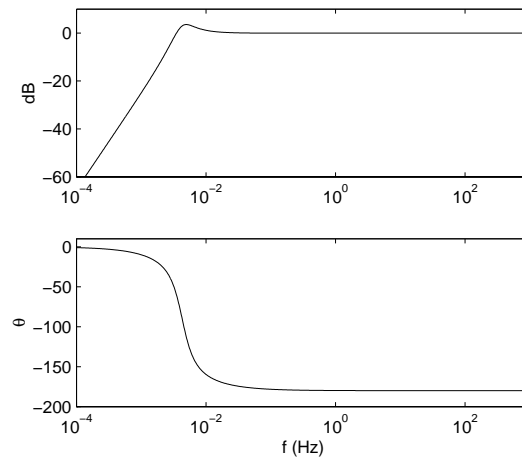
Figure 3.11: Simulated tracking frequency response $\frac{V_s(s)}{V_{ref}(s)}$ of the prototype current source.
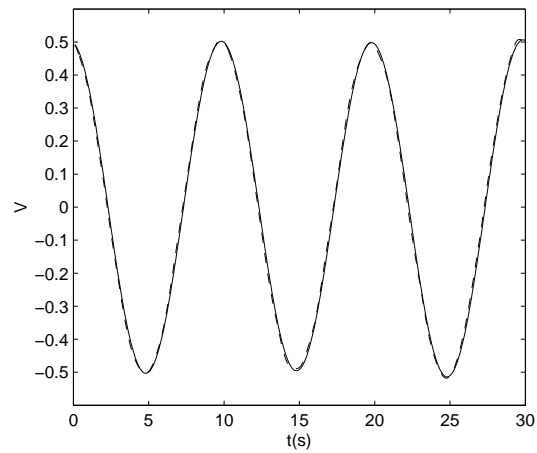
Figure 3.12: Reference (−) and measured current (- -).
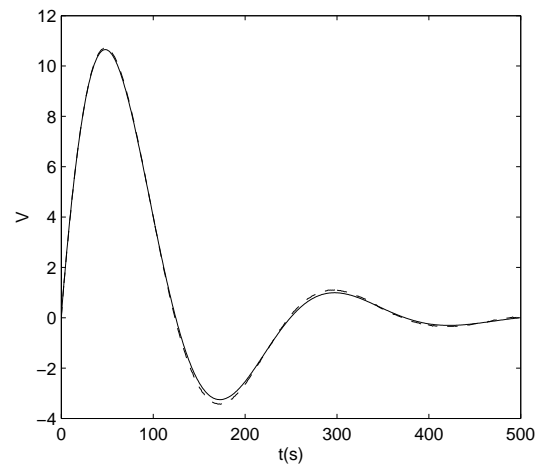
Figure 3.13: Simulated (–) and measured (- -) compliance response to a step change in current offset.
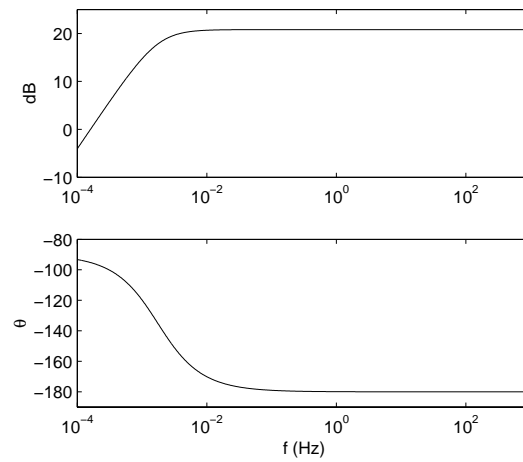
Figure 3.14: Simulated compliance frequency response $\frac{V_o(s)}{V_{ref}(s)}$ of the prototype charge amplifier.
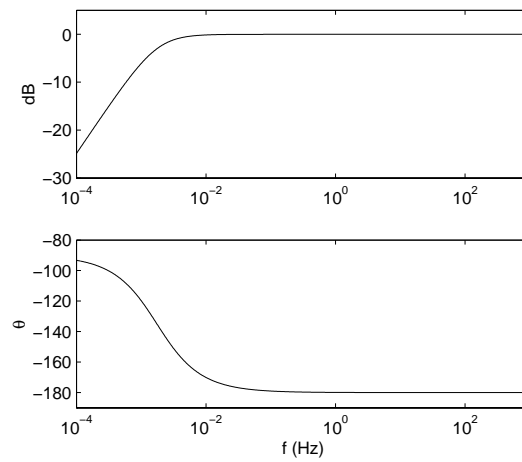
Figure 3.15: Simulated tracking response $\frac{V_s(s)}{V_{ref}(s)}$ of the prototype charge amplifier.
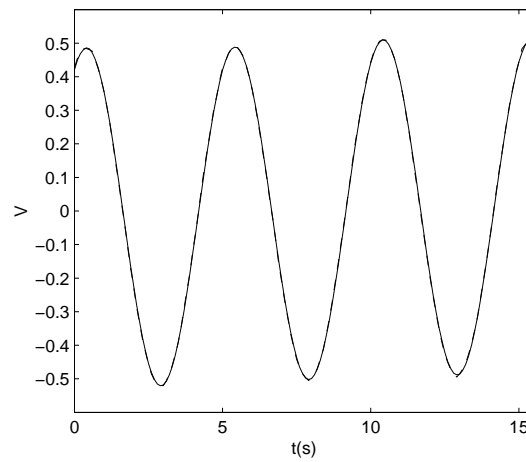
Figure 3.16: Reference (−) and measured charge (- -).
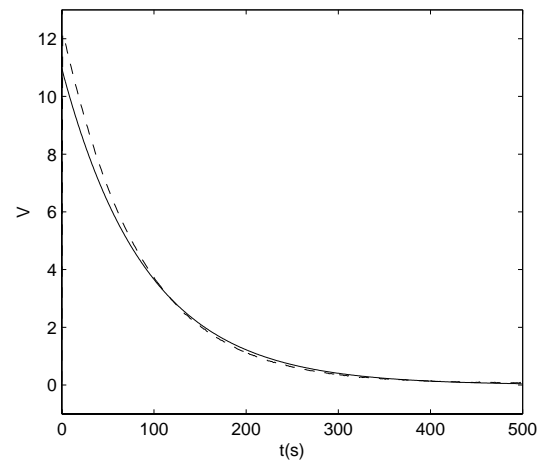
Figure 3.17: Simulated (−) and measured (- -) compliance response to a step change in reference offset.

3.2 Implementation of Admittance/Impedance Transfer Functions

Referring to Figure 3.18, the terminal impedance of an arbitrary electrical network $Z_T(s)$ can be implemented by either: (a) measuring the terminal current i_z and controlling the terminal voltage v_z, or (b) measuring the terminal voltage v_z and controlling the terminal current i_z. The motivation and benefits behind such techniques are thoroughly discussed in Chapter 2.

The choice of configuration, either synthetic impedance or admittance, will depend on the relative order of the desired impedance. As implementation of improper transfer functions is impractical [64], the choice should be made such that the required transfer function $Z(s)$ or $Y(s)$ is at least proper [64].
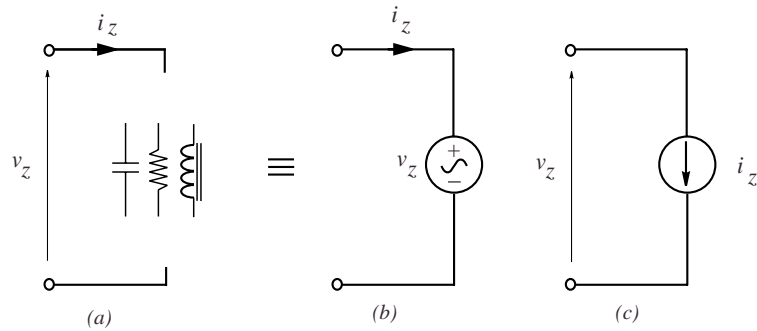
Figure 3.18: An arbitrary terminal impedance (a), a synthetic impedance (b), and a synthetic admittance (c).

3.2.1 Block Diagram Transformations

As discussed above, to synthesize an electrical network, a filter is required with the same transfer function as the impedance or admittance of that circuit. When using a DSP system, the filter can be implemented simply by calculating the electrical impedance and implementing that transfer function directly. This task may become tedious or complicated if the electrical circuit contains a large number of components. A 'current blocking' piezoelectric shunt circuit [124] may contain up to 18 individual components in a 3 mode

circuit. The admittance transfer function would contain 15 states and be parameterized in up to 18 variables.

Analog implementation adds further difficulty. Traditional filter synthesis techniques [114] typically require a partial fraction decomposition, followed by the implementation of each second order section.

Neither direct analog nor digital implementation is particularly straight-forward for complicated impedance structures. For second order transfer functions and above, the resulting digital or analog filter can be difficult to tune.

To simplify the process of impedance or admittance transfer function implementation, this section introduces a link between the topology of system block diagrams and circuit schematics. In the digital case, if a graphical compilation package such as the real time workshop for Matlab or similar is available, no impedance calculation from the circuit diagram is required at all. The resulting block diagram bears a natural resemblance to its corresponding circuit, is clearly parameterized, and is consequently easy to tune. In the analog case, the circuit can be broken down into a number of simple opamp integrators and amplifiers whose gains correspond directly to component values. The resulting filter circuit is practical, easy to implement, expandable, and simple to tune.

Following are the transformations of interest for both the impedance and admittance synthesis cases. In Section 3.2.2, two examples are presented to clarify the application.

Impedance Synthesis

Parallel equivalence. Consider the parallel network components $Z_1, Z_2, \ldots, Z_m$ as shown in Figure 3.19. The terminal impedance and admittance corresponding to this network is:

$$Z_T(s) = \frac{1}{\frac{1}{Z_1} + \frac{1}{Z_2} + \ldots + \frac{1}{Z_m}} \qquad Y_T(s) = \frac{1}{Z_1} + \frac{1}{Z_2} + \ldots + \frac{1}{Z_m} \ . \qquad (3.12)$$
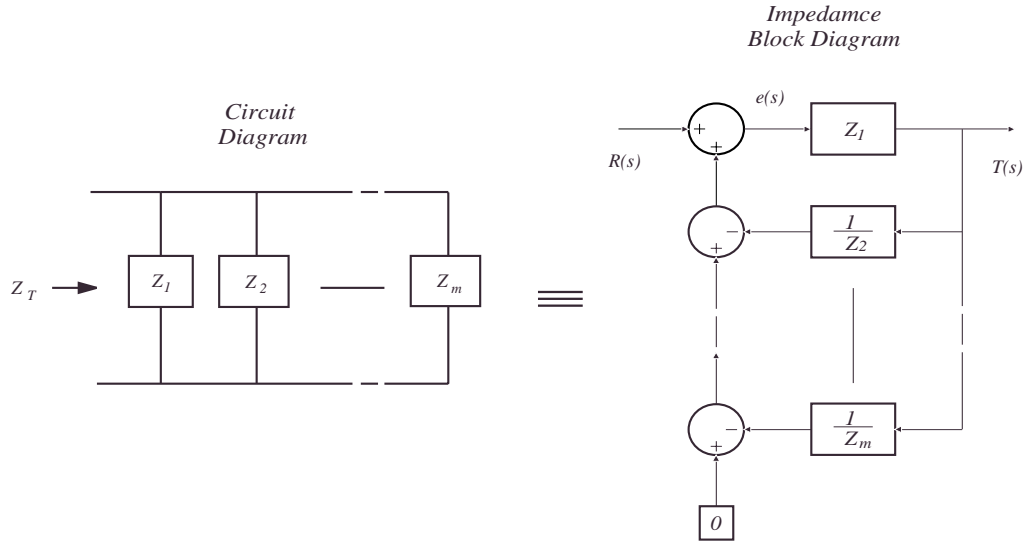
Figure 3.19: Parallel equivalence for impedance block diagrams.

Now consider the transfer function block diagram, also shown in Figure 3.19,

$$G(s) = \frac{T(s)}{R(s)} = \frac{Z_1}{1 + Z_1 \frac{1}{Z_2} + \ldots + Z_1 \frac{1}{Z_m}}$$
$$= \frac{1}{\frac{1}{Z_1} + \frac{1}{Z_2} + \ldots + \frac{1}{Z_m}}. \tag{3.13}$$

Observe that $Y_T(s)$ and $G(s)$ as described in equations (3.12) and (3.13) are identical. Therefore, if a synthetic impedance as shown in Figure 3.18 (b) is implemented with a transfer function equal to $G(s)$, the impedance seen from the terminals is identical to the impedance of the parallel network shown in Figure 3.19 (with impedance $Z_T(s)$ given by (3.12)).

Series equivalence. Consider the series network components $Z_1, Z_2, \ldots, Z_m$ as shown in Figure 3.20. The terminal impedance and admittance of this network are:

$$Z_T(s) = Z_1 + Z_2 + \ldots + Z_m \quad Y_T(s) = \frac{1}{Z_1 + Z_2 + \ldots + Z_m}. \tag{3.14}$$

Now consider the transfer function block diagram, also shown in Figure 3.20,

$$G(s) = \frac{T(s)}{R(s)} = Z_1 + Z_2 + \ldots + Z_m. \tag{3.15}$$

Observe that $Y_T(s)$ and $G(s)$ as described in equations (3.14) and (3.15) are identical. Therefore, if a synthetic impedance as shown in Figure 3.18 (b) is implemented with a
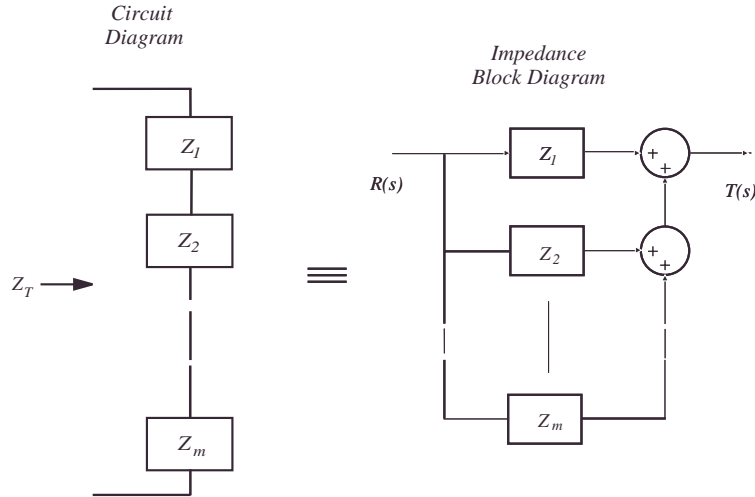
Figure 3.20: Series equivalence for impedance block diagrams.

transfer function equal to $G(s)$, the impedance seen from the terminals will be identical to the impedance of the series network shown in Figure 3.20 (with impedance $Z_T(s)$ given by (3.14)).

Admittance Synthesis

Parallel equivalence. Consider the parallel network components $Z_1, Z_2, \ldots, Z_m$ as shown in Figure 3.21. The terminal impedance and admittance of this network is

$$Z_T(s) = (\tfrac{1}{Z_1} + \tfrac{1}{Z_2} + \ldots + \tfrac{1}{Z_m})^{-1} \quad Y_T(s) = \tfrac{1}{Z_1} + \tfrac{1}{Z_2} + \ldots + \tfrac{1}{Z_m}. \tag{3.16}$$

Now consider the transfer function block diagram, also shown in Figure 3.21.

$$G(s) = \frac{T(s)}{R(s)} = \frac{1}{Z_1} + \frac{1}{Z_2} + \ldots + \frac{1}{Z_m}. \tag{3.17}$$

Observe that $Y_T(s)$ and $G(s)$, as described in equations (3.16) and (3.17) are identical. Therefore, if a synthetic impedance as shown in Figure 3.18 (c) is implemented with a transfer function equal to $G(s)$, the impedance seen from the terminals is identical to the impedance of the parallel network shown in Figure 3.21 (with impedance $Z_T(s)$ given by (3.16)).
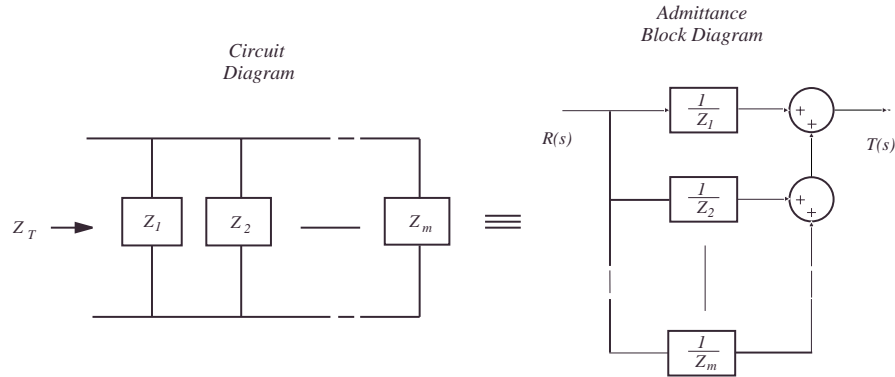
Figure 3.21: Parallel equivalence for admittance block diagrams.

Series equivalence. Consider the series network components $Z_1, Z_2, \ldots, Z_m$ as shown in Figure 3.22. The terminal impedance and admittance of this network is:

$$Z_T(s) = Z_1 + Z_2 + \ldots + Z_m \quad Y_T(s) = \tfrac{1}{Z_1 + Z_2 + \ldots + Z_m}. \tag{3.18}$$

Now consider the transfer function block diagram, also shown in Figure 3.22,

$$\begin{aligned} G(s) = \tfrac{T(s)}{R(s)} \quad &= \tfrac{\frac{1}{Z_1}}{1 + \frac{1}{Z_1}Z_2 + \ldots + \frac{1}{Z_1}Z_m} \\ &= \tfrac{1}{Z_1 + Z_2 + \ldots + Z_m}. \end{aligned} \tag{3.19}$$

Observe that $Y_T(s)$ and $G(s)$ as described in equations (3.18) and (3.19) are identical. Therefore, if a synthetic impedance as shown in Figure 3.18 (c) is implemented with a transfer function equal to $G(s)$, the impedance seen from the terminals is identical to the impedance of the series network shown in Figure 3.22 (with impedance $Z_T(s)$ given by (3.18)).

3.2.2   Examples

Digital Synthesis

Consider the current blocking circuit [124] shown in Figure 3.23. The corresponding admittance block diagram is shown in Figure 3.24. Each subsystem can be further decomposed or implemented by parameterized state space system, both methods facilitate simplified online tuning.
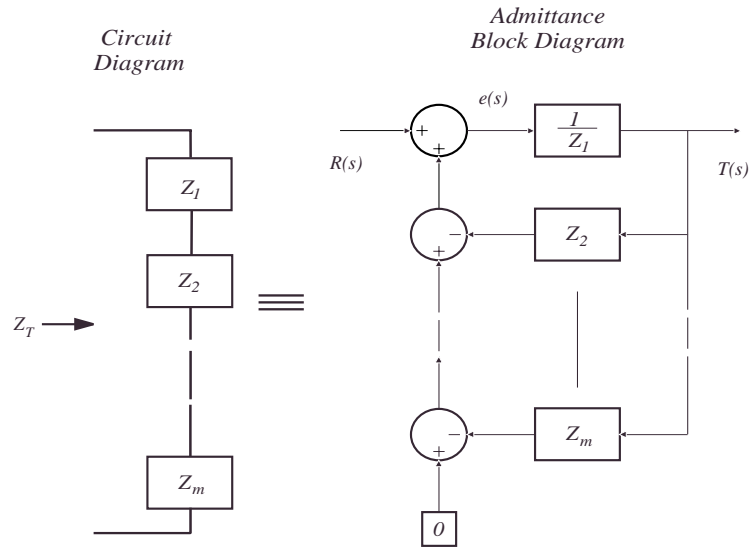
Figure 3.22: Series equivalence for admittance block diagrams.
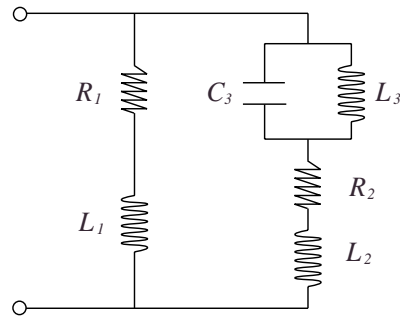
Figure 3.23: Current blocking shunt circuit.

Analog Synthesis

Current flowing shunt circuits have recently been introduced [12]. The shunt circuit is simple and increases in order only linearly as the number of modes to be shunt damped simultaneously increases.

To implement the admittance of a current flowing shunt circuit, a filter that represents a single circuit branch is required. The output of each branch filter can then be summed to produce a filter representing the entire multi-mode circuit.
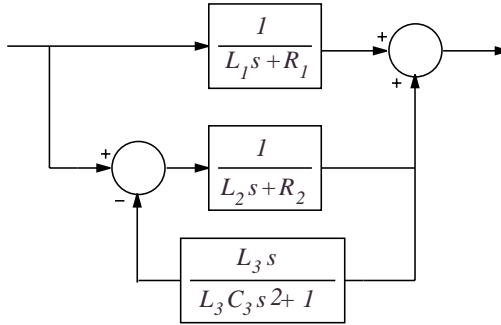
Figure 3.24: Admittance transfer function block diagram of a current flowing shunt circuit.
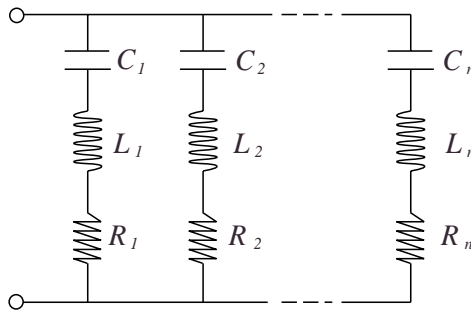
Figure 3.25: Current flowing shunt circuit.

One may first consider the traditional filter synthesis techniques of state-variable or Sallen-Key [114]. Such techniques result in a circuit whose component values are a complicated function of the original shunt components, severely impeding any attempt at online tuning. Alternatively, using the transformations presented in this section, each admittance branch can be implemented first as a system block diagram, then as an analog circuit containing only summers, integrators, and gains.

The admittance block diagram of a single mode current flowing shunt circuit is shown in Figure 3.26. A simple but effective analog implementation is shown in Figure 3.27. The transfer function is easily found to be,

$$\frac{V_{out}(s)}{V_{in}(s)} = \frac{1}{R_1 C_1 s + \frac{R_2}{R_3} + \frac{1}{R_4 C_4 s}}. \tag{3.20}$$
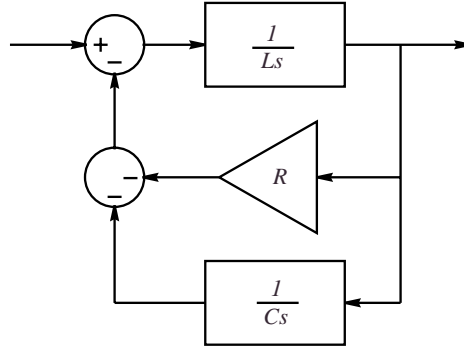
Figure 3.26: A single current flowing branch admittance block diagram.

The filter components are related to the original shunt circuit branch by,

$$L = R_1 C_1 \qquad\qquad (3.21)$$

$$R = \frac{R_2}{R_3}$$

$$C = R_4 C_4.$$

Although there are more opamps than would normally be required, the transfer function is explicitly parameterized in terms of the parent circuit. The resistors R_1, R_2, and R_4 can be varied independently to tune the shunt circuit inductance, resistance, and capacitance.

A practical implementation is shown in Figure 3.28. For flexibility, the filter is manufactured as a small board that can be installed or removed as necessary. The pictured current source has a maximum supply voltage of +/- 45 Volts, includes an on-board low voltage supply, and can hold up to two impedance cards.

The high voltage amplifier presented in Section 3.1.3 is also capable of accepting impedance cards. This technology represents a considerable increase in the practicality and simplicity of piezoelectric shunt damping systems.
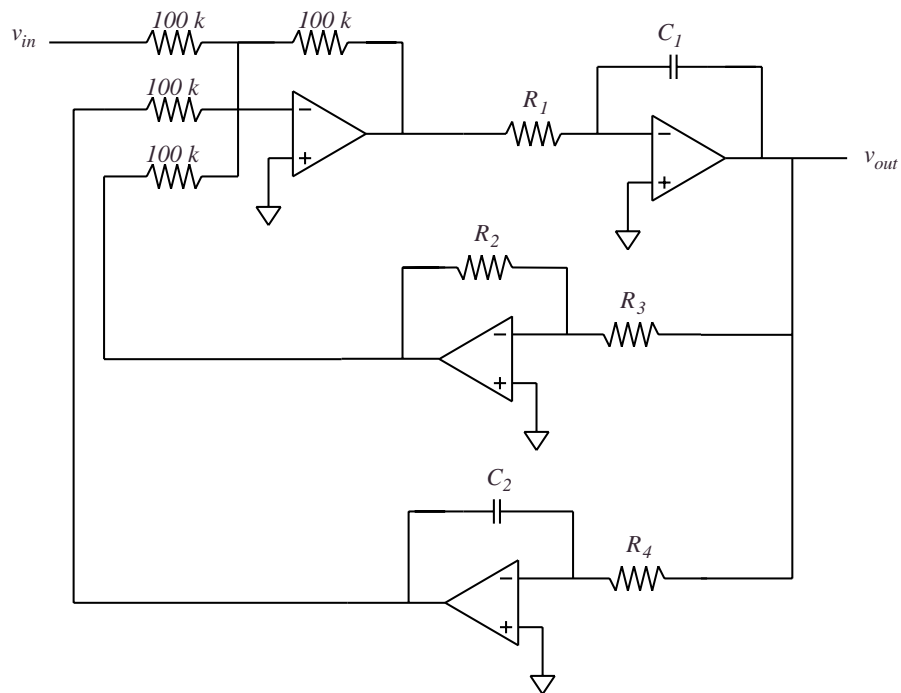
Figure 3.27: Analog implementation of the block diagram shown in Figure 3.26.
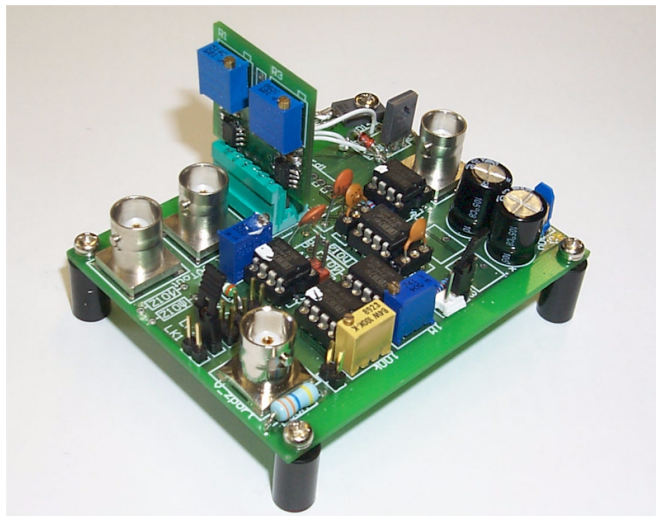
Figure 3.28: An opamp based current source with impedance card mounted vertically.

3.3   Switch-Mode Implementation

This section introduces an alternative method for implementation of piezoelectric and electromagnetic shunt damping circuits. The *switch-mode synthetic admittance* requires no high voltage linear components, is small in size, and is ideal for high-power or industrial scale applications. Switch-mode devices are capable of recycling reactive power and offer much higher operating efficiencies than comparable linear techniques.

3.3.1   Device Operation

A simplified circuit diagram of the switch-mode synthetic admittance is shown in Figure 3.29. The basic operation is much the same as that discussed previously, the device maintains an arbitrary relationship between the measured terminal voltage and applied current, i.e. between i_T and v_T.

We begin with some preliminary circuit analysis. In the Laplace domain,

$$I_T(s) = \frac{V_T(s) - V_{pwm}(s)}{Z_c(s)}.$$
(3.22)

In this case, the desired relationship between terminal voltage and current is the impedance $Z_T(s)$,

$$I_T(s) = \frac{1}{Z_T(s)}V_T(s).$$
(3.23)

Combining (3.22) and (3.23) yields the relationship required to maintain (3.23) at the terminals,

$$V_{pwm}(s) = V_T(s)\left(1 - \frac{Z_c(s)}{Z_T(s)}\right).$$
(3.24)

The reader may recognize the similarity between the circuit on the right hand side of Figure 3.29 and a controlled single phase switch-mode rectifier, or a four quadrant switch-mode amplifier. Indeed the only difference between such devices is the selection of control impedance and bridge control algorithm. Although we can not synthesize $v_{pwm}(t)$ exactly, we can do so in the average sense. The relationship between the reference signal and the control duty cycle is

$$D = \frac{1}{2}\left(\frac{v_{ref}}{V_{dc}} + 1\right).$$
(3.25)
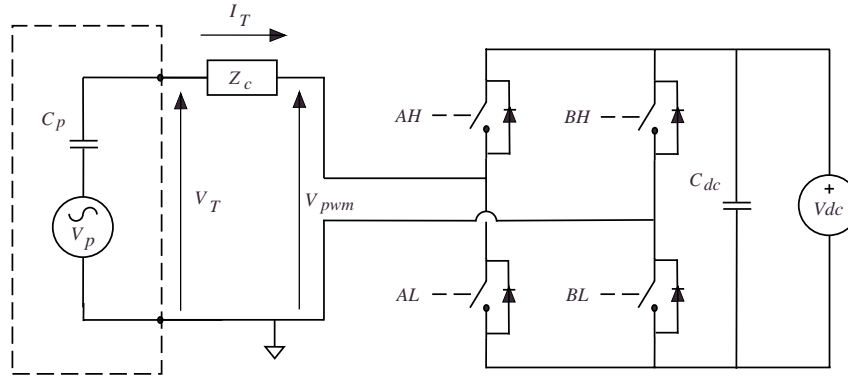
Figure 3.29: The switched mode synthetic admittance.

Boost Configuration

In this sub-section we consider a specific choice for the control impedance Z_c, a series inductor and resistor. In this configuration, the structure of the circuit resembles that of a single phase boost rectifier. The primary motivation is to allow the flow of real and reactive power back to the source.

Assuming that the inductance is large enough to maintain an approximately constant current over the switching interval, when the applied potential v_{pwm} opposes the current i_T, the inductor overcomes the source potential and forces the current to flow through the anti-parallel diodes back to the source.

This configuration also has the advantage of greatly reducing the high frequency content applied to the piezoelectric transducer. The inherent capacitance of the PZT together with the control impedance creates a second order low pass power filter,

$$V_T(s) = \frac{\frac{1}{L_c C_p}}{s^2 + \frac{R_c}{L_c}s + \frac{1}{L_c C_p}} V_{pwm}(s). \tag{3.26}$$

For reasonable values of R_c, L_c, and C_p (300 Ω, 0.1 H, 400 ηF), the filter has a cutoff frequency of around 800 Hz. If we consider a system with a switching frequency of 8 kHz, such a filter would attenuate the fundamental switching component by 40 dB. Taking into

account the additional low pass dynamics of the plant, the actual realized disturbance due to switching is negligible.

3.3.2 Efficiency

If we consider a sinusoidal voltage source V_s connected to an impedance Z_T, the real dissipated power is

$$P_T = \frac{1}{2}\,|V_s|^2\,\mathbf{Re}\left\{\frac{1}{Z_T}\right\} = \frac{1}{2}\left|\frac{V_s}{Z_T}\right|^2\mathbf{Re}\left\{Z_T\right\}. \tag{3.27}$$

We define the efficiency of a switch-mode synthetic admittance as the ratio of power absorbed by V_{dc}, to the power that would normally be dissipated if the impedance Z_T was implemented using ideal physical components, i.e.

$$\eta(Z_c, Z_T, \omega) = 100\% \times \frac{P_{V_{dc}}}{P_T}. \tag{3.28}$$

By this definition, virtual or linear synthetic implementations will always result in a negative efficiency, i.e. they absorb no real power. In fact, the situation is worse, such implementations must actually supply power to synthesize the flow of apparent power. For our application, i.e. synthesizing inductors to form a highly resonant circuit, the realized efficiency is extremely poor (large and negative).

The quantity $P_{V_{dc}}$ is easily found by performing a power balance. Obviously, the real power as seen from the terminals will be equal to P_T. The only remaining contribution to the net real power flow is that dissipated by the control impedance,

$$P_c = \frac{1}{2}\left|\frac{V_s}{Z_T}\right|^2\mathbf{Re}\left\{Z_c\right\} \tag{3.29}$$

$$\eta(Z_c, Z_T, j\omega) = 100\% \times \frac{P_T - P_c}{P_T} \tag{3.30}$$

$$= 100\% \times \left[1 - \frac{\mathbf{Re}\left\{Z_c\right\}}{\mathbf{Re}\left\{Z_T\right\}}\right]. \tag{3.31}$$

The best efficiency (100%) is achieved if the control impedance contains no real component. If the control impedance has a larger real component than the terminal impedance, the efficiency is negative, i.e. the source V_{dc} must supply real power to the system.

3.3.3 Practical Advantages and Considerations

The switch-mode synthetic admittance has a number of advantages over its linear counterpart. Some difficulties also arise that are not present in the linear case.

- **Cost**. Discrete power switches can be obtained for a fraction of the cost of HV linear components.

- **Size / Density.** The switching circuit shown in Figure 3.29 does not dissipate any real or reactive power flowing between the source and the controlling impedance. There is also no requirement for quiescent or bias current. Coupled with the small physical size of power switches, a low heat dissipation allows the circuit to be manufactured in an extremely small enclosure. Another significant factor is the size of the power supply. In the linear case, a large supply is required to power the components and to supply reactive power to the structure. As we have seen, in the switching case, not only is the power supply small, but if the synthesized terminal impedance has a larger real component than the controlling impedance, no power supply is required at all.

- **Control Conditioning.** The switch-mode synthetic admittance manipulates the terminal current by controlling the average voltage across a control impedance Z_c. In practice, the circuit must be conditioned so that the expected current range results in realizable voltage differences across the control impedance. At a specific frequency, this is easily achieved by ensuring $|Z_c(s)| >> |Z_T(s)|$, i.e. by choosing a control impedance much greater in magnitude than $Z_T(s)$. Another simple technique is to design $Z_c(s)$ having an opposite or significantly different phase angle with respect to $Z_T(s)$. In the boost configuration, we are limited in choice to an inductor and resistor.

  The impedance of passive shunt damping circuits is typically comprised of inductive resistive branches. In the active frequency range, the reactance of each branch is heavily dominated by the inductor, this is expected as resonant circuits operate at very low power factors (implying small real impedance).

We must consider a number of factors: For efficiency we wish to keep the control resistance R_c small. If R_c is small, the only way to increase the control impedance, is to increase the size of the inductance L_c. As both the control and terminal impedance have a similar impedance angle (approximately $+\pi$), we cannot improve the control conditioning by relying on a phase difference. Thus, to obtain a well conditioned voltage drop across the control impedance Z_T, the control inductance must be a reasonable fraction of the terminal inductance. e.g. $L_c = \frac{L_T}{10}$. Multi-mode shunt circuits include at least one inductance per branch, in this case, we must consider the lowest frequency branch, (the branch with the greatest inductance).

- **Common Mode Instrumentation Performance.** The return terminals of the load PZT and supply V_{dc} must be electrically isolated. Ideally, the acquisition of v_T should be performed using a circuit completely isolated from both references. As this is impossible in practice, the instrumentation amplifier must have a high common mode rejection ratio to attenuate components resulting from the varying potential between the two references.

3.3.4   Power Harvesting

The switch-mode synthetic admittance is capable of absorbing energy from an electrical source. When the efficiency (3.31) is positive, and the device is being used to implement some network containing a finite resistance, the net real power flow into the DC source is also positive.

According to [38], the damped system transfer function from an applied actuator voltage to the measured output V_z is

$$G_{v_z v} = \frac{V_z(s)}{V_a(s)} = \frac{K(s)G_{vv}(s)}{1 + K(s)G_{vv}(s)}, \tag{3.32}$$

where $K(s)$ is defined in Chapter 2 as

$$K(s) = \frac{Z(s)}{Z(s) + \frac{1}{C_T s}}. \tag{3.33}$$

Given the terminal voltage (3.32), and the operating efficiency (3.31), we can quantify the harvested real power. At a specific frequency, the real power dissipated by the terminal impedance is

$$P_T(j\omega) = \frac{1}{2} |V_Z(j\omega)|^2 \, \mathbf{Re}\left\{\frac{1}{Z_T(j\omega)}\right\}, \qquad (3.34)$$

thus,

$$\begin{aligned} P_{V_{dc}}(j\omega) &= \eta \frac{1}{2} \left|\frac{V_z(j\omega)}{Z_T(j\omega)}\right|^2 \mathbf{Re}\left\{Z_T(j\omega)\right\} \qquad (3.35) \\ &= \frac{1}{2}\left|\frac{V_z(j\omega)}{Z_T(j\omega)}\right|^2 \left[\mathbf{Re}\left\{Z_T(j\omega) - Z_c(j\omega)\right\}\right], \end{aligned}$$

where $V_z(s) = G_{v_z v}(s) V_a(s)$, and η denotes $\eta(Z_c, Z_T, j\omega)$.

3.3.5 Experimental Results

The switch-mode synthetic admittance was employed to implement a dual-mode current-blocking piezoelectric shunt damping circuit. In theory, the circuit is capable of harvesting power from the structure. To date, practical difficulties have avoided such operation.

The problems with power harvesting are due mainly to the highly reactive nature of piezoelectric shunt damping circuits. In the frequency range of interest, the impedance of a typical shunt circuit results in a net power flow that is 90-99 % reactive. Thus, to harvest power, the device must efficiently recycle reactive power and absorb only the minute amount of real power normally dissipated by the resistance. In practice, losses due to switching, imperfect boost inductors, and other parasitic effects have prevented such ideal operation.

Experimental Setup

The experimental beam apparatus, pictured in Figure 3.30, is a uniform aluminum bar with rectangular cross section and experimentally pinned boundary conditions at both ends. A pair of piezoelectric ceramic patches (PIC151) are attached symmetrically to either side of the beam surface. One patch is used as an actuator and the other as a shunting
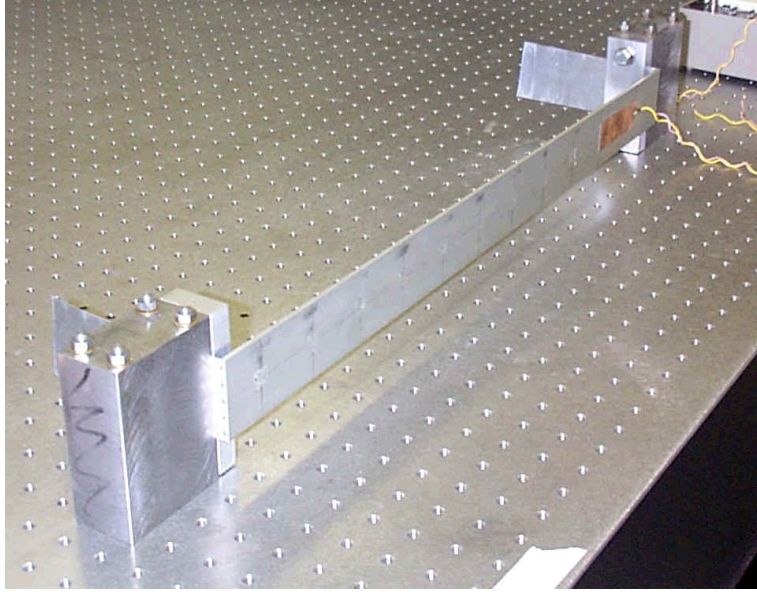
Figure 3.30: The experimental beam.

layer. Physical parameters of the experimental beam and piezoelectric transducers are summarized in Tables 3.1 and 3.2. Note that the transducer location offers little control authority over the first mode. In this work, the structures second and third modes are targeted for reduction.

A prototype switch-mode admittance is shown in Figure 3.31. The board contains two isolated sub-circuits, the gate-drive and MOSFET bridge on the left, and the ground referenced instrumentation on the right. The MOSFET devices used in this circuit permit

Length, L	$0.6\ m$
Width, w_b	$0.05\ m$
Thickness, h_b	$0.003\ m$
Youngs Modulus, E_b	$65 \times 10^9\ N/m^2$
Density, ρ	$2650\ kg/m^2$

Table 3.1: Experimental Beam Parameters.

Length	0.070 m
Charge Constant, d_{31}	-210×10^{-12} m/V
Voltage Constant, g_{31}	-11.5×10^{-3} Vm/N
Coupling Coefficient, k_{31}	0.340
Capacitance, C_p	0.105 μF
Width, w_s w_a	0.025 m
Thickness, h_s h_a	0.25×10^{-3} m
Youngs Modulus, E_s E_a	63×10^9 N/m^2

Table 3.2: Piezoelectric Transducer Properties.
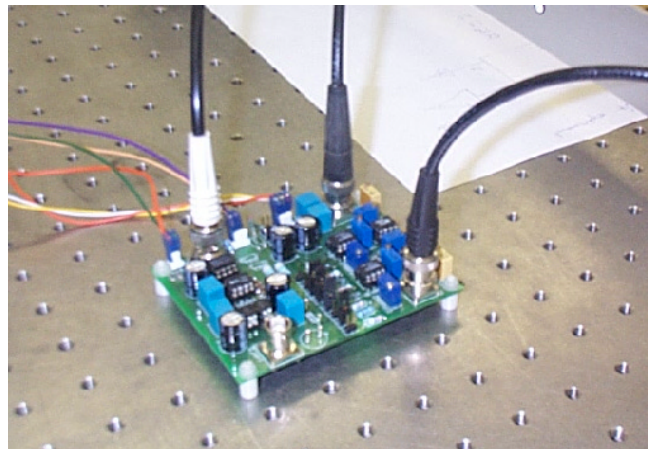
Figure 3.31: A switch-mode synthetic admittance connected to the experimental beam and dSpace signal processor.

R_1	1543 Ω	L_1	43 H
R_2	1145 Ω	L_2	20.9 H
C_3	100 nF	L_3	45.2 H

Table 3.3: Component values.

a peak-to-peak output voltage of 120 V at 2 Amps.

The displacement and voltage frequency responses are measured using a Polytec scanning laser vibrometer (PSV-300) and HP spectrum analyzer (35670A).

Damping Performance

In reference [37], a current-blocking piezoelectric shunt damping circuit is designed to minimize the $\mathcal{H}_2$ norm of the beam described in Section 3.3.5. The circuit schematic and component values can be found in Figure 2.15 and Table 3.3.

Using a control impedance of 67 mH + 33 $k\Omega$, the switch-mode admittance was used to implement the shunt circuit. The experimental open- and closed-loop transfer functions from an applied actuator voltage to the resulting displacement at a point $G_{yv}(r = 0.17m, s)$ are shown in Figure 3.32. The amplitudes of the second and third mode are reduced by 21.6 and 21.3 dB respectively.

To assess the linearity of switch-mode implementation, a sine wave was applied at the second mode resonance frequency, the power spectral density of the resulting voltage applied to the piezoelectric transducer is shown in Figure 3.33. The harmonic content and switching noise applied to the piezoelectric transducer is negligible (< 60 dB).

3.4   Conclusions

A new class of current and charge amplifier has been introduced. By feeding back the amplifier's compliance voltage, the effect of DC circuit offsets can be eliminated. Experimental results show excellent low frequency current and charge tracking and complete
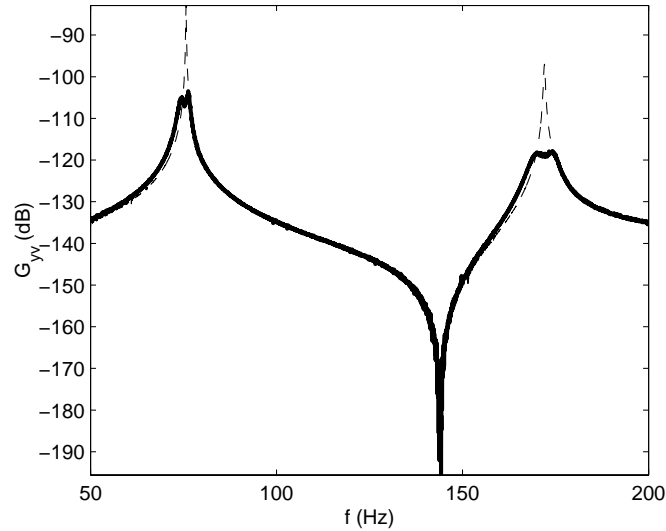
Figure 3.32: Experimental open-loop (- -) and damped system transfer (—) functions.

rejection of DC offsets. A prototype compliance feedback amplifier connected to a purely capacitive load is shown to accurately realize low frequency current and charge signals.

One application for capacitive-load current sources is in the field of shunt damping. To avoid implementing impractically large inductors or non-ideal virtual circuits, the synthetic admittance can be employed to implement an ideal electrical network. Block diagram transformations have been presented to simplify the design of analog or digital signal processing algorithms. In the previous chapter, the prototype current amplifier and presented block diagram transformations were applied to damp 4 modes of a simply supported beam.

The switch-mode synthetic admittance has been presented as a low cost, high power, and extremely efficient alternative to linear implementation. The combination of the load and the control impedance act as a low-pass power filter. This allows highly linear synthesis of the voltage V_z applied to a piezoelectric transducer with negligible harmonic or switching components. Two modes of a simply supported beam were successfully reduced in amplitude by 21.6 and 21.3 dB. Although ideally, the device is capable of harvesting power when implementing a circuit with non-zero resistance, the difficulties involved when attempting to synthesize a highly reactive impedance preclude such operation.
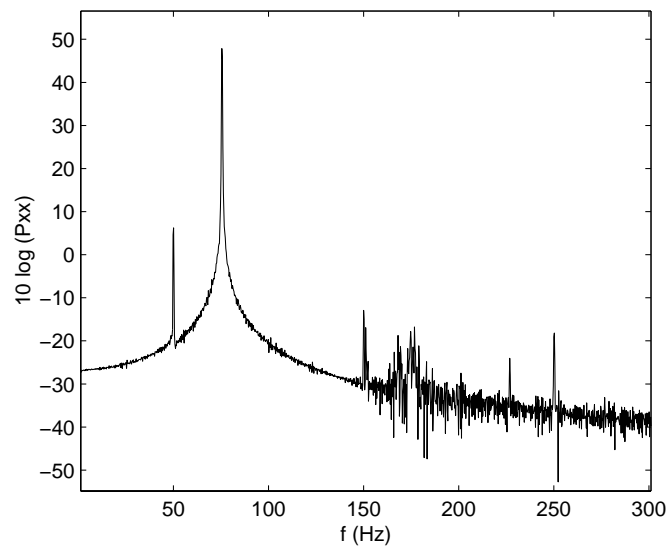
Figure 3.33: Power spectral density of the terminal voltage V_z applied to the piezoelectric transducer.

Active Piezoelectric Shunt

Control

In Chapter 2, a technique was presented for the implementation of piezoelectric shunt damping circuits. Through the use of a controlled current source and voltage measurement, or *vice versa,* an arbitrary impedance can be presented to the terminals of a piezoelectric transducer. In this chapter, the arbitrary nature of such implementation will be exploited to synthesize new possibly-multivariable, possibly-active piezoelectric shunt impedances. A simple modeling framework is introduced that lends the problem to such synthesis techniques as LQR, LQG, $\mathcal{H}_\infty$, and $\mathcal{H}_2$. Previous problems including the *ad-hoc* nature of shunt circuit tuning, limited performance, and the strong dependence on structural resonance frequencies are significantly alleviated.

4.1 Introduction

As shown in Figure 4.1, an electrical impedance $Z(s)$ can be synthesized with the use of a controlled voltage source, charge measurement, and signal filter. The electric charge $q(t)$, measured in Coulombs (C), is simply the time integral of current. When dealing with capacitive loads, measuring or controlling the charge is convenient as the associated terminal voltage is related proportionally. In contrast, current is related to the terminal voltage through a derivative. If measuring the current and operating over a wide frequency bandwidth, the resulting impedance transfer function is dominated by the derivative and has a correspondingly large dynamic range of at least 20 dB per decade. For practical
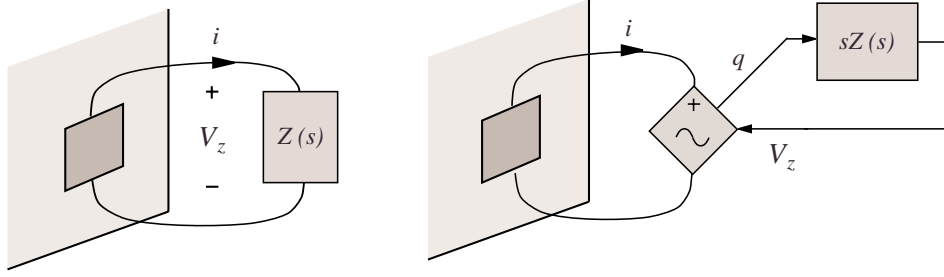
Figure 4.1: Impedance synthesis using a charge controlled voltage source.

reasons, it is advantageous to maintain a constant signal level over all frequencies, hence the motivation for controlling or measuring charge.

To implement a specified impedance $Z(s)$, the terminal voltage V_z, as shown in Figure 4.1, should be related to the current i by,

$$V_z(s) = Z(s)i(s), \qquad (4.1)$$

which implies,

$$V_z(s) = sZ(s)q(s). \qquad (4.2)$$

For obvious reasons, the filter $sZ(s)$, will be referred to as an s-impedance.

By viewing the charge q as a measurable system output, and the voltage V_z as an applied control signal, the design of an appropriate s-impedance can be cast as a standard regulator problem. After first modeling the dynamics of a shunted piezoelectric laminate structure in Section 4.2, LQG, $\mathcal{H}_\infty$, and $\mathcal{H}_2$ synthesis techniques are applied in Section 4.3.

4.2   Modeling

With the aim of facilitating active shunt design, this section introduces a charge-based modeling technique for piezoelectric laminate structures.

Consider the piezoelectric laminate structure shown in Figure 4.2. Through the use of a shunt patch driven by the voltage V_z, the goal is to suppress vibration resulting from two
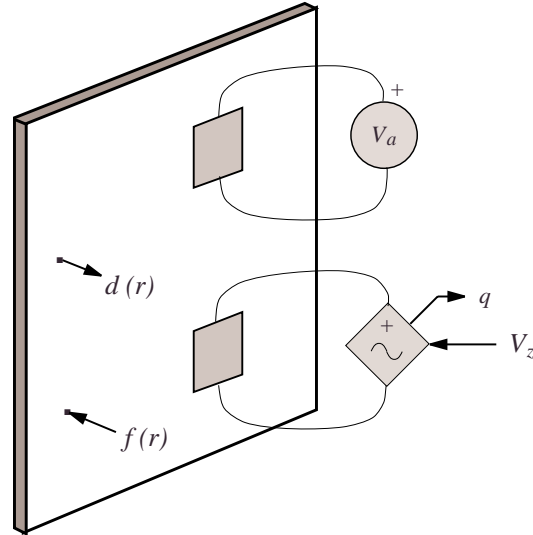
Figure 4.2: A general piezoelectric laminate structure excited by a distributed force $f(r, t)$ and the voltage $V_a(t)$ applied to a disturbance patch. The resulting vibration $d(r, t)$ is suppressed through the presence of an electrical impedance connected to the shunt transducer.

disturbances: V_a, the voltage applied to a disturbance patch, and $f(r, t)$ a generally distributed external force. The implemented transfer function between the measured charge q and applied voltage V_z effectively presents an electrical impedance $Z(s)$ to the transducer. The remainder of this section is dedicated to modeling the interaction between structure, transducer, and impedance.

4.2.1 Composite Piezoelectric-mechanical System

Consider the piezoelectric laminate structure shown in Figure 4.3 (a). The structure is disturbed by m transducers on the left side, and controlled by a further m collocated transducers on the other. The task of modeling the composite piezoelectric-mechanical system will proceed much as that presented in [91]. The possibility of multiple transducers
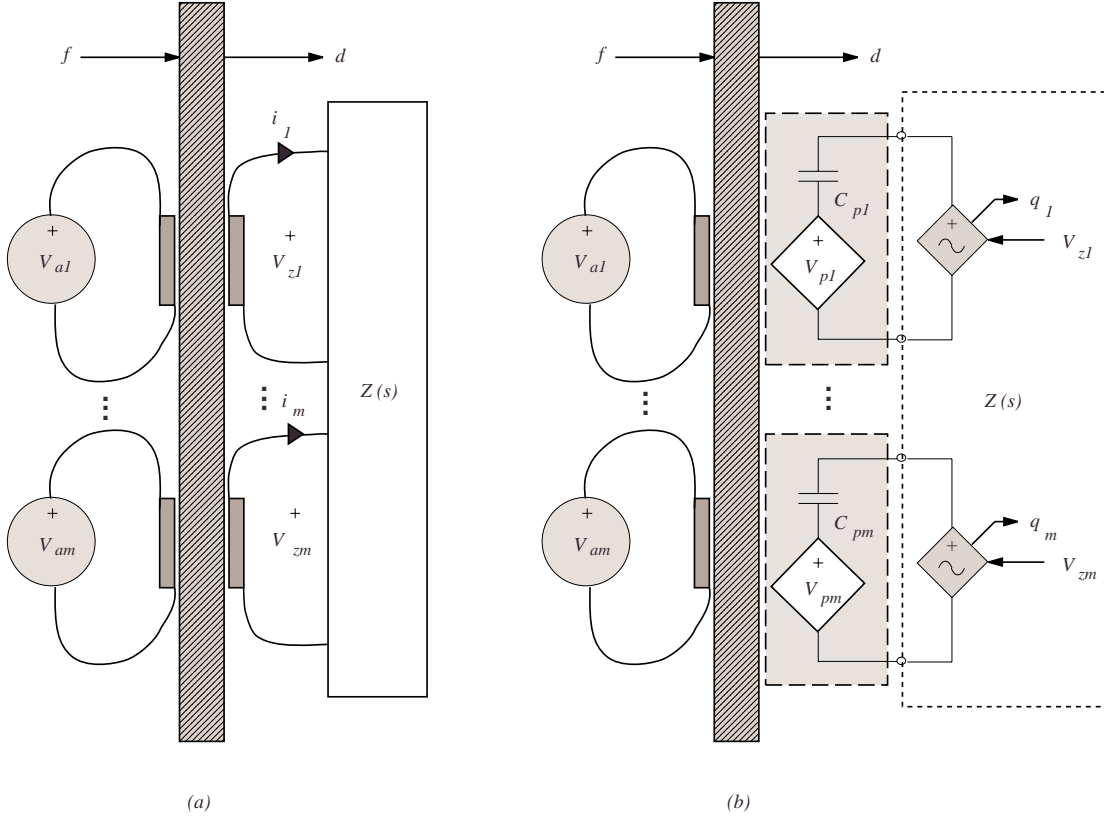
Figure 4.3: A shunted multi-transducer structure (a). Synthetic implementation of the impedance (b).

will be considered. To begin, let us define,

$$V_z = \begin{bmatrix} V_{z1} \\ V_{z2} \\ \vdots \\ V_{zm} \end{bmatrix} \quad V_p = \begin{bmatrix} V_{p1} \\ V_{p2} \\ \vdots \\ V_{pm} \end{bmatrix} \quad V_a = \begin{bmatrix} V_{a1} \\ V_{a2} \\ \vdots \\ V_{am} \end{bmatrix} \quad i = \begin{bmatrix} i_{z1} \\ i_{z2} \\ \vdots \\ i_{zm} \end{bmatrix}. \tag{4.3}$$

By applying Ohm's law, and writing Kirchoff's Voltage Law (KVL) around the kth loop we obtain,

$$V_z(s) = Z(s)\, i(s) \tag{4.4}$$

$$V_{zk}(s) = V_{pk}(s) - \frac{1}{C_{pk}s} i(s). \tag{4.5}$$
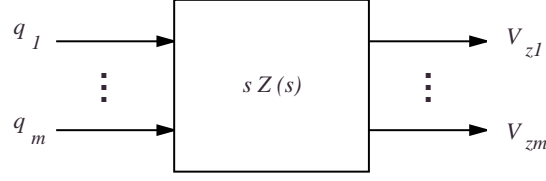
Figure 4.4: The multi-variable transfer function required to present an impedance

$Z(s)$ to the shunt transducers shown in Figure 4.3 (b).

Assembling the results for each loop,

$$V_z(s) = V_p(s) - \frac{1}{s}\Lambda\ i(s), \tag{4.6}$$

$$q = -\Lambda^{-1}V_z + \Lambda^{-1}V_p, \tag{4.7}$$

where

$$\Lambda = \begin{bmatrix} \frac{1}{C_{p1}} & & & \\ & \frac{1}{C_{p2}} & & \\ & & \ddots & \\ & & & \frac{1}{C_{pm}} \end{bmatrix}. \tag{4.8}$$

After applying the principle of superposition, the strain contribution from each disturbance
and shunt voltage is

$$V_p(s) = G_{va}(s)V_a(s) + G_{vv}(s)V_z(s), \tag{4.9}$$

where $G_{va}(s)$ and $G_{vv}(s)$ are the multi-variable transfer functions from an applied distur-
bance and shunt voltage to the piezoelectric voltage V_p, i.e.

$$G_{va}(s) = \frac{V_p(s)}{V_a(s)} \qquad G_{vv}(s) = \frac{V_p(s)}{V_z(s)}\ . \tag{4.10}$$

In the case where each disturbance and shunt transducer pair are identical, collocated,
and poled in opposite directions, $G_{va}(s) = -G_{vv}(s)$.

Note that this analysis does not require an equal number of disturbance and shunt trans-
ducers. This case is considered only to allow a simplified representation of the feed-back
diagram associated with the system.

The shunted composite system, alternatively referred to as the closed-loop system, can be obtained from equations (4.4), (4.5), and (4.9),

$$V_p(s) = \left[I - G_{vv}(s) \; Z(s) \; \left(Z(s) + \frac{1}{s}\Lambda \right)^{-1} \right]^{-1} G_{va}(s) \; V_a(s). \qquad (4.11)$$

In a similar fashion, the composite displacement transfer function can also be derived,

$$d(r, s) = \left[I - G_{vv}(s) \; Z(s) \; \left(Z(s) + \frac{1}{s}\Lambda \right)^{-1} \right]^{-1} G_{da}(s) \; V_a(s), \qquad (4.12)$$

where $G_{da}(s)$ is the transfer function from an applied disturbance V_a to the resulting displacement d at a point r.

By again applying the principle of superposition, the effect of a generally distributed disturbance force $f(r, s)$ can be included in the composite equations (4.11) and (4.12),

$$V_p(s) = \left[I - G_{vv}(s) Z(s) \left(Z(s) + \frac{1}{s}\Lambda \right)^{-1} \right]^{-1} (G_{va}(s) \; V_a(s) + G_{vf}(s) \; f(s)), \qquad (4.13)$$

$$d(r, s) = \left[I - G_{vv}(s) \; Z(s) \left(Z(s) + \frac{1}{s}\Lambda \right)^{-1} \right]^{-1} (G_{da}(s) \; V_a(s) + G_{df}(s) \; f(r, s)), \qquad (4.14)$$

where $G_{df}(s)$ and $G_{vf}(s)$ are the respective transfer functions from an applied force f to the displacement d and shunt transducer piezoelectric voltage V_p. i.e.

$$G_{vf}(s) = \frac{V_p(s)}{f(r,s)} \qquad G_{df}(s) = \frac{d(r,s)}{f(r,s)} \; . \qquad (4.15)$$

As introduced in Chapter 2, the presence of an electrical shunt impedance can be viewed as parameterizing an equivalent collocated strain feedback controller. The corresponding multi-transducer interpretation is revealed in equations (4.11) and (4.12). In Figure 4.5, the multi-transducer feedback interpretation is shown to be a direct extension of the single transducer case.

Specific models for the transfer functions G_{va}, G_{da}, and G_{vv} will be required throughout the upcoming process of control design. The technique of modal analysis [85, 41] has been used extensively throughout the literature for obtaining structural models. Under certain assumptions [85], the force, transducer voltage, or moment applied to a linear structure
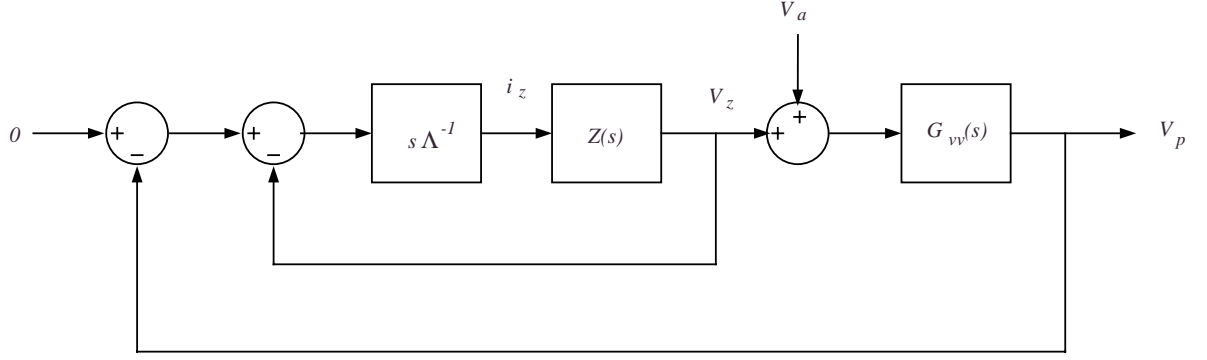
Figure 4.5: The equivalent feedback diagram representing Equation (4.11). In this case, the disturbance and shunt transducers are identical and collocated. i.e. $G_{va}(s) = G_{vv}(s)$.

can be related to the resulting sensor voltage, strain, or displacement through a transfer function of the following form,

$$G(s) = \sum_{k=1}^{\infty} \frac{\Psi_k}{s^2 + 2\varsigma_k\omega_k s + \omega_k^2}, \tag{4.16}$$

where $G(s)$ is intuitively parameterized by the structural resonance frequencies ω_k, modal damping ratios ς_k, and vector coefficients Ψ_k. In practical applications, where only the first N modes are of importance, the summation is usually truncated accordingly. i.e.

$$G(s) = \sum_{k=1}^{N} \frac{\Psi_k}{s^2 + 2\varsigma_k\omega_k s + \omega_k^2} + D. \tag{4.17}$$

The feed-through term D is included to correct in-bandwidth zero locations that are perturbed by the truncation of higher order modes [92]. Based on (4.17), the system transfer function G_{vv} is defined as,

$$G_{vv}(s) = \sum_{k=1}^{N} \frac{\Psi_k^{vv}}{s^2 + 2\varsigma_k\omega_k s + \omega_k^2} + D_{vv}. \tag{4.18}$$

Likewise for the transfer functions G_{va}, G_{da}, G_{df} and G_{vf}.
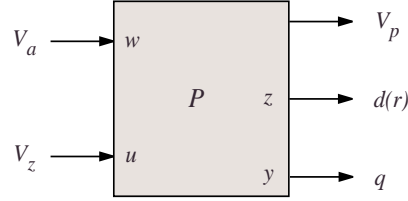
Figure 4.6: The composite structural piezoelectric plant P.

4.2.2   Abstracted Plant Model

The general input-output model of a piezoelectric laminate structure is shown in Figure 4.6. In conformance with the standard MIMO control formulation [109], the plant contains two sets of inputs: the disturbance signals w, and the control signals u. For the case under consideration, the disturbance and control signals are realized through a set of voltages V_a and V_z applied to a number of laminated piezoelectric patches. The system outputs V_p, $d(r)$, and q, correspond respectively to the piezoelectric voltages induced in each shunt patch, the dynamic displacement measured at a point r, and the charge resident on each patch. The displacement signal $d(r)$ is chosen as our performance variable z, while the measured charge q is our feedback variable y. Although the induced shunt piezoelectric voltages V_p are not required during the design, their inclusion aids in the modeling process. Given a specific s-impedance, the signal V_p also allows us to compute the equivalent collocated active feedback controller.

A state-space realization of (4.18) is easily generated to represent the system P,

$$\dot{x} = \mathbf{A}x + \mathbf{B} \begin{bmatrix} V_a \\ V_z \end{bmatrix} \tag{4.19}$$

$$\begin{bmatrix} V_p \\ d(r) \\ q \end{bmatrix} = \mathbf{C}x + \mathbf{D} \begin{bmatrix} V_a \\ V_z \end{bmatrix},$$

where,

$$
\mathbf{A} =
\begin{bmatrix}
0 & 1 & & & \\
-\omega_1^2 & -2\varsigma_i\omega_1^2 & & & \\
& & \ddots & & \\
& & & 0 & 1 \\
& & & -\omega_N^2 & -2\varsigma_N\omega_N^2
\end{bmatrix}
\tag{4.20}
$$

$$
\mathbf{B} =
\begin{bmatrix} \mathbf{B}_1 & \mathbf{B}_2 \end{bmatrix} =
\begin{bmatrix}
0 & 0 \\
F_1 & H_1 \\
\vdots & \vdots \\
0 & 0 \\
F_N & H_N
\end{bmatrix}
\tag{4.21}
$$

$$
\mathbf{C} =
\begin{bmatrix} \mathbf{C}_1 \\ \mathbf{C}_2 \\ C_p\mathbf{C}_1 \end{bmatrix} =
\begin{bmatrix}
E_1 & 0 & \cdots & E_N & 0 \\
1 & 0 & \cdots & 1 & 0 \\
C_pE_1 & 0 & \cdots & C_pE_N & 0
\end{bmatrix}
\tag{4.22}
$$

$$
\mathbf{D} =
\begin{bmatrix}
D_{11} & D_{12} \\
D_{21} & D_{22} \\
D_{11}C_p & -C_p + D_{12}C_p
\end{bmatrix},
\tag{4.23}
$$

where F_k and H_k $k \in \{1, 2, \cdots N\}$ are the state-input weightings of each disturbance and shunt transducer. The vectors E_k $k \in \{1, 2, \cdots N\}$ represent the contribution of each mode to the induced piezoelectric voltages.

As an alternative to the parameterized modeling approach presented above, a multi-variable time or frequency domain system identification technique could be employed to estimate the plant P directly from experimental data [77, 84, 82].

Figure 4.7: The composite plant with charge feedback controller $C(s)$.

4.3   s-Impedance Control Design

4.3.1   *LQG* **Design**

Given the composite model discussed in Section 4.2, the problem of designing an appropriate impedance can be cast as a standard regulator problem. As shown in Figure 4.7, the regulator $C(s)$ accepts the measured charge q to provide a control signal V_z counteractive to the applied disturbance V_a. The objective is to minimize the structural displacement $d(r)$ subject to a weighting on the magnitude of the required terminal voltage V_z. In a linear quadratic sense, the objective is to minimize

$$J = \int_0^\infty \left\{ d(r,t)^2 + V_z(t)' \mathbf{k}_u V_z(t) \right\} \, dt, \tag{4.24}$$

where $\mathbf{k}_u$ is a weighting matrix representing the performance penalty on the shunt voltages V_z. Based on the composite plant model (4.19), the performance signal $d(r,t)$ is represented by,

$$d(r,t) = \mathbf{C}_2 x(t) + D_{21} V_a(t) + D_{22} V_z(t). \tag{4.25}$$

Considering only the homogeneous component and substituting (4.25) into (4.24), the objective function (4.24) can be rewritten as

$$J = \int_0^\infty \left\{ x'(t)\mathbf{C}_2'\mathbf{C}_2 x(t) + V_z(t)'D_{22}'D_{22}V_z(t) + 2x'(t)\mathbf{C}_2'D_{22}V_z(t) + V_z(t)'\mathbf{k}_u V_z(t) \right\} \, dt.$$

(4.26)

Restated in the standard LQR context,

$$J = \int_0^\infty \left\{ x'(t)\mathbf{Q}x(t) + u(t)'\mathbf{R}u(t) + 2x'(t)\mathbf{N}u(t) \right\} \, dt,$$

(4.27)

where,

$$\mathbf{Q} = \mathbf{C}_2'\mathbf{C}_2$$

$$\mathbf{R} = D_{22}'D_{22} + \mathbf{k}_u$$

(4.28)

$$\mathbf{N} = \mathbf{C}_2'D_{22}.$$

Through the solution of an algebraic Ricatti equation [109], a state feedback matrix K can be found that minimizes the objective function J.

Observer Design

As the state variables of the system $x(t)$ are not available directly, a linear observer is required.

For s-impedance design, where the controlled plant $\frac{q(s)}{V_z(s)}$ is dominated by direct feed-through, the *ad-hoc* pole-placement approach to linear observer design becomes difficult. Although an LQR state-feedback regulator is guaranteed (if $\mathbf{R}$ is chosen diagonal) to result in a phase margin of at least 60 degrees at each plant input channel [66, 104], it is well known that considerable degradation of the stability-margins is to be expected after inclusion of the observer dynamics.

A more automated choice in observer design is the Kalman filter [17]. Here, as shown in Figure 4.8, the controller $C(s)$ consists of an optimal state-feedback regulator K and Kalman observer O. By the Certainty Equivalence Principle or Separation Theorem [109],

Figure 4.8: The composite plant P controlled by $C(s)$, an s-impedance consisting of the optimal state-feedback regulator K and Kalman filter O.

the two entities can be designed independently. After first finding a K to minimize (4.27), we then design a Kalman filter to minimize

$$J_k = \lim_{t \to \infty} E\left\{[x(t) - \tilde{x}(t)]\, [x(t) - \tilde{x}(t)]'\right\}. \tag{4.29}$$

By the Certainty Equivalence Principle, the optimal K and O also result in minimization of the stochastic performance objective,

$$J = E\left\{\lim_{T \to \infty} \frac{1}{T} \int_0^T \left\{x'(t)\mathbf{Q}x(t) + u(t)'\mathbf{R}u(t) + 2x'(t)\mathbf{N}u(t)\right\}\, dt\right\}. \tag{4.30}$$

In this scenario we are referring to the original state-space system (4.19) with zero-mean uncorrelated Gaussian process models for the disturbance V_a and additive measurement noise v. With the inclusion of measurement noise, the system representation (4.19) becomes

$$\dot{x} = \mathbf{A}x + \mathbf{B}_1 V_a + \mathbf{B}_2 V_z \tag{4.31}$$

$$\begin{bmatrix} V_p \\ d(r) \\ q \end{bmatrix} = \mathbf{C}x + \mathbf{D}\begin{bmatrix} V_a \\ V_z \end{bmatrix} + \begin{bmatrix} \mathbf{0} \\ 0 \\ v \end{bmatrix},$$

where V_a and v satisfy,

$$E\left\{V_a V_a'\right\} = \mathbf{Q}_n \tag{4.32}$$

$$E\left\{vv'\right\} = \mathbf{R}_n.$$

Based on $\mathbf{Q}_n$ and $\mathbf{R}_n$, a Kalman observer that minimizes (4.29) can be found through the solution of an algebraic Ricatti equation [109]. The ratio of $\mathbf{Q}_n$ to $\mathbf{R}_n$ essentially represents the confidence in the measured variable q and plant model P. In this work, $\mathbf{Q}_n$, $\mathbf{R}_n$, and $\mathbf{k}_u$, are not quantified exactly and simply treated as design parameters influencing the closed-loop pole locations, damping performance, and closed-loop stability.

4.3.2 $\mathcal{H}_2$ and $\mathcal{H}_\infty$ Design

In contrast to the observer based approaches presented in the previous sub-section, direct output feedback synthesis techniques can also be applied. Figure 4.9 illustrates the problem of s-impedance synthesis cast as a standard $\mathcal{H}_2$ or $\mathcal{H}_\infty$ control design problem [34, 33].

In an $\mathcal{H}_2$ sense, the goal is to minimize the transfer function from an applied disturbance w to the performance signal z, i.e. we seek to minimize

$$
\begin{aligned}
J &= \left\| \frac{z(s)}{w(s)} \right\|_2 \\
&= \left\| \frac{d(r,s) + \mathbf{k}_u V_z(s)}{V_a(s)} \right\|_2,
\end{aligned} \tag{4.33}
$$

where the $\mathcal{H}_2$ norm $\|F(s)\|_2$ of $F(s)$ is defined as

$$\|F(s)\|_2^2 = \frac{1}{2\pi} \int_{-\infty}^{\infty} tr\left\{F(j\omega)F(j\omega)'\right\}\ d\omega. \tag{4.34}$$

By Parseval's equality, the optimal $\mathcal{H}_2$ controller minimizes the expected root-mean-square (RMS) value of z. An optimal $\mathcal{H}_2$ controller can be found through the solution of an algebraic Ricatti equation [34, 33].

Disadvantages associated with $\mathcal{H}_2$ and LQG methods include the unrealistic Gaussian disturbance model, and problems related to integral performance constraints [109]. $\mathcal{H}_\infty$
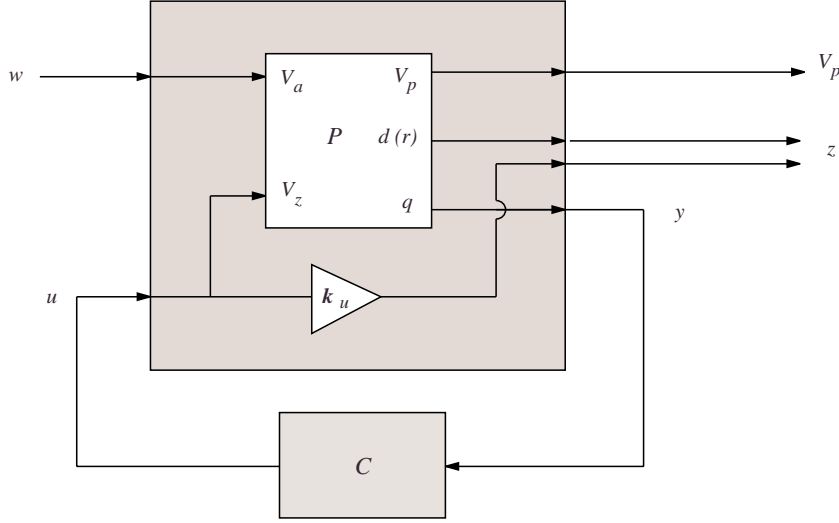
Figure 4.9: The standard $\mathcal{H}_2$ and $\mathcal{H}_\infty$ design problem containing the composite

plant P and a secondary performance signal weighting the applied shunt voltage

V_z.

optimization and robust control, originally championed by Zames [128], is an alternative

to $\mathcal{H}_2$ and LQG methods.

Applying $\mathcal{H}_\infty$ control to the problem of s-impedance synthesis involves finding a controller

$C(s)$ that minimizes

$$J = \left\| \frac{z(s)}{w(s)} \right\|_\infty \tag{4.35}$$
$$= \left\| \frac{d(r,s) + \mathbf{k}_u V_z(s)}{V_a(s)} \right\|_\infty,$$

where the $\mathcal{H}_\infty$ norm $\|F(s)\|_\infty$ of $F(s)$ is defined as

$$\|F(s)\|_\infty = \max_\omega \ \bar{\sigma}\left(F(j\omega)\right), \tag{4.36}$$

where $\bar{\sigma}$ denotes the maximum singular value.

In the time domain, $\mathcal{H}_\infty$ control can be interpreted as minimizing the worst-case induced

2-norm of z, i.e.

$$\left\| \frac{z(s)}{w(s)} \right\|_\infty = \max_{w(t) \neq 0} \ \frac{\|z(t)\|_2}{\|w(t)\|_2}, \tag{4.37}$$

where $\|f(t)\|_2^2 = \int_0^\infty \sum_i |f_i(t)|^2 \ dt$.

Closely resembling the solution to $\mathcal{H}_2$ synthesis, an optimal $\mathcal{H}_\infty$ controller can be found through the solution of an algebraic Ricatti equation [34, 33].

4.3.3 Disturbance Rejection *versus* Damping

Before concluding the topic of control synthesis, it is worth comparing our original objectives to that which we have been able to specify within the LQG (4.24), $\mathcal{H}_2$ (4.33), and $\mathcal{H}_\infty$ (4.35) design frameworks.

The fundamental intention of many active and passive structural control strategies is simply to augment the natural damping inherent in any structure. Using piezoelectric transducers, the only techniques to actually achieve this goal involve full-information state-variable feedback. Measuring selectively and directly the strain, displacement, or velocity of individual modes, requiring the use of distributed modal sensors [74], is a formidable and often deemed impractical approach. More commonly, the controller contains a state-observer designed either explicitly, as in LQR design, or implicitly and possibly internally, as in LQG, $\mathcal{H}_2$, and $\mathcal{H}_\infty$ design. The question arises, "Even if the structural poles are moved to a desirable location, what influence do the additional observer dynamics have on the closed-loop system ?". Given the spatially distributed nature of the system, an even more fundamental issue is whether a particular design objective results in augmented structural damping (by moving the closed-loop poles), or merely rejection of the represented disturbance. Although rejection of the disturbance w is desirable, in most cases that particular disturbance is only representative, included for the sake of facilitating control design by standard methods. In the case of disturbance rejection, mitigation of a general unmodeled disturbance is not guaranteed. As it occurs in this investigation, both of these issues become especially acute.

Firstly, for LQG design, the desired open- and closed-loop pole locations are shown in Figure 4.10. The controller acts to move the lightly damped structural poles further into the complex left-half plane. In addition to the damped structural poles, observer poles, appearing further to the left, are also present. Because of the high degree of damping in

these poles, their contribution to the closed-loop system is insignificant. In this scenario, the controller is referred to as augmenting the natural damping of the system. Any applied disturbance encounters a system with heavily damped poles. If a controller exists to arise in such a scenario, through inverse control, the design weights in an LQG problem can be chosen to reproduce it. Unfortunately for conventional choices in the design parameters (4.28) and (4.32), the closed-loop pole pattern is likely to present as illustrated in Figure 4.11. Even though both scenarios, Figures 4.10 and 4.11, result in identical closed-loop performance, the controller resulting in the second pole pattern is obviously not augmenting the system damping. The residues, and hence contribution to closed-loop performance, of the lightly damped poles in Figure 4.11 are negligible when considering that particular representative disturbance. In the case of disturbances applied through different input channels, the residues of such poles are not insignificant; in fact, they can be disastrous - introducing auxiliary lightly damped resonances and severely degrading performance.

As might be expected due to similarities in LQG and $\mathcal{H}_2$ control design, the same situation arises. The performance of an optimal $\mathcal{H}_2$ controller may be heavily dependent on the disturbance channel. The problem also exists for $\mathcal{H}_\infty$ control.

Being more than just an example, Figures 4.10 and 4.11, are actually the closed-loop pole locations corresponding to two LQG controllers designed for the experimental system introduced in Section 4.4.1. Although both controllers achieve comparable performance, only the first results in augmented system damping. One can observe that controllers resulting in pole locations resembling Figure 4.11, have approximately inverted the open-loop dynamics of the composite plant. During the design we wish to exclude such controllers from the set of all permissible controllers that achieve the specified performance objective. This seemingly complicated restriction can be accomplished in an *ad-hoc* but effective fashion by simply increasing the dimension of the disturbance input w until the plant is no longer square and hence uninvertible. The necessary additional disturbance signals should be unique, but are not required to represent a genuine system disturbance. Their inclusion is simply to remove the possibility of plant inversion from the range of outcomes pending control design. In the $\mathcal{H}_2$ and $\mathcal{H}_\infty$ cases, to avoid distortion of the original performance specification, the influence of such auxiliary disturbances should be chosen small. To a
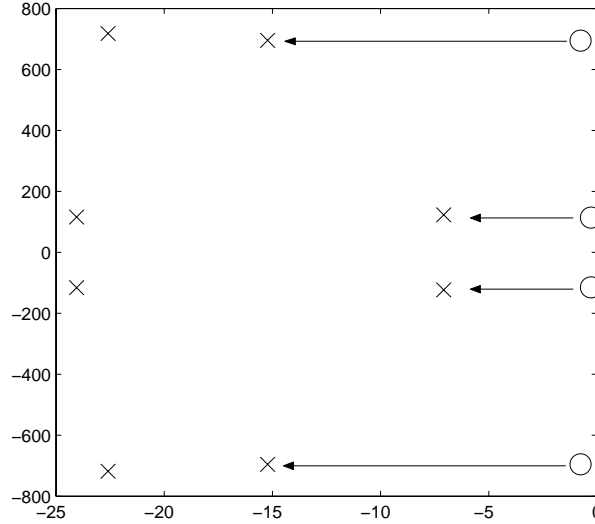
Figure 4.10: The pole locations of an open- ($\bigcirc$) and closed-loop ($\times$) structural system where the controller augments natural damping.

lesser extent, similar care should be taken in the LQG case.

For the pole patterns shown in Figures 4.10 and 4.11, the corresponding closed-loop $\mathcal{H}_2$ performance metrics are comparable. The only difference in each problem specification is a small auxiliary input included when designing the controller in Figure 4.10. The composite system originally included a single disturbance based on the use of a single shunt patch. The disturbance V_a to the following system was increased in dimension from 1 to 2 by setting $F_k = \begin{bmatrix} F_k & \alpha_k F_k \end{bmatrix}$, where α_k is a small random number,

$$\dot{x} = \mathbf{A}x + \mathbf{B} \begin{bmatrix} V_a \\ V_z \end{bmatrix} \tag{4.38}$$

$$\begin{bmatrix} V_p \\ d(r) \\ q \end{bmatrix} = \mathbf{C}x + \mathbf{D} \begin{bmatrix} V_a \\ V_z \end{bmatrix},$$
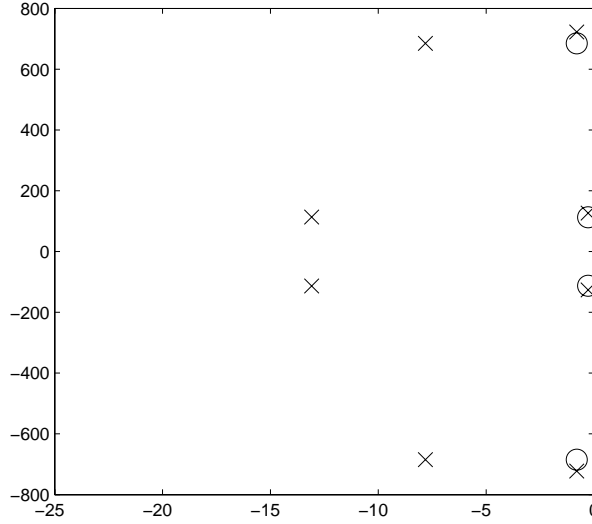
Figure 4.11: The pole locations of an open- ($\bigcirc$) and closed-loop ($\times$) structural system where the controller does not augment natural damping.

where

$$\mathbf{B} = \left[\begin{array}{cc} \mathbf{B}_1 & \mathbf{B}_2 \end{array} \right] = \begin{bmatrix} 0 & 0 \\ F_1 & H_1 \\ \vdots & \vdots \\ 0 & 0 \\ F_N & H_N \end{bmatrix}. \tag{4.39}$$

The result is the difference between true system damping and disturbance rejection.

4.4 Experimental Results

In the following sub-sections, LQG, $\mathcal{H}_2$, and $\mathcal{H}_\infty$ s-impedance controllers are designed and applied experimentally to control a piezoelectric laminate cantilever beam.

4.4.1 Experimental Apparatus

The experimental apparatus, shown in Figure 4.13 and pictured in Figure 4.12, consists of a uniform aluminium cantilever beam. Three piezoelectric transducers are laminated onto

Length, L	376 mm
Thickness, h	3 mm
Width, W	50 mm
Density, ρ	$2.770{\times}10^3$ kg/m^3
Young's Mod., E	$7.00{\times}10^{10}$ N/m^2

Table 4.1: Beam Parameters.

Length, L_{pz}	50 mm
Thickness, h_{pz}	0.25 mm
Width, W_{pz}	15 mm
Charge Constant, d_{31}	$-210{\times}10^{-12}$ m/V
Voltage Constant, g_{31}	$-11.5{\times}10^{-3}$ Vm/N
Coupling Coefficient, k_{31}	0.34
Capacitance, C_p	43 nF
Young's Mod., E_{pz}	$63{\times}10^9$ N/m^2

Table 4.2: Properties of the PI Transducers (PIC151 Ceramic).

the front face and connected electrically in series to the voltage source V_z. A single collocated disturbance transducer, identical to each of the shunt transducers, is also mounted onto the back face and driven with the disturbance voltage V_a. Physical parameters of the beam and piezoelectric transducers can be found in Tables 4.1 and 4.2.

The displacement measurement $d(r, t)$ is acquired using a Polytec PSV300 scanning laser vibrometer.

Voltage Driver with Charge Instrumentation

The circuit pictured in Figure 3.9 is configured to operate as a high-voltage power amplifier with charge instrumentation. As shown in Figure 4.14, a high-gain opamp is used to maintain a reference voltage V_{ref} across the load $Z_L(s)$. An arbitrary voltage gain can be
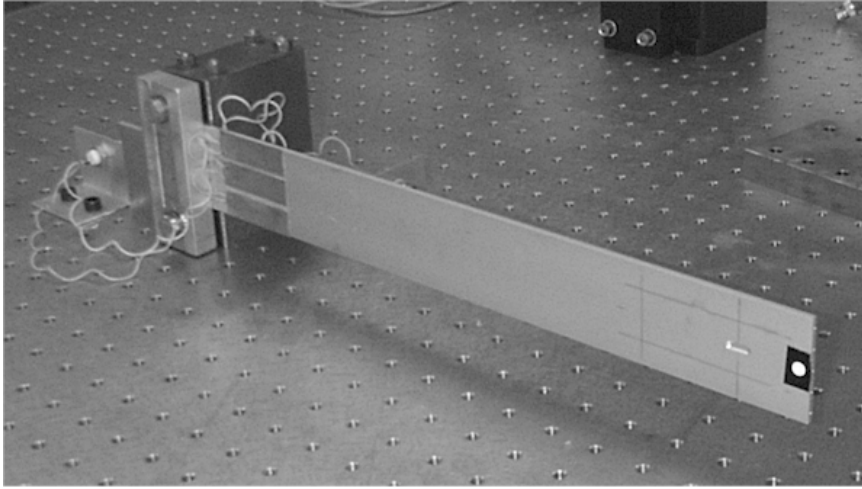
Figure 4.12: The cantilever beam.
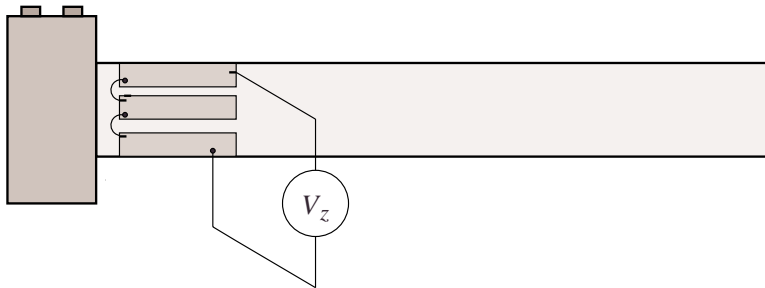
Figure 4.13: A front elevation of the cantilever beam. A single collocated disturbance transducer excited by the voltage V_a, is also mounted on the back face.
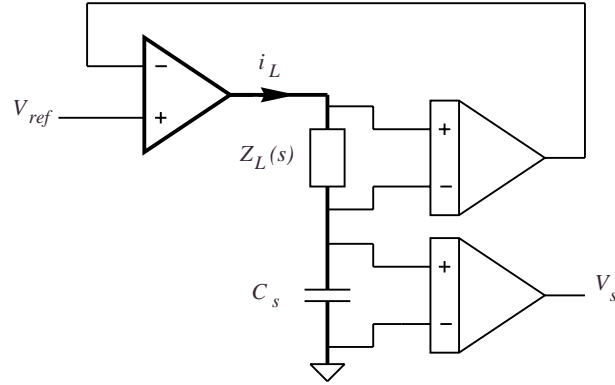
Figure 4.14: A voltage amplifier with charge measurement.

implemented by controlling attenuation in the feedback path. The voltage V_s, measured across the sensing capacitor C_s, is proportional to the load charge q. The charge gain in Volts per Coulomb is equal to $\frac{1}{C_s}$, i.e.

$$\frac{V_s}{q} = \frac{1}{C_s}\frac{V}{C}. \tag{4.40}$$

For implementation of s-impedance controllers, the charge q is defined flowing out of the load, in this case the charge instrumentation gain is negative. An alternative to the circuit shown in Figure 4.14 is to interchange the load and sensing impedances. In this case, the feedback voltage is taken directly across the grounded load.

4.4.2   System Identification

Before beginning the control design, a model must first be obtained for the composite system P. As the variables V_a, V_z, q, and $d(r)$ are not driven or accessible directly, the amplifier and instrumentation dynamics will also be included in the model. Shown in Figure 4.15, the dynamics encountered through each I/O channel are listed in Table 4.3.

Referring to the system model (4.19), after inclusion of the amplifier and instrumentation

Voltage Gain, k_1	-10 $\frac{V}{V}$
Displacement Gain, k_2	$1 \times 10^3 \frac{V}{m}$
Voltage Gain, k_3	$4 \frac{V}{V}$
Charge Gain, k_4	$\frac{-1}{100 \times 10^{-9}} \frac{V}{C}$

Table 4.3: The experimental system gains.
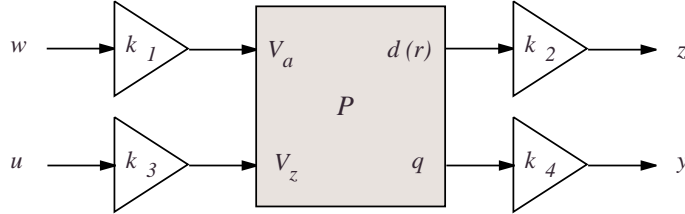
Figure 4.15: The composite plant P with external power amplifier and instrumentation gains included.

gains, the $\mathbf{B}$, $\mathbf{C}$, and $\mathbf{D}$ matrices become,

$$\mathbf{B} = \left[\begin{array}{cc} k_1\mathbf{B}_1 & k_3\mathbf{B}_2 \end{array}\right] = \left[\begin{array}{cc} 0 & 0 \\ k_1F_1 & k_3H_1 \\ \vdots & \vdots \\ 0 & 0 \\ k_1F_N & k_3H_N \end{array}\right] \tag{4.41}$$

$$\mathbf{C} = \left[\begin{array}{c} \mathbf{C}_1 \\ k_2\mathbf{C}_2 \\ k_4C_p\mathbf{C}_1 \end{array}\right] = \left[\begin{array}{ccccc} E_1 & 0 & \cdots & E_N & 0 \\ k_2 & 0 & \cdots & k_2 & 0 \\ C_pk_4E_1 & 0 & \cdots & C_pk_4E_N & 0 \end{array}\right] \tag{4.42}$$

$$\mathbf{D} = \left[\begin{array}{cc} D_{11} & D_{12} \\ k_1k_2D_{21} & k_3k_2D_{22} \\ k_1k_4D_{11}C_p & k_3k_4\left[-C_p + D_{12}C_p\right] \end{array}\right]. \tag{4.43}$$

To determine the model parameters, a simple optimization scheme is employed. From an initial guess, ω_i and ς_i, are found through a simplex optimization based on the frequency

response from an applied disturbance to the measured displacement,

$$\begin{bmatrix} \omega_k & \varsigma_k \end{bmatrix} = \arg \ \min \ \left\| \tilde{P}_{dV_a}(j\omega) - P_{dV_a}(j\omega) \right\|_2, \tag{4.44}$$

where $\tilde{P}_{dV_a}(j\omega)$ is the measured frequency response from an applied disturbance $V_a(s)$ to the displacement $d(r, s)$. With these parameters in hand, those remaining are determined from a final global optimization,

$$\arg \ \min \ \left\| \tilde{P}(j\omega) - P(j\omega) \right\|_{2, \ W} . \tag{4.45}$$

As gains from channel to channel vary greatly, a multivariable frequency weight W is required to normalize the cost of each error transfer function.

The magnitude and phase response of the measured system and resulting model are shown in Figures 4.16 and 4.17. The model is an accurate representation of the measured system.

In the following sections, it will be of interest to examine the robustness of each control strategy subject to a change in the structural resonance frequencies. Experimentally, such variation is accomplished by affixing a mass 60 mm from the beam tip. The corresponding change in structural resonance frequencies is illustrated in Figure 4.18.
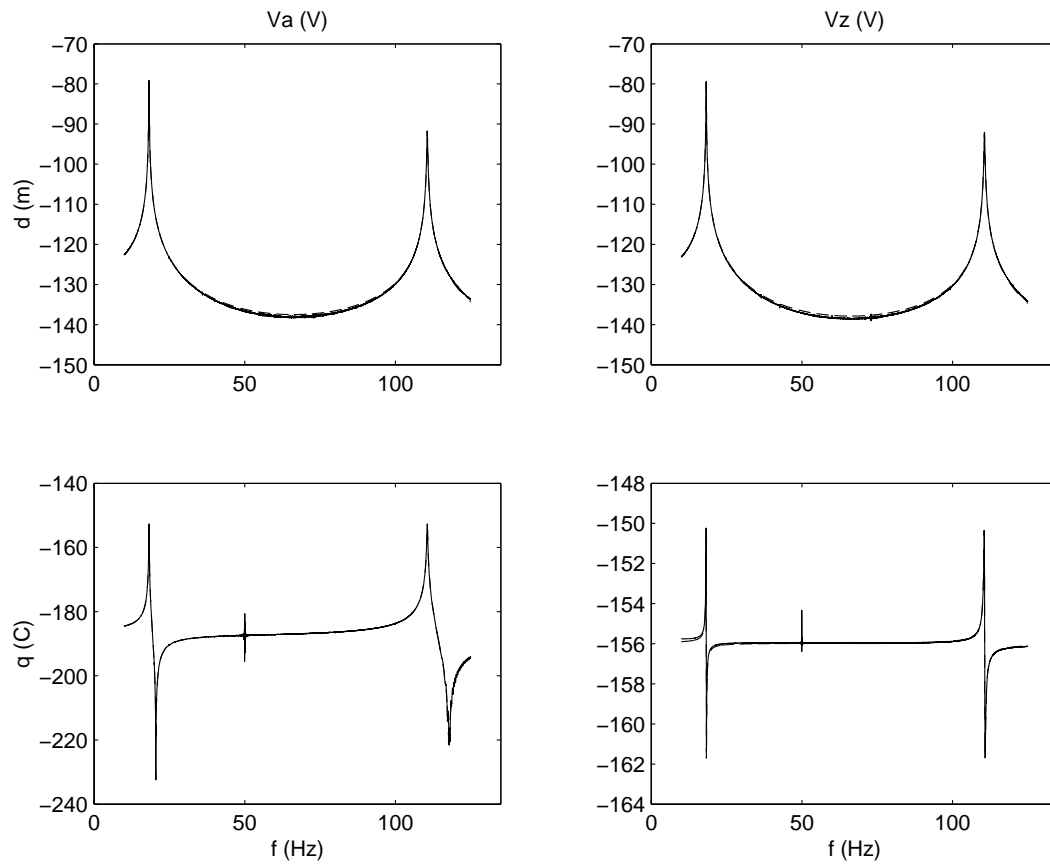
Figure 4.16: The simulated (- -) and experimental (—) magnitude frequency response of the shunt voltage controlled piezoelectric beam (in decibels).
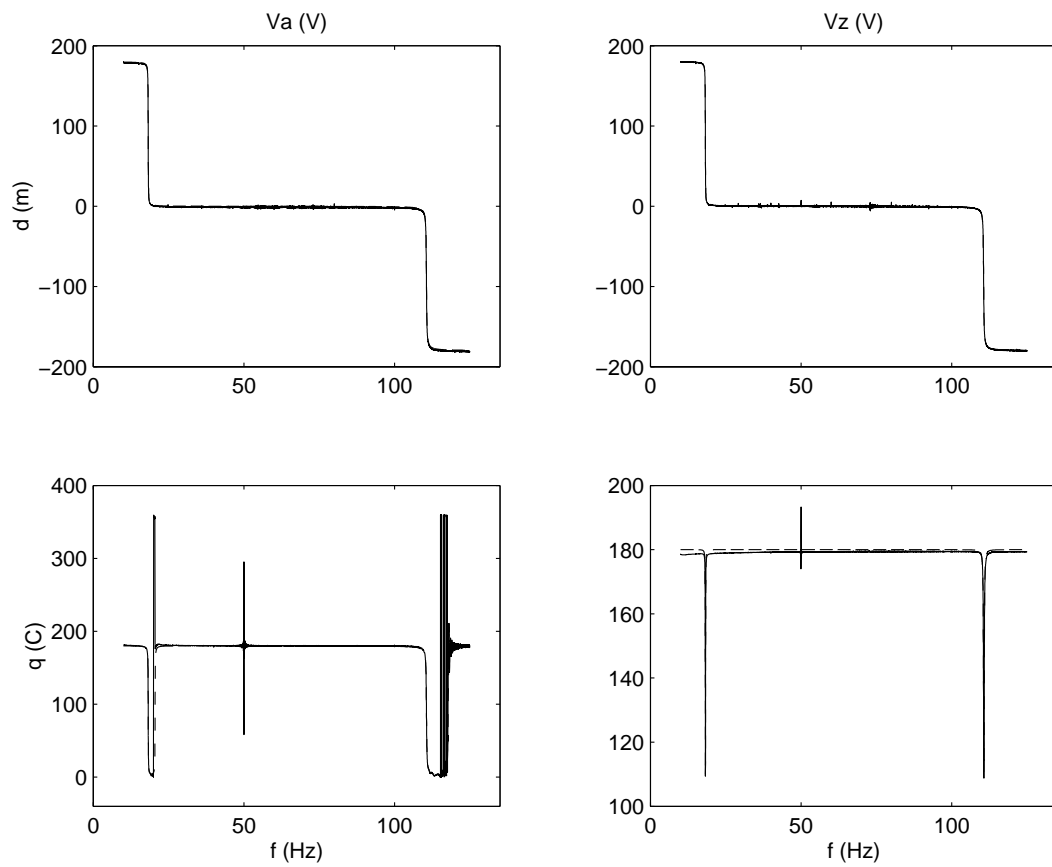
Figure 4.17: The simulated (- -) and experimental (—) phase frequency response of the shunt voltage controlled piezoelectric beam (in degrees).
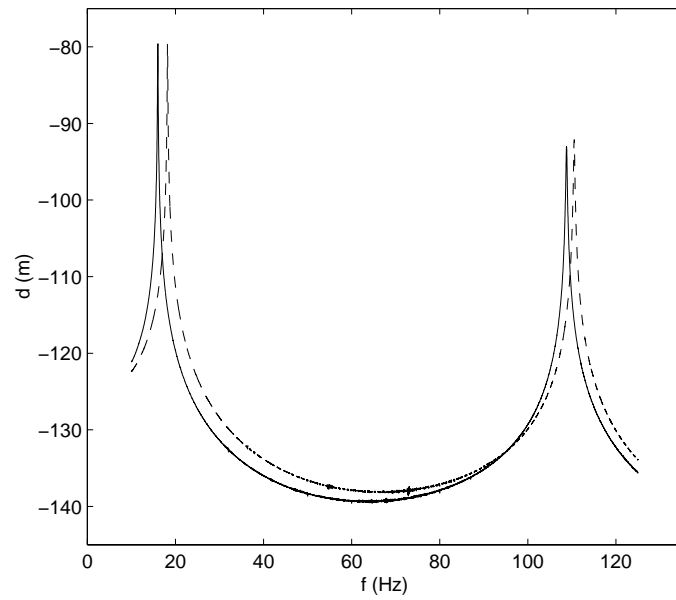
Figure 4.18: The experimental frequency response from an applied disturbance voltage V_a (V) to the resulting tip displacement d (m). Free (- -), With Mass (—).

C_1	10 nF	C_2	10 nF
L_1	11690 H	L_2	348 H
R_1	15 $k\Omega$	R_2	9 $k\Omega$

Table 4.4: Component values of the current-flowing shunt circuit.
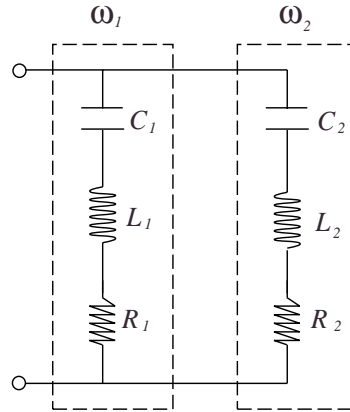
Figure 4.19: A dual-mode current-flowing piezoelectric shunt damping circuit [13].

4.4.3   Passive Shunt Design

For the sake of comparison, each LQG, $\mathcal{H}_2$, and $\mathcal{H}_\infty$ shunt impedance will be judged against a traditional resonant piezoelectric shunt damping circuit applied to the same structure. A current-flowing shunt circuit [13] was designed and tuned to minimize the $\mathcal{H}_2$ norm of the cantilever beam. The schematic and component values can be found in Figure 4.19 and Table 4.4.

4.4.4   LQG Shunt Design

Following the procedure described in Section 4.3.1, an s-impedance can be designed and implemented to minimize an LQG performance objective. Based on the state-space model procured in Section 4.4.2, an LQR gain matrix was designed to minimize the following cost function,

$$J = \int_0^\infty \left\{ d(r,t)^2 + k_u\, V_z(t)^2 \right\}\, dt. \tag{4.46}$$

where k_u, the control signal weighting, was chosen to be 2.6×10^{-11}. Considering the relative difference in magnitude between the displacement $d(r,t)$ and $V_z(t)$, a small value for k_u is not unexpected.

With the addition of an auxiliary input to avoid plant inversion, a Kalman observer was designed to estimate the system state $x(t)$ utilizing the measured shunt transducer charge $q(t)$ and control signal $V_z(t)$. Referring to Section 4.3.1, the disturbance and output noise process covariance matrices, $\mathbf{Q}_n$ and $\mathbf{R}_n$, were chosen as 1 and 0.1 respectively. Such a weighting, although not quantitative, expresses a moderate confidence in the fidelity of the measured variable q.

By concatenating the LQR gain matrix and Kalman observer, and compensating for the system gains k_3 and k_4, the actual impedance presented to the shunt transducer can be determined. In Figure 4.20, the complex s-impedance of the resulting controller is plotted together with the s-impedance of an ideal negative capacitor controller [10, 125]. The LQG controller mimics the response of an ideal negative capacitor at frequencies in the vicinity of each structural resonance. Unlike the negative capacitor which theoretically applies an infinite gain at all frequencies, the LQG controller exerts influence only where necessary and has the benefit of rolling off at higher frequencies. The LQG controller pole-zero map is shown in Figure 4.21.

After examining the open- and closed-loop pole locations shown in Figure 4.22, it can be concluded that the controller is clearly acting to increase the system damping. Corresponding mitigation of the transfer function from an applied disturbance to the measured displacement can be seen in both the frequency domain, Figure 4.23, and time domain,

Figure 4.24. The magnitude of the first and second structural modes are reduced by 27.2 and 19.2 dB respectively. As the second mode contributes significantly less to the LQG cost function, the majority of control effort is expended on the first and most dominant mode. Damping ratios of the first and second structural modes are increased from 0.00246 to 0.0948, and from 0.0011 to 0.00989.

An unexpected feature of the LQG s-impedance is its smooth frequency response; there are no localized peaks at the resonance frequencies. In contrast, high-performance active strain-, velocity-, and acceleration-feedback controllers characteristically apply a highly localized gain at the frequencies of structural resonance. In the advent of model variation, such localized behavior can result in considerable performance degradation. In order to examine system robustness, the nominal system is perturbed by adding a mass 60 mm from the beam tip. Aside from the disturbance to the underlying PDE, the first and second resonance frequencies are decreased by 13.5 and 2.2 % respectively. The consequence on both passive and active shunt circuits is shown in Figure 4.25. While the LQG shunt loses only 1.7 and 0.2 dB from its unperturbed attenuation of the first and second modes, the passive shunt loses 13.4 and 4.8 dB. Corresponding time domain results are shown in Figure 4.26.

In a final test to validate the LQG s-impedance, an acoustic loud speaker was used to spatially excite the structure. The measured frequency response, shown in Figure 4.27, verifies that the achieved performance is disturbance-channel independent.
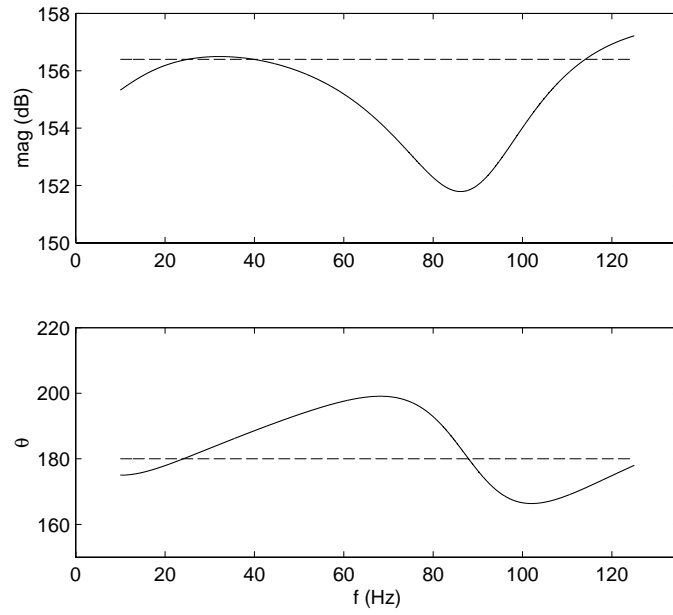
Figure 4.20: Complex s-impedance of the LQG (—), and ideal negative capacitor (- -) shunt controller.
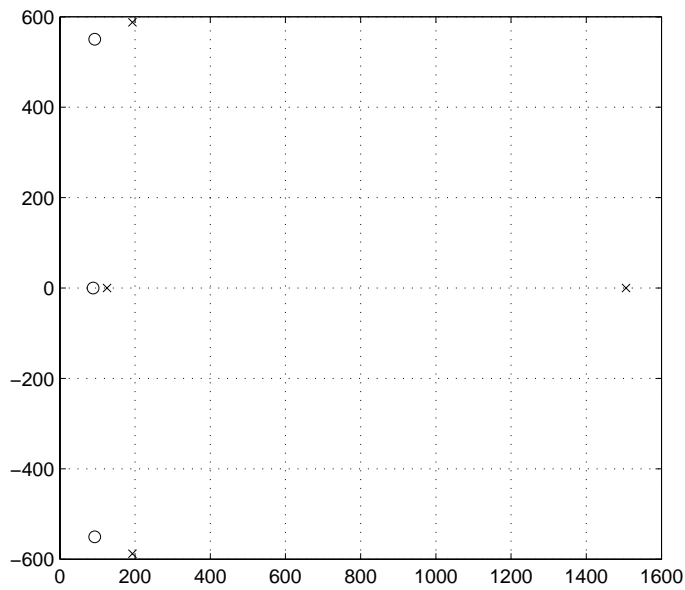
Figure 4.21: The LQG shunt controller pole ($\times$) and zero ($\bigcirc$) locations.
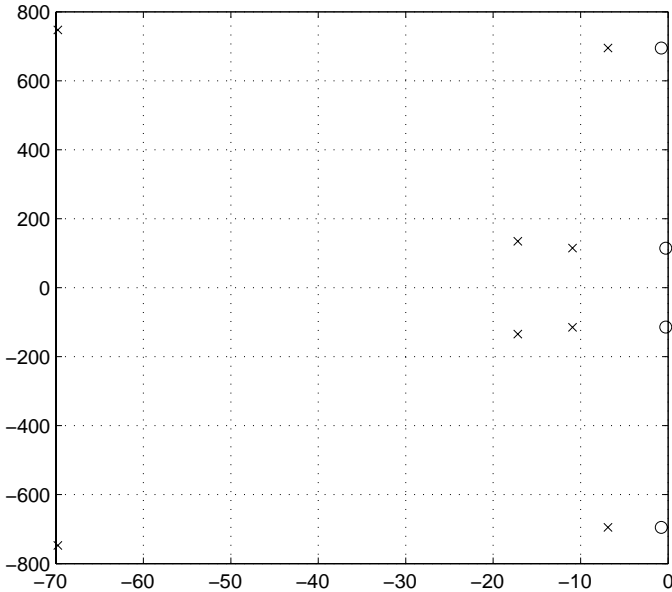
Figure 4.22: The open- ($\bigcirc$), and closed-loop ($\times$) pole locations of the LQG shunt controlled system.
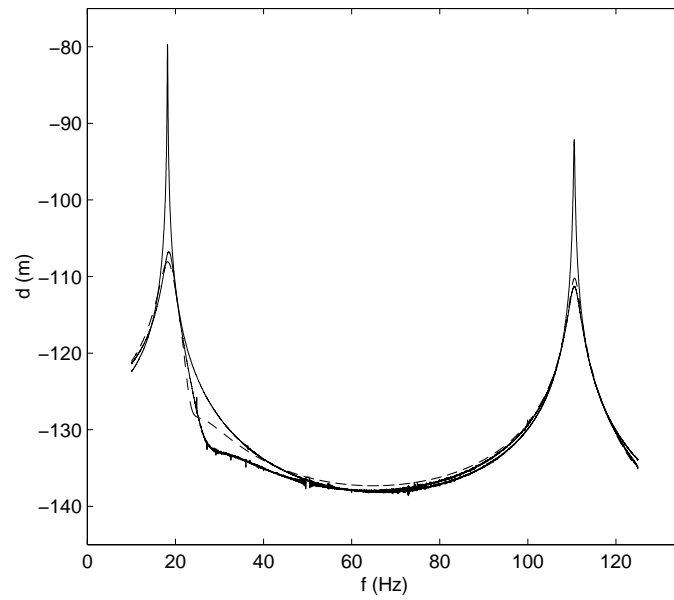
Figure 4.23: The experimental (—), and simulated (- -), LQG shunt controlled frequency responses from an applied disturbance voltage V_a (V) to the resulting tip displacement d (m) (in decibels). The open-loop frequency response is also shown (—).
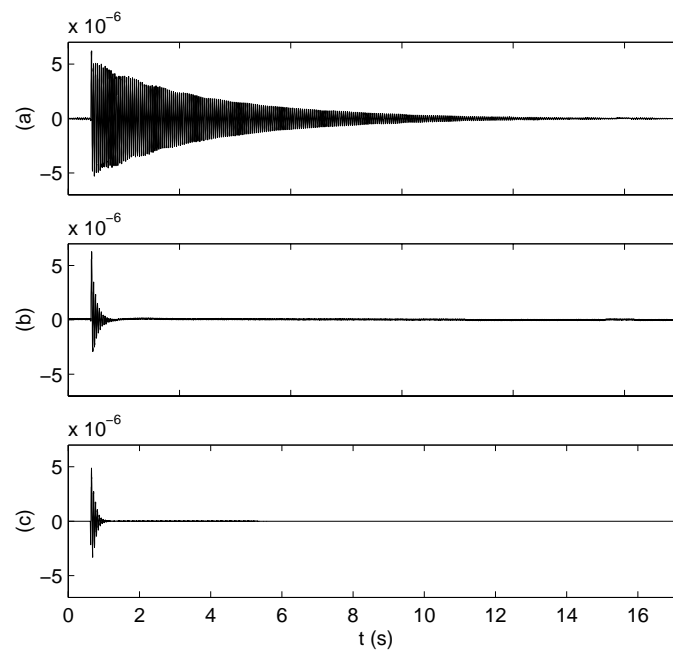
Figure 4.24: Tip displacement response d (m) of the LQG shunt controlled system to a step disturbance in V_a. Experimental open-loop (a), closed-loop (b), and simulated closed-loop (c).
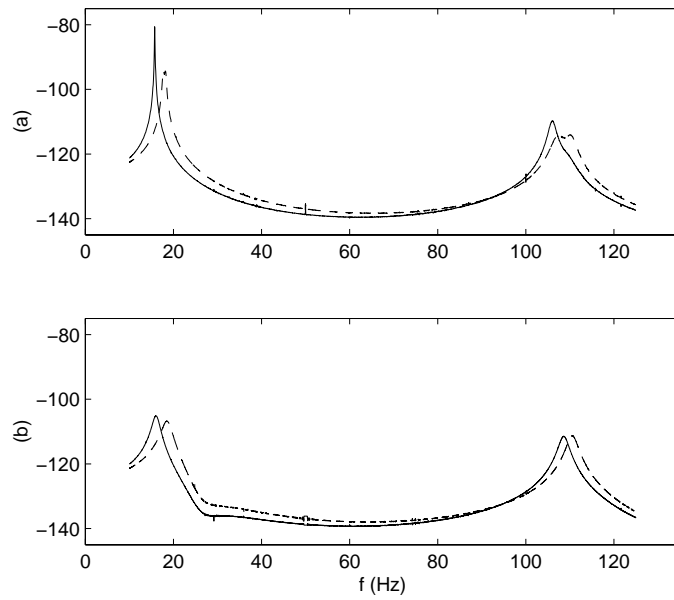
Figure 4.25: The free (- -), and with-mass (—), passive (a) and LQG shunt controlled (b) experimental frequency responses from an applied disturbance voltage V_a (V) to the resulting tip displacement d (m) (in decibels).
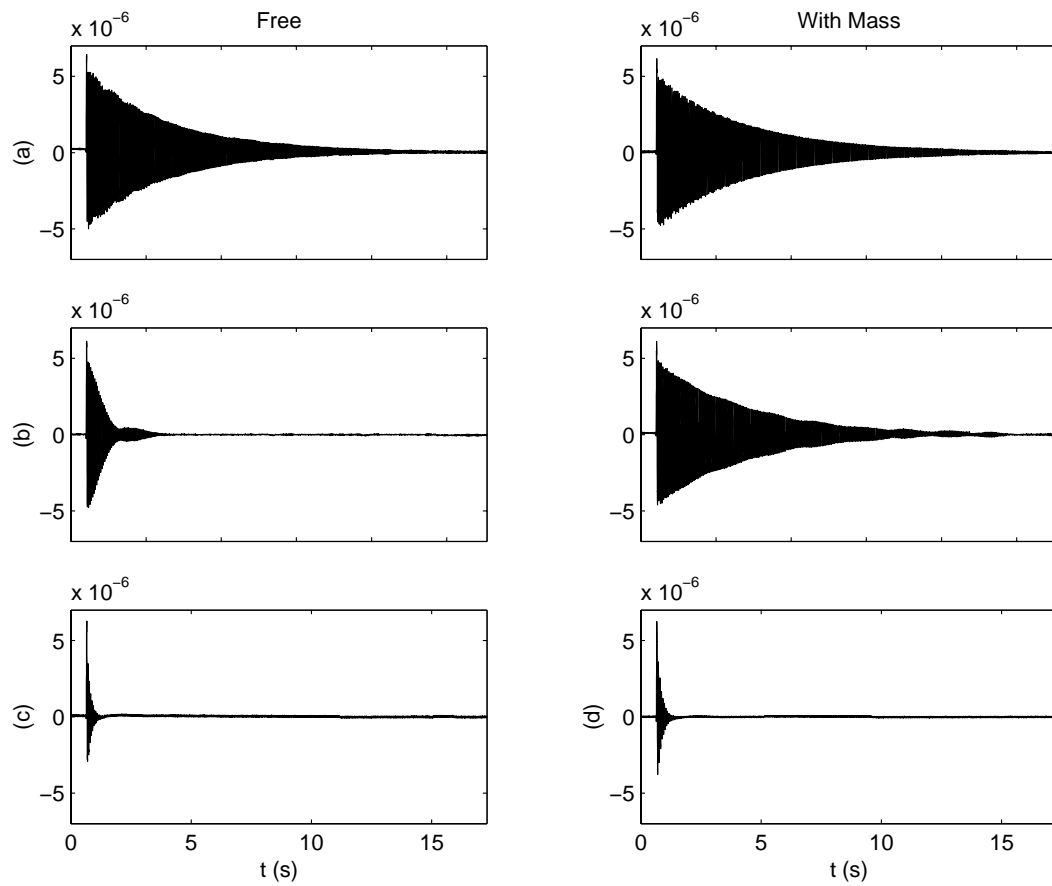
Figure 4.26: The free (left column) and with-mass (right column) tip displacement response d (m) to a step disturbance in V_a. Experimental open-loop (a), passive shunt controlled (b), and LQG shunt controlled (c) systems.
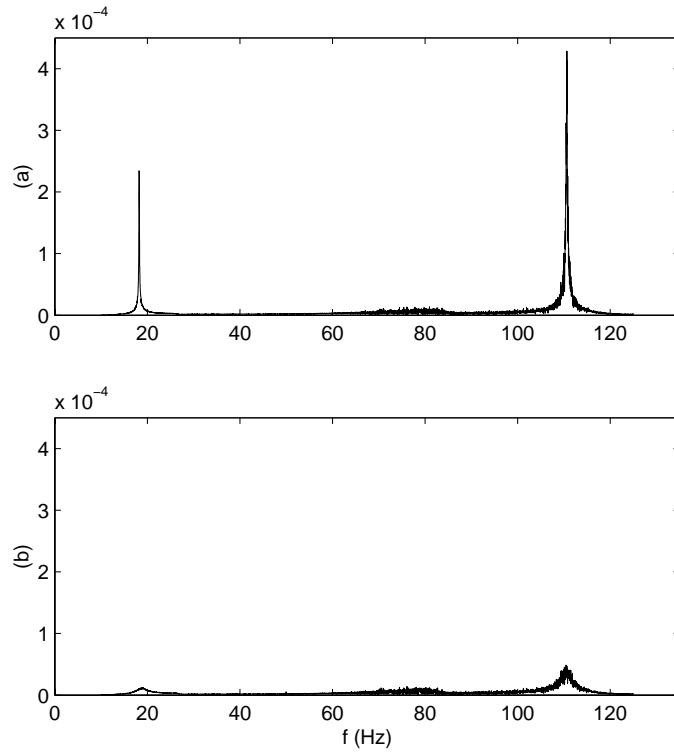
Figure 4.27: The open-loop (a), and LQG shunt controlled (b) linear magnitude response from an applied acoustic disturbance to the resulting tip displacement d (m).

4.4.5 $\mathcal{H}_2$ **Shunt Design**

In analogy to Section 4.4.4, this sub-section documents the design and implementation of an $\mathcal{H}_2$ s-impedance. As discussed in Section 4.3.2, an $\mathcal{H}_2$ s-impedance is designed to minimize the following cost function,

$$J = \left\| \frac{d(r,s) + k_u V_z(s)}{V_a(s)} \right\|_2, \tag{4.47}$$

where k_u, the control signal weighting, was chosen to be 3.2×10^{-7}. A random auxiliary input of negligible influence was also included to avoid plant inversion.

The complex s-impedance of the resulting $\mathcal{H}_2$ controller, plotted in Figure 4.28 is similar in response to the LQG controller shown in Figure 4.20. The controller pole-zero map is shown in Figure 4.29.

Examining the open- and closed-loop pole locations shown in Figure 4.30, the controller is clearly augmenting the system damping. Corresponding mitigation of the transfer function from an applied disturbance to the measured displacement can be seen in both the frequency domain, Figure 4.31, and time domain, Figure 4.32. The magnitudes of the first and second structural modes are reduced by 27.1 and 23.1 dB respectively.

Robustness of the controller is again investigated by affixing a mass to the beam. The effect on closed-loop performance can be seen in Figures 4.33 and 4.34. The $\mathcal{H}_2$ controller loses 1.3 and 0.2 dB from its nominal closed-loop attenuation of the first and second modes.

Acoustic excitation results are shown in Figure 4.35.
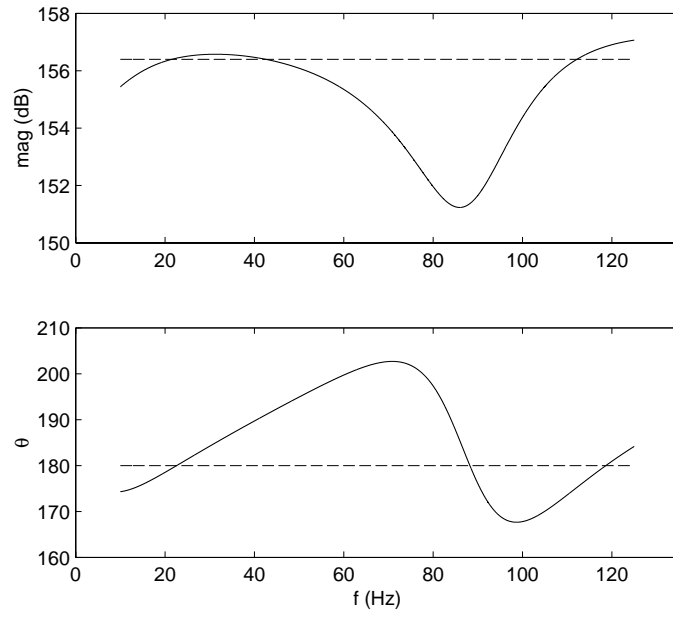
Figure 4.28: Complex s-impedance of the $\mathcal{H}_2$ (—), and ideal negative capacitor (- -) shunt controller.
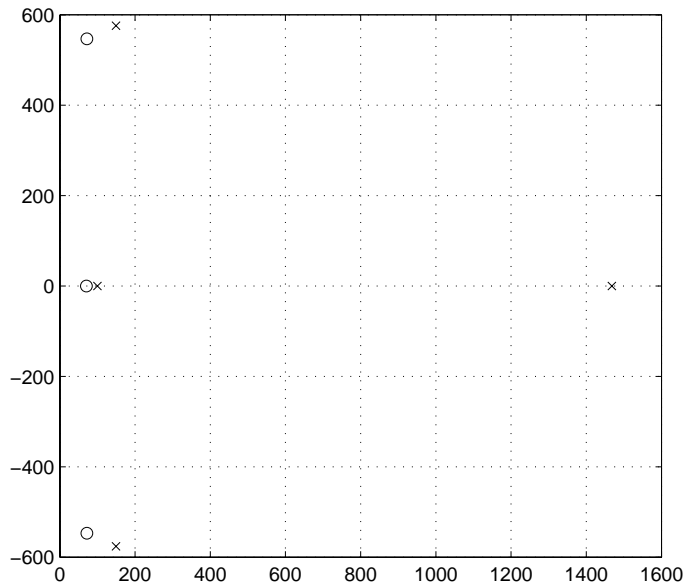
Figure 4.29: The $\mathcal{H}_2$ shunt controller pole ($\times$) and zero ($\bigcirc$) locations.
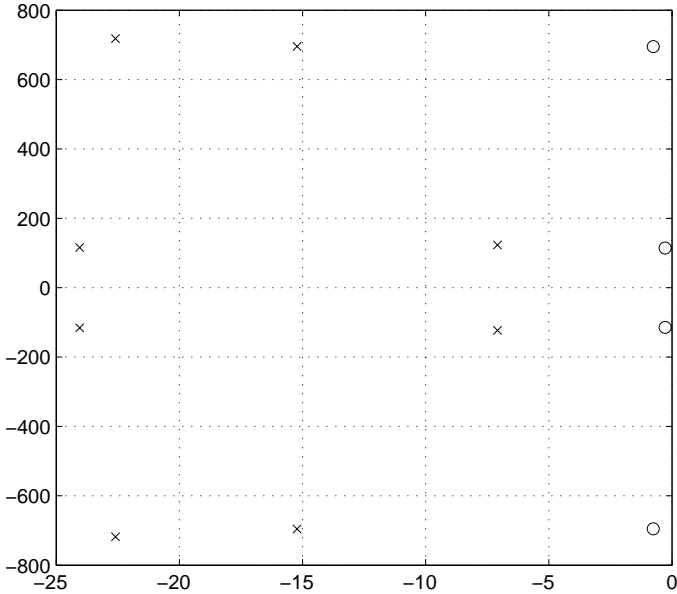
Figure 4.30: The open- ($\bigcirc$), and closed-loop ($\times$) pole locations of the $\mathcal{H}_2$ shunt controlled system.
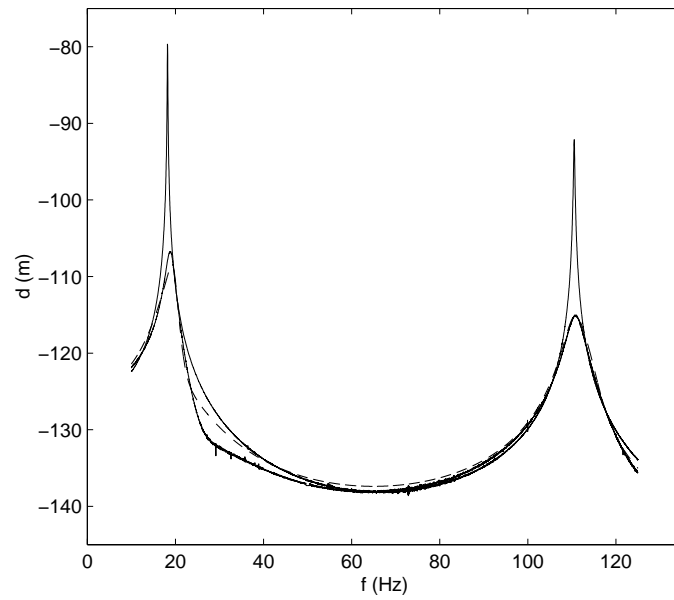
Figure 4.31: The experimental (—), and simulated (- -), $\mathcal{H}_2$ shunt controlled frequency responses from an applied disturbance voltage V_a (V) to the resulting tip displacement d (m) (in decibels). The open-loop frequency response is also shown (—).
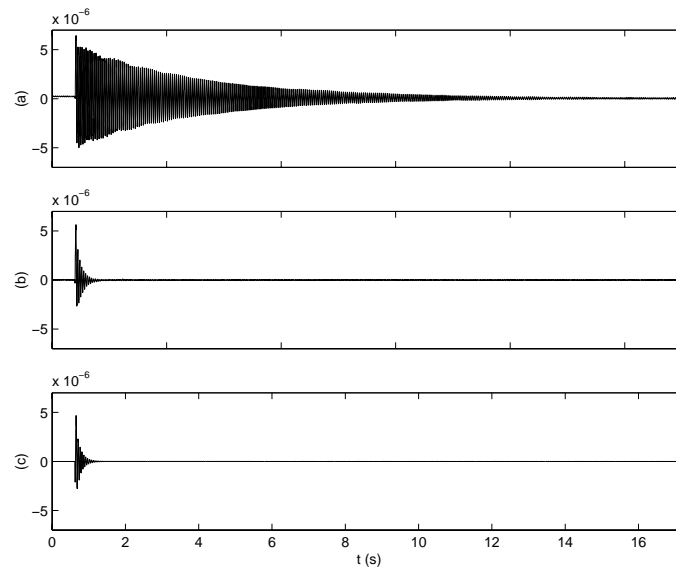
Figure 4.32: Tip displacement response d (m) of the $\mathcal{H}_2$ shunt controlled system to a step disturbance in V_a. Experimental open-loop (a), closed-loop (b), and simulated closed-loop (c).
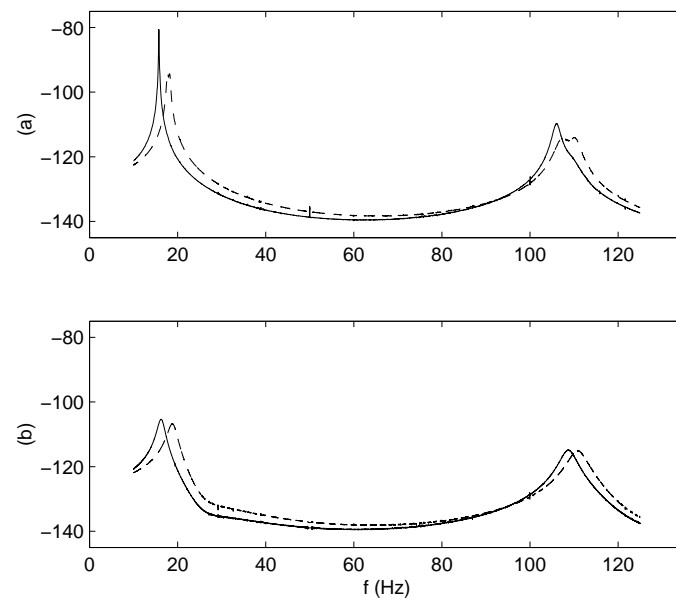
Figure 4.33: The free (- -), and with-mass (—), passive (a) and $\mathcal{H}_2$ shunt controlled (b) experimental frequency responses from an applied disturbance voltage V_a (V) to the resulting tip displacement d (m) (in decibels).
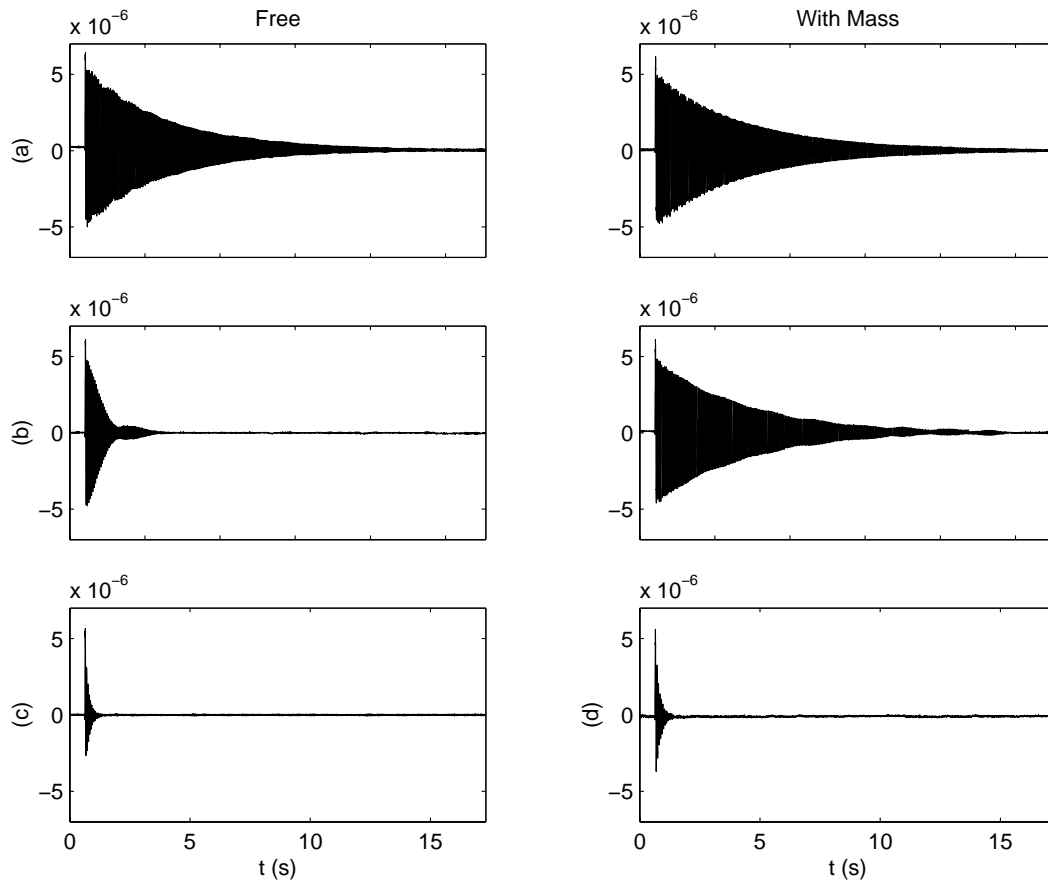
Figure 4.34: The free (left column) and with-mass (right column) tip displacement response d (m) to a step disturbance in V_a. Experimental open-loop (a), passive shunt controlled (b), and $\mathcal{H}_2$ shunt controlled (c) systems.
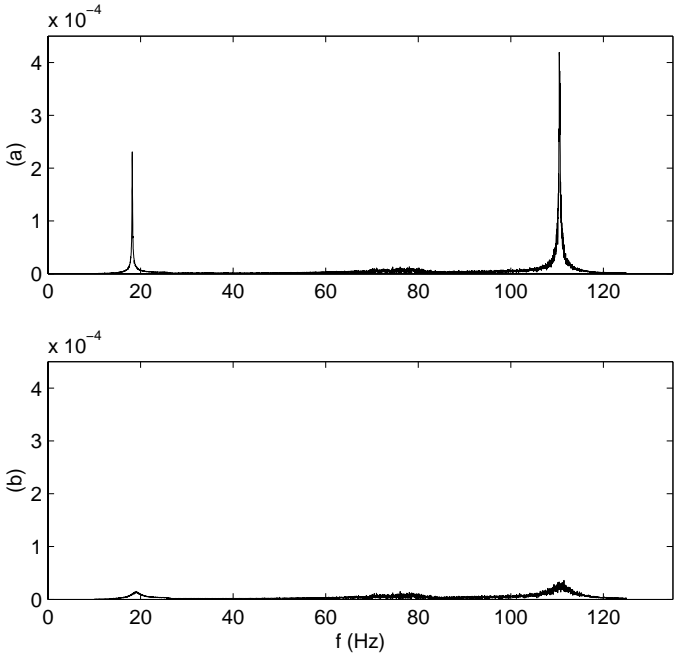
Figure 4.35: The open-loop (a), and $\mathcal{H}_2$ shunt controlled (b) linear magnitude response from an applied acoustic disturbance to the resulting tip displacement d (m).

4.4.6 $\mathcal{H}_\infty$ Shunt Design

This sub-section documents the design and implementation of an $\mathcal{H}_\infty$ s-impedance. As discussed in Section 4.3.2, an $\mathcal{H}_\infty$ s-impedance is designed to minimize the following cost function,

$$J = \left\| \frac{d(r,s) + k_u V_z(s)}{V_a(s)} \right\|_\infty, \tag{4.48}$$

where k_u, the control signal weighting, was chosen to be 3.2×10^{-7}. A random auxiliary input of negligible influence was also included to avoid plant inversion.

The complex s-impedance and pole-zero map of the resulting $\mathcal{H}_\infty$ controller are plotted in Figures 4.36 and 4.37.

Examining the open- and closed-loop pole locations shown in Figure 4.38, the controller is clearly augmenting the system damping. Corresponding mitigation of the transfer function from an applied disturbance to the measured displacement can be seen in both the frequency domain, Figure 4.39, and time domain, Figure 4.40. The magnitudes of the first and second structural modes are reduced by 30.3 and 24.0 dB respectively. Damping ratios are increased from 0.00246 to 0.0288, and from 0.0011 to 0.00766.

The effect of additional mass can be observed in Figures 4.41 and 4.42. The $\mathcal{H}_\infty$ controller loses 3.3 and 0.8 dB from its nominal closed-loop attenuation of the first and second modes.

Acoustic excitation results in both the frequency and time domains are shown in Figures 4.44 and 4.43.
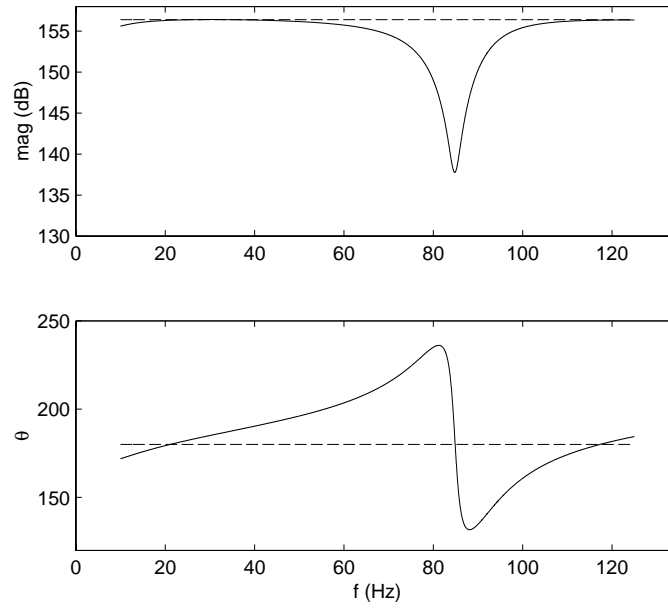
Figure 4.36: Complex s-impedance of the $\mathcal{H}_\infty$ (—), and ideal negative capacitor (- -) shunt controller.
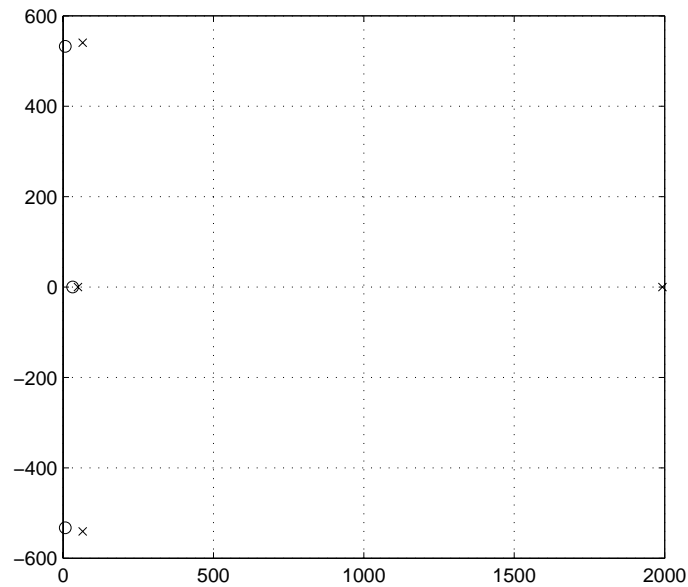
Figure 4.37: The $\mathcal{H}_\infty$ shunt controller pole ($\times$) and zero ($\bigcirc$) locations.
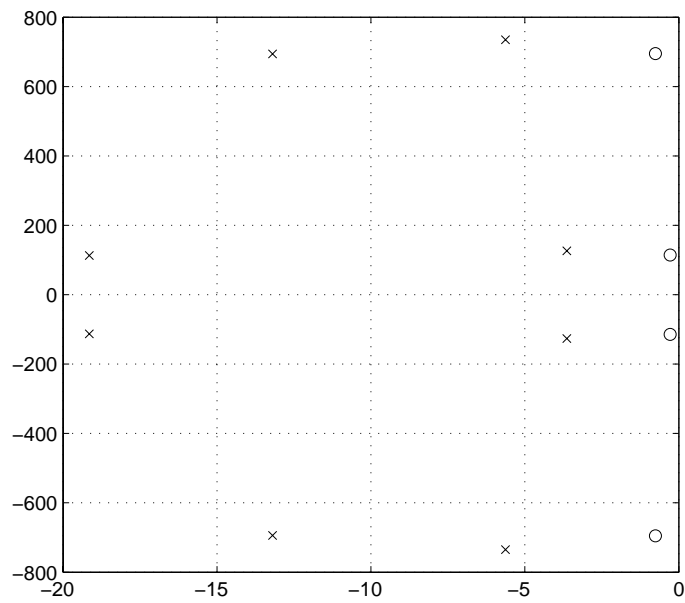
Figure 4.38: The open- ($\bigcirc$), and closed-loop ($\times$) pole locations of the $\mathcal{H}_\infty$ shunt controlled system.
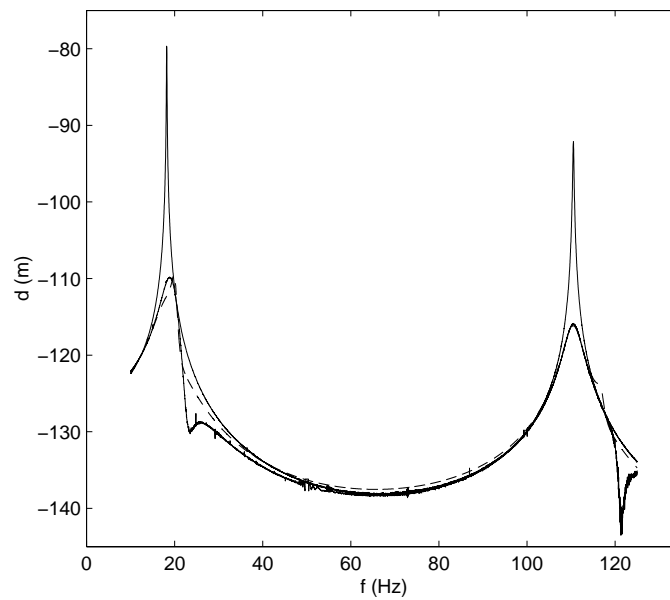
Figure 4.39: The experimental (—), and simulated (- -), $\mathcal{H}_\infty$ shunt controlled frequency responses from an applied disturbance voltage V_a (V) to the resulting tip displacement d (m) (in decibels). The open-loop frequency response is also shown (—).
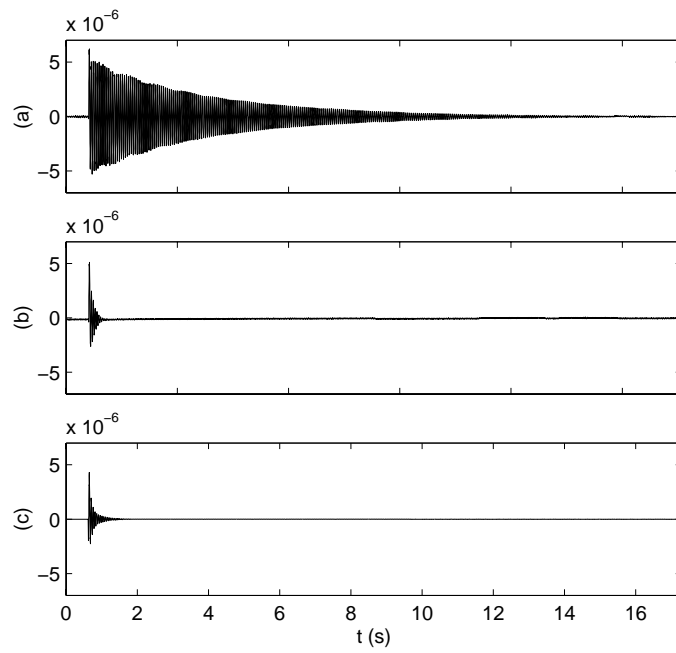
Figure 4.40: Tip displacement response d (m) of the $\mathcal{H}_\infty$ shunt controlled system to a step disturbance in V_a. Experimental open-loop (a), closed-loop (b), and simulated closed-loop (c).
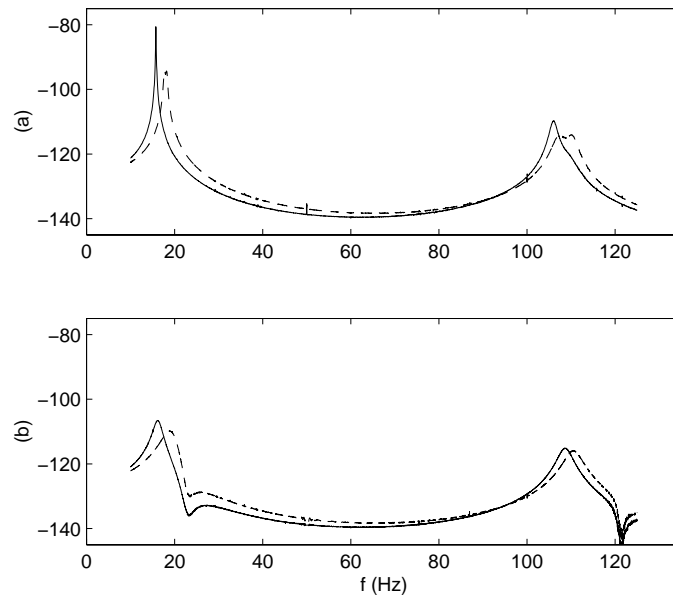
Figure 4.41: The free (- -), and with-mass (—), passive (a) and $\mathcal{H}_\infty$ shunt controlled (b) experimental frequency responses from an applied disturbance voltage V_a (V) to the resulting tip displacement d (m) (in decibels).
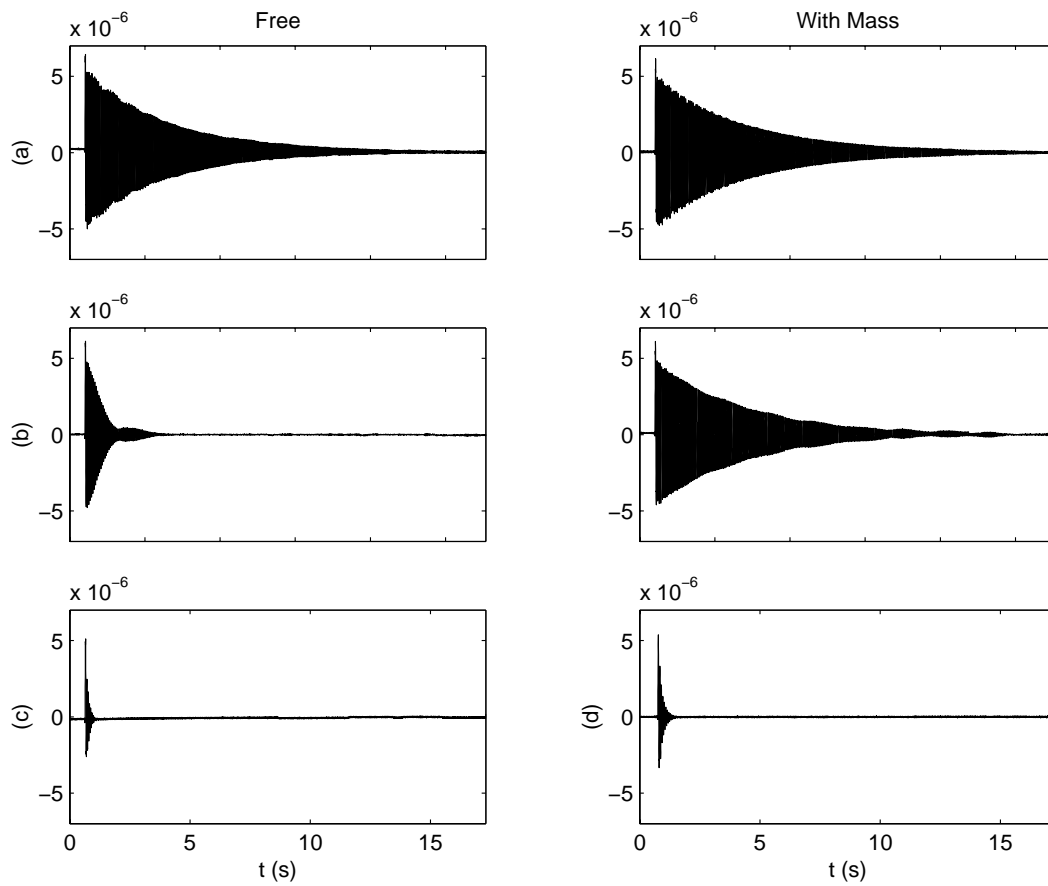
Figure 4.42: The free (left column) and with-mass (right column) tip displacement response d (m) to a step disturbance in V_a. Experimental open-loop (a), passive shunt controlled (b), and $\mathcal{H}_\infty$ shunt controlled (c) systems.
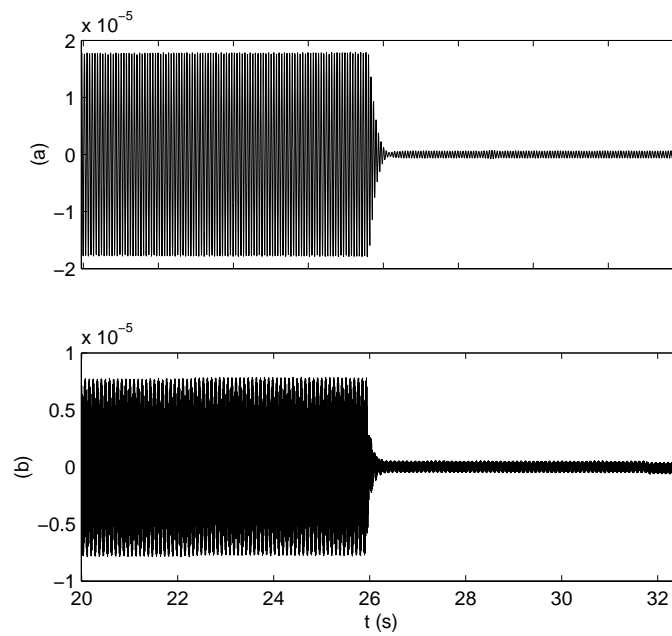
Figure 4.43: The open-loop and $\mathcal{H}_\infty$ shunt controlled tip displacement response d (m) to an acoustic sinusoidal disturbance at the 1st (a) and 2nd (b) structural resonance frequencies. Control is applied at approximately time 25.8 s.
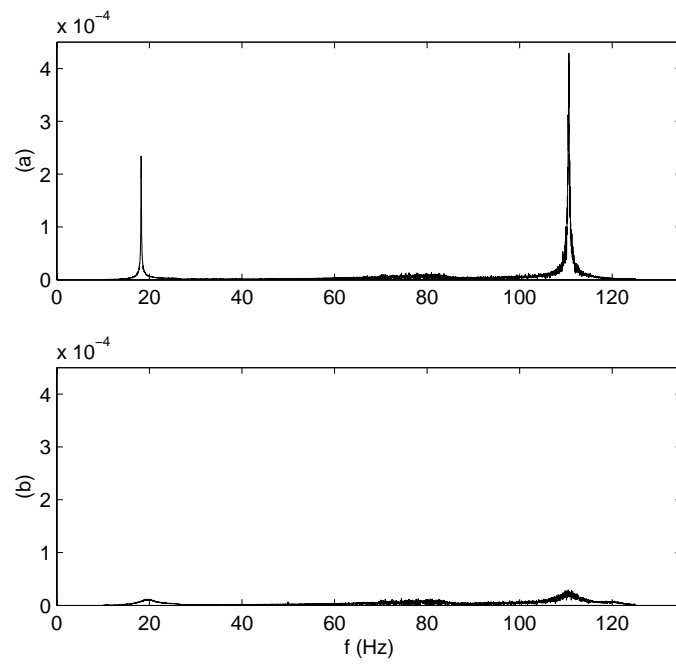
Figure 4.44: The open-loop (a), and $\mathcal{H}_\infty$ shunt controlled (b) linear magnitude response from an applied acoustic disturbance to the resulting tip displacement d (m).

	1st Mode		2nd Mode	
Frequency	Unperterbed	Perterbed	Unperterbed	Perterbed
Passive	14.2 dB	0.8 dB	22.1 dB	17.3 dB
LQG	27.2 dB	25.5 dB	19.2 dB	19.4 dB
$\mathcal{H}_2$	27.1 dB	25.8 dB	23.1 dB	22.9 dB
$\mathcal{H}_\infty$	30.3 dB	27.0 dB	24.0 dB	23.2 dB

Table 4.5: Modal attenuation summary.

4.5   Conclusions

A framework has been presented for the design of active shunt impedances. By viewing a piezoelectric laminate structure as a system with voltage inputs and charge outputs, the task of shunt impedance design can be accomplished through the solution of a standard control problem e.g. by LQG, $\mathcal{H}_2$, or $\mathcal{H}_\infty$ synthesis. The resulting controller, effectively the derivative of impedance, can be implemented directly with a voltage amplifier and charge measurement.

Although the fundamental goal in smart structure design is often to augment system damping, this cannot be specified directly as an LQG, $\mathcal{H}_2$, or $\mathcal{H}_\infty$ performance objective. The approach has been to achieve this indirectly through mitigation of the performance transfer function $\frac{d(s)}{V_a(s)}$.

As the system we are considering is spatially distributed, our controller should ensure performance subject to any realizable disturbance. To achieve this, an *ad-hoc* technique has been proposed to avoid the possibility of disturbance channel sensitivity and plant inversion.

Experimentally, the active shunts have proven to introduce significant system damping, up to 30.3 dB attenuation of the first cantilever mode. A comparison of modal attenuation for each active shunt impedance can be found in Table 4.5. The performance of a current-flowing passive shunt circuit is included as a reference.

While achieving levels of performance previously only available through sensor-based feed-back control, active shunt impedances are remarkably insensitive to variation in the structural resonance frequencies. By adding a mass to the beam, a 13.5 % change in the first resonance frequency results in only a slight loss in performance. By comparison, the same variation has a disastrous consequence on a current-flowing shunt circuit. Such sensitivity has previously limited the practical application of active and passive vibration control systems in smart structure design.

Another well known problem associated with passive shunt damping is the lack of control influence. Given a lightly damped structure, even the small counteractive forces associated with passive shunt circuits can significantly increase system damping. Many practical mechanical structures naturally exhibit higher levels of damping. In such cases, passive piezoelectric shunt circuits are of limited use. As the amount of control influence associated with active shunt impedances is arbitrary, the possibility now exists for controlling more heavily damped systems. In such cases, the control voltage V_z is expected to become quite large. At high drive voltages it may be necessary to address the inherent piezoelectric hysteresis.

The reader will appreciate that the presented techniques are quite general and valid for structures incorporating multiple piezoelectric transducers. Although the application of sensor-based feedback control is well defined and feasible for structures with multiple sensors and actuators, the same can not be said for multi-transducer shunt circuits [91]. Present multi-transducer, multi-mode shunt circuits are simply a direct extension of single transducer shunt circuits. Each circuit is restricted to be independent and attached to a single transducer. If a single mode is to be targeted by two or more transducers, the task of tuning the shunt circuit can become extremely tedious. In addition to the complicated interaction between transducers at those frequencies, there are now as many more tuning parameters as there are transducers per mode. The design freedom afforded with active shunts not only eliminates the complicated task of tuning, but allows for full utilization of each patch. The resulting impedance is unstructured, multivariable, and able to exploit benefits that may arise from inter-transducer coupling.

Potential applications for active piezoelectric shunt control include sensor-less, high performance vibration control of acoustic panels, flexible structures, and positioning systems. Future work includes multi-transducer structures and passive impedance design. The LQG, $\mathcal{H}_2$, and $\mathcal{H}_\infty$ impedances contained negative reactive components and are unstable in a systems perspective. Although the connection of the transducer and control impedance is stable, an inherently stable controller is desirable. It is presently unclear if negative reactive components are necessary to result in effective vibration reduction.

ELECTROMAGNETIC SHUNT CONTROL

Piezoelectric transducers exhibit an electro-mechanical coupling between the terminal voltage and developed strain. When laminated onto the surface of a host structure, a strain transducer provides authority over out-of-plane vibrations.

In a similar fashion, electromagnetic transducers exhibit a coupling between the coil current and force. Electromagnetic transducers are used in vibration control for direct in-plane force actuation. This chapter introduces a new technique for the control of electromagnetically actuated systems. In analogy to previous concepts presented in this thesis, an electromagnetic shunt impedance can be designed to minimize vibration.

5.1 Introduction

Electromagnetic transducers [86, 101, 54] can be used as actuators, sensors, or both. When a current is applied to the terminals of an electromagnetic transducer, a force is exerted, conversely, when a transducer experiences a velocity, an open-circuit voltage is induced. Piezoelectric transducers [42], exhibit similar electromechanical properties but are characterized by a high mechanical impedance. Electromagnetic transducers are capable of significantly greater strokes, typically in the millimeter range compared to the micrometer range.

Physically, electromagnetic devices are robust and can be manufactured on all scales from

MEMS devices [6], to large $100kN$ electrodynamic shakers. Such transducers have found application in the fields of: car suspension systems [69], isolation platforms [106], acoustic speakers [55], magnetic levitation [119, 20], and magnetic bearings [93].

In analogy to the technique of piezoelectric self-sensing [32, 7], a recent literature has also developed on the topic of electromagnetic self-sensing actuators [119, 20, 93, 54, 72]. This technique involves estimating the relative velocity experienced by the transducer from the measured coil current and driving voltage. An example of this technique can be found in [21], where the acoustic pressure of an enclosed-sound field is estimated from the measured current flowing through an actuating speaker coil. A feedback loop, driving the speaker voltage, is constructed around the estimate to minimize acoustic pressure within the enclosure.

This chapter demonstrates the modeling, design, and implementation of active impedance and admittance controllers for electromagnetically actuated systems. By measuring the coil terminal voltage and controlling the resultant current or *vice-versa*, it is possible to control a coupled mechanical system. By revealing the underlying feedback structure, the problem is cast as a standard MIMO control problem, for which the application of synthesis techniques such as LQR and $\mathcal{H}_2$ is straight-forward. Using this technique, the need for an external sensor is eliminated, significantly reducing the cost, complexity, and sensitivity to transducer failure that in many applications, may preclude the use of an active control system.

Although, the focus is on the control of a system similar to an isolation column, the generality of the modeling and design framework is intended to be extensible to a large class of mechanical systems. Such applications include: MIMO vehicle suspension systems, vibration isolation platforms, and the control of enclosed-sound fields. Active admittance and impedance controllers require no external sensors, are capable of minimizing a pre-specified performance objective, and can also be used to estimate physical variables dynamically related to the system states such as velocity.

Three applications presently under investigation are shown in Figures 5.1, 5.2, and 5.3 :
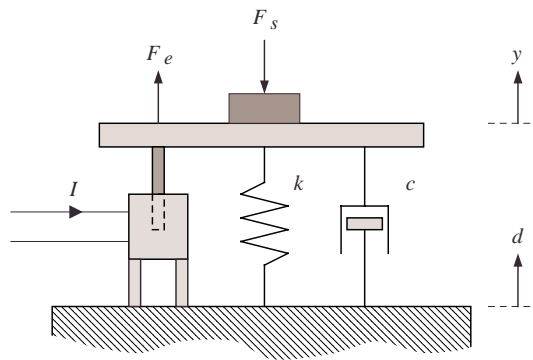
Figure 5.1: An electromagnetic isolation platform.
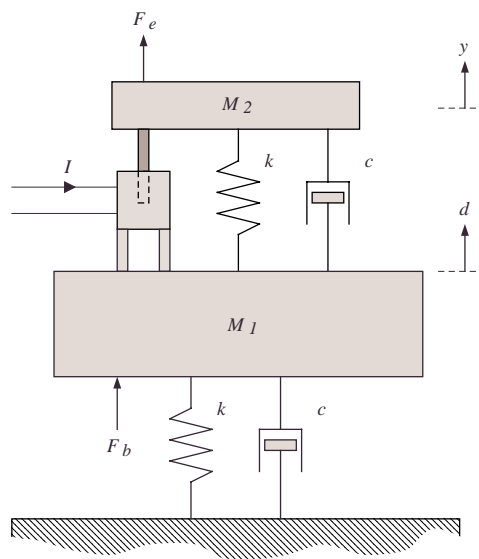
Figure 5.2: An electromagnetic proof-mass damper.

- An isolation platform attempts to mitigate the specimen displacement y resulting from a base disturbance d and on-board force F_s. As shown in Figure 5.1, a low-frequency spring-mass damper is often employed as a mechanical filter. Additional attenuation and control of the mechanical resonance can be achieved with a force F_e generated by an electromagnetic transducer.

- A proof-mass or inertial damper is a device mounted onto a vibrating body in order to counteract an applied disturbance F_b. The mass, spring constant, and damping can be tuned to suppress a single structural mode of the vibrating body. Additional broad-band attenuation can be achieved through the use of active feedback control and an electromagnetic force actuator.

- Acoustic drivers are a common form of electromagnetic actuator. In active noise control scenarios, the baffle velocity ν_b is used to mitigate the sound preasure P resulting from a disturbance particle velocity ν_d. This particular problem is complicated by a secondary feedback loop resulting from the acoustic back-preasure F_p. In all other aspects the problem reduces to that presented in the following discussion.

This chapter is presented in five sections. Section 2 begins with the modeling of mechanical, electromagnetic, and composite systems. A method is then presented in Section 3 for the design of active impedance and admittance controllers to minimize a time domain (LQR) and frequency domain ($\mathcal{H}_2$) performance objective. The presented techniques are then applied to an experimental electromagnetic system in Section 4. Finally, conclusions are drawn in Section 5.

5.2   Modeling

This section introduces a modeling technique for the design and analysis of shunted electromechanical systems. Although the focus is on a single-degree-of-freedom system, the process is quite general and can easily be extended to more complex mechanical systems.

5.2.1 Electromagnetic System

When an electrical conductor moves in a magnetic field as shown in Figure 5.4 (a), a voltage V proportional to the velocity ν is induced and appears across the terminals of the coil,

$$V \propto \nu. \tag{5.1}$$

Specifically,

$$\frac{V}{\nu} = Dl, \tag{5.2}$$

where D is the magnetic flux (in Teslas), l is the length of the conductor (in meters), and ν is the velocity of the conductor relative to the magnetic field (in ms^{-1}). A permanent magnet is usually the source of the magnetic field. In another configuration the coil is kept stationary and the magnet is made to move.

Assuming the coil is exposed to a field of constant flux density and the relative displacement is small, equation (5.2) can be rewritten [101] as

$$\frac{V}{\nu} = \frac{F}{I} = Dl = C_n, \tag{5.3}$$

where F denotes the force (in Newtons) acting on the coil carrying a current I (Amps), and C_n is the ideal electro-mechanical coupling coefficient.

As shown in Figure 5.4 (b), when the coil is employed as a force actuator, equation (5.3) relates the induced force to an applied current. Electrodynamic shakers and acoustic speakers operate on this principle.

As shown in Figure 5.5, the coil can be modeled as the series connection of an inductor L, a resistor R, and a dependent voltage source V_e [54]. When coupled to a mechanical system, the induced electro-motive-force (emf) and hence mechanical velocity can be determined from the open-circuit coil terminal voltage.

5.2.2 Mechanical System

The general model of a mechanical system is shown in Figure 5.6. In addition to various application specific inputs and outputs, to couple the system to an electromagnetic actu-
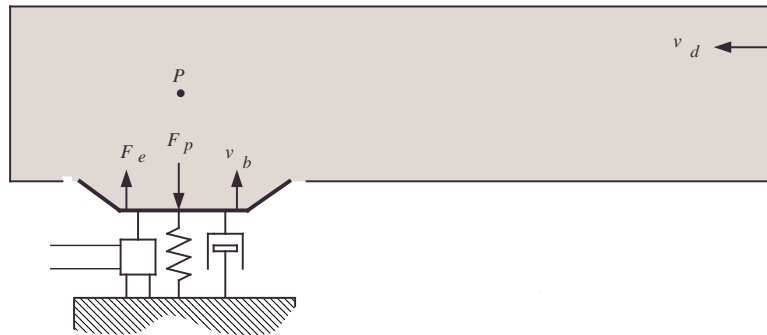
Figure 5.3: Voice coil acoustic control.
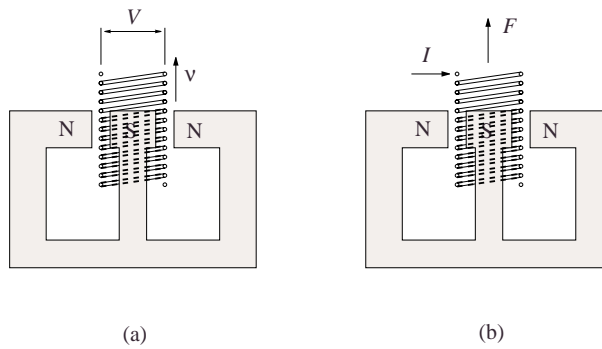
Figure 5.4: Electromagnetic transducer, (a) sensing and (b) actuating.
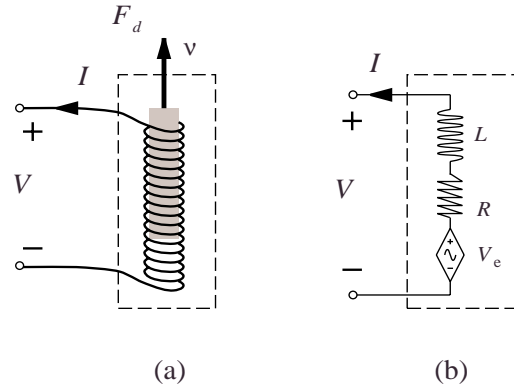
Figure 5.5: The mechanical (a) and electrically equivalent model (b) of an electromagnetic transducer.
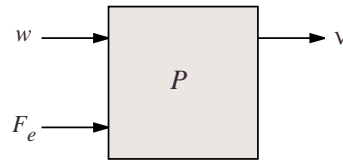
Figure 5.6: The general mechanical plant model.

ator, the model requires a force input F_e and a velocity output ν. In a typical scenario, the model would also describe the influence of a specific disturbance input w.

In many cases where vibration becomes an issue, the mechanical structure can be modeled as a simple mass-spring-damper system shown in Figure 5.7 (a). Examples include, but are not limited to: isolation columns, magnetic bearings, and suspension systems.

The equation of motion for a forced one degree of freedom system is

$$M\dot{\nu}(t) + C\nu(t) + Kd(t) = F_d(t), \qquad (5.4)$$

where $F_d(t)$ is the applied force, M is the equivalent mass (in kg), K is the spring constant (in N/m), C is the damping constant (in Ns/m), and $\dot{\nu}(t)$, $\nu(t)$ and $d(t)$ are the acceleration, velocity and displacement respectively. The dimensionless representation of
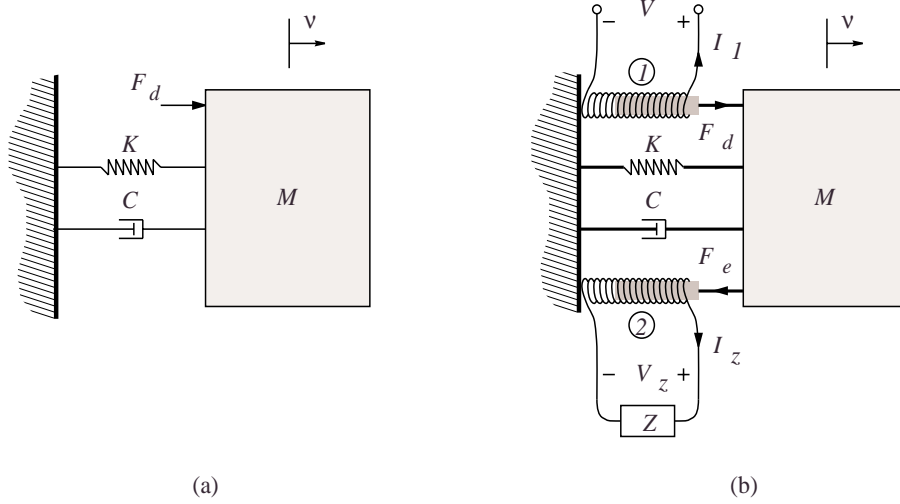
Figure 5.7: Mass-spring-damper system (a), coupled to two electromagnetic coils

(b).

equation (5.4) is

$$\dot{\nu}(t) + 2\zeta_n\omega_n\nu(t) + \omega_n^2 d(t) = f_d(t),\tag{5.5}$$

where ω_n is the natural frequency of the system and ζ_n is the damping ratio. Note that $\omega_n = \sqrt{\frac{K}{M}}$, $\zeta_n = \frac{C}{\sqrt{4MK}}$ and $f_d(t) = \frac{F_d(t)}{M}$. In the Laplace domain, the transfer function $G_{\nu F}(s)$ from an applied force to the resulting velocity is

$$G_{\nu F}(s) = \frac{\nu(s)}{F_d(s)} = \frac{s\frac{1}{M}}{s^2 + s\frac{C}{M} + \frac{K}{M}}.\tag{5.6}$$

In later sections, the following minimal state-space model for $G_{\nu F}(s)$ will also be required,

$$\dot{x}_p(t) = \mathbf{A}_p x_p(t) + \mathbf{B}_p F_e(t)\tag{5.7}$$

$$\nu(t) = \mathbf{C}_p x_p(t).$$

Consider Figure 5.7 (b), where a single-degree-of-freedom system is coupled to two elec-tromagnetic coils. Coil 1 is used to introduce a force disturbance, and coil 2, to control the resulting vibration. The corresponding mechanical plant model P is shown in Figure 5.8. The general constants C_1 through C_4 represent the various electro-mechanical coupling
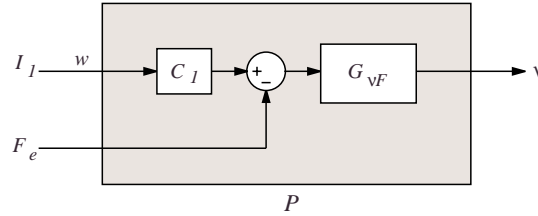
Figure 5.8: The mechanical plant P with a current disturbance I_1, and command

input F_e.

constants as defined in (5.8). The constants are defined individually as the two coils will

neither be perfectly matched nor have exactly identical force-current or velocity-voltage

ratios. By definition,

$$C_1 = \frac{F_d}{I_1} \quad C_2 = \frac{V_{e_1}}{\nu}$$

$$(5.8)$$

$$C_3 = \frac{F_e}{I_2} \quad C_4 = \frac{V_{e_2}}{\nu}$$

Using the constants defined in (5.8), the electromagnetic system E associated with coil

2 is shown in Figures 5.9 (a) and (b) for both combinations of voltage and current drive

respectively.

5.2.3   Shunted Composite Electromechanical System

A mechanical system $G_{\nu F}(s)$ coupled to a shunted electromagnetic transducer as shown

in Figure 5.7 (b) is now considered. In this case, where coil 1 is used to introduce a force

disturbance F_d, coil 2, the shunted coil, is used to reduce the resulting vibration.

Within the modeling framework introduced in the previous two subsections, i.e. by treating

the mechanical plant and shunted electromagnetic coil as shown in Figures 5.8 and 5.9,

it is a simple and intuitive task to construct the composite system. For both the current

and voltage driven coil models, the interconnection of each electromagnetic system with

the mechanical plant model is shown in Figures 5.10 (a) and 5.11 (a).

In Figure 5.10 (a) the admittance $Y(s)$, interpreted simply as the transfer function relating
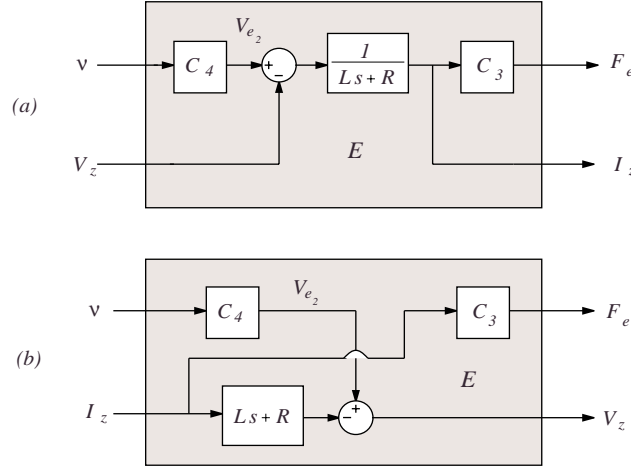
Figure 5.9: Block diagram representation of a voltage driven (a) and current driven (b) electromagnetic actuator.

the coil terminal voltage to current, appears like a feedback controller for the electromechanical system. By concatenating the mechanical and electromagnetic systems, P and E, as shown in Figure 5.10 (b), the composite system is cast as a typical regulation problem for the abstracted system G. It is easily shown that the closed-loop transfer function from an applied disturbance current $I_1(s)$ to the resulting plunger velocity ν is

$$\frac{\nu(s)}{I_1(s)} = \frac{G_{\nu F}(s)C_1}{1 + K(s)C_3C_4G_{\nu F}(s)}, \tag{5.9}$$

where $K(s)$, the equivalent velocity feedback controller is

$$K(s) = \frac{Y(s)}{1 + Y(s)(Ls + R)}. \tag{5.10}$$

Similarly, in Figure 5.11 (a) the impedance $Z(s)$, interpreted simply as a transfer function relating the coil terminal current to voltage, appears like a feedback controller for the electromechanical system. By concatenating the mechanical and electromagnetic systems, P and E, as shown in Figure 5.11 (b), the composite system is cast as a typical regulation problem for the abstracted system G. In this case, the equivalent velocity feedback controller is,

$$K(s) = \frac{1}{Ls + R + Z(s)}. \tag{5.11}$$
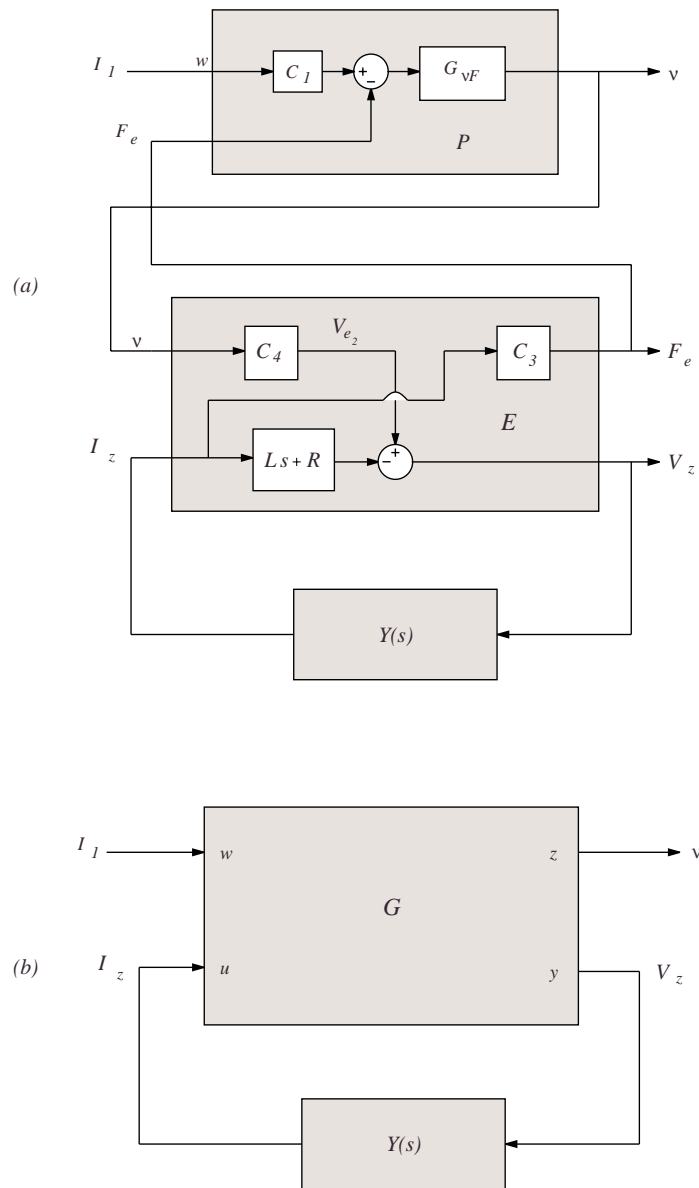
Figure 5.10: The shunt impedance controlled electromechanical system (a), in generalized plant/controller form (b).
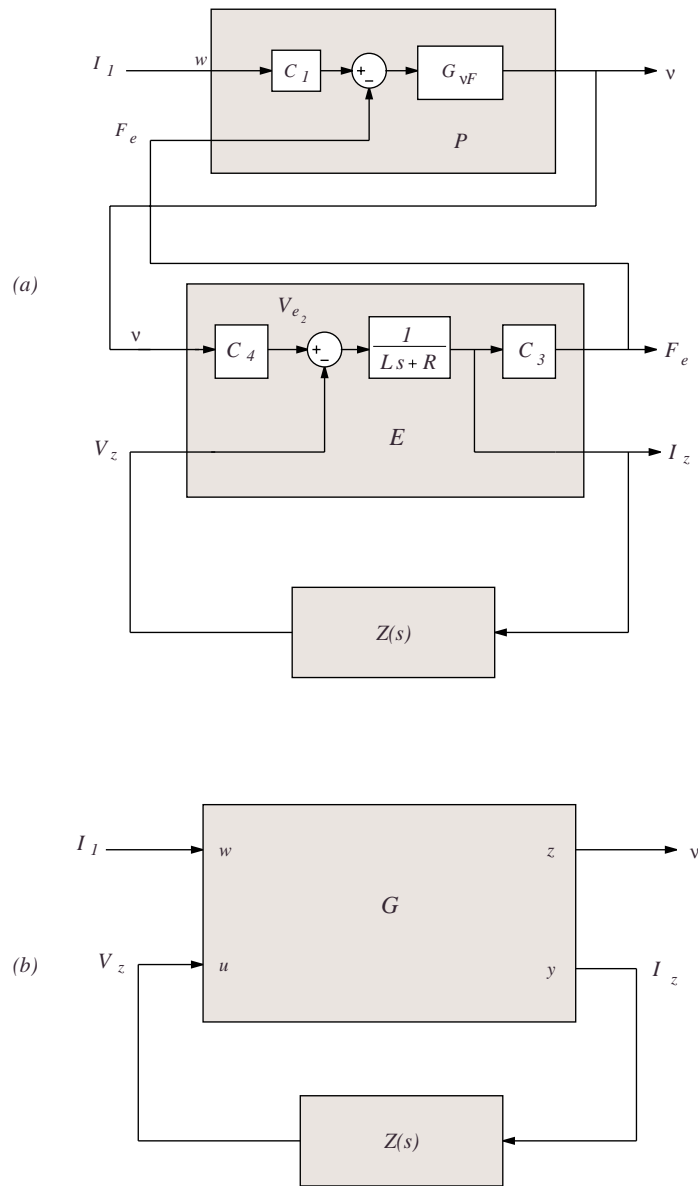
Figure 5.11: The shunt admittance controlled electromechanical system (a), in generalized plant/controller form (b).
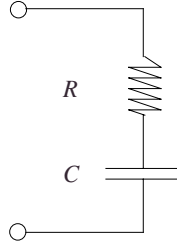
Figure 5.12: A resonant shunt circuit for electromagnetic transducers.

5.3   Control Design

As shown in Figures 5.10 and 5.11, and in equation (5.9), an impedance or admittance can be viewed as parameterizing an equivalent velocity feedback controller for the mechanical system $G_{\nu F}(s)$. The following subsections introduce a number of techniques for the synthesis of active impedance and admittance controllers designed to minimize structural vibration.

5.3.1   Passive Shunt Circuits

Alike the piezoelectric analogy, a resonant shunt circuit can be used to compensate for the reactive source impedance over a small frequency band. In reference [9] the circuit shown in Figure 5.12 was shown to significantly attenuate a lightly damped mechanical system. The circuit requires a negative resistance to cancel the natural resistance of the coil.

Resonant shunt circuits provide a fixed performance objective, they introduce additional dynamics that attenuate a highly resonant structural mode. Although this is desirable in piezoelectric applications, the same objective is unlikely to arise in electromagnetic applications. Firstly, considering the three examples shown in Figures 5.1, 5.2, and 5.3, the mechanical system is likely to contain a naturally high degree of damping. Resonant shunt circuits provide no additional performance is such cases. The exception is an isolation platform where the system may be lightly damped in order to achieve a faster local roll-off after the resonance. Secondly, the objective of resonant shunt circuits - to intro-

duce additional damping, may not be useful at all. In both Figures 5.2 and 5.1 in fact the reverse is true, a lightly damped resonance is required to counteract the structural modes of the system. It may actually be necessary to reduce the system damping. For these reasons, the only techniques discussed in detail, are those capable of minimizing an arbitrary performance objective, one that can be applied in any situation.

5.3.2 Ideal Negative-Inductor Controller

By substituting the equivalent impedance parameterized feedback controller (5.11) into the closed-loop transfer function (5.9), we obtain,

$$\frac{\nu(s)}{I_1(s)} = \frac{G_{\nu F}(s)C_1\left(Ls + R + Z(s)\right)}{Ls + R + Z(s) + C_3 C_4 G_{\nu F}(s)}. \tag{5.12}$$

Observe that the numerator is affine in the transfer function $Ls + R + Z(s)$. Thus, ideally, by equating $Ls + R + Z(s)$ to zero, we can reduce the closed-loop transfer function $\frac{\nu(s)}{I_1(s)}$ to zero. In other words, by choosing

$$Z(s) = -Ls - R, \tag{5.13}$$

or

$$Y(s) = \frac{1}{-Ls - R}, \tag{5.14}$$

any introduced disturbance will have little or no effect on the mechanical system. A similar result exists for piezoelectric transducers [10, 8, 126].

As is the case for piezoelectric transducers, and as one might expect, such a 'miracle' controller has limited practical use. By implementing (5.14) or (5.13) the effective controller is simply a proportional feedback loop of infinite gain. Besides the magnitude of control energy required, the stability and performance is extremely sensitive to small changes in the transducer dynamics.

In practice, by tuning the magnitudes of the negative inductor and resistor, the control effort can be toned down. Due to the *ad-hoc* nature of this approach, it is difficult to accurately manipulate the trade-off between control effort and damping performance. For example, using a negative inductor-resistor controller, it is impossible to distribute,

concentrate, or mitigate the control energy associated with individual structural modes. Neither is it possible to minimize a specific performance function not proportionally related to the plunger velocity. In cases where the goal is not simply to reduce the magnitude of plunger velocity, such as in acoustic, isolation, and suspension systems, the negative inductor controller is of little use.

In spite of the associated problems, this technique warrants mention due to its inherent simplicity and utility in gaining an intuitive understanding of the abstract controllers generated from an automated synthesis process such as LQR.

5.3.3 Impedance Synthesis

Referring to Figure 5.11, the shunted electromechanical system can be regarded as a typical feedback control system where a disturbance I_1 results in a vibration characterized by the velocity $\nu(t)$.

In order to apply standard synthesis techniques such as LQR, we require a minimal state space model representing the composite system. By defining the following state-space model for the coil admittance $\frac{1}{Ls+R}$,

$$\dot{x}_y(t) = \mathbf{A}_y x_y(t) + \mathbf{B}_y V(t) \tag{5.15}$$

$$I_z(t) = \mathbf{C}_y x_y(t),$$

where, $\mathbf{A}_y = \left[-\frac{R}{L}\right]$, $\mathbf{B}_y = [1]$, and $\mathbf{C}_y = \left[\frac{1}{L}\right]$, the following state-space model is easily derived for the composite system G,

$$\dot{x}_g(t) = \mathbf{A}_g x_g(t) + \mathbf{B}_g \begin{bmatrix} I_1(t) \\ V_z(t) \end{bmatrix} \tag{5.16}$$

$$\begin{bmatrix} \dot{x}(t) \\ I_z(t) \end{bmatrix} = \mathbf{C}_g x_g(t),$$

where,

$$x_g(t) = \begin{bmatrix} x_p(t) \\ x_y(t) \end{bmatrix}, \quad \mathbf{B}_g = \begin{bmatrix} \mathbf{B}_p C_1 C_4 & \mathbf{0} \\ \mathbf{0} & -\mathbf{B}_y \end{bmatrix}, \tag{5.17}$$

and

$$\mathbf{A}_g = \begin{bmatrix} \mathbf{A}_p & \mathbf{B}_p \mathbf{C}_y C_3 C_4 \\ \mathbf{B}_y \mathbf{C}_p & \mathbf{A}_y \end{bmatrix}, \ \mathbf{C}_g = \begin{bmatrix} \frac{1}{C_4} \mathbf{C}_p & \mathbf{0} \\ \mathbf{0} & \mathbf{C}_y \end{bmatrix}. \tag{5.18}$$

Our design objective is to minimize the velocity $\nu(t)$ whilst restraining the magnitude of the control signal V_z. In a linear quadratic sense, the objective is to minimize

$$J = \int_{-\infty}^{\infty} \left[\nu^2(t) + (k_u V_z(t))^2 \right] \ dt, \tag{5.19}$$

where k_u is the control signal weighting. Restated, in the standard LQR context,

$$J = \int_{-\infty}^{\infty} \left[x_g'(t) Q x_g(t) + u'(t) R u(t) \right] \ dt, \tag{5.20}$$

the corresponding Q and R matrices are $Q = \begin{bmatrix} \frac{1}{C_4} \mathbf{C}_p & \mathbf{0} \end{bmatrix}' \begin{bmatrix} \frac{1}{C_4} \mathbf{C}_p & \mathbf{0} \end{bmatrix}$, and $R = k_u^2$.

We can also consider the $\mathcal{H}_2$ control objective where we seek to minimize, in the $\mathcal{H}_2$ sense, the weighted sum of velocity and the control signal in response to a specific disturbance I_1, i.e. we seek to minimize

$$J = \left\| \frac{\nu(s) + k_u V_z(s)}{I_1(s)} \right\|_2. \tag{5.21}$$

This specification is easily cast as a standard $\mathcal{H}_2$ problem by considering the modified plant $\tilde{G}$ shown in Figure 5.13. Minimizing (5.19) is now equivalent to minimizing

$$J = \left\| \frac{z(s)}{w(s)} \right\|_2, \tag{5.22}$$

where the modified plant model is that of (5.16) with a non-zero D matrix,

$$\tilde{\mathbf{D}}_g = \begin{bmatrix} \mathbf{0} & k_u \\ \mathbf{0} & \mathbf{0} \end{bmatrix}. \tag{5.23}$$

5.3.4   Admittance Synthesis

Referring to Figure 5.10, the shunted electromechanical system can be regarded as a typical feedback control system where a disturbance I_1 results in a vibration characterized by the velocity $\nu(t)$.
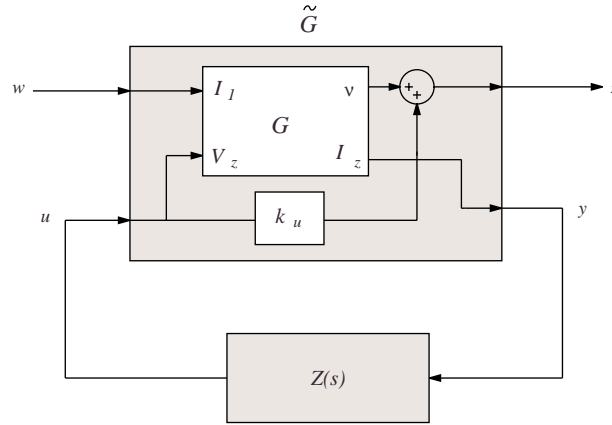
Figure 5.13: The modified plant model required for $\mathcal{H}_2$ impedance synthesis.

Due to the improper transfer function from the applied current I_z to the voltage V_z, we cannot directly apply, as in Section 5.3.3, the standard state-space design methodologies. To overcome this difficulty, we introduce the notion of a *current fluxion* amplifier.

As opposed to a regular current amplifier that drives an output current proportional to the applied reference signal, a current fluxion amplifier, as its name suggests, drives a current-rate-of-change proportional to the applied reference signal. Figures 5.14 (a) and (b), compare the operation of a current and current fluxion amplifier. Where the current amplifier in Figure 5.14 (a) has a gain of 1 A/V, the current fluxion amplifier in Figure 5.14 (b) has a gain of 1 As^{-1}/V. Such an amplifier, when connected to an electromagnetic coil, can also be viewed as a self-induced-voltage amplifier, the voltage drop across the transducer's self inductance is proportional to the derivative of current.

In practice, to avoid the large low frequency gains associated with integration, the current fluxion amplifier is best implemented by controlling the voltage across a sensing inductance L_s and resistance R_s. In this case, the current fluxion amplifier includes some internal dynamics as shown in Figure 5.14 (c). The resistance results in a limited gain at low frequencies. More details on the practical implementation of a current fluxion amplifier can be found in Section 5.4.2.
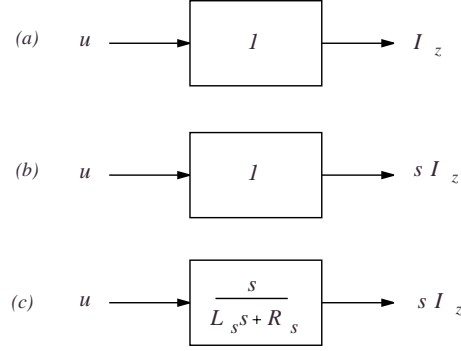
Figure 5.14: A unity gain current amplifier (a), a unity gain current fluxion amplifier (b), and a current fluxion amplifier with internal dynamics (c).

When dealing with a current fluxion driven transducer, the modified composite system is as shown in Figure 5.15 (a). By concatenating the transfer functions of coil impedance and amplifier dynamics, the resulting generalized plant model as shown in Figure 5.15 (b), is proper.

Inadvertently, by solving the problem associated with the improper coil impedance, we have also achieved a better conditioning of the transfer function from the command input to V_z. The dynamic range of this response was previously dominated by the coil impedance, but when driving the coil with current fluxion rather than current, the dynamic range is almost solely dependent on the mechanical response. As will become clearer in Section 5.4, this characteristic affords a more accurate estimation of the structural state.

In order to apply standard synthesis techniques such as LQR, we require a minimal state space model representing the current fluxion driven composite system. By defining the following state-space model for the concatenated coil impedance and amplifier dynamics $\frac{Ls+R}{L_s s+R_s}$,

$$\dot{x}_z(t) = \mathbf{A}_z x_z(t) + \mathbf{B}_z V_3(t) \tag{5.24}$$

$$\begin{bmatrix} V_c(t) \\ I_z(t) \end{bmatrix} = \begin{bmatrix} \mathbf{C}_{z1} \\ \mathbf{C}_{z2} \end{bmatrix} x_z(t) + \begin{bmatrix} \mathbf{D}_{z1} \\ \mathbf{0} \end{bmatrix} V_3(t),$$

where, $\mathbf{A}_z = \left[-\frac{R_s}{L_s} \right]$, $\mathbf{B}_z = [1]$, $\mathbf{C}_{z1} = \left[\frac{R}{L_s} - \frac{R_s L}{L_s^2} \right]$, $\mathbf{C}_{z2} = \left[\frac{1}{L_s} \right]$, $\mathbf{D}_{z1} = \left[\frac{L}{L_s} \right]$, a state-space
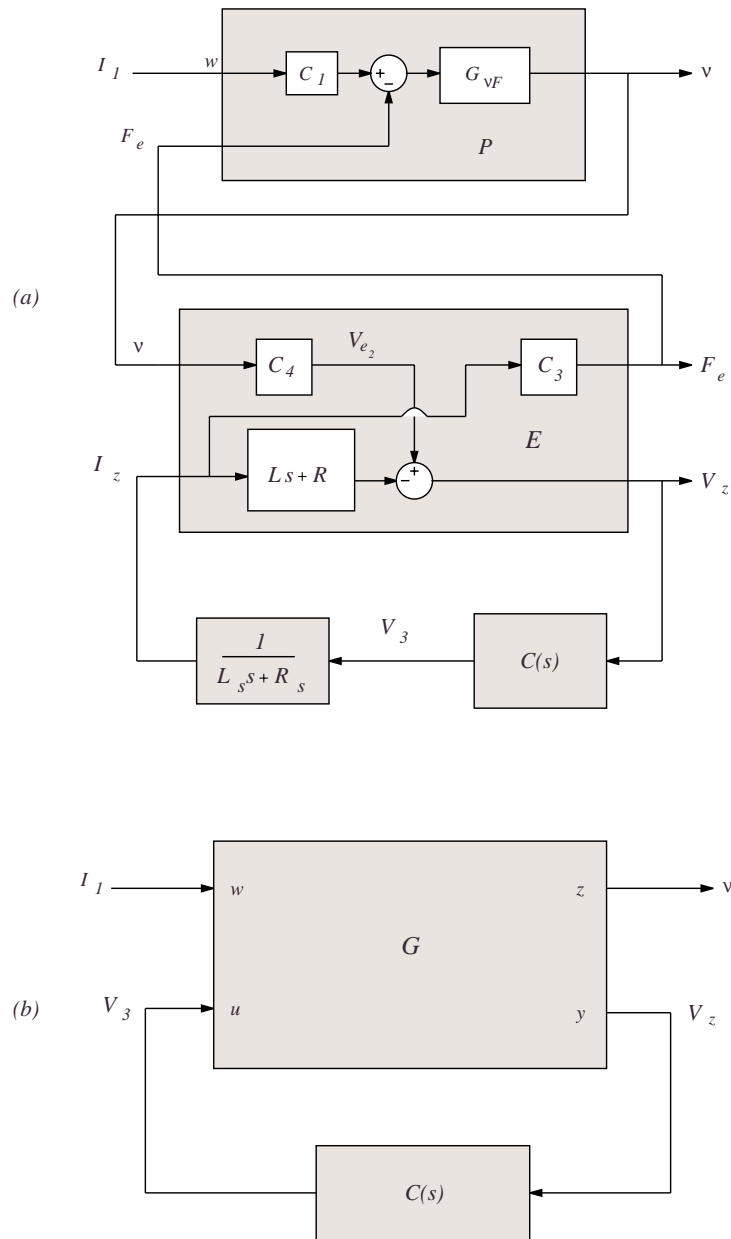
Figure 5.15: The electromechanical system including the dynamics of a current fluxion amplifier (a), in generalized plant/controller form (b).

model can be derived for the composite system G. V_c is the voltage dropped across the internal impedance of the transducer,

$$\dot{x}_g(t) = \mathbf{A}_g x_g(t) + \mathbf{B}_g \begin{bmatrix} I_1(t) \\ V_3(t) \end{bmatrix} \tag{5.25}$$

$$\begin{bmatrix} \dot{x}(t) \\ V_z(t) \end{bmatrix} = \mathbf{C}_g x_g(t) + \mathbf{D}_g \begin{bmatrix} I_1(t) \\ V_3(t) \end{bmatrix},$$

where,

$$x_g(t) = \begin{bmatrix} x_p(t) \\ x_z(t) \end{bmatrix}, \quad \mathbf{B}_g = \begin{bmatrix} \mathbf{B}_p C_1 C_4 & \mathbf{0} \\ \mathbf{0} & \mathbf{B}_z \end{bmatrix}, \quad \mathbf{D}_g = \begin{bmatrix} \mathbf{0} & \mathbf{0} \\ \mathbf{0} & -\mathbf{D}_{z1} \end{bmatrix} \tag{5.26}$$

$$\mathbf{A}_g = \begin{bmatrix} \mathbf{A}_p & -\mathbf{B}_p C_{z2} C_3 C_4 \\ \mathbf{0} & \mathbf{A}_z \end{bmatrix}, \quad \mathbf{C}_g = \begin{bmatrix} \mathbf{C}_p \frac{1}{C_4} & \mathbf{0} \\ \mathbf{C}_p & -\mathbf{C}_{z1} \end{bmatrix}. \tag{5.27}$$

Our design objective is to minimize the velocity $\nu(t)$, whilst, as opposed to restraining the control signal $V_3(t)$, it remains of interest to limit the magnitude of the terminal voltage V_z. In a linear quadratic sense, the objective is to minimize

$$J = \int_{-\infty}^{\infty} \left[\nu^2(t) + (k_y V_z(t))^2 \right] \, dt, \tag{5.28}$$

where k_y is the weighting on the terminal voltage V_z. This specification can be cast as a standard LQR problem by considering the modified plant $\tilde{G}$ shown in Figure 5.16. The state-space representation of which is

$$\dot{x}_g(t) = \mathbf{A}_g x_g(t) + \mathbf{B}_g \begin{bmatrix} w(t) \\ u(t) \end{bmatrix} \tag{5.29}$$

$$\begin{bmatrix} z(t) \\ y(t) \end{bmatrix} = \tilde{\mathbf{C}}_g x_g(t) + \tilde{\mathbf{D}}_g \begin{bmatrix} w(t) \\ u(t) \end{bmatrix},$$

where,

$$\tilde{\mathbf{C}}_g = \begin{bmatrix} \tilde{\mathbf{C}}_{g1} \\ \tilde{\mathbf{C}}_{g2} \end{bmatrix} = \begin{bmatrix} \begin{bmatrix} \mathbf{C}_p \frac{1}{C_4} & \mathbf{0} \end{bmatrix} + k_y \begin{bmatrix} \mathbf{C}_p & -\mathbf{C}_{z1} \end{bmatrix} \\ \begin{bmatrix} \mathbf{C}_p & -\mathbf{C}_{z1} \end{bmatrix} \end{bmatrix}, \tag{5.30}$$
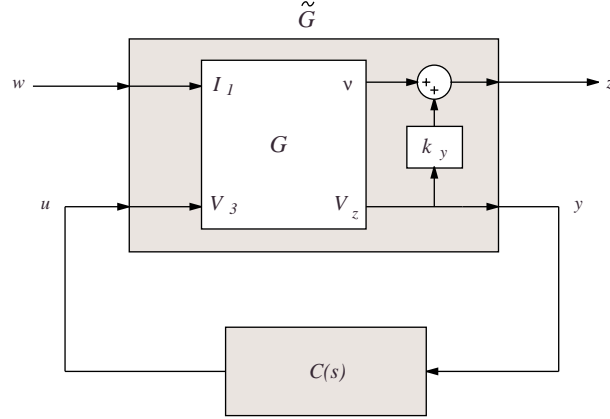
Figure 5.16: The modified plant model required for admittance synthesis.

$$\tilde{\mathbf{D}}_g = \begin{bmatrix} \tilde{\mathbf{D}}_{g11} & \tilde{\mathbf{D}}_{g12} \\ \tilde{\mathbf{D}}_{g21} & \tilde{\mathbf{D}}_{g22} \end{bmatrix} = \begin{bmatrix} \begin{bmatrix} \mathbf{0} & \mathbf{0} \end{bmatrix} + k_y \begin{bmatrix} \mathbf{0} & -\mathbf{D}_{z1} \end{bmatrix} \\ \begin{bmatrix} \mathbf{0} & -\mathbf{D}_{z1} \end{bmatrix} \end{bmatrix}.$$

Minimizing (5.28) is now equivalent to minimizing

$$J = \int_{-\infty}^{\infty} z^2(t) \ dt \tag{5.31}$$

$$= \int_{-\infty}^{\infty} \left[\tilde{\mathbf{C}}_{g1} x_g(t) + \tilde{\mathbf{D}}_{g12} u(t) \right]' \left[\tilde{\mathbf{C}}_{g1} x_g(t) + \tilde{\mathbf{D}}_{g12} u(t) \right] \ dt \tag{5.32}$$

$$= \int_{-\infty}^{\infty} \left[x_g'(t) \tilde{\mathbf{C}}_{g1}' \tilde{\mathbf{C}}_{g1} x_g(t) + u'(t) \tilde{\mathbf{D}}_{g12}' \tilde{\mathbf{D}}_{g12} u(t) + 2 x_g'(t) \tilde{\mathbf{C}}_{g1}' \tilde{\mathbf{D}}_{g12} u(t) \right] \ dt. \tag{5.33}$$

Restated, in the standard LQR context,

$$J = \int_{-\infty}^{\infty} \left[x_g'(t) Q x_g(t) + u'(t) R u(t) + x_g'(t) N u(t) \right] \ dt. \tag{5.34}$$

The corresponding Q, R, and N matrices are,

$$Q = \tilde{\mathbf{C}}_{g1}' \tilde{\mathbf{C}}_{g1}$$
$$R = \tilde{\mathbf{D}}_{g12}' \tilde{\mathbf{D}}_{g12} \tag{5.35}$$
$$N = \tilde{\mathbf{C}}_{g1}' \tilde{\mathbf{D}}_{g12}.$$

We can also consider the $\mathcal{H}_2$ control objective where we seek to minimize, in the $\mathcal{H}_2$ sense, the weighted sum of velocity and the terminal voltage in response to a specific disturbance

I_1, i.e. we seek to minimize

$$J = \left\| \frac{\nu(s) + k_y V_z(s)}{I_1(s)} \right\|_2 . \tag{5.36}$$

By considering the modified plant $\tilde{G}$ described in equation (5.29), this specification is easily cast into a standard $\mathcal{H}_2$ synthesis problem. Minimizing (5.36) is now equivalent to minimizing

$$J = \left\| \frac{z(s)}{w(s)} \right\|_2 . \tag{5.37}$$

5.4 Experimental Results

To verify the modeling and design techniques presented in the preceding sections, each method has been applied to an experimental electromechanical system.

5.4.1 Electromagnetic Transducer

A photograph of the electromagnetic transducer showing the rigid body, flexible end supports, mounting plate, and coils is provided in Figure 5.17. The apparatus is essentially a translational solenoid with two identical fixed coils and a magnetic plunger supported at either end by flexible disks. A side section including dimensions and magnetic orientations is shown in Figure 5.18.

The coils are wound from 0.25 mm diameter enamel coated copper wire and have an electrical impedance of 3.3 Ω + 1 mH. In order to prevent distortion of the magnetic flux field, only non-magnetic materials, such as aluminum and copper, were used in the construction of the rigid body, flexible end supports and mounting plate.

In practice, the magnetic field strength, as well as being a function of the magnetic material, is limited by the maximum allowable dimensions and weight of the magnets. In these experiments, three rare earth magnets (Neodymium Iron Boron), are arranged to form the magnetic plunger as shown in Figure 5.18. At the two points where opposing poles meet (at the center of each winding), a strong magnetic field exits at right angles to the plunger. When the plunger is in motion, the strong parallel field flowing through the

Parameter	Value
Spring constant K	56 kNm^{-1}
Damping coefficient C	2.667 Nsm^{-1}
Plunger mass M	0.150 kg
Electromagnetic Coupling C_1	3.55
Electromagnetic Coupling C_2	4.06
Electromagnetic Coupling C_3	3.55
Electromagnetic Coupling C_4	4.06
Coil Inductance L	1 mH
Coil Resistance R	3.3 Ω

Table 5.1: Electromechanical system parameters.

coil results in a high flux density and correspondingly large induced voltage. The physical parameters of the electromagnetic and mechanical systems are summarized in Table 5.1.

The plunger velocity is measured using a PSV-300 Polytec Scanning Laser Vibrometer.

5.4.2   Power Amplifier and Instrumentation

In order to implement the arbitrary shunt impedance and admittances resulting from the control design, a power amplifier was developed capable of driving either differential terminal voltages or load current fluxions. During either mode of operation, the device is also capable of instrumenting the respective load current or terminal voltage.

The simplified schematic of two circuits realizing each mode of operation are shown in Figures 5.19 (a) and (b). Both circuits incorporate a high gain feedback loop to control either the measured load or sensing impedance voltage.

In Figure 5.19 (a), within the high frequency bandwidth of the control loop, the reference potential V_{ref} appears across the load, i.e. we have a unity gain voltage amplifier. The
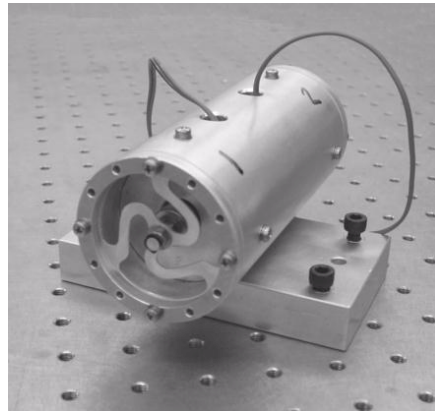
Figure 5.17: An external photograph of the experimental electromagnetic apparatus.
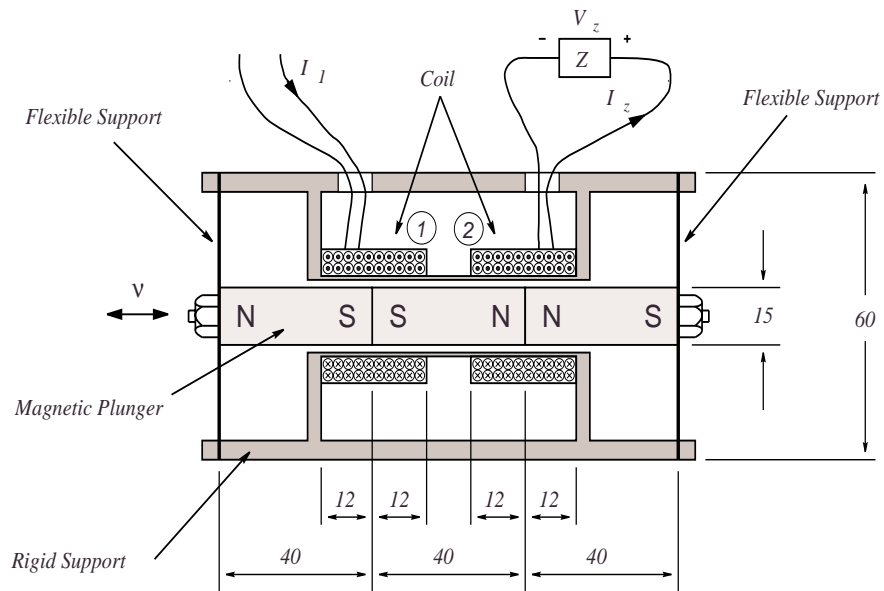
Figure 5.18: Side section of the experimental electromagnetic apparatus. All dimensions are in millimeters (mm).

additional resistance and differential amplifier generate the current measurement V_R with gain R_s V/A.

In Figure 5.19 (b), within the high frequency bandwidth of the control loop, the reference potential V_{ref} appears across the sensing impedance $L_s s + R_s$, thus, the resulting load current is described by

$$\frac{I_L(s)}{V_{ref}(s)} = \frac{1}{L_s s + R_s} \tag{5.38}$$
$$\approx \frac{1}{L_s s}.$$

Neglecting the resistance R_s, the amplifier can be thought of as an integrator connected in series to the reference of a current source (with gain $\frac{1}{L_s}$ A/V). Alternatively, as it is defined in this paper, we could also refer to the device as a current fluxion amplifier (with gain $\frac{1}{L_s}$ As^{-1}/V) where the reference signal V_{ref} commands the rate of change in load current. The parasitic coil resistance R_s is beneficial and effectively limits the low frequency gain of the amplifier eliminating the normal practical problems associated with integration. The following in-bandwidth transfer function of the current fluxion amplifier is determined by the parameters of the sensing inductor,

$$\frac{s I_L(s)}{V_{ref}(s)} = \frac{s}{L_s s + R_s}. \tag{5.39}$$

A practical implementation of a combination voltage and current fluxion amplifier is shown in Figure 5.20. The device is capable of +/- 250 V operation at a maximum DC current of 32 Amps. Further analysis and a more detailed discussion of the implementation can be found in Chapter 3.

A dSpace 1005 based system is used to implement the required impedance and admittance transfer functions.

5.4.3 Impedance Synthesis

Figure 5.21 shows the instrumentation and driver gains associated with the underlying electromechanical system. The voltages V_1 through V_4 represent the signals applied to, or measured from, the power amplifiers and instrumentation. The gain and units associated
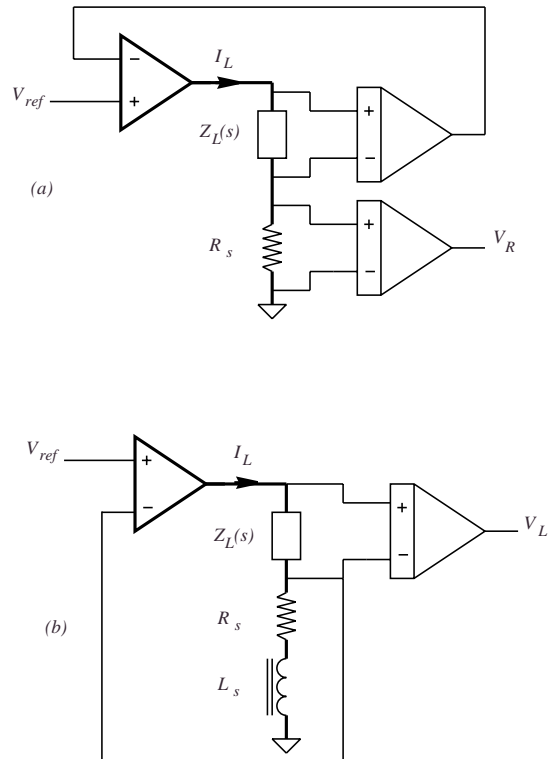
Figure 5.19: The simplified schematic of a differential voltage feedback amplifier

(a), and current fluxion feedback amplifier (b).
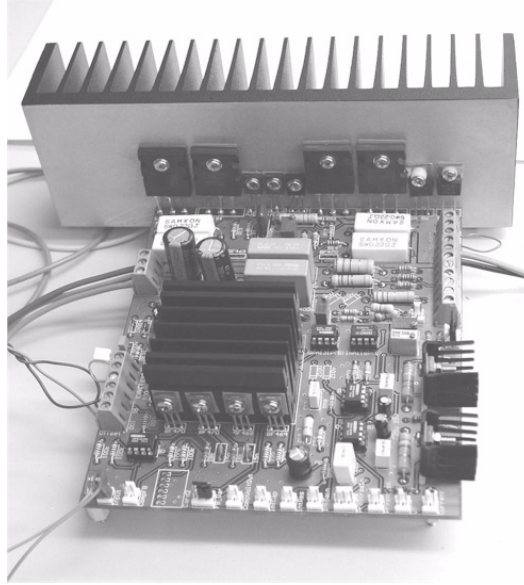
Figure 5.20: Implementation of a voltage and current fluxion amplifier.

with each signal can be found in Table 5.2. The actual electrical shunt impedance presented to the coil is related to the controller through the gains k_3 and k_4, specifically,

$$Z_c(s) = \frac{V_z(s)}{I_z(s)} = k_3 C(s) k_4. \qquad (5.40)$$

To assess the accuracy of the analytic model (discussed in Section 5.2.3), the simulated frequency response is compared to that measured directly from the experimental system.

Gain	Value
k_1	$1\ A/V$
k_2	$40\ V/ms^{-1}$
k_3	$-4\ V/V$
k_4	$10\ V/A$

Table 5.2: External gains associated with the shunt voltage controlled electromagnetic system.
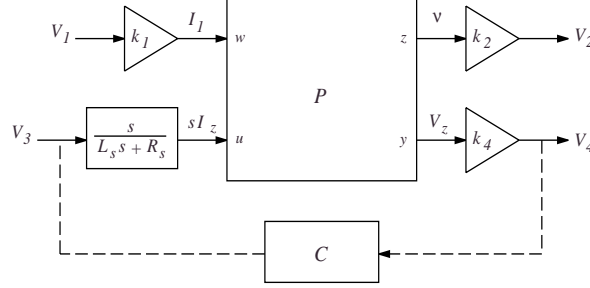
Figure 5.21: Open-loop external gains of the shunt voltage controlled electromagnetic system.

A multivariable frequency response is measured successively from each input to output pair. During the component SISO frequency response measurements, the residual input is set to zero. The magnitude and phase frequency responses are shown respectively in Figures 5.22 and 5.23. In the frequency domain, a good correlation can be observed between the analytic model and measured system.

LQR Impedance Synthesis

As discussed in Section 5.3.3, a linear quadratic regulator can be designed to command the shunt terminal voltage V_z with a view to regulating a performance signal consisting of the weighted sum of plunger velocity and control signal. An observer is required to estimate the system states from the measured shunt current I_z. Once designed, the concatenation of the observer and LQR gain matrix results in a system, interpreted as an active shunt impedance, that can be applied to one of the electromagnetic coils in order to reduce structural vibration.

Based on the physical model (including external gains) that was validated in the previous sub-section, and referring to the notation introduced in Section 5.3.3, an LQR gain matrix was designed to minimize the following performance function,

$$J = \int_{-\infty}^{\infty} \left[(k_2\nu(t))^2 + \left(\frac{7}{k_3} V_z(t) \right)^2 \right] \, dt, \tag{5.41}$$
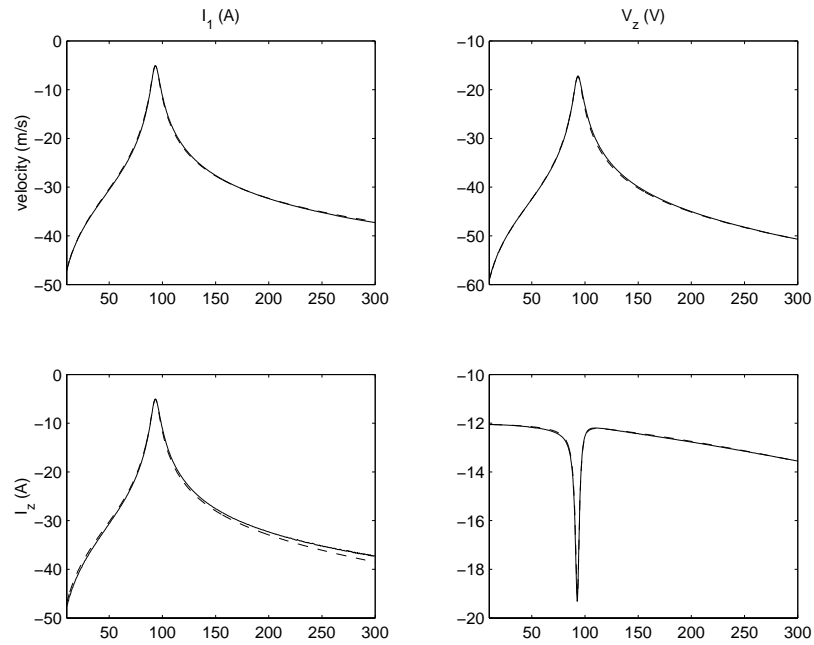
Figure 5.22: The simulated (—), and experimental (- -), magnitude frequency response (in decibels) of the shunt voltage controlled electromagnetic system.
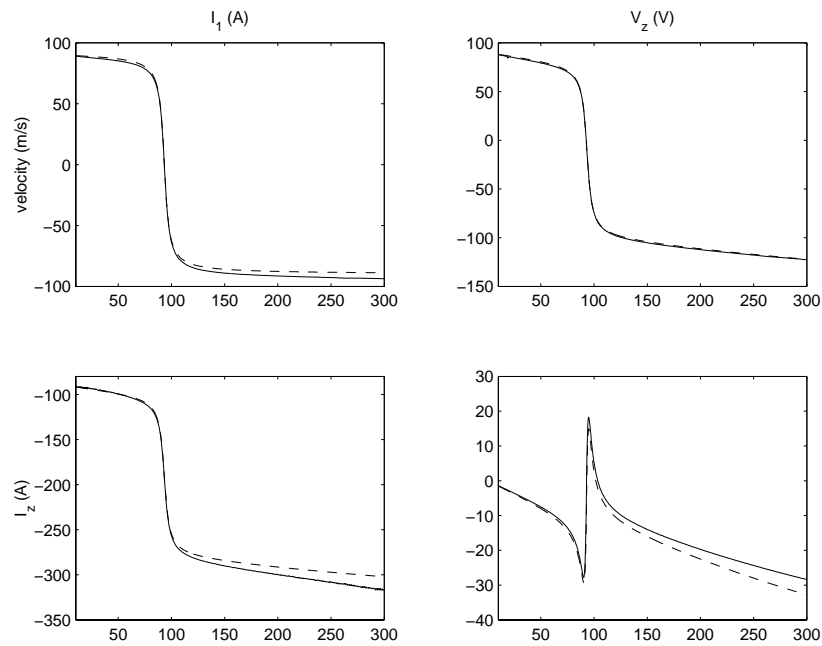
Figure 5.23: The simulated (—), and experimental (- -), phase frequency response (in degrees) of the shunt voltage controlled electromagnetic system.

where the factor 7 represents the relative control weighting. The gains k_2 and k_3 are included as the design is based on the input-output model which includes the amplifier and instrumentation dynamics. The observer was designed by pole placement, where the target poles were chosen as that of the closed-loop system with real components multiplied by 2. As is routine in control system design, the control weighting of 7 and observer pole locations were chosen experimentally to achieve a reasonable trade-off between damping performance, robustness, and the control signal magnitude.

The complex impedances of the implemented LQR and ideal negative inductor-resistor controller are plotted in Figure 5.24. It can be observed that at frequencies close to the resonance of the system, 92 Hz, the impedance of the LQR designed controller closely resembles that of the ideal negative inductor-resistor controller. Beneficially, the LQR designed impedance is proper, has a limited bandwidth, and exerts control effort only at frequencies close to the resonance of the system (which can be deduced from the following closed-loop performance plots).

The damping performance of the LQR controller was assessed in both the frequency and time domains. With the controller in the loop, a disturbance current I_1, proportional to a force disturbance, is applied to the system. Experimental and simulated open- and closed-loop frequency responses are shown in Figure 5.25. The controller was measured to reduce the resonant peak by 19.4 dB. The corresponding time domain velocity response to a 300 Hz low-pass filtered step change in disturbance current I_1 is shown in Figure 5.26. The simulated closed-loop step response was obtained by recording the applied step signal and applying it in simulation to the closed-loop model. The action of the controller can be further understood by observing the open- and closed-loop pole locations shown in Figure 5.27. Disregarding the observer poles, the controller has acted to increase system damping by shifting the associated poles further into the left half plane. The pole corresponding to the coil admittance remains effectively unchanged.
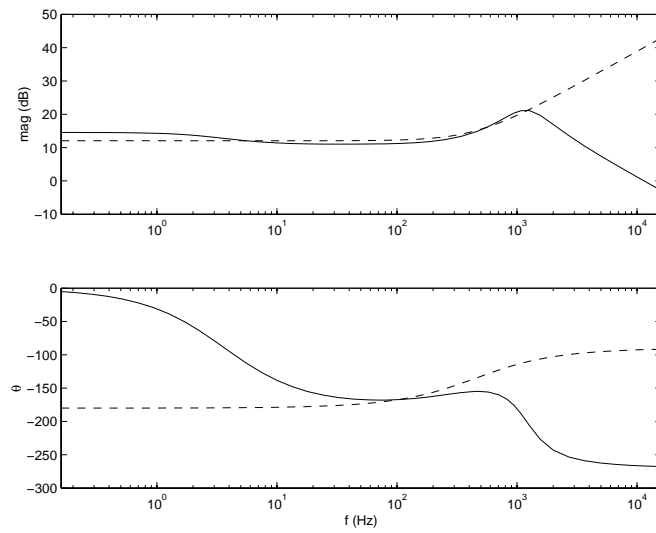
Figure 5.24: Complex impedance of the LQR (—) and ideal negative inductor-resistor controller (- -).
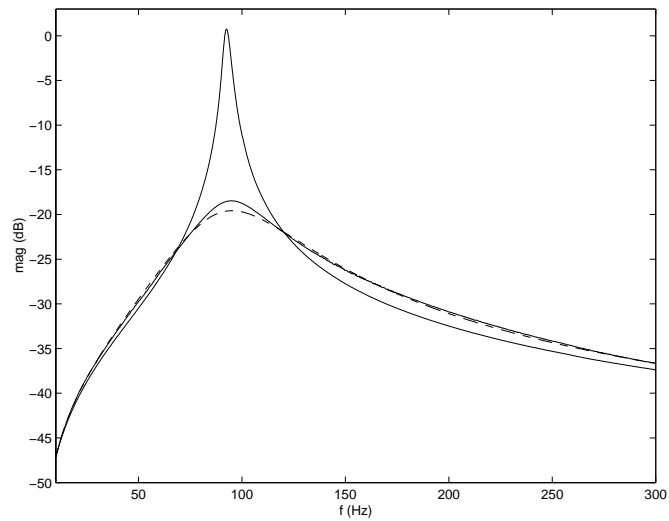
Figure 5.25: The experimental (—) and simulated (- -), open- and closed-loop frequency response from an applied disturbance current I_1 (A) to the resulting plunger velocity ν $\left(ms^{-1}\right)$ for the LQR impedance controlled system. The open-loop frequency response is also shown (—).
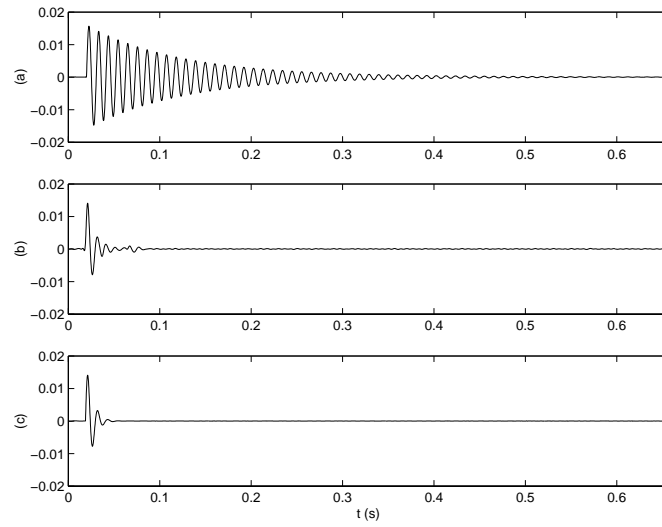
Figure 5.26: Velocity response ν (ms^{-1}) of the LQR impedance controlled system to a step disturbance current I_1. (a) experimental open-loop, (b) closed-loop (b), and (c) simulated closed-loop.
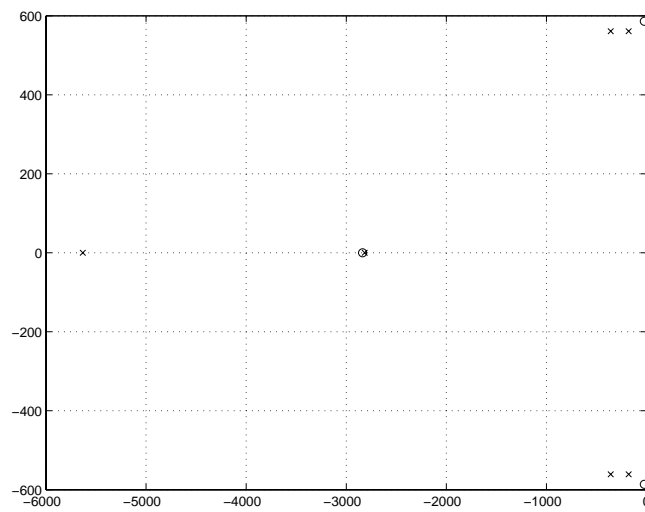
Figure 5.27: The open- ($\bigcirc$) and closed-loop ($\times$) pole locations of the LQR impedance controlled system.

$\mathcal{H}_2$ Impedance Synthesis

In analogy to Section 5.4.3, and as discussed in Section 5.4.3, this sub-section documents the implementation of an active shunt impedance designed to minimize the $\mathcal{H}_2$ norm of the transfer function between a disturbance current I_1 and a performance signal z. As in Section 5.4.3, the performance signal consists of the weighted sum of plunger velocity and control signal. Specifically, for the electromagnetic system including external gains, we seek to minimize:

$$J = \left\| \frac{k_2 \nu(s) + \frac{k_u}{k_3} V_z(s)}{I_1(s)/k_1} \right\|_2 , \tag{5.42}$$

where k_u is the control signal weighting.

For the plant under consideration, the $\mathcal{H}_2$ problem is well defined and feasible. All of the standard requirements are met, i.e. the plant is minimal, proper, controllable, observable, and of finite dimension. However, in order to find a solution using existing tools, i.e. the algebraic Riccati solution implemented by the μ-Synthesis Toolbox for Matlab$^{\copyright}$, the system must meet some additional requirements. The most problematic of which, is the requisite full rank condition on the standard plant matrices D_{21} and D_{12}. In this case, where each of the signals w, u, y, and z are uni-dimensional, this condition requires that the feed-through term from w to y, and u to z, is non-zero. As the performance signal z already contains a direct weighting on the control signal V_z, the only condition not met is that on D_{21}. To overcome this problem, for the purpose of controller synthesis, we include an artificial feed-through term D_{21}. We now have two design parameters: k_u and D_{21}. These were chosen to be 0.1 and 1 respectively. Our experience indicates that both parameters tend to have a similar effect on the controller bandwidth and closed-loop performance. As either is decreased, the controller bandwidth and closed-loop damping increases.

The electrical shunt impedance of the resulting $\mathcal{H}_2$ controller is shown in Figure 5.28. Unlike the complex impedance of the LQR controller shown in Figure 5.24, the $\mathcal{H}_2$ impedance shows a closer resemblance to the ideal negative inductor-resistor over a wide frequency band. Under the same test conditions as discussed in Section 5.4.3, the resulting damp-
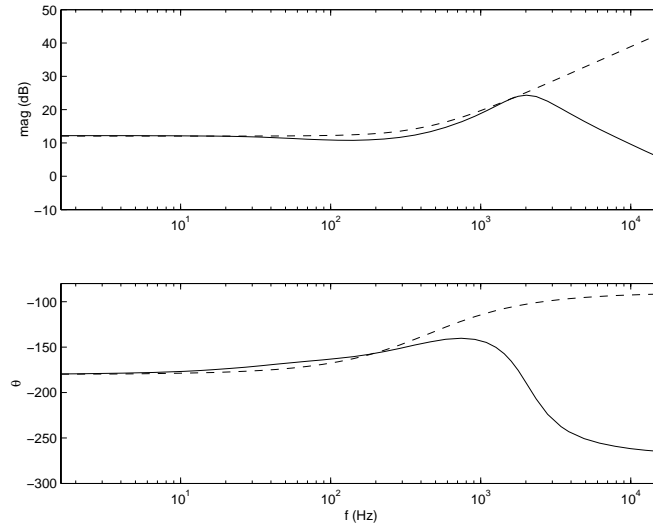
Figure 5.28: Complex impedance of the $\mathcal{H}_2$ (—) and ideal negative inductor-resistor controller (- -).

ing performance of the $\mathcal{H}_2$ controller is illustrated by the closed-loop frequency response, step response, and pole locations shown in Figures 5.29, 5.30, and 5.31 respectively. The damping performance of the $\mathcal{H}_2$ controller, measured to be 19.25 dB, is slightly inferior to that obtained for the LQR controller in Section 5.4.3. One of the characteristics of the $\mathcal{H}_2$ controller was that it resulted in a bandwidth greater than the LQR controller designed to obtain a similar performance. The poor correlation with the simulated response may be attributable to the problems involved in implementing such a high bandwidth controller. For real-time implementation using the Runge-Kutta analog solver, the sampling delay associated with analog to digital conversion and *vice versa* results in a significant unmodeled phase delay at frequencies approaching to the Nyquist rate. In addition, at such frequencies, the actual impedance presented to the coil is a series concatenation of the implemented transfer function and the high frequency low-pass dynamics of the power amplifier.
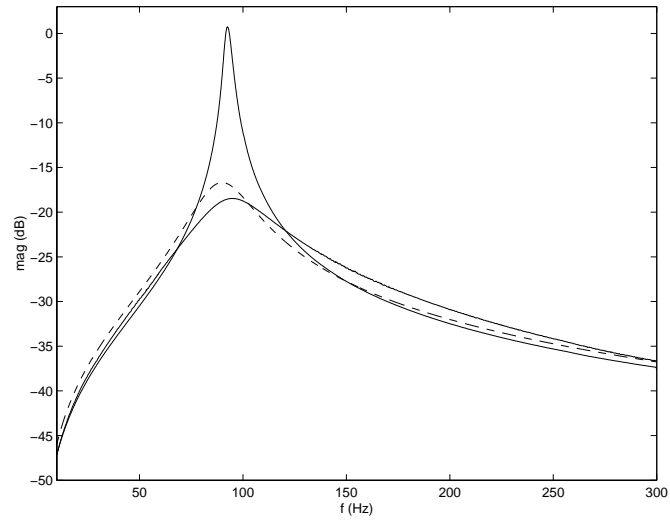
Figure 5.29: The experimental (—) and simulated (- -), open- and closed-loop frequency responses from an applied disturbance current I_1 (A) to the resulting plunger velocity ν (ms^{-1}) for the $\mathcal{H}_2$ impedance controlled system. The open-loop frequency response is also shown (—).
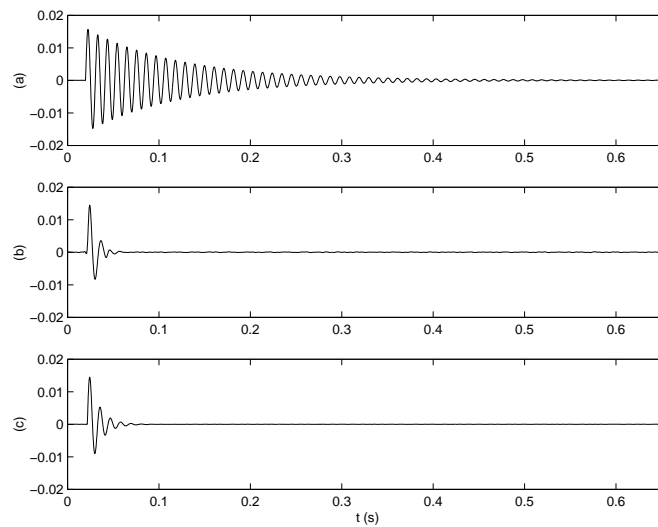
Figure 5.30: Velocity response ν (ms^{-1}) of the $\mathcal{H}_2$ impedance controlled system to a step disturbance current I_1. (a) experimental open-loop, (b) closed-loop (b), and (c) simulated closed-loop.
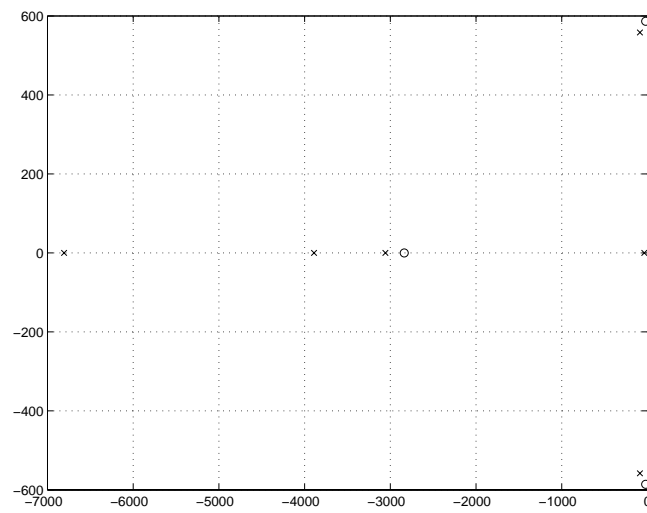
Figure 5.31: The open- (○) and closed-loop (×) pole locations of the $\mathcal{H}_2$ impedance controlled system.
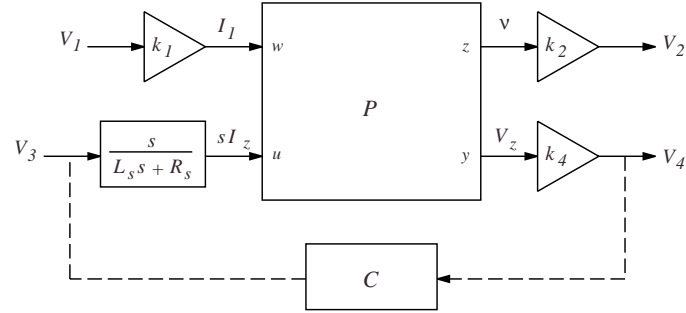
Figure 5.32: Open-loop external gains for the shunt current controlled electro-magnetic system.

5.4.4 Admittance Synthesis

Figure 5.32 shows the instrumentation and driver gains associated with the underlying electromechanical system. The voltages V_1 through V_4 represent the signals applied to, or measured from the power amplifier and instrumentation. The gain and units associated with each signal can be found in Table 5.3. The actual electrical shunt admittance presented to the coil is related to the controller designed for such a system through the gain k_4 and the dynamics of the current fluxion amplifier. It can be shown that,

$$Y_c(s) = \frac{I_z(s)}{V_z(s)} = \frac{1}{L_s s + R_s} C(s) k_4. \tag{5.43}$$

The controller $C(s)$ can be likened to the approximation of an admittance derivative, i.e.

$$C(s) \approx \frac{s L_s Y_c(s)}{k_4}. \tag{5.44}$$

In this section, rather than considering only the physical variables such as current, voltage, and velocity *etc.*, we now consider the reference current fluxion $V_3(s)$, in preference to $I_z(s)$. The magnitude and phase frequency responses are shown respectively in Figures 5.33 and 5.34. In the frequency domain, a good correlation can be observed between the analytic model and measured system.

Gain	Value
k_1	1 A/V
k_2	40 V/ms^{-1}
L_s	466 μH
R_s	1.1065 Ω
k_4	1.77 V/V

Table 5.3: External gains associated with the shunt current controlled electromagnetic system.
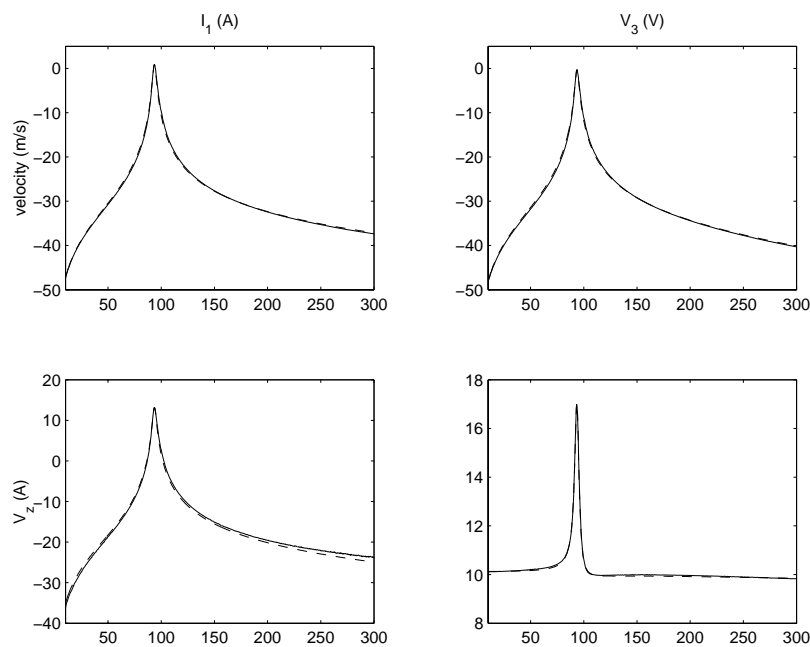
Figure 5.33: The simulated (—), and experimental (- -), magnitude frequency response (in decibels) of the shunt current controlled electromagnetic system.
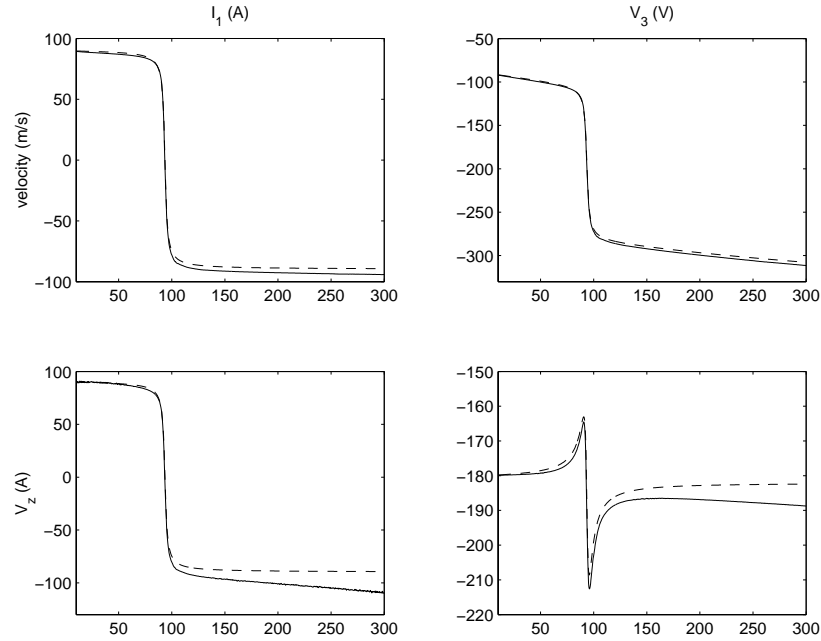
Figure 5.34: The simulated (—), and experimental (- -), phase frequency response (in degrees) of the shunt current controlled electromagnetic system.

LQR **Admittance Synthesis**

In analogy to Section 5.4.3, and as discussed in Section 5.3.4, a linear quadratic regulator can be designed to command the shunt current fluxion V_3 and hence the current I_z. Although V_z now appears as an output, it remains in our interest to weight this signal as a component of the performance objective. The connection of the coil and amplifier discussed in Section 5.4.2 has an operational range constrained only by the magnitude of the output voltage.

Based on the physical model (including external gains) that was validated in the previous sub-section, an LQR gain matrix was designed to minimize the following performance function,

$$J = \int_{-\infty}^{\infty} \left[(k_2 \nu(t))^2 + \left(\frac{k_y}{k_4} V_z(t) \right)^2 \right] \, dt, \tag{5.45}$$

where the factor k_y represents the relative weighting on the measured output voltage V_z. Even though the control and measurement variables differ from the impedance based

design in Section 5.4.3, the performance objective remains the same. In Section 5.3.4, equation (5.45) is cast as a standard LQR performance objective. Following the design of a gain matrix (for $k_y = 0.5$), an observer was designed following the same technique as in Section 5.4.3, the poles were chosen with a real component twice that of the closed-loop system poles.

The frequency response of the resulting LQR shunt admittance is shown in Figure 5.35. Like the $\mathcal{H}_2$ impedance designed and implemented in Section 5.4.3, the complex admittance of the LQR controller closely resembles that of the ideal negative inductor-resistor controller at low frequencies. As the frequency increases, the response can be likened to a small and decreasing negative real valued admittance.

The closed-loop response of the LQR controller shown in Figures 5.36 and 5.37 shows a significant peak damping of 20.6 dB, this closely resembles that predicted in simulation. The general coherence between the simulated and experimental results is likely due to the tendency of the LQR admittance to have a significantly lesser bandwidth than that experienced with the impedance controllers of Sections 5.4.3 and 5.4.3. As the admittance of the ideal negative inductor-resistor is low-pass compared to the impedance which has an infinite bandwidth, the characteristic of lesser control bandwidth when implementing an admittance follows naturally. In addition, the increase in relative dynamic range associated with the transfer function from V_3 to V_z contributes to a more accurate state estimate and better correlation with simulated results.

The simulated pole locations of the closed-loop system are shown in Figure 5.38. As expected, due to the explicit specification of observer poles, the closed-loop pole-zero maps for both the LQR admittance and impedance controlled systems are extremely similar.
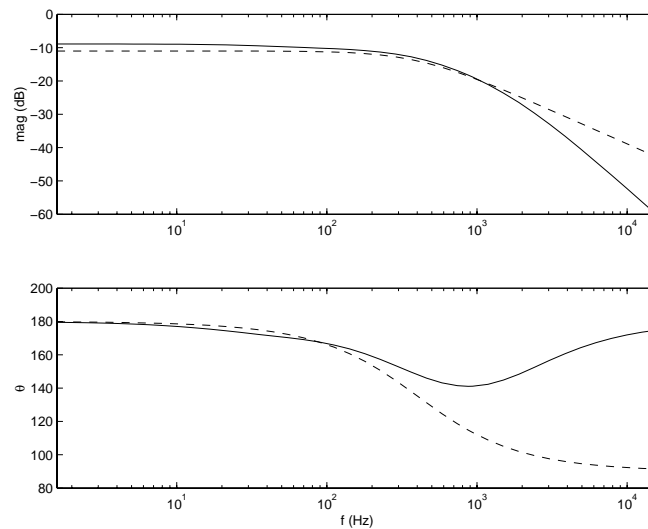
Figure 5.35: Complex admittance of the LQR (—) and ideal negative inductor-resistor controller (- -).
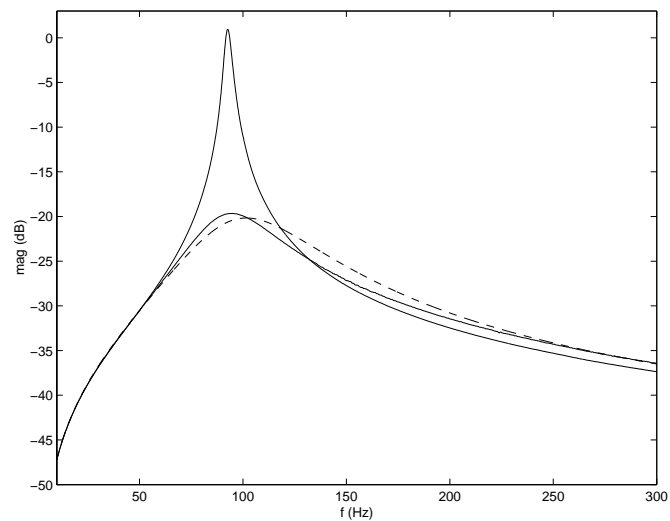
Figure 5.36: The experimental (—) and simulated (- -), open- and closed-loop frequency responses from an applied disturbance current I_1 (A) to the resulting plunger velocity ν (ms^{-1}) for the LQR admittance controlled system. The open-loop frequency response is also shown (—).
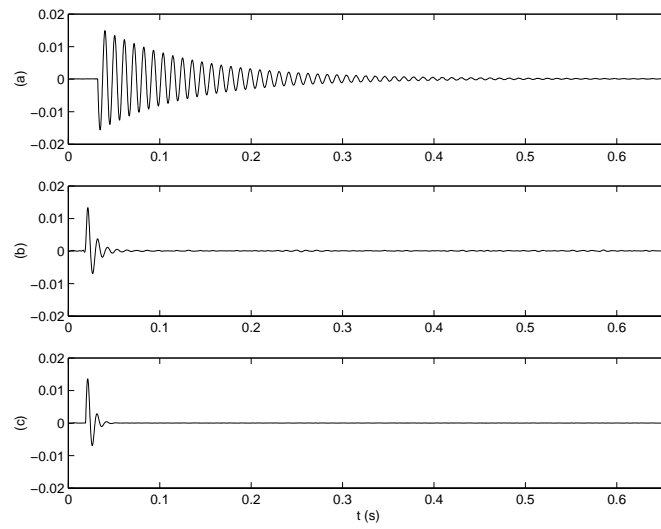
Figure 5.37: Velocity response ν (ms^{-1}) of the LQR admittance controlled system to a step disturbance current I_1. (a) experimental open-loop, (b) closed-loop (b), and (c) simulated closed-loop.
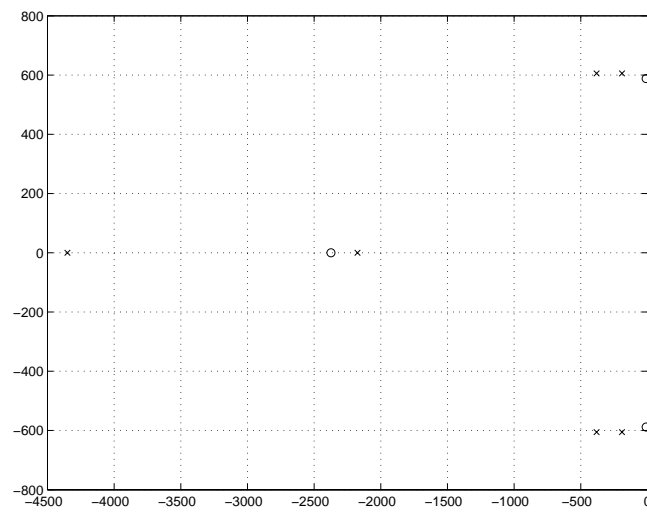
Figure 5.38: The open-($\bigcirc$) and closed-loop ($\times$) pole locations of the LQR admittance controlled system.

$\mathcal{H}_2$ Admittance Synthesis

This sub-section documents the implementation of an active shunt admittance designed to minimize the $\mathcal{H}_2$ norm of the transfer function from a disturbance current I_1 to a performance signal z. In analogy to LQR admittance design, the $\mathcal{H}_2$ performance function remains unchanged from $\mathcal{H}_2$ impedance synthesis. i.e.

$$J = \left\| \frac{k_2 \nu(s) + \frac{k_y}{k_3} V_z(s)}{I_1(s)/k_1} \right\|_2, \tag{5.46}$$

where k_y is the weighting on V_z.

Again, for the plant under consideration, the $\mathcal{H}_2$ problem is well defined and feasible. All of the standard requirements are met, i.e. the plant is minimal, proper, controllable, observable, and of finite dimension. However, in order to find a solution using existing tools, i.e. the algebraic Riccati solution implemented by the μ-Synthesis Toolbox for Matlab$^©$, the system must meet some additional requirements. The most problematic of these requirements is the requisite full rank condition on the standard plant matrices D_{21} and D_{12}. In this case, where each of the signals w, u, y, and z are uni-dimensional, this condition requires that the feed-through term from w to y, and u to z, is non-zero. As both of the plant outputs already contain a direct feed-through from V_3, (due to the existence of k_y), the only condition not met is that on D_{21}. To overcome this problem, for the purpose of controller synthesis, we include an artificial feed-through term D_{21}. We now have two design parameters: k_y and D_{21}. These were chosen to be 0.17 and 0.6 respectively.

The electrical shunt impedance of the resulting $\mathcal{H}_2$ controller is shown in Figure 5.39. The damping performance of the $\mathcal{H}_2$ controller is assessed from the closed-loop frequency response, step response, and pole locations, as shown in Figures 5.40, 5.41, and 5.38 respectively. Attenuation of the resonant peak was measured to be 19.65 dB.
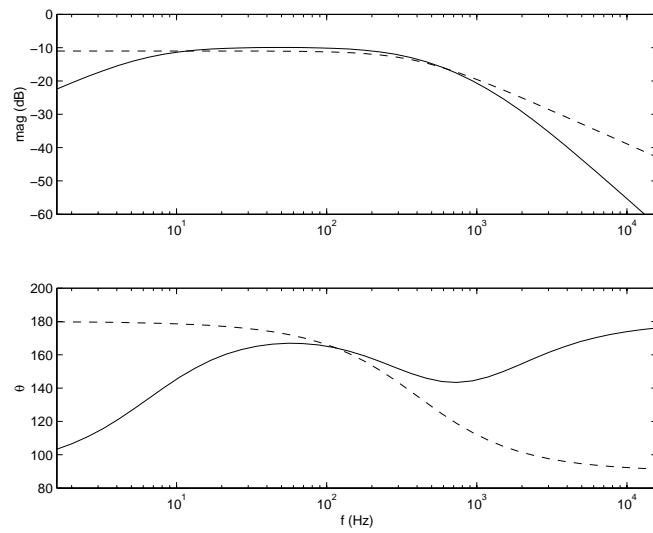
Figure 5.39: Complex admittance of the $\mathcal{H}_2$ (—) and ideal negative inductor-resistor controller (- -).
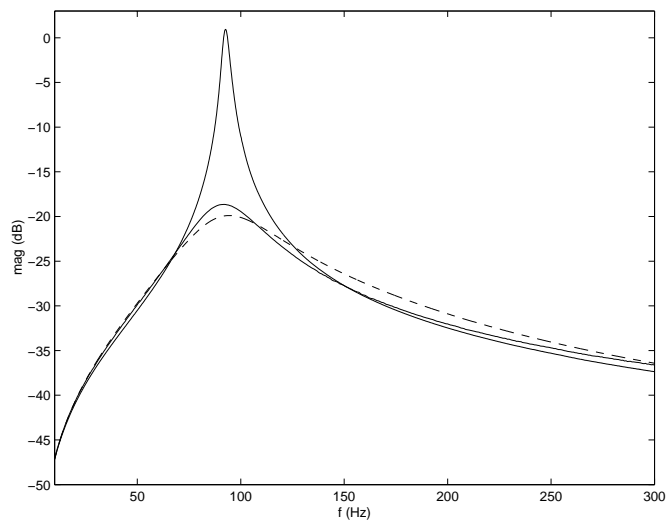
Figure 5.40: The experimental (—) and simulated (- -), open- and closed-loop frequency responses from an applied disturbance current I_1 (A) to the resulting plunger velocity ν (ms^{-1}) for the $\mathcal{H}_2$ admittance controlled system. The open-loop frequency response is also shown (—).
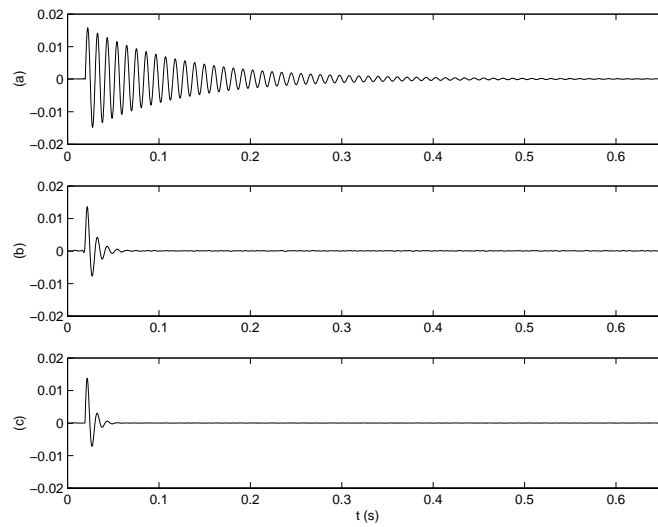
Figure 5.41: Velocity response ν (ms^{-1}) of the $\mathcal{H}_2$ admittance controlled system to a step disturbance current I_1. (a) experimental open-loop, (b) closed-loop (b), and (c) simulated closed-loop.
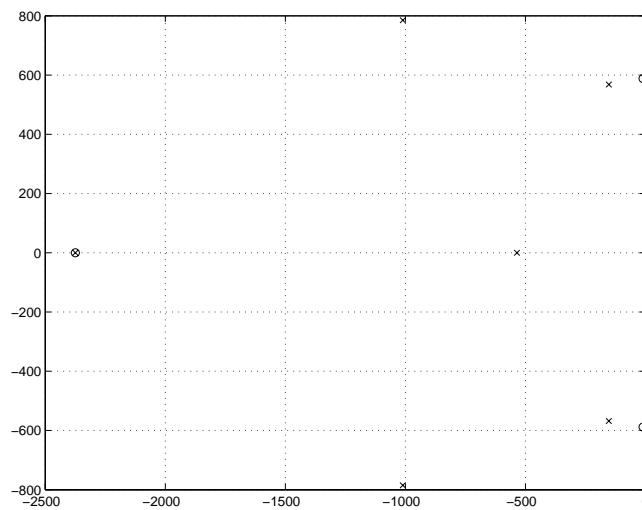
Figure 5.42: The open- ($\bigcirc$) and closed-loop ($\times$) pole locations of the $\mathcal{H}_2$ admittance controlled system.

5.4.5   Discussion

For the practitioner, when confronted with the various options for shunt control of an electromagnetic system, the obvious questions are: "which is the easiest to implement ?", and "which provides the best performance ?". Although there is of course no general answer to either of these questions, we wish to highlight some important characteristics raised throughout this chapter. All of the synthesized LQR and $\mathcal{H}_2$ controllers tend to resemble the complex impedance of an ideal negative inductor-resistor over some frequency band. Correspondingly, and as it occurs in practice, the impedance based controllers tend to be of a higher bandwidth and more difficult to implement. Thus, the technique of shunt admittance control is recommended. To this end, a current fluxion amplifier is required. Although such a device is no more difficult to construct than a typical voltage feedback amplifier, at present, they are commercially unavailable.

As there is no direct measurement of the plunger velocity, one would expect the performance of a shunt controlled system to be lesser than a fully instrumented active feedback system. Better performance is typically obtained for systems with a large dynamic range in the transfer function from an applied control signal to the measured variable. Work is continuing on the design of transducers with strong electromagnetic coupling coefficients, and hence, a greater dynamic range in the impedance transfer function.

Another issue associated with electromagnetic shunt control is that of negative reactive components. All of the impedance and admittance transfer functions contained right-half plane poles. Such an impedance can only be represented by a circuit comprising at least one of: negative resistors, negative capacitors, or negative inductors. Although the connection of the coil and control impedance is stable, an inherently stable controller is desirable.

5.5   Conclusions

Electromagnetic transducers have been employed extensively in active vibration control systems as force actuators, velocity sensors, or both. Compared to other transducers such

as piezoelectric materials and shape memory alloys, their large stroke, physical robustness, high bandwidth, and low-cost render them useful in a wide range of applications.

The connection of an electrical impedance or admittance to the terminals of an electromagnetic coil is equivalent to implementing a standard feedback controller around the mechanical system. By revealing the underlying feedback structure and casting it as a typical MIMO control problem, an impedance or admittance can be found that minimizes some arbitrary performance objective.

No external sensor is required to implement the control loop. This significantly reduces the cost, complexity, and sensitivity to transducer failure that in many applications, may preclude the use of an active control system.

The presented techniques are successfully applied to the design and implementation of an LQR and $\mathcal{H}_2$ based, active impedance and admittance controller. Without the need for any external sensors, the resonant peak of an experimental single-degree-of-freedom system was substantially reduced in magnitude by up to 20.6 dB.

Current and future work involves both the exploration of additional applications and development of the control theory associated with the synthesis step. A priority is the inclusion of uncertainty in the mechanical plant model with consideration during the synthesis process to achieve robust stability and performance objectives. For practical reasons it may also be desirable to enforce strictly-positive-realness (passivity) on the synthesis result. It is expected that without negative reactive components the achievable performance will be somewhat lesser.

SPATIAL SYSTEM IDENTIFICATION

In the analysis and control of distributed parameter systems it is of great benefit to possess a spatial model. That is, a model that describes system dynamics over an entire spatial domain. This chapter is concerned with the spatial system identification of flexible structures.

6.1   Introduction

The motivation for finding a spatial model lies in both the fields of analysis and synthesis. During analysis the user may simply wish to observe the mode shapes of the structure, or in a more complete utilization of the model, mathematically estimate the spatial feedback control performance of a system utilizing discrete sensors, actuators, and control objectives. For example, consider reference [52] where a standard H_∞ controller [109, 130] is designed to minimize vibration at a single point on a piezoelectric laminate simply supported beam. A spatial model is required to analyze the overall performance of such a controller. The fact that a point-wise controller is shown to provide good local performance but poor spatial performance leads us to the primary application of spatial models - spatial controller synthesis. A number of standard control synthesis variants have emerged that address the control design of spatially distributed systems with discrete sensors and actuators. Recent examples include: spatial feed forward control [90], spatial resonant control [51], spatial H_2 control [53], and spatial H_∞ control [52].

The modal analysis procedure has been used extensively throughout the literature for

obtaining spatial models of structural [85, 41] and acoustic systems [55]. Its major disadvantage is the requirement for detailed physical information regarding the sensors, actuators, and underlying mechanical system. Practical application typically involves the use of experimental data and a non-linear optimization to identify unknown parameters, such as modal amplitudes, resonance frequencies and damping ratios. Even in this case, the descriptive partial differential equations must still be solved (as functions of the unknown parameters) to obtain the mode shapes. This may be difficult or impossible for realistic structural or acoustic systems with complicated boundary conditions.

Another popular technique for obtaining spatial models is that of finite element (FE) analysis [26]. This is an approximate method that results in high order spatially discrete models. If the dynamics of sensors and actuators are known, the integrated model can be cast in a state-space form to facilitate control design and analysis [75]. The approximate nature of finite element modeling eliminates the need for solving descriptive partial differential equations. Detailed information regarding the structures' material properties and boundary conditions is still required. As with the modal analysis procedure, FE models are usually tuned with experimental data [35].

A considerable literature has also developed on the topic of *Experimental Modal Analysis*, (see [79] for a compilation of such methods). These methods can be predominantly described as frequency domain transfer function methods. The system is assumed to consist solely of parallel second order resonant sections. Sensor, actuator, and additional non-modal dynamics are neglected. One of the most popular methods, widely used in commercial frequency domain modal analysis packages, is the rational fraction polynomial method [79]. As a transfer function method, the model is poorly conditioned, incorrectly describes the system zero dynamics [92], and neglects non-modal dynamics.

All of the mentioned experimental modal analysis techniques neglect the fundamental limitations in spatial sampling, i.e. the reconstructed mode shapes can be distorted due to violation of the Nyquist criterion spatially in one or two dimensions.

This chapter introduces an efficient and correct method for identifying the above class of systems directly from measured frequency response data.

6.2 Modeling

The Lagrangian/modal expansion, or Ritz-Kantorovitch method [85], is commonly used to express the spatial deflection of a distributed parameter system as an infinite summation of modes. The modes are a product of two functions, one of the spatial co-ordinate vector $\mathbf{r}$, and another of the temporal t,

$$d\left(\mathbf{r}, t\right) = \sum_{i=1}^{\infty} q_i\left(t\right) \phi_i\left(\mathbf{r}\right), \tag{6.1}$$

where the $q_i(t)$s are the modal displacements, the $\phi_i\left(\mathbf{r}\right)$s are the system eigenfunctions, $d\left(\mathbf{r}, t\right)$ is the displacement at a point, and $\mathbf{r} \in \mathcal{R}$ is a co-ordinate vector on the spatial domain $\mathcal{R}$. The mode shapes $\phi_i(\mathbf{r})$ must form a complete coordinate basis for the system, satisfy the geometric boundary conditions, and for analytic analysis be differentiable over the spatial domain to at least the degree required by the describing partial differential equations. Many practical systems also obey certain orthogonality conditions.

As discussed in [85] the model (6.1) can also be expressed in the frequency domain as

$$G_y\left(\mathbf{r}, s\right) = \sum_{i=1}^{\infty} \frac{F_i \phi_i\left(\mathbf{r}\right)}{s^2 + 2\zeta_i \omega_i s + \omega_i^2}, \tag{6.2}$$

where $G_y(\mathbf{r}, s)$ is the transfer function from an external force, or for the system considered in this chapter, the applied piezoelectric voltage to the displacement at a point $\mathbf{r}$.

For practical reasons, (6.2) is often truncated to include only a certain number of modes that approximate the response over a limited bandwidth. Reference [92] introduces a model reduction technique for systems that satisfy certain modal orthogonality conditions. The following truncated model structure is proposed,

$$\widetilde{G}_y\left(\mathbf{r}, s\right) = \sum_{i=1}^{N} \frac{F_i \phi_i\left(\mathbf{r}\right)}{s^2 + 2\zeta_i \omega_i s + \omega_i^2} + \sum_{i=N+1}^{\infty} k_i \phi_i\left(\mathbf{r}\right), \tag{6.3}$$

where, (referring to [92]), the k_i terms are found by minimizing the spatial $\mathcal{H}_2$ norm of the resulting error system, (ω_c is the retained bandwidth),

$$k_i = \frac{F_i}{2\omega_c \omega_i} \ln\left(\frac{\omega_i + \omega_c}{\omega_i - \omega_c}\right). \tag{6.4}$$

We define the model of a general single input spatially distributed system as

$$\widehat{G}_y\left(\mathbf{r}, s\right) = H\left(s\right)\left[\sum_{i=1}^{N} \frac{\Phi_i\left(\mathbf{r}\right)}{s^2 + 2\zeta_i\omega_i s + \omega_i^2} + D\left(\mathbf{r}\right)\right], \tag{6.5}$$

where $H(s)$ is the concatenation of all non-distributed transfer functions, $\Phi_i(\mathbf{r})$ is the ith mode shape incorporating the modal gain F_i, and $D(\mathbf{r})$ is the feed-through function included to compensate for all higher order truncated contributions to zero dynamics. The filter $H(s)$ is used to model the additional dynamics of sensors, actuators, and for example, anti-aliasing filters. In this work $H(s)$ is not identified automatically.

The objective will be to identify the parameters $\theta = \left[\begin{array}{cccc} \Phi_i(\mathbf{r}) & D(\mathbf{r}) & \zeta_i & \omega_i \end{array}\right]$ from a number of measured spatially distributed point-wise frequency responses,

$$G_y\left(j\omega, \mathbf{r}\right) \qquad \begin{array}{l} \mathbf{r} \in \{\mathbf{r}_1, \dots, \mathbf{r}_{N_r}\} \in \mathcal{R} \\ \omega \in \{\omega_1, \dots, \omega_{N_\omega}\}, \end{array} \tag{6.6}$$

where N_r is the number of measured spatial locations and N_ω is the number of measured frequency points per location.

The system (6.5) has a corresponding state space representation:

$$\dot{\mathbf{x}}(t) = \mathbf{A}\mathbf{x}(t) + \mathbf{B}u(t) \tag{6.7}$$

$$d(\mathbf{r}, t) = \mathbf{C}(\mathbf{r})\mathbf{x}(t) + D(\mathbf{r})u(t),$$

where $\mathbf{C}(\mathbf{r}) = \left[\begin{array}{ccccc} \Phi_i(\mathbf{r}) & 0 & \cdots & \Phi_N(\mathbf{r}) & 0 \end{array}\right]$, $\mathbf{B} = \left[\begin{array}{ccccc} 0 & 1 & \cdots & 0 & 1 \end{array}\right]^T$, $D(\mathbf{r})$ is a scalar function of $\mathbf{r}$, N is the number of modes to be identified, and

$$\mathbf{A} = \left[\begin{array}{cccc} 0 & 1 & 0 & 0 \\ -\omega_1^2 & -2\zeta_1\omega_1 & 0 & 0 \\ & & \ddots & \\ 0 & 0 & 0 & 1 \\ 0 & 0 & -\omega_N^2 & -2\zeta_N\omega_N \end{array}\right] \in \mathbf{R}^{2N \times 2N}. \tag{6.8}$$

6.3   Spatial Sampling

Considering the model structure (6.5), the spatial functions $\Phi_i(\mathbf{r})$ and $D(\mathbf{r})$ must be reconstructed from their identified samples. For a uniformly sampled one-dimensional system,

the samples of our continuous functions $\Phi_i(\mathbf{r})$ and $D(\mathbf{r})$ are

$$\begin{aligned}
\Phi_i(r) & \qquad r = n\,\Delta r \in \mathcal{R} \\
D(r) & \qquad n \in \{0, 1, ..., N_r\},
\end{aligned} \tag{6.9}$$

where the scalar r specifically denotes a one-dimensional system and Δr is the spatial sampling interval.

There are a number of options available for reconstructing the continuous functions, two of which are traditional linear reconstruction and spline reconstruction. The following two subsections, 6.3.1 and 6.3.2, examine the application of each technique to the two cases of band-limited and non-band-limited functions. The aim is to quantify the expected mean square difference between the original continuous function and its corresponding reconstruction. This will allow us to evaluate the required spatial sampling interval as a function of the permissible error. An example of this procedure is performed for a simply supported beam in Section 6.3.3.

6.3.1 Whittaker-Shannon Reconstruction

The discrete magnitude spectra of a band-limited spatial function $f(r)$ is shown in Figure 6.1. To satisfy the Nyquist sampling criterion, the spatial sampling frequency $\frac{2\pi}{\Delta r}$ (in $\frac{rad}{m}$) must be greater than twice the highest frequency component of $f(r)$ [63]. Shannon's Reconstruction Theorem states that $f(r)$ can be reconstructed from its samples,

$$f(r) = \Delta r \sum_{k=-\infty}^{\infty} f(k\Delta r) \frac{\sin\left(\frac{\pi}{\Delta r}(r - k\Delta r)\right)}{\pi(r - k\Delta r)}. \tag{6.10}$$

Theoretically, a perfect reconstruction is possible, however, in practice, there are two significant sources of degradation:

1. For finite time signals, truncating the summation (6.10) introduces a systematic *truncation error*. Expressions for bounding the truncation error and references to relevant work can be found in [63].

2. In many practical situations the samples will also contain an additive stochastic disturbance. An expression for the mean integral squared reconstruction error (MISE)
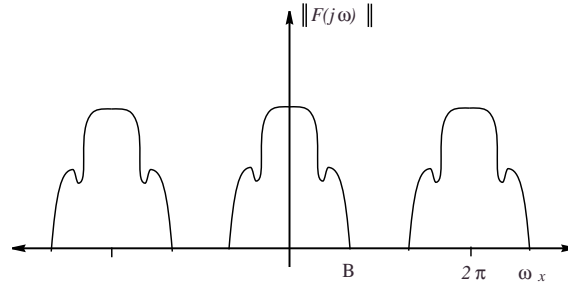
Figure 6.1: Discrete magnitude spectra of an over sampled band-limited function.

experienced when recovering a signal from its corrupted samples can be found in [98]. It is also shown that Shannon reconstruction is not a consistent estimator for band-limited signals recovered from noisy samples, i.e. as the number of signal samples approaches ∞, the MISE does not approach zero, in fact the error diverges and also approaches ∞. Convergent estimators for such scenarios can be found in [99] and [70].

In general, the spatial function $f(r)$ will not be band-limited. Examples include but are not limited to, the mode shapes of a cantilever beam [41], and the feed-through function for a simply supported beam [92]. Since the samples are obtained indirectly from point-wise frequency response data, no form of low-pass filtering is possible. The objective of the following will be to quantify the under-sampling error as a function of the spatial sampling interval.

In their paper reviewing sources of error in linear reconstruction, Thomas and Liu [111] present an expression for the mean square reconstruction error as a function of the power spectral density outside the Nyquist range. The following expression assumes an absence of the optimal low-pass filter, which in our application, cannot be applied to the continuous signal,

$$||f(r) - Q^s\ f(r)||_2 = \left[\frac{1}{\pi} \int_{|\omega_r| > \frac{\pi}{\Delta r}} |F(j\omega_r)|^2\ d\omega_r \right]^{\frac{1}{2}}, \tag{6.11}$$

where $Q^s f(r)$ is the Shannon representation of the sampled function, ω_r is the spatial

frequency in radians per meter and $|F(j\omega_r)|^2$ is the power spectral density of $f(r)$. In the case where the optimal pre-filter can be applied, the RHS[1] of equation 6.11 is reduced by one half.

6.3.2 Spline Reconstruction

In recent years, splines have been recognized for their usefulness in curve and surface fitting problems [71, 112]. A function $f(r)$ can be approximately reconstructed from a spline basis $\varphi(r)$, with coefficients $c(k)$ derived from $f(k\Delta r)$,

$$\overset{sp}{Q^n} f(r) = \sum_{k \in Z} c(k)\varphi^n(\frac{r}{\Delta r} - k), \qquad (6.12)$$

where $c(k) \in l_2$ are the (finite square summable) spline coefficients, $\overset{sp}{Q^n} f(r)$ is the spline reconstruction of $f(r)$ and $\varphi^n(r)$ is the spline generating function. We will limit our choice of generating functions to the nth degree β-splines (of order $n + 1$) [112]. The condition $c(k) \in l_2$ ensures that $\overset{sp}{Q^n} f(r)$ is a well-defined subspace of L_2, the set of square integrable functions, a considerably larger space than the traditional Shannon space of band-limited functions. References [113] and [59] present a unified sampling theory for a wide class of approximation operators. In likeness to the Shannon sampling theorem, the optimal spline reconstruction involves an optimal pre-filtering of the continuous signal before sampling and reconstruction by the chosen spline basis. The results in this area, including expressions for the root mean square (RMS) error, are summarized in [112]. The technique of quantitative Fourier analysis can be applied to quantify the RMS reconstruction error [16]. The sampling phase averaged error is given by,

$$\left\| f(r) - \overset{sp}{Q^n} f(r) \right\|_2 = \left[\frac{1}{2\pi} \int_{-\infty}^{\infty} |F(j\omega_r)|^2 E^n(\Delta r\ \omega_r)\ d\omega_r \right]^{\frac{1}{2}}, \qquad (6.13)$$

where $E^n(\Delta r\ \omega_r)$ is defined as the frequency error kernel parameterized by the interpolant and Δr. Analytic expressions for $E^n(\Delta r\ \omega_r)$ have been given for the β-splines of order up to 6 [16].

In our application where there is no access to the continuous signal, we cannot apply the optimal pre-filter nor achieve the optimal (least squares) fit by projecting our signal onto

---

[1]The part of an equation on the right hand side of the equals sign.

the approximation space [112]. Instead, we shall simply perform an interpolation. The penalty in doing so is illustrated in Figure 6.2, where the error kernels $E^n(\omega_r)$ for spline and Shannon reconstruction, optimal and interpolation, are shown for $\Delta r = 1$. It can be observed that although the spline interpolant error is globally greater than that of the projector, within the Nyquist range $|\omega_r| < \pi$ the difference is slight. In analogy to Shannon reconstruction, for frequencies beyond the Nyquist rate, the magnitude of the spline interpolant error kernel approaches twice that of the projector.

The spline basis functions also have some interesting variational properties. It is well known that interpolation by the Shannon basis functions in the presence of truncation error and/or sample noise, tends to result in an overly 'peaky' or oscillatory reconstruction. In contrast, spline interpolation is the interpolant that oscillates the least (in a certain sense [105, 112]). Cubic splines are a special case, these interpolants minimize the 2-norm of the error's second derivative and hence possess the property of minimum curvature [112]. As this property is also shared by constrained thin elastic beams and plates, it is natural to reason that cubic splines may be well suited to approximating mechanical functions, such as the mode shapes of a simply-supported beam.

In the case of noisy samples, we can achieve some degree of immunity by relaxing the interpolation condition and imposing a smoothness constraint, i.e. for the cubic splines, by minimizing

$$\sum_k \left(f(k\Delta r) - \overset{sp}{Q^n} f(k\Delta r) \right)^2 + \lambda \int_0^L \left(\frac{d^2 \overset{sp}{Q^n} f(r)}{dr^2} \right)^2, \tag{6.14}$$

where the second term is a measure of the smoothness. The parameter λ is based on the additive noise variance [112].

6.3.3   Spatial Sampling of a Simply-supported Beam

This chapter demonstrates how the results presented in Section 6.3.2 can be applied to spatial systems. We present an example analysis for the simply-supported beam described in Section 3.3.5. The objective is to arrive at a point where Equations (6.11) and (6.13) can be applied. Both expressions require only the function's power spectral density.
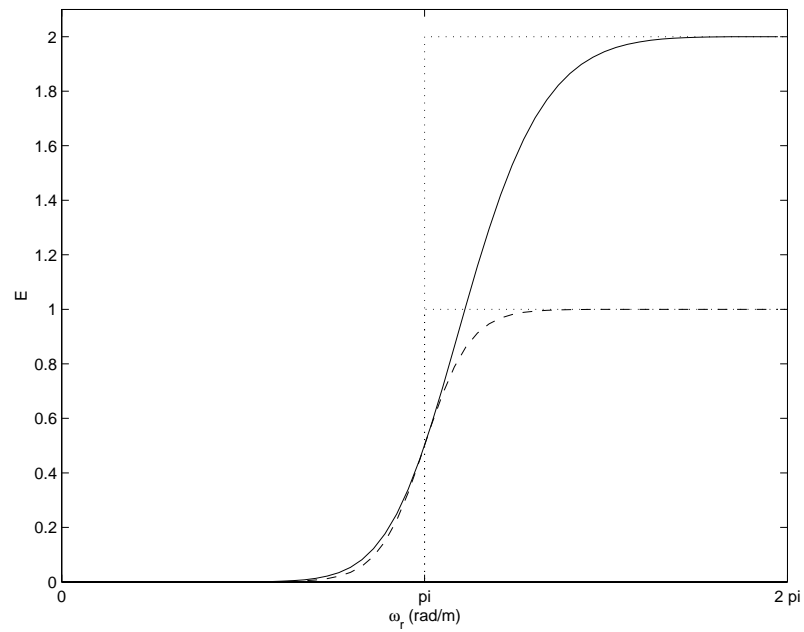
Figure 6.2: Unit sampled, cubic spline error kernels. Optimal (with pre-filter) (- -), interpolation (—). Shannon reconstruction ($\cdots$) $E(|\omega| > \pi) = 1$, interpolation ($\cdots$) $E(|\omega| > \pi) = 2$.

Mode Shapes

The mode shapes of a simply-supported beam are given by [85],

$$\phi_i(r) = \sqrt{\frac{2}{\rho A_r L}} \sin\left(\frac{i\pi r}{L}\right) \tag{6.15}$$

$$= \alpha \sin\left(\frac{i\pi r}{L}\right), \tag{6.16}$$

where ρ is the material density, A_r is the cross-sectional area and L is the length of the beam. The spatial spectra of $\sum_{i=1}^{N} \phi_i(r)$ is impulsive and can be easily determined,

$$\mathcal{F}\left\{\sum_{i=1}^{N} \phi_i(r)\right\} = j\pi\sqrt{\frac{2}{\rho A_r L}} \sum_{i=1}^{N} \left[\delta(\omega_r + \frac{i\pi}{L}) - \delta(\omega_r - \frac{i\pi}{L})\right]. \tag{6.17}$$

The highest frequency component of $\phi_i(r)$, $i \in \{1, \ldots, N\}$ is $\frac{N\pi}{L}$. Thus, if we were to apply Shannon's Theorem[2] to reconstruct N mode shapes of a simply-supported beam,

$$\frac{2\pi}{\Delta r} > 2\frac{N\pi}{L}, \tag{6.18}$$

that is,

$$\Delta r < \frac{L}{N}. \tag{6.19}$$

This simple and complete result applies in general to a sub-class of the systems (6.2). Such systems are characterized by sinusoidal mode shapes. Examples include uniform beams and strings in one dimension, plates in two dimensions and closed acoustic systems in three dimensions.

The Feed-through Function $D(r)$

The feed-through function $D(r)$ can be found analytically for systems of the form (6.2),

$$D(r) = \sum_{i=N+1}^{\infty} k_i \phi_i(r), \tag{6.20}$$

where $\phi_i(r)$ is given by (6.15) and k_i is given by (6.4). We can think of (6.20) as being equivalent to the Fourier series,

$$D(r) = \sum_{i=-\infty}^{\infty} c_i e^{\frac{j 2\pi i r}{T_r}}, \tag{6.21}$$

---

[2]Neglecting truncation errors.

where $T_r = 2L$ is the period of repetition,

$$
c_i = \begin{cases}
\frac{j}{2}\alpha\frac{F_i}{2\omega_c\omega_i}\ln\left(\frac{\omega_i+\omega_c}{\omega_i-\omega_c}\right) & i \in \{\ldots, -N-2, -N-1\} \\
0 & i \in \{-N, \ldots, N\} \\
\frac{-j}{2}\alpha\frac{F_i}{2\omega_c\omega_i}\ln\left(\frac{\omega_i+\omega_c}{\omega_i-\omega_c}\right) & i \in \{N+1, N+2, \ldots\}\,.
\end{cases}
\tag{6.22}
$$

The complex coefficients c_i reveal the spatial Fourier transform of $D(r)$,

$$
\mathcal{F}\{D(r)\} = \mathcal{F}\left\{\sum_{i=N+1}^{\infty} k_i\phi_i(r)\right\}
\tag{6.23}
$$

$$
= \sum_{i=-\infty}^{\infty} 2\pi c_i\delta(\omega_r - i\omega_f),
\tag{6.24}
$$

where

$$
\omega_f = \frac{2\pi}{T_r} = \frac{\pi}{L}.
\tag{6.25}
$$

That is,

$$
\mathcal{F}\{D(r)\} = \sum_{i=-\infty}^{\infty} 2\pi c_i\delta(\omega_r - i\frac{\pi}{L}).
\tag{6.26}
$$

Immediately, by the properties of the Fourier transform, we learn some characteristics of the feed-through function $D(r)$.

1. As verification, $\mathcal{F}\{D(r)\} = d(j\omega_r) = d(-j\omega_r)^* \Leftrightarrow \text{Im}\{D(r)\} = 0$, which is known *a priori*. Also $\text{Re}\{d(j\omega_r)\} = 0$ and $|d(j\omega_r)|$ are even functions of ω_r [100] and $\text{Im}\{d(j\omega_r)\}$ is an odd function of ω_r [100].

2. Since $\mathcal{F}\{D(r)\}$ is purely imaginary, $D(r)$ is an odd function. It is true in general that $\text{Re}\{d(j\omega_r)\} = 0 \Leftrightarrow D(r) = -D(-r)$ [100].

3. $D(r)$ is periodic with period $2L$.

As $\mathcal{F}\{D(r)\}$ does not have compact support on the interval $(-j\infty, j\infty)$, $D(r)$ cannot be exactly reconstructed from any finite number of samples. It is also obvious from (6.26) that the spectra of $D(r)$ lies completely outside the bandwidth of the mode shapes, thus dictating the spatial sampling requirements of the system.

We can now apply Equation (6.13) to determine the required spatial sampling interval. For a periodic signal $g(r)$, the energy density per unit frequency is given by [36],

$$|G(f)|^2 = T \sum_{n \in Z} |c_n|^2 \, \delta(f - n\frac{1}{T}), \tag{6.27}$$

where T is the period, $G(f)$ denotes the Fourier transform and c_n are the Fourier coefficients of $g(r)$. By making a change of variables we can find the power spectral density of $D(r)$,

$$|\mathcal{F}\{D(r)\}|^2 = 2\pi T_r \sum_{i \in Z} |c_i|^2 \, \delta(\omega_r - i\frac{2\pi}{T_r}). \tag{6.28}$$

Hence, from equation (6.13), the error in reconstructing $D(r)$ from an nth order spline basis can be obtained,

$$\left\| D(r) - \overset{sp}{Q^n} \, D(r) \right\|_2 = \left[2L \int_{-\infty}^{\infty} \left(\sum_{i \in Z} |c_i|^2 \, \delta(\omega_r - i\frac{\pi}{L}) \right) \, E^n(\Delta r \, \omega_r) \, d\omega_r \right]^{\frac{1}{2}} \tag{6.29}$$

$$= \left[2L \sum_{i \in Z} |c_i|^2 \, E^n(i\pi\frac{\Delta r}{L}) \right]^{\frac{1}{2}}, \tag{6.30}$$

where $\overset{sp}{Q^n} \, D(r)$ is the spline reconstruction of $D(r)$. The error kernel for a cubic spline $E^3(i\pi\frac{\Delta r}{L})$ is plotted together with the equivalent Shannon kernel in Figure 6.2.

We can also apply Parseval's equality to find the mean square value of $D(r)$ over one period,

$$\sum_{i=-\infty}^{\infty} |c_i|^2 = \frac{1}{2L} \int_{-L}^{L} |D(r)|^2 \, dr. \tag{6.31}$$

We now consider a specific example: the simply-supported beam described in Section 3.3.5, where 3 modes are retained for identification. The feed-through function resulting from an analytic model [88] is shown in Figure 6.3. The RMS value of the reconstruction error (L_2 norm on $[-L, L]$) is plotted against the sampling interval Δr in Figure 6.4. As the sampling interval increases, the RMS error approaches the RMS value of the continuous function[3]. This plot can be used to select a spatial sampling interval that achieves some error specification on $D(r)$.

---

[3]In this analysis we have considered $D(r) \notin L_2$. This arises from the periodic nature of the mode shapes. When we refer to the RMS or mean square value of such signals, we are implicitly referring to the RMS or mean square value over a single period.
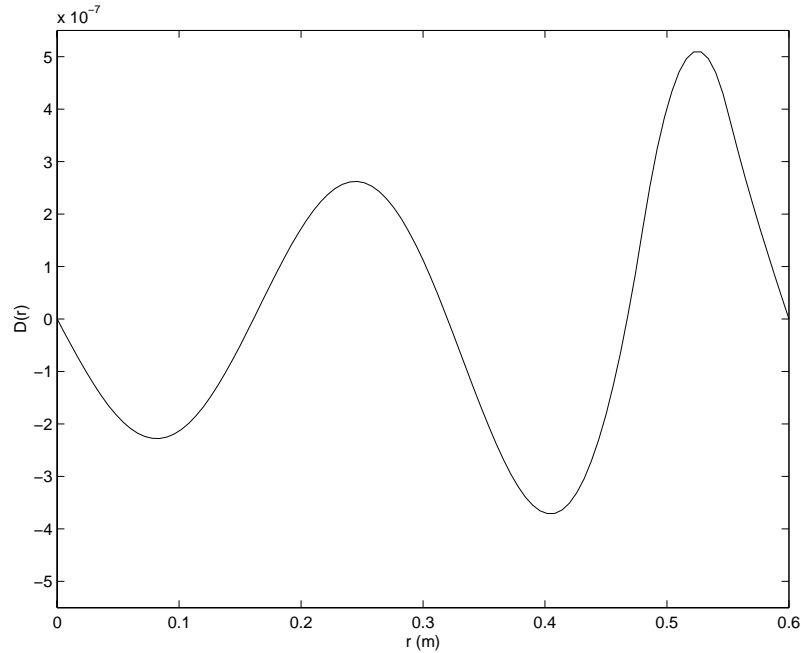
Figure 6.3: Analytic feed-through function for the beam described in Section 3.3.5/

Other Considerations

The above analysis has considered only a one-dimensional system. The Shannon sampling theorem is easily extended to multi-variate functions [63]. By using tensor-product basis functions, spline sampling theory is extended in a similar fashion [112]. Both techniques require an equidistant sampling grid and are based on the application of uni-variate results in each dimension. For irregular sampling and other complicated reconstructions (e.g. by blending functions [71], or finite element methods [71]) no such results are known.

In the previous subsection, i.e. Section 6.3.3, the sampling limitations for a simply supported beam were derived. Even when the mode shapes are known *a priori*, this analysis can be difficult to perform. For the practitioner, we offer a rough rule of thumb.

1. Estimate, by means of a similar system or finite element analysis, the highest significant spatial frequency component of the highest order mode to be identified.
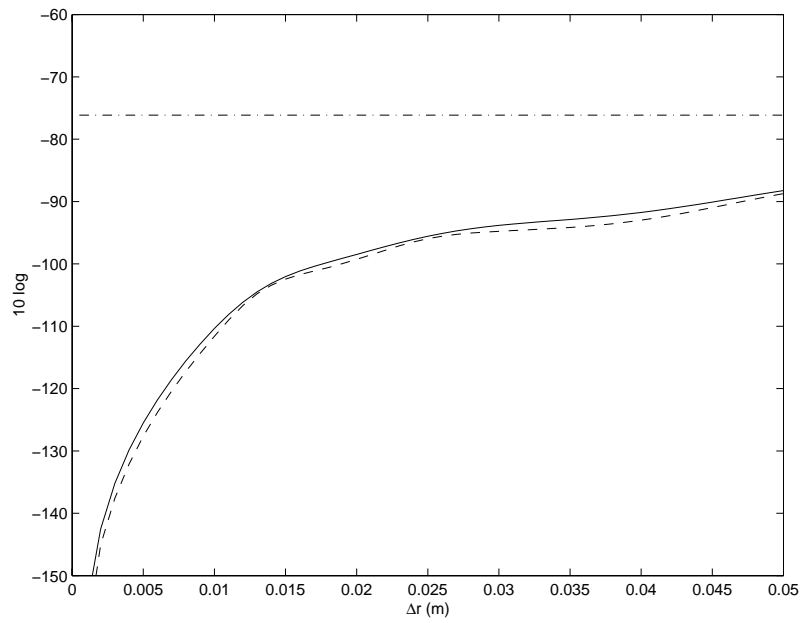
Figure 6.4: The RMS reconstruction error $||D(r) - Q^n\ D(r)||_2$ plotted against the spatial sampling interval Δr. (—) Optimal, (- -) Interpolation. The dashed-dot line indicates the RMS value of the function $D(r)$.

2. Consider the feed-through function $D(\mathbf{r})$. Assume that its highest significant frequency component is three times that estimated in step (1). (This step is suggested on the experience of studying and identifying a number of such systems).

3. Sample the structure as would be done in practice for a function with spatial bandwidth derived in step (2). Taking into consideration the limited domain of the structure, (allowing for truncation errors), this would normally be between 2 to 5 times the rate suggested by the Nyquist criterion.

6.4   Identifying the System Matrix

The first step in the identification procedure is to obtain an estimate for $\mathbf{A}$, the system matrix whose eigenvalues reveal the parallel dynamics of each mode. On first inspection, this problem may appear trivial as the transfer function obtained from a single frequency response would perform the task.

For spatially distributed systems we need to redefine our measures of model quality and stochastic performance. In essence, the two main sources of error in the identification arise from measurement noise and slight changes in system dynamics over the spatial domain. Intuitively, we would like to distribute the resulting model error in a similar, equally distributed fashion.

The problem can be cast as a MIMO system identification problem where each point is regarded as a single output. In the case of a two-dimensional system, where a large number of point-wise frequency response measurements are available, it may be necessary to limit the data space by selecting only a subset of the available points. The *virtual system* as seen by the system identification algorithm has a single input and $\widetilde{N}_r$ outputs, where $\widetilde{N}_r$ may be equal to N_r or less than N_r if the data set is to be truncated. The frequency response of such a system is similar to (6.6) and can be expressed as

$$G_y\left(j\omega, \mathbf{r}\right) \quad \begin{array}{l} \mathbf{r} \subset \{\mathbf{r}_1, \dots, \mathbf{r}_{N_r}\} \in \mathcal{R} \\[6pt] \omega \in \{\omega_1, \dots, \omega_{N_\omega}\}. \end{array} \tag{6.32}$$

For generality, we treat the identification algorithm as a general matrix function of the

data, i.e. $\mathbf{A} = f\left(G_y\left(j\omega, \mathbf{r}\right)\right).$

Methods that identify state space models by exploiting geometric properties of the input and output sequences are commonly known as subspace methods. These methods have received considerable attention in the literature, (see [117] for a survey of time domain methods). The reader is referred to [76] and [82] for a full discussion of frequency domain techniques. Frequency domain subspace-based algorithms have proven particularly useful for identifying high order multi-variable resonant systems [83]. In this chapter the algorithm introduced in [82] will be employed.

6.5 Identifying the Mode Shapes and Feed-through Function

Samples of the spatial modal and feed-through functions are first identified from the frequency response data and system matrix. The continuous functions are then approximated by linear or spline reconstruction.

6.5.1   Identifying the Samples

Samples of the spatial functions will now be identified from the available frequency response data. First, in order to simplify notation, we make a number of definitions.

The spatial response matrix is defined as

$$
\mathbf{G} = \begin{bmatrix}
G_y(j\omega_1, \mathbf{r}_1) & \cdots & G_y(j\omega_1, \mathbf{r}_{N_r}) \\
\vdots & \ddots & \vdots \\
G_y(j\omega_{N_\omega}, \mathbf{r}_1) & \cdots & G_y(j\omega_{N_\omega}, \mathbf{r}_{N_r})
\end{bmatrix} \in \mathbf{C}^{N_\omega \times N_r}. \tag{6.33}
$$

The dynamic response matrix is defined as

$$
\mathbf{P}^{tf} = \begin{bmatrix}
P_1^{-1}(j\omega_1) & \cdots & P_N^{-1}(j\omega_1) \\
\vdots & \ddots & \vdots \\
P_1^{-1}(j\omega_{N_\omega}) & \cdots & P_N^{-1}(j\omega_{N_\omega})
\end{bmatrix} \in \mathbf{C}^{N_\omega \times N}, \tag{6.34}
$$

where $P_i^{-1}(j\omega)$ is the response of the ith mode found from the system matrix $\mathbf{A}$

$$P_i^{-1}(j\omega) = \left. \frac{1}{[s + (\alpha_i + j\sigma_i)]\,[s + (\alpha_i - j\sigma_i)]} \right|_{s=j\omega}. \tag{6.35}$$

The modal function matrix is defined as

$$\Psi = \begin{bmatrix} \Phi_1(\mathbf{r}_1) & \cdots & \Phi_1(\mathbf{r}_{N_r}) \\ \vdots & \ddots & \vdots \\ \Phi_N(\mathbf{r}_1) & \cdots & \Phi_N(\mathbf{r}_{N_r}) \end{bmatrix} \in \mathbf{R}^{N \times N_r}. \tag{6.36}$$

The feed-through vector is defined as

$$\mathbf{D} = \begin{bmatrix} D(\mathbf{r}_1) & \cdots & D(\mathbf{r}_{N_r}) \end{bmatrix} \in \mathbf{R}^{1 \times N_r}. \tag{6.37}$$

From these definitions, we can form the following complex matrix equation,

$$\mathbf{G} = \begin{bmatrix} \mathbf{P}^{tf} & 1_{N_\omega \times 1} \end{bmatrix} \begin{bmatrix} \widehat{\Psi} \\ \widehat{\mathbf{D}} \end{bmatrix}, \tag{6.38}$$

where $1_{N_\omega \times 1}$ denotes a matrix with dimension $N_\omega \times 1$, whose entries are all 1. Equation (6.38) has a unique least squares solution if $N_\omega \geqslant N$, this condition is automatically satisfied if the restrictions for the subspace estimation in Section 6.4 are met, i.e. if $N_\omega \geqslant q+p$, where p is the model order and q is the auxiliary order [82]. Since we are interested in real valued functions we restrict the matrices $\widehat{\Psi}$ and $\widehat{D}$ accordingly.

6.5.2 Linear Reconstruction

Here the ordering and dimension of the co-ordinate vector $\mathbf{r}$ becomes important. For notational simplicity, we assume $\mathbf{r}$ is single dimensional. Shannon's formula for linear reconstruction can be restated in context,

$$\Phi_i(r) = \Delta r \sum_{k=0}^{N_x} \Phi_i(r_k) \frac{\sin\left(\frac{\pi}{\Delta r}(r - r_k)\right)}{\pi(r - r_k)} \tag{6.39}$$

$$= [\Phi_i(r_1) \quad \cdots \quad \Phi_i(r_{N_r})] \begin{bmatrix} \text{sinc}\ \left(\frac{\pi}{\Delta r}(r - r_1)\right) \\ \vdots \\ \text{sinc}\ \left(\frac{\pi}{\Delta r}(r - r_{N_r})\right) \end{bmatrix}.$$

$D(r)$ can be reconstructed in a similar fashion. For convenience we write an equation describing all spatial functions,

$$
\begin{bmatrix} \Phi_i(r) \\ \vdots \\ \Phi_N(r) \\ D(r) \end{bmatrix} = \begin{bmatrix} \widehat{\Psi} \\ \widehat{\mathbf{D}} \end{bmatrix} \begin{bmatrix} \text{sinc} \left(\frac{\pi}{\Delta r}(r - r_1) \right) \\ \vdots \\ \text{sinc} \left(\frac{\pi}{\Delta r}(r - r_{N_r}) \right) \end{bmatrix}
$$

$$
= \begin{bmatrix} \widehat{\Psi} \\ \widehat{\mathbf{D}} \end{bmatrix} \mathbf{B}_r(r), \tag{6.40}
$$

where $\mathbf{B}_r(r)$ is the basis of reconstruction.

The spatial system can be written in state space form as

$$
\dot{\mathbf{x}} = \mathbf{A}\mathbf{x} + \mathbf{B}u \tag{6.41}
$$

$$
Y(r) = \mathbf{B}_r(r)'\widehat{\Psi}'J\mathbf{x} + \widehat{\mathbf{D}}\mathbf{B}_r(r)u,
$$

where $J = \begin{bmatrix} e_1' & e_3' & \cdots & e_{(2N-1)}' \end{bmatrix}' \in \mathbf{R}^{N \times 2N}$ and e_i is the i shifted unit impulse, e.g. $e_3 = \begin{bmatrix} 0 & 0 & 1 & 0 & \cdots & 0 \end{bmatrix}$. Note the equivalence of system (6.41) to (6.7), where $\mathbf{B}_r(r)'\widehat{\Psi}'J$ and $\widehat{\mathbf{D}}\mathbf{B}_r(r)$ represent the identified function matrix $\mathbf{C}(r)$ and feed-through function $\mathbf{D}(r)$.

6.5.3   Spline Reconstruction

The spline reconstructed system is similar to (6.41) with the exception that the function samples $\begin{bmatrix} \widehat{\Psi} \\ \widehat{\mathbf{D}} \end{bmatrix}$ and reconstruction basis $\mathbf{B}_r$ are replaced by the spline coefficients and chosen spline basis.

Finding the Spline Coefficients $c(k)$

Many standard procedures exist for finding the spline coefficients $c(k)$ as defined in Equation (6.12). The reader is referred to reference [112] for an overview of such techniques.

Summary

After computing the spline coefficients for each mode, the spatial system can be expressed in state space form:

$$\dot{\mathbf{x}} = \mathbf{A}\mathbf{x} + \mathbf{B}u \tag{6.42}$$

$$Y(r) = B^n(r)'\mathbf{C}'_s J\mathbf{x} + \mathbf{D}_s B^n(r)u,$$

where $\mathbf{D}_s = \begin{bmatrix} c_d(1) & c_d(2) & c_d(N_r) \end{bmatrix}$ are the spline coefficients of $D(r)$, $\mathbf{C}_s$ is the matrix containing the modal spline coefficients and $B^n(r)$ is the spline reconstruction basis,

$$\mathbf{C}_s = \begin{bmatrix} c_1(1) & \cdots & c_1(N_r) \\ \vdots & \ddots & \vdots \\ c_N(1) & \cdots & c_N(N_r) \end{bmatrix} \tag{6.43}$$

$$B^n(r) = \begin{bmatrix} \beta^n(\frac{r}{\Delta r}) \\ \beta^n(\frac{r}{\Delta r} - 1) \\ \vdots \\ \beta^n(\frac{r}{\Delta r} - (N_r - 1)) \end{bmatrix}. \tag{6.44}$$

6.6   Experimental Results

The presented technique will now be applied to identify two spatially distributed systems, a simply-supported beam and an asymmetric cantilever plate. Both structures are excited using bonded piezoelectric actuators. Although the simply-supported beam is easily modeled using analytic methods (albeit with experimental tuning), applying such techniques to the plate is significantly more difficult. The problem is complicated by the irregular geometry of the plate boundary.

The experimental beam and plate apparatus are shown in Figures 3.30 and 6.11 respectively.

Frequency Range	10-200 (Hz)
Equidistant F Samples	3031
Spatial Sampling interval	2.5 cm
Identification Samples	13
Validation Samples	13
Excitation	Colored Noise

Table 6.1: Identification Parameters.

6.6.1   Beam Identification

Experimental Setup

The physical parameters of the beam and properties of the piezoelectric transducer can be found in Tables 3.1 and 3.2.

Colored noise is applied to the actuator and the spatial response is measured sequentially using a Polytec scanning laser vibrometer. Details of the data set are given in Table 6.1.

Spatial Functions

The extracted mode shape and feed-through function samples together with their spline and linear reconstructions are shown in Figures 6.5, 6.6 and 6.7. It can be observed that the identified feed-though function is similar to that derived analytically, shown in Figure 6.3.

The Shannon reconstructed mode shapes are significantly distorted by the combination of truncation error and sample noise. It is interesting to note the effect of piezoelectric stiffness on the mode shapes of the beam shown in Figure 6.6. The length of the beam bonded to the piezoelectric patch is obviously more restricted in its deflection. Such structures with localized changes in stiffness are very difficult to model in closed form using present analytic techniques.
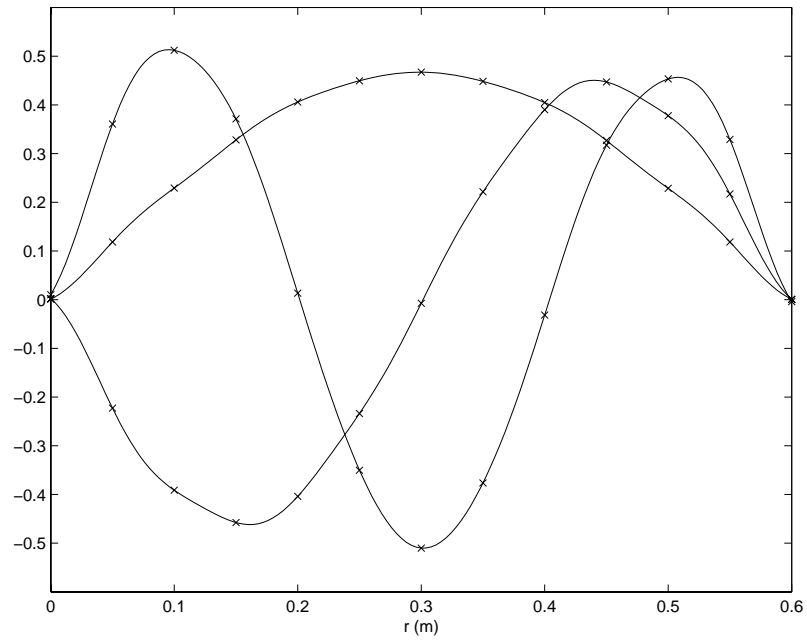
Figure 6.5: The extracted mode samples (×) and linear reconstruction.
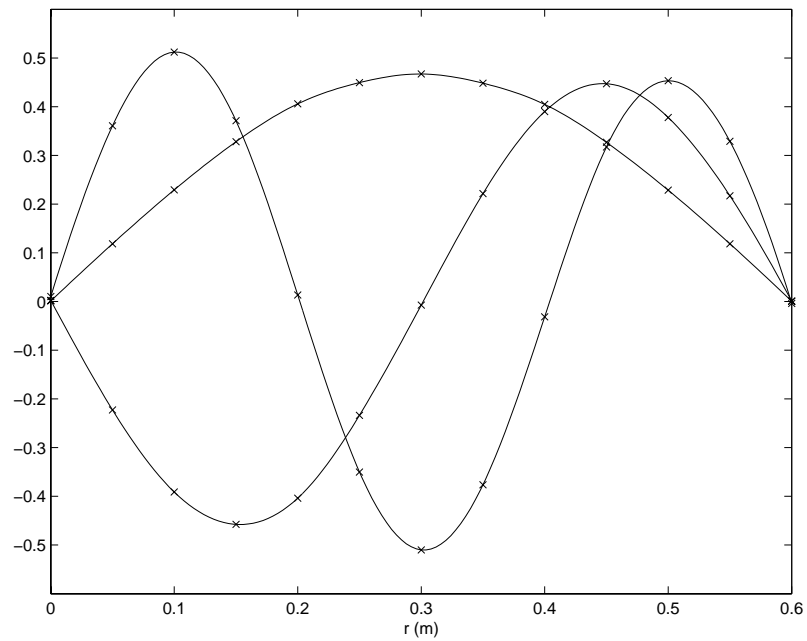
Figure 6.6: The extracted mode samples (×) and spline reconstruction.
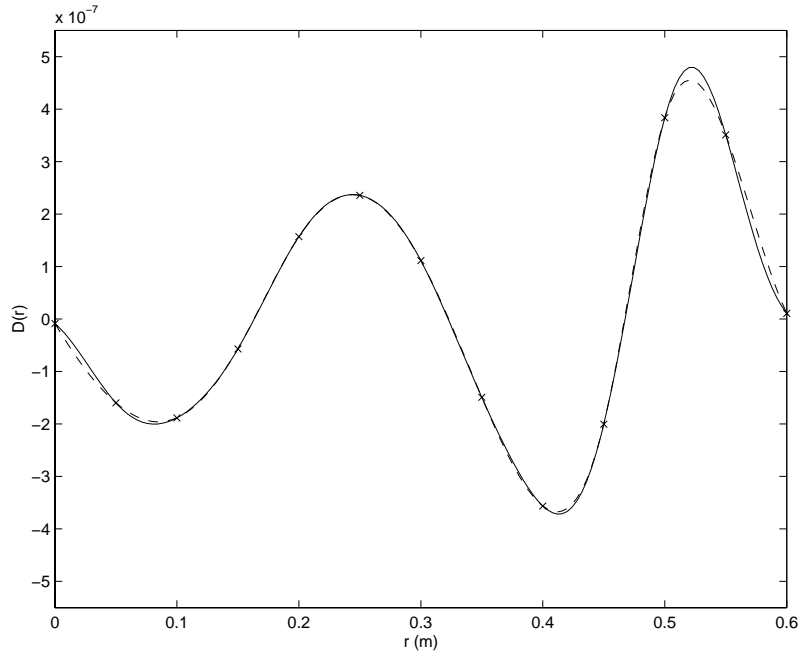
Figure 6.7: The extracted feed-through function samples ($\times$), the linear recon-

struction (–), and spline reconstruction (- -).

Spatial Response

To evaluate model quality, the measured spatial beam response plotted in Figure 6.8 is compared to the identified model response plotted in Figure 6.9. Each point-wise frequency response is measured from the applied actuator voltage (in volts) to the resulting displacement (in meters). A separate interlaced set of 13 points was used to perform the validation. The magnitude response of the error system, $G_y\left(j\omega, r\right) - \hat{G}_y\left(j\omega, r\right)$, where $\hat{G}_y(j\omega, r)$ denotes the model response, is plotted in Figure 6.10. In the frequency domain, the identified model is observed to accurately represent the physical system.
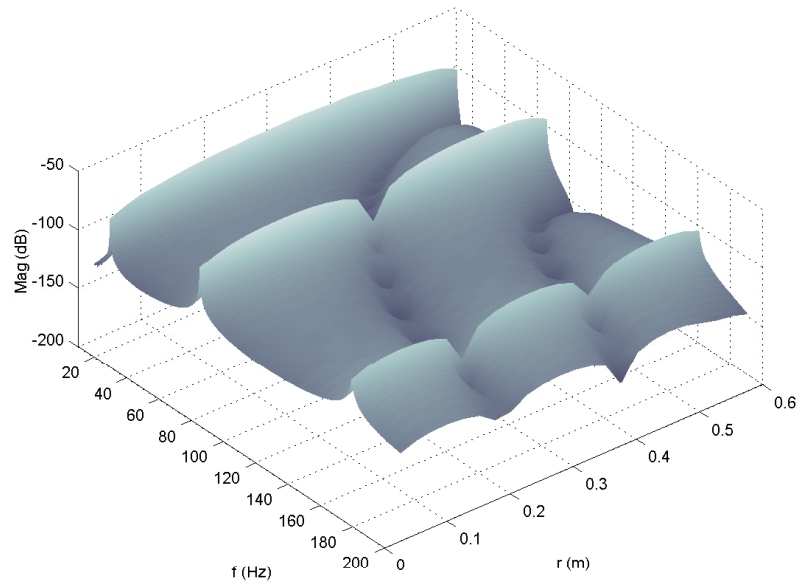
Figure 6.8: The experimental beam spatial frequency response from an applied actuator voltage to the measured displacement $G_y(j\omega, r)$.
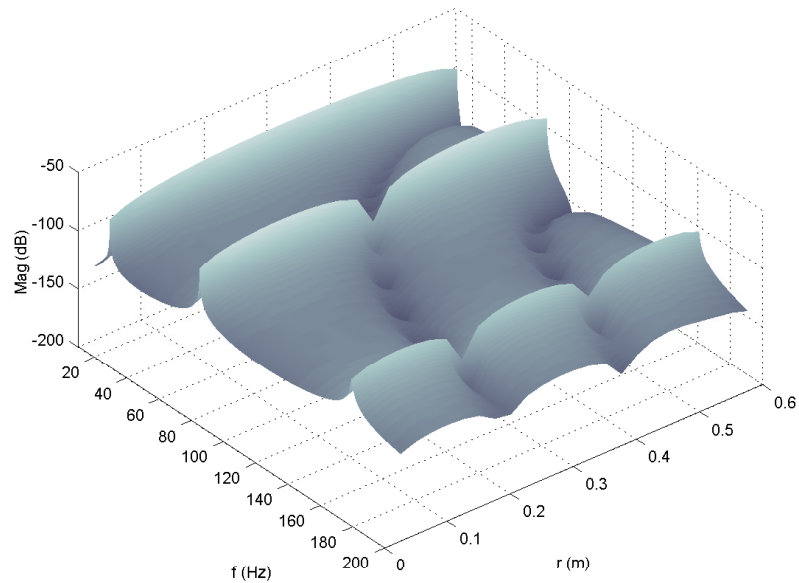
Figure 6.9: The spline reconstructed model response, from an applied actuator voltage to the measured displacement $\hat{G}_y(j\omega, r)$.
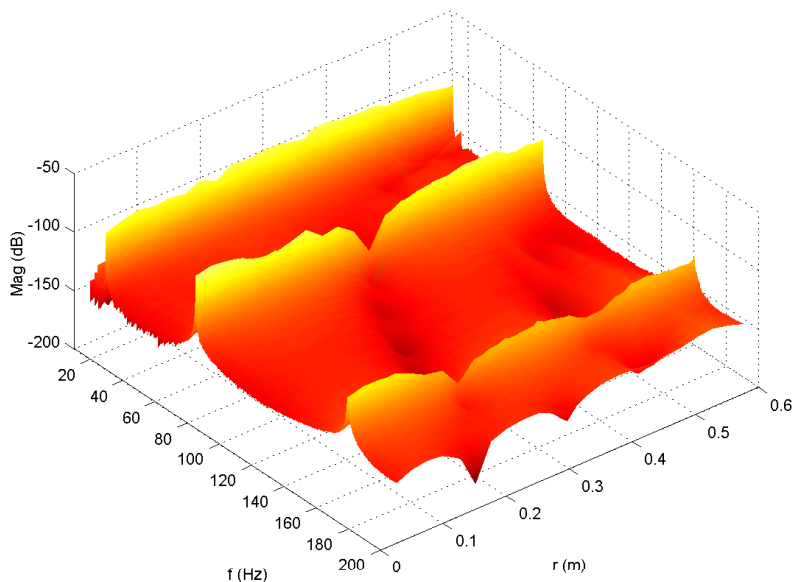
Figure 6.10: The error system response, $G_y \left(j\omega, r \right) - \hat{G}_y \left(j\omega, r \right)$.

Frequency Range	10-100 (Hz)
Equidistance F Samples	577
Number of Spatial Samples	468
Spatial Sampling interval	2.63 cm
Excitation	Colored Chirp

Table 6.2: Plate Identification Parameters.

6.6.2   Plate Identification

Experimental Setup

The experimental plate is constructed from aluminum of 4 mm thickness. Figure 6.11 shows the experimental plate, clamped vertically by its bottom edge to an optical table. Geometry and dimensions are shown in Figure 6.12. System identification parameters are given in Table 6.2.
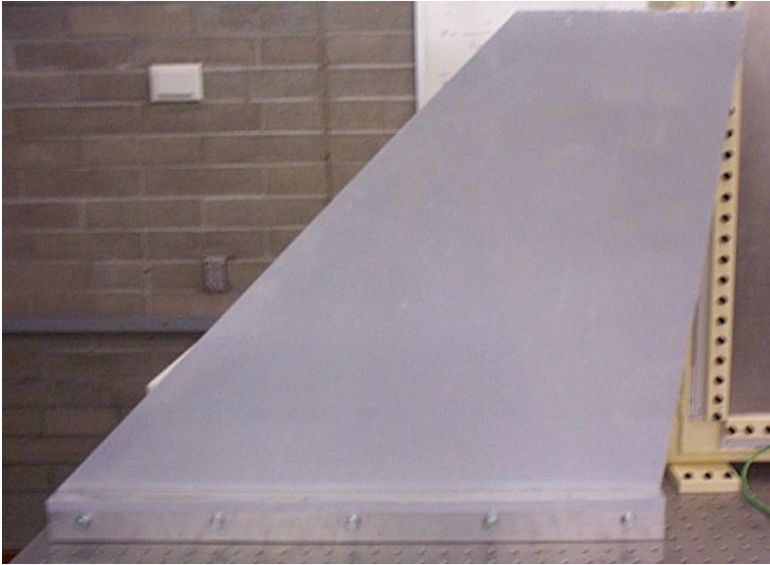
Figure 6.11: Experimental plate apparatus.
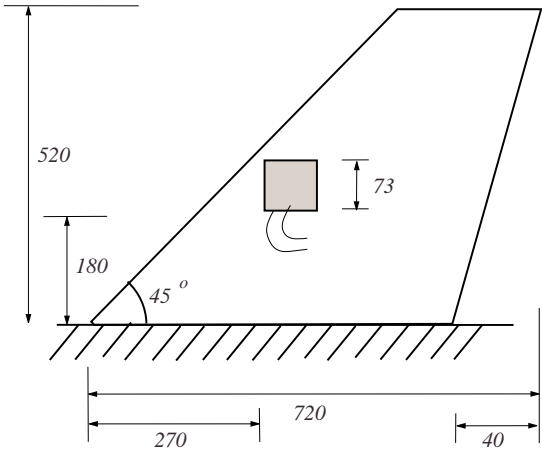
Figure 6.12: Plate geometry (mm).
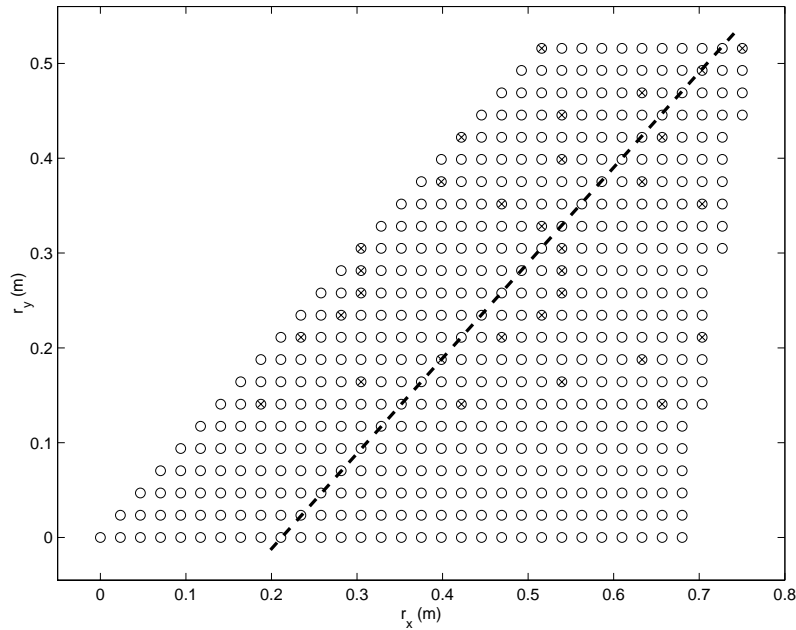
Figure 6.13: Distribution of the spatial samples. An '×' represents the location of a sample used to identify the system matrix **A**. The dashed line represents the side elevation of a spatial frequency response cross section used to analyze model quality.

Spatial Functions

An estimate for the system matrix **A** is first obtained using a scattered subset of the spatial frequency samples. The location of subset points is shown in Figure 6.13. Equation (6.38) is solved to identify the mode shapes and feed-through function. The resulting mode shapes and feed-through function are plotted in Figures 6.14 and 6.15.

Spatial Response

Due to the difficulties in visualizing a four-dimensional quantity, we evaluate model quality by taking a planar section of the spatial frequency response. An elevation of the section is shown in Figure 6.13. The measured, identified model, and error system $G_y\left(j\omega, r\right) - \hat{G}_y\left(j\omega, r\right)$ frequency responses are shown in Figures 6.16, 6.17 and 6.18 respec-
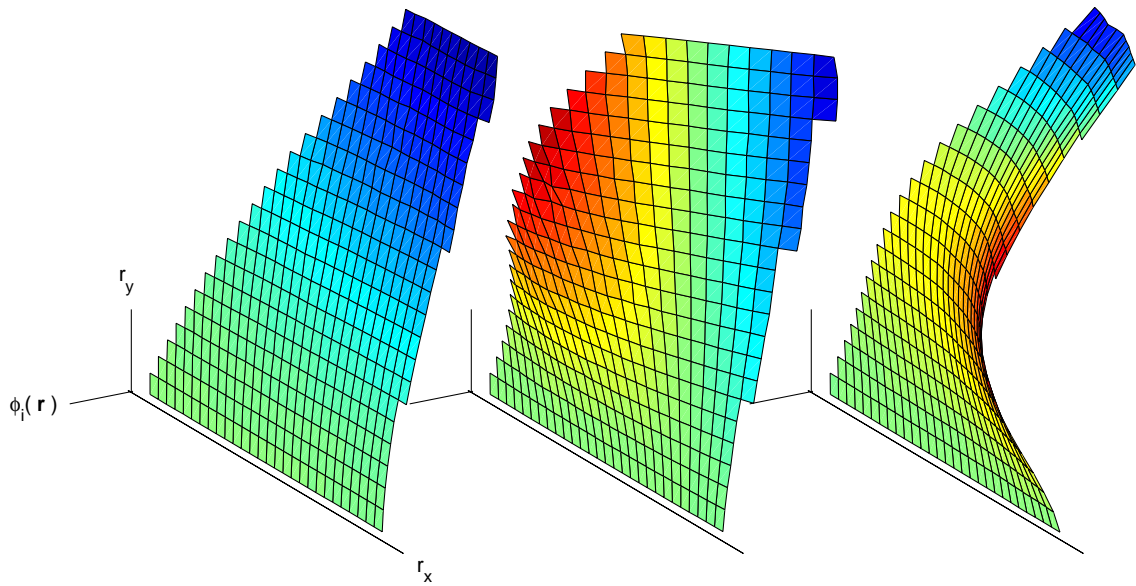
Figure 6.14: The normalized first, second, and third modes of the cantilever fin.
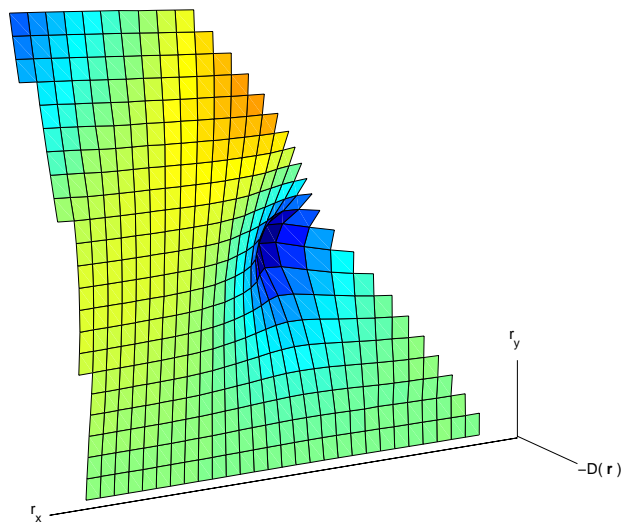
Figure 6.15: The identified feed-through function $D(\mathbf{r})$.
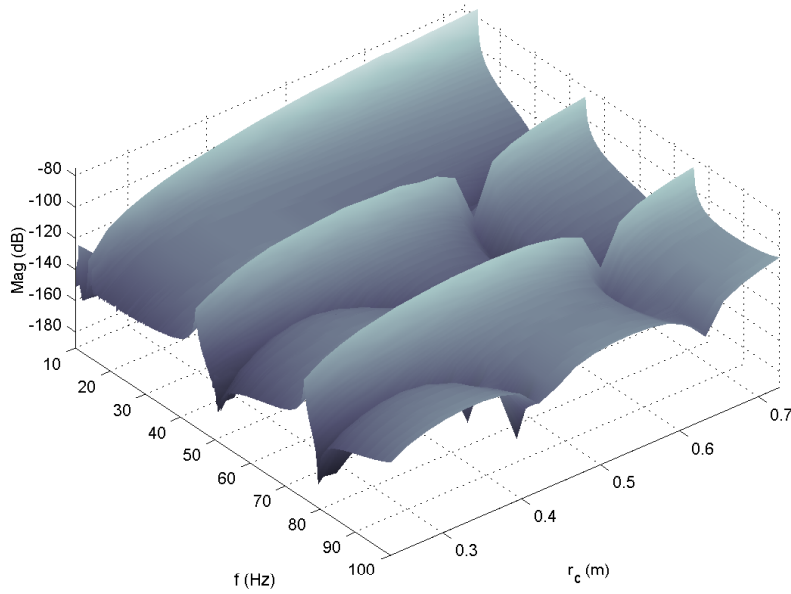
Figure 6.16: A cross section of the cantilever plate measured spatial frequency response. The response is measured from the applied actuator voltage to the resulting displacement.

tively. Each point-wise frequency response is measured from the applied actuator voltage to the resulting displacement (in meters). As shown by the magnitude of the error system response, in the frequency domain, a good correlation between the experimental data and model response can be observed.

6.7   Conclusions

A technique has been presented for identifying a class of distributed parameter systems from a set of spatially distributed frequency responses. The systems are modeled as a finite sum of second order transfer functions with spatially variant numerators and a feed-through term.

In an attempt to evenly distribute model error, the identification is cast as a single-input multi-output identification problem. An estimate for the system dynamics is sought using a frequency domain subspace algorithm. Samples of the mode shapes and feed-through
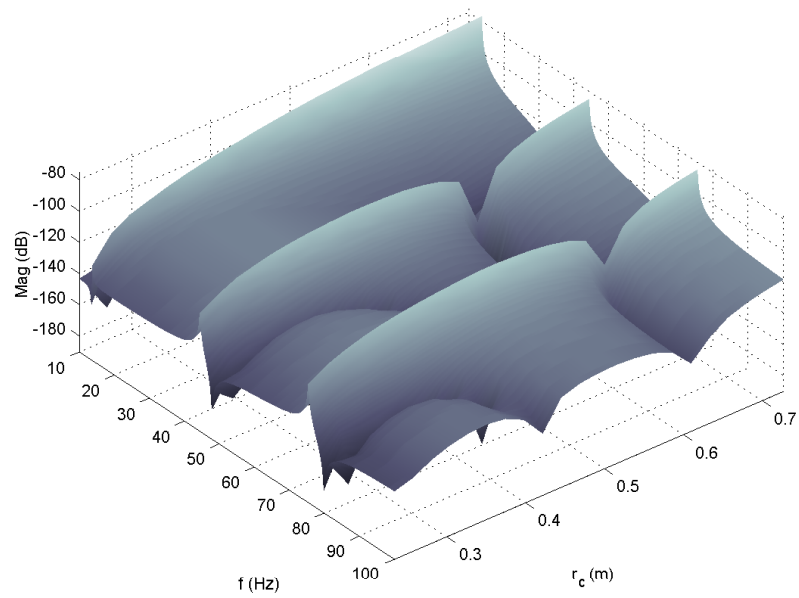
Figure 6.17: A cross section of the spline reconstructed model response.
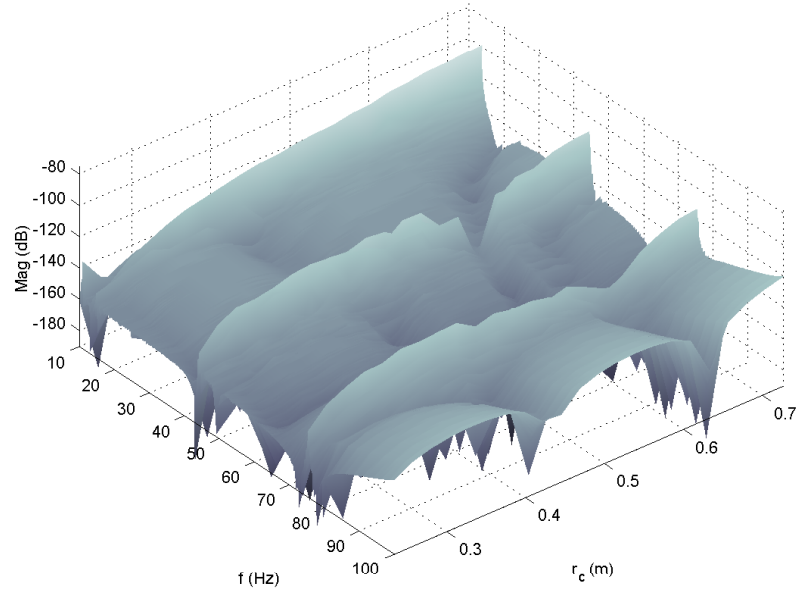
Figure 6.18: A cross section of the plate error system frequency response, $G_y\left(j\omega, r\right) - \hat{G}_y\left(j\omega, r\right)$.

function are then identified and used to reconstruct the continuous functions. If the spatial Fourier transform is known, the error due to under sampling can be quantified.

Experimental identification of a simply-supported beam and cantilever plate has shown an adequate correlation in the frequency domain between the measured system and identified model. In both cases the majority of discrepancy is due to small errors in the resonance frequencies. It is anticipated that future contributions in this area will involve the development of an efficient optimization algorithm to minimize such errors.

Other outstanding problems to date include: the automatic identification of non-distributed dynamics $H(s)$, experimental identification incorporating piezoelectric sensor voltages, time domain identification techniques, and stochastic analysis.

7

CONCLUSIONS

This thesis has presented new techniques for the control and system identification of electromagnetic and piezoelectric actuated smart structures. Conclusions specific to each topic, and directions for future research can be found at the close to each chapter. Following is a summary of the main arguments, contributions, and results presented throughout this thesis.

7.1 Summary and Conclusions

An initial review of piezoelectric shunt damping techniques presented in Chapter 2 concluded that resonant shunt circuits provide good performance but are impractical to implement using physical components or virtual circuits. The synthetic impedance was introduced as a practical method for the implementation of arbitrary shunt impedances.

The synthetic impedance requires a voltage controlled current source and analog or digital signal filter. In Chapter 3, the compliance feedback current source was introduced to alleviate problems associated with present current and charge driver designs. A technique was also presented for the design of digital and analog impedance filters. This technology significantly simplifies the implementation of piezoelectric shunt vibration control systems.

In Chapter 4, the arbitrary nature of synthetic implementation was exploited to facilitate the design and implementation of active shunt controllers. By casting the problem of impedance design as a standard regulator problem, traditional synthesis techniques such as LQR, LQG, $\mathcal{H}_2$, and $\mathcal{H}_\infty$ can be applied. Active shunt controllers can be designed

to minimize an arbitrary performance objective, are easily extended to multi-transducer structures, and do not suffer the same performance limitations as passive circuits. Experimental application to a cantilever beam has shown significantly better performance than passive techniques. One of the most outstanding features of active shunt control is the independence to variation in structural resonance frequencies. Where small changes in structural resonance frequencies can severely effect the performance of active feedback and passive vibration control systems, the nature of active shunt control offers high immunity to such variation.

Electromagnetic transducers have long been employed as actuators and sensors in the field of mechanical vibration control. In contrast to piezoelectric transducers, they are suitable for in-plane force control, have large displacement strokes, and are physically robust for industrial applications. As presented in Chapter 5, an impedance can be connected to the terminals of an electromagnetic transducer with a view to minimizing structural vibration. Alike piezoelectric shunt control, passive and active impedances can be designed to reduce structural vibration. A framework is presented for the design and analysis of active electromagnetic shunt controllers. An experimental electromagnetic system is successfully controlled using an LQR and $\mathcal{H}_2$ active shunt impedance. Applications of electromagnetic shunt control include, vibration isolation, acoustic noise control, and inertial force control.

With the advent of active impedance control, the possibility now exists for mitigation of an arbitrary performance objective. In analogy to active control systems, a single structural point is chosen to represent structural vibration. Inevitably, the chosen point will express a weighting on the modes most dominant at that location. Spatial control is a technique for modifying a performance objective to account for the global vibration in a flexible structure. In Chapter 6, spatial system identification is presented as a method for procuring spatial models of flexible structures. By performing a subspace identification and least-squares fit, a spatially continuous model can be obtained. The model can be employed in the synthesis of spatially weighted controllers.

Bibliography

[1] *IEEE Standard on Piezoelectricity.* ANSI/IEEE standard 176-1987, 1987.

[2] S. Acrabelli and A. Tonoli. System properties of flexible structures with self-sensing piezoelectric transducers. *Journal of sound and vibration*, 235(1):1–23, 2000.

[3] H. J. M. T. A. Adriaens, W. L. de Koning, and R. Banning. Modeling piezoelectric actuators. *IEEE/ASME transactions on mechatronics*, 5(4):331–341, December 2000.

[4] T. E. Alberts and J. A. Colvin. Observations on the nature of transfer functions for control of piezoelectric laminates. *Journal of Intelligent Material Systems and Structures*, 8(5):605–611, 1991.

[5] J. B. Aldrich, N. W. Hagood, A. von Flotow, and D. W. Vos. Design of passive piezoelectric shunt damping for space structures. In *Proc. SPIE Conference of Smart Structures and Intelligent Systems, SPIE Vol. 1917*, pages 629–705, 1993.

[6] R. Amirtharajah and A. P. Chandrakasan. Self-powered signal processing using vibration-based power generation. *IEEE Journal of Solid-State Circuits*, 33(5):687–695, May 1998.

[7] E. H. Anderson, N. W. Hagood, and J. M. Goodliffe. Self-sensing piezoelectric actuation: Analysis and application to controlled structures. In *Proc. AIAA/ASME/ASCE/AHS/ASC Structures, Structural Dynamics, and Materials*, pages 2141–2155, 1992.

[8] S. Behrens. Passive and semi-active control of piezoelectric laminates. Master's thesis, Dept. of Electrical and Computer Engineering, University of Newcastle, Australia, 2000.

[9] S. Behrens, A. Fleming, and S. O. R. Moheimani. Electrodynamic vibration suppression. In *Proc. SPIE Smart Structures and Materials 2003 - Damping and Isolation, Paper No. 4697-24*, San Diego, CA, December 2002.

[10] S. Behrens, A. J. Fleming, and S. O. R. Moheimani. A broadband controller for piezoelectric shunt damping of structural vibration. *IOP Smart Materials and Structures*, 12:18–28, January 2003.

[11] S. Behrens and S. O. R. Moheimani. Optimal resistive elements for multiple mode shunt-damping of a piezoelectric laminated beam. In *Proc. IEEE Conference on Decision and Control*, pages 4018–4023, Sydney, Australia, December 2001.

[12] S. Behrens and S. O. R. Moheimani. Current flowing multiple mode piezoelectric shunt dampener. In *Proc. SPIE Smart Materials and Structures, Paper No. 4697-24*, pages 217–226, San Diego, CA, March 2002.

[13] S. Behrens, S. O. R. Moheimani, and A. J. Fleming. Multiple mode current flowing passive piezoelectric shunt controller. *Journal of Sound and Vibration*, 266(5):929–942, 2003.

[14] S. Behrens, S. O. R. Moheimani, and A. J. Fleming. Multiple mode passive piezoelectric shunt dampener. In *Proc. IFAC Mechatronics 2002*, Berkerley, CA, December 2002.

[15] E. Bianchini, R. Spangler, and C. Andrus. The use of piezoelectric devices to control snowboard vibrations. In *Proc. SPIE Smart Structures and Materials: Smart Structures and integrated systems, SPIE Vol. 3329*, pages 106–114, 1998.

[16] T. Blu and M. Unser. Quantitative fourier analysis of approximation techniques: Part 1 - interpolators and projectors. *IEEE Transactions on Signal Processing*, 47(10):2783–2795, October 1999.

[17] R. G. Brown and P.Y.C. Hwang. *Introduction to Random Signals and Applied Kalman Filtering*. John Wiley and Sons Inc., 1997.

[18] J. R. Carstens. *Electrical sensors and transducers*. Prentice-Hall, 1993.

[19] S. Chandrasekaran, D. K. Lindner, and R. C. Smith. Optimized design of switching amplifiers for piezoelectric actuators. *Journal of Intelligent Material Systems and Structures*, 11:887–901, November 2000.

[20] C. Choi and K. Park. Self-sensing magnetic levitation using LC resonant circuits. *Sensors and Actuators*, pages 1276–1281, 1999.

[21] R. L. Clark and K. D. Frampton. Phase compensation for feedback control of enclosed sound fields. *Journal of Sound and Vibration*, 195(5):701–718, 1996.

[22] R. L. Clark, W. R. Saunders, and G. P. Gibbs. *Adaptive Structures: Dynamics and Control*. John Wiley and Sons Inc., 1998.

[23] W. W. Clark. Vibration control with state-switched piezoelectric materials. *Journal of Intelligent Material Systems and Structures.*, 11:263–271, April 2000.

[24] D. G. Cole and R. L. Clark. Adaptive compensation of piezoelectric sensoriactuators. *Journal of Intelligent Material Systems and Structures*, 5:665–672, 1994.

[25] R. Comstock. Charge control of piezoelectric actuators to reduce hysteresis effects. *Japan Journal of Applied Physics, part 2 - Letters*, 1981.

[26] R.. D. Cook. *Finite Element Modeling for Stress Analysis*. John Wiley and Sons, 1995.

[27] L. R. Corr and W. W. Clark. Comparison of low-frequency piezoelectric switching shunt techniques for structural damping. *IOP Smart Materials and Structures*, 11:370–376, 2002.

[28] D. Croft, G. Shedd, and S. Devasia. Creep, hysteresis and vibration compensation for piezoactuators: Atomic force microscopy application. In *Proc. American Control Conference*, pages 2123–2128, Chicago, Illinois, June 2000.

[29] J. M. Cruz-Hernandez and V. Hayward. Phase control approach to hysteresis reduction. *IEEE transactions on control systems technology*, 9(1):17–26, January 2001.

[30] C. L. Davis and G. A. Lesieutre. An actively tuned solid-state vibration absorber using capacitive shunting of piezoelectric stiffness. *Journal of Sound and Vibration*, 232(3):601–617, 2000.

[31] K. K. Denoyer, S. F. Griffin, and D. Sciulli. Hybrid structural/acoustic control of a subscale payload fairing. In *Proc. SPIE Smart Structures and Materials: Smart Structures and Integrated Systems, SPIE Vol. 3329*, pages 237–243, 1998.

[32] J. J. Dosch, D. J. Inman, and E. Garcia. A self-sensing piezoelectric actuator for collocated control. *Journal of Intelligent Material Systems and Structures*, 3:166–185, January 1992.

[33] J. C. Doyle, B. A. Francis, and A. R. Tannenbaum. *Feedback Control Theory*. Macmillan Pub. Co., New York, 1992.

[34] J. C. Doyle, K. Glover, P. Khargonekar, and B. Francis. State-space solutions to standard $\mathcal{H}_2$ and $\mathcal{H}_\infty$ problems. *IEEE Transactions on Automatic Control*, 34(8):831–847, August 1989.

[35] D. J. Ewins. Modal testing as an aid to vibration analysis. In *Proc. Conference on Mechanical Engineering*, May 1990.

[36] Ronald L. Fante. *Signal Analysis and Estimation. An Introduction.* John Wiley and Sons, 1988.

[37] A. J. Fleming, S. Behrens, and S. O. R. Moheimani. Optimization and implementation of multi-mode piezoelectric shunt damping systems. *IEEE/ASME Transactions on Mechatronics*, 7(1):87–94, March 2002.

[38] A. J. Fleming and S. O. R. Moheimani. Adaptive piezoelectric shunt damping. *IOP Smart Materials and Structures*, 12:36–48, January 2003.

[39] A. J. Fleming and S. O. R Moheimani. Reducing the inductance requirements of piezoelectric shunt damping circuits. *IOP Smart Materials and Structures*, 12:57–64, January 2003.

[40] R. L. Forward. Electronic damping of vibrations in optical structures. *Applied Optics*, 18(5):690–697, March 1979.

[41] A. R. Fraser and R. W. Daniel. *Pertubation Techniques for Flexible Manipulators*. Kluwer Academic Publishers, 1991.

[42] C. R. Fuller, S. J. Elliott, and P. A. Nelson. *Active Control of Vibration*. Academic Press, 1996.

[43] K. Furutani, M. Urushibata, and N. Mohri. Improvement of control method for piezoelectric actuator by combining charge feedback with inverse transfer function compensation. In *Proc. IEEE International Conference on Robotics and Automation*, pages 1504–1509, Leuven, Belgium, May 1998.

[44] P. Gao, Y. Lou, and K. Okada. Detection and suppression for mechanical resonance in hard disk drives with built-in piezoelectric sensors. In *Proc. SPIE Smart Structures and Materials: Smart Sensor Technology and Measurement Systems, SPIE Vol. 4694*, pages 78–85, 2002.

[45] E. Garcia, J. D. Dosch, and D. J. Inman. Vibration attenuation in an active antenna structure. In *Proc. Conference on recent advances in active control of sound and vibration*, pages S35–S42, Viginia Polytechnique Institute and State University, Blacksburg, April 15-17 1991.

[46] E. Garcia, D. J. Inman, and J. D. Dosch. Vibration suppression using smart structures. In *Proc. SPIE Smart Structures and Materials*, pages 167–172, 1991.

[47] P. Ge and M. Jouaneh. Tracking control of a piezoelectric actuator. *IEEE Transactions on control systems technology*, 4(3):209–216, May 1996.

[48] N. W. Hagood and A. Von Flotow. Damping of structural vibrations with piezoelectric materials and passive electrical networks. *Journal of Sound and Vibration*, 146(2):243–268, 1991.

[49] N. W. Hagood, W. H. Chung, and A. von Flotow. Modeling of piezoelectric actuator dynamics for active structural control. *Journal of Intelligent Material Systems and Structures*, 1:327–354, 1990.

[50] N. W. Hagood and E. F. Crawley. Experimental investigation of passive enhancement of damping for space structures. *Journal of Guidance, Control and Dynamics*, 14(6):1100–1109, 1991.

[51] D. Halim and S. O. R. Moheimani. Spatial resonant control of flexible structures - application to a piezoelectric laminate beam. *IEEE Transactions on Control Systems Technology*, 9(1):37–53, January 2001.

[52] D. Halim and S. O. R. Moheimani. Experimental implementation of spatial h_∞ control on a piezoelectric laminate beam. *IEEE/ASME Transactions on Mechatronics*, 7(3):346–356, September 2002.

[53] D. Halim and S. O. R. Moheimani. Spatial H_2 control of a piezoelectric laminate beam: Experimental implementation. *IEEE Transactions on Control Systems Technology*, 10(4):533–546, July 2002.

[54] B. M. Hanson, M. D. Brown, and J. Fisher. Self sensing: Closed-loop estimation for a linear electromagnetic actuator. In *Proc. IEEE American Control Conference*, pages 1650–1655, Arlington, VA USA, June 2001.

[55] J. Heng, J. C. Akers, R. Venugopal, M. Lee, A. G. Sparks, P. D. Washabaugh, and D. Bernstien. Modeling, identification, and feedback control of noise in an acoustic duct. *IEEE Transactions on Control Systems Technology*, 4(3):283–291, 1996.

[56] J. J. Hollkamp. Multimodal passive vibration suppression with piezoelectric materials and resonant shunts. *Journal of Intelligent Materials Systems and Structures*, 5:49–56, 1994.

[57] M. A. Hopkins, D. A. Henderson, R. W. Moses, T. Ryall, D. G. Zimcik, and R. L. Spangler. Active vibration-suppression systems applied to twin-tail buffeting. In *Proc. SPIE Smart Structures and Materials: Industrial and Commercial Applications of Smart Structures Technologies, SPIE Vol. 3326*, pages 27–33, 1998.

[58] P. Horowitz and W. Hill. *The Art of Electronics*. Cambridge University Press, 1980.

[59] R. Hummel. Sampling for spline reconstruction. *SIAM Journal of Applied Mathematics*, 43(2):278–288, April 1983.

[60] B. Jaffe, W. R. Cook, and H. Jaffe. *Piezoelectric Ceramics.* Academic Press, 1971.

[61] H. Janocha. Actuators in adaptronics. In B. Clephas, editor, *Adaptronics and Smart Structures*, chapter 6. Springer, 1999.

[62] H. Janocha. *Adaptronics and Smart Structures - Basics, Material, Design, and Applications.* Springer, 1999.

[63] A. J. Jerri. The shannon sampling theorem - its various extensions and applications: A tutorial review. *Proceedings of the IEEE*, 65(11):1565–1596, November 1977.

[64] T. Kailath. *Linear Systems.* Printice-Hall, Upper Saddle River, NJ 07458, 1980.

[65] H. Kaizuka and B. Siu. Simple way to reduce hysteresis and creep when using piezo-electric actuators. *Japan Journal of Applied Physics, part 2 - Letters*, 27(5):773–776, May 1988.

[66] R. Kalman. When is a linear control system optimal. *Journal of Basic Engineering - Transaction on ASME - Series D*, 86:51–60, 1964.

[67] J. Kim, J. Choi, and R. H. Cabell. Noise reduction performance of smart panels incorporating piezoelectric shunt damping. In *Proc. SPIE Smart Structures and Materials: Industrial and Commercial Applications of Smart Structures Technologies, SPIE Vol. 4698*, pages 143–149, 2002.

[68] S. Kim, C. Han, and C. Yun. Improvement of aeroelastic stability of hingeless helicopter rotor blade by passive piezoelectric damping. In *Proc. SPIE Smart Structures and Materials: Passive damping and isolation, SPIE Vol 3672*, pages 131–141, Newport Beach, CA, March 1999.

[69] Y. B. Kim, W. G. Hwang, C. D. Kee, and H. B. Yi. Active vibration control of suspension system using an electromagnetic damper. In *Proc. Of the Int. MECH Eng. Part D Journal of Automoblie Engineering (Professional Engineering Publishing)*, volume 8, pages 865–873, 2001.

[70] A. Krzyzak and E Rafajłowicz M. Pawlak. Moving average restoration of bandlimited signals from noisy observations. *IEEE transactions on signal processing*, 45(12):2967–2976, December 1997.

[71] P. Lancaster and K. Salkauskas. *Curve and Surface Fitting*. Academic Press, 1986.

[72] S. A. Lane and R. L. Clark. Improving loudspeaker performance for active noise control. *Journal of the Audio Engineering Society*, 46(6):508–519, June 1998.

[73] K. B. Lazarus and E. F. Crawley. Multivariable active lifting surface control using strain actuation: analytical and experimental results. In *Proc. 3rd International conference on adaptive structures*, pages 87–101, San Diego, CA, 1992.

[74] C. K. Lee and F. C. Moon. Modal sensors/actuators. *ASME Journal of Applied Mechanics*, 57:434–441, June 1990.

[75] Y. Lim, V. V. Varadan, and V. K. Varadan. Closed-loop finite element modeling of active/passive damping in structural vibration control. In *Proc. SPIE Smart Materials and Structures 1997: Mathematics and Control in Smart Structures, SPIE Vol. 3039*, San Diego, CA, March 1997.

[76] K. Liu, R. N. Jacques, and D. W. Miller. Frequency domain structural system identification by observability range space extraction. In *Proc. American Control Conference, Vol. 1*, pages 107–111, Baltimore, MD, June 1994.

[77] L. Ljung. *System Identification: Theory for the User*. Prentice Hall, 1999.

[78] D. G. MacMartin. Collocated structural control: motivation and methodology. In *Proc. IEEE International Conference on Control Applications*, pages 1092–1097, Albany, New York USA, September 1995.

[79] N. M. M. Maia and J. M. Montalvao de Silva, editors. *Theoretical and Experimental Modal Analysis*. Research Studies Press, Hertfordshire, England, 1997.

[80] J. A. Main, E. Garcia, and D. V. Newton. Precision position control of piezoelectric actuators using charge feedback. *Journal of Guidance, control, and dynamics*, 18(5):1068–1073, September-October 1995.

[81] I. D. Mayergoyz. *Mathematical Models of Hysteresis*. Springer Verlag, New York, 1991.

[82] T. McKelvey, H. Akcay, and L. Ljung. Subspace based multivariable system identification from frequency response data. *IEEE Transactions on Automatic Control*, 41(7):960–978, July 1996.

[83] T. McKelvey, A. J. Fleming, and S. O. R. Moheimani. Subspace based system identification for an acoustic enclosure. *ASME Journal of Vibration and Acoustics*, 124(3):414–419, July 2002.

[84] T. McKelvy and L. Ljung. Frequency domain maximum likelihood identification. In *Proc. IFAC Symposium on System Identification*, pages 1741–1746, Fukuoda, Japan, July 1997.

[85] L. Meirovitch. *Elements of Vibration Analysis*. McGraw-Hill, Sydney, 2nd edition, 1996.

[86] S. Mirzaei, S. M. Saghaiannejad, V. Tahani, and M. Moallem. Electromagnetic shock absorber. In *IEEE International Conference on Electric Machines and Drives Conference IEMDC 2001*, pages 760–764, 2001.

[87] N. Mohan, T. M. Undeland, and W. P. Robbins. *Power Electronics: Converters, Applications, and Design*. Wiley, New York, 1995.

[88] S. O. R. Moheimani. Experimental verification of the corrected transfer function of a piezoelectric laminate beam. *IEEE Transactions on Control Systems Technology*, 8(4):660–666, July 2000.

[89] S. O. R. Moheimani, A. J. Fleming, and S. Behrens. On the feedback structure of wideband piezoelectric shunt damping systems. *IOP Smart Materials and Structures*, 12:49–56, January 2003.

[90] S. O. R. Moheimani, H. R. Pota, and I. R. Petersen. Broadband disturbance attenuation over an entire beam. *Journal of Sound and Vibration*, 227(4):807–832, 1999.

[91] S. O. R. Moheimani, S. Behrens, and A. J. Fleming. Dynamics and stability of wide-band vibration absorbers with multiple piezoelectric transducers. In *IFAC Mechatronics*, Berkeley, CA, December 9-11 2002.

[92] S. O. R. Moheimani. Minimizing the effect of out-of-bandwidth dynamics in the models of reverberant systems that arise in modal analysis: Implications on spatial H_∞ control. *Automatica*, 36:1023–1031, 2000.

[93] N. Morse, R. Smith, B. Paden, and J. Antaki. Position sensed and self-sensing magnetic bearing configuations and associated robustness limitations. In *Proc. IEEE Conference on Decision and Control*, pages 2599–2604, Tampa, Florida USA, December 1998.

[94] A. J. Moulson and J. M. Herbert. *Electroceramics: Materials, Properties, Applications*. London: Chapman and Hall, 1990.

[95] C. V. Newcomb and I. Flinn. Improving the linearity of piezoelectric ceramic actuators. *IEE Electronics Letters*, 18(11):442–443, May 1982.

[96] D. Niederberger, M. Morari, and S. Pietrzko. Adaptive resonant shunted piezoelectric devices for vibration supression. In *Proc. SPIE Smart Structures and Materials - Damping and Isolation*, San Diego, CA USA, March 2003.

[97] C. Niezrecki and H. H. Cudney. Feasibility to control launch vehicle internal acoustics using piezoelectric actuators. *Journal of Intelligent Material Systems and Structures*, 12:647–660, September 2001.

[98] M. Pawlak and E. Rafajłowicz. On restoring band-limited signals. *IEEE Transactions on Information Theory*, 40(5):1490–1503, September 1994.

[99] M. Pawlak and U. Stadtmüller. Recovering band-limited signals under noise. *IEEE transactions on information theory*, 42(5):1425–1438, September 1996.

[100] A. D. Poularikas. *Handbook of Formulas and Tables for Signal Processing*. CRC Press, 1999.

[101] S. S. Rao. *Mechanical Vibrations*. Addison-Wesley Publishing Company, 3rd edition, 1995.

[102] C. Richard, D. Guyomar, D. Audigier, and H. Bassaler. Enhanced semi-passive damping using continuous switching of a piezoelectric devices on an inductor. In *Proc. SPIE Smart Structures and Materials, Damping and Isolation, SPIE Vol. 3989*, pages 288–299, Newport Beach, CA, March 2000.

[103] R. H. S. Riordan. Simulated inductors using differential amplifiers. *IEE Electronics Letters*, 3(2):50–51, 1967.

[104] M. G. Safonov and M. Athans. Gain and phase margin for multiloop LQG regulators. *IEEE Transactions on automatic control*, AC-22(2):173–179, 1977.

[105] I. J. Schoenberg. *Cardinal Spline Interpolation*. PA: Society of Industrial and Applied Mathematics, 1973.

[106] J. Shaw. Active vibration isolation by adaptive control. In *Proc. IEEE International Conference on Control Applications*, pages 1509–1514, Hawaii, USA, August 1999.

[107] W. H. Shields, J. Ro, and A. M. Baz. Control of sound radiation from a plate into an acoustic cavity using active piezoelectric-damping composites. In *Proc. SPIE Smart Structures and Materials: Mathematics and Control in Smart Structures, SPIE Vol. 3039*, pages 70–90, 1997.

[108] J. Simpson and J. Schweiger. Industrial approach to piezoelectric damping of large fighter aircraft components. In *Proc. SPIE Smart Structures and Materials: Industrial and Commercial Applications of Smart Structures Technologies, SPIE Vol. 3326*, pages 34–46, 1998.

[109] S. Skogestad and I. Postlethwaite. *Multivariable Feedback Control*. John Wiley and Sons, 1996.

[110] D. Stansfield. *Underwater Electroacoustic Transducers*. Bath University Press and Institute of Acoustics, Bath, UK, 1991.

[111] J. B. Thomas and B. Liu. Error problems in sampling representation. *IEEE Int. Conv. Rec. (USA)*, 12(5):269–277, 1964.

[112] M. Unser. Splines, a perfect fit for signal and image processing. *IEEE Signal Processing Magazine*, 16(6):22–38, Novenmber 1999.

[113] M. Unser, A. Aldroubi, and M. Eden. Polynomial spline signal approximations: Filter design and asymptotic equivalence with shannon's sampling theorem. *IEEE Transactions on Information Theory*, 38(1):95–103, January 1992.

[114] M. E. Van Valkenburg. *Analog Filter Design.* CBS College Publishing, 1982.

[115] P. Vallone. High-performance piezo-based self-sensor for structural vibration control. In *Proc. SPIE Smart Structures and Materials: Smart Structures and Integrated systems, SPIE Vol. 2443*, pages 643–655, 1995.

[116] P. Van Overschee and B. De Moor. Continuous-time frequency domain subspace system identification. *Signal Processing*, 52:179–194, 1996.

[117] M. Viberg. Subspace-based methods for the identification of linear time invariant systems. *Automatica*, 31(12):1835–1851, 1995.

[118] J. S. Vipperman and R. L. Clark. Hybrid analog and digital adaptive compensation of piezoelectric sensoriactuators. In *Proc. AIAA/ASME Adaptive Structures Forum*, pages 2854–2859, New Orleans, LA, 1995.

[119] D. Vischer and H. Bleuler. Self-sensing active magnetic levitation. *IEEE Transactions on Magnetics*, 29(2):169–177, 1993.

[120] C. C. Won. Piezoelectric transformer. *Journal of Guidancce, Control, and Dynamics*, 18(1):96–101, 1995.

[121] S. Wu, T. L. Turner, and S. A. Rizzi. Piezoelectric shunt vibration damping of an F-15 panel under high-acoustic excitation. In *Proc. SPIE Smart Structures and Materials: Damping and Isolation, SPIE Vol. 3989*, pages 276–287, 2000.

[122] S. Y. Wu. Piezoelectric shunts with parallel R-L circuit for structural damping and vibration control. In *Proc. SPIE Smart Structures and Materials: Passive Damping and Isolation, SPIE Vol. 2720*, pages 259–269, March 1996.

[123] S. Y. Wu. Method for multiple mode shunt damping of structural vibration using a single PZT transducer. In *Proc. SPIE Smart Structures and Materials, Smart Structures and Intelligent Systems, SPIE Vol. 3327*, pages 159–168, Huntington Beach, CA, March 1998.

[124] S. Y. Wu. Multiple PZT transducers implemented with multiple-mode piezoelectric shunting for passive vibration damping. In *Proc. SPIE Smart Structures and Materials, Passive Damping and Isolation, SPIE Vol. 3672*, pages 112–122, Huntington Beach, CA, March 1999.

[125] S. Y. Wu. Broadband piezoelectric shunts for structural vibration control. Patent No. 6,075,309, June 2000.

[126] S. Y. Wu. Broadband piezoelectric shunts for passive structural vibration control. In *Proc. SPIE Smart Structure and Materials 2001: Damping and Isolation, SPIE Vol. 4331*, pages 251–261, Newport Beach CA, USA, March 2001.

[127] S. Y. Wu and A. S. Bicos. Structural vibration damping experiments using improved piezoelectric shunts. In *Proc. SPIE Smart Structures and Materials, Passive Damping and Isolation, SPIE Vol. 3045*, pages 40–50, March 1997.

[128] G. Zames. Feedback and optimal sensitivity: Model reference transformations, multiplicitive seminorms, and approximate inverse. *IEEE Transactions on automatic control*, AC-26:301–320, 1981.

[129] J. M. Zhang, W. Chang, V. K. Varadan, and V. V. Varadan. Passive underwater acoustic damping using shunted piezoelectric coatings. *IOP Journal of Smart Materials and Structures*, 10:414–420, 2001.

[130] K. Zhou, J. C. Doyle, and K. Glover. *Robust and Optimal Control*. Prentice Hall, Upper Saddle River, N.J., 1996.